eman ta zabal zazu

Universidad del País Vasco

Euskal Herriko Unibertsitatea

ELECTRO AND MAGNETICALLY ACTIVE POLYMER-BASED HYBRID MICROENVIRONMENTS FOR MUSCLE TISSUE ENGINEERING

Bruno Filipe da Costa Hermenegildo

2022

Supervisors: Dr. Senentxu Lanceros-Méndez

Dra. Leyre Pérez-Álvarez

Acknowledgements

This work was carried out from November 2018 to December 2021 at the Basque Center for Materials, Applications and Structures and at the University of the Basque Country, with various international stays at the University of Minho, in Braga, Portugal. However, its origin, as well as my scientific career, can be traced back to 2010 when, still a Physics grade student, I decided to apply to a Research Initiation Grant and had my first contact with an academic research environment. It was a fascinating moment, and I will be forever grateful to Dr. Elisabete Castanheira for welcoming me into her research group, and to Dr. Ana S. Abreu for the time she took to teach me about the research environment and about that completely new environment and experience, and Dr. Ana Hortelão, not just for her tutoring but for her friendship over the years. It has been a long road, with more than a few bumps and rocky moments over the years, some good choices and some poor ones, but all of these moments in life are moments for growth, realization and development. Never, in my wildest dreams back in 2010, did I come close to imagine I would one day be here.

First of all, I would like to thank University of the Basque Country, for accepting me in the Materials Science and Technology Doctorate. Particularly to the Macromolecular Chemistry Research Group and their leader, Dr. José Luis Vilas-Vilela, for welcoming me and for their constant support and assistance, all the way back from when I first met them, during my ERASMUS stay at UPV/EHU.

I would like to express my thanks to my colleagues at BCMaterials, Ander Reizabal Lopez-Para, Cristian Mendes Felipe, Nélson Castro, Mikel Rincón Iglesias, Fangyuan Zheng and Sheila Maiz Fernández for their constant availability, invaluable assistance and precious friendship during these years. My debt to them is greater than what I can put into words. My gratitude also to Dr. Jose Manuel Laza, Dr. Daniel Salazar Jaramillo, Dr. Javier Reguera, Dr. Javier del Campo, Dr. Eduardo Fernandez, Dr. Roberto Fernandez and Dr. Carmen Rial Tubio for their advice and assistance, often taking time from their own work to assist me.

Acknowledgements

My thanks to my supervisor, Dr. Senentxu Lanceros-Mendez, for actively supporting me during this doctorate at any time I required it, for the shared scientific expertise, ideas and knowledge, and always having an open door to receive me with tranquility and insight when listening to my worries. Thank you for giving me the opportunity to being a part of a fantastic research group. To my co-supervisor, Dr. Leyre Perez-Alvarez, for her assistance and advice, availability and enormous patience.

My heartfelt thanks to Dr. Clarisse Ribeiro, Dr. Daniela Correia, Dr. Pedro Libânio Martins, Dr. Carlos Costa and Dr. Pedro Manuel Martins for their help during my stays in Portugal. And to Rafaela Meira, João Serra and André Macedo for all their precious help. And to my friend, Ana Silva, for her priceless assistance in reviewing many written texts.

To my friends Raul Machado and Nuno Venda, for pushing me to be better and smacking me in the head when I (often!) needed or (more often!) deserved it. To Eduardo Dias and Catarina Ferreira – you have no idea how much I miss our days organizing ENEF (those were the good days!). To Liliana Fernandes and João Teixeira, not only for the many work-related discussions, but for the laughs, jests and mockings over the years, reminding me that laughing at oneself is a balm to the soul. To all my other friends, old and new, for the many advices, for putting up with me during both good and bad times, laughing with me and listening to my rants for all these years. This work is not just the latest step in my personal journey, but in our journey.

In closing, I'd like to dedicate this to the memory of my friend, Pedro Gama. Your unending repository of trivia left us too soon and in a most unfair manner. But the memory of all the fun and laughter, nonsense and wisdom lives forever.

"We are just an advanced breed of monkeys on a minor planet of a very average star. But we can understand the Universe. That makes us something very special."

— Stephen Hawking

"Study hard what interests you the most in the most undisciplined, irreverent and original manner possible."

— Richard P. Feynman

"What an astonishing thing a book is. It's a flat object made from a tree with flexible parts on which are imprinted lots of funny dark squiggles. But one glance at it and you're inside the mind of another person (…). A book is proof that humans are capable of working magic."

— Carl Sagan

"Remember kids, the only difference between screwing around and science is writing it down."

— Adam Savage

Abstract

Polymer scaffolds play an increasing role in tissue engineering (TE), but often their role is merely that of a passive support for cellular development and tissue growth. Thus, they do not take into consideration the various stimuli required by different cells and tissues, and therefore, do not provide an accurate biomimicry of the living microenvironment where the natural growth and development of cells takes place. This results in less-than-optimal results when applying tissue regeneration strategies. The demand for the improvement of the biomimicry of polymer-based cellular microenvironments led to the introduction of smart materials in TE applications, and resulted in relevant advancements in both the knowledge of the suitable conditions for the development of tissues, and in the materials and technologies capable of providing said conditions. Particularly, active scaffolds able to deliver controllable mechanical, piezoelectric, and electric stimuli, have been shown to be of great importance for the development of many types of tissues, such as bone and muscle tissue, due to their increased biomimicry.

In this context, the present thesis focuses on the processing and development of smart polymer-based materials, with various fillers that give them electroactive and magnetoactive response, processed in various morphologies to be used as active scaffolds for TE applications.

Poly(vinylidene fluoride) (PVDF) was selected as a piezoelectric polymer matrix for applications where biodegradability is not a concern or requirement, and was combined with cobalt ferrite ($CoFe_2O_4$) nanoparticles (NP) and magnetite (Fe_3O_4) NPs, coated with polyaniline (PANI) and polypyrrole (PPy) conductive polymers, and blended with choline bis(trifluoromethylsulfonyl) imide ([Chol][TFSI]) and choline acetate ([Chol][Ac]) conductive ionic liquids (IL). PVDF was processed into three different morphologies, microspheres, via electrospraying, fibers by electrospinning, and films using the doctor blade coating technique. For applications where a slow degradation of the materials is required, the piezoelectric polymer poly(hydroxybutyrate-co-hydroxyvalerate) (PHBV) was selected as a polymer matrix, blended with [Chol][Ac] IL, and processed both in fiber morphology, by electrospinning, and as films via doctor blading.

Finally, when a faster degradation is required, poly(lactide-co-glycolide) (PLGA), in a 50:50 monomer ratio, was the selected polymer matrix, and was combined with Fe_3O_4 NPs and blended with [Chol][TFSI] IL, processed by electrospinning in a fiber morphology, and by doctor blade into film morphology.

Through this work, a number of techniques was used to characterize the processed samples. Morphology was evaluated by Scanning Electron Microscopy (SEM), and, when relevant, by Transmission Electron Microscopy (TEM), Energy-dispersive X-ray (EDX), and Atomic Force Microscopy (AFM) as well. The magnetic properties of the samples were assessed by Vibrating Sample Magnetometry (VSM), and an analysis of possible interactions between a polymer matrix and the respective filler was performed by Fourier-Transform Infrared (FTIR) spectroscopy, also allowing for the determination of the electroactive phases of PVDF. Thermal studies were performed with Thermogravimetric Analysis (TGA) and by Differential Scanning Calorimetry (DSC), with DSC being used to determine the crystallinity degree of the polymers. Ionic conductivity measurements were used to evaluate the effect of conductive IL loads in the polymers, and the wettability of the polymers, after inclusion of the various fillers, was assessed by surface contact angle measurements. Finally, cytotoxicity assays were performed to evaluate the biocompatibility of the processed composite samples.

This work begins with the development and optimization of PVDF microspheres with different (20, 30 and 40 wt.%) $CoFe_2O_4$ NP content, that were then incorporated in a Methacrylated Gellan Gum (MAGG) biodegradable hydrogel. The optimized composite spheres with 20 wt.% load of $CoFe_2O_4$ NP presented a mean diameter of ≈1 μm, β-phase contents of ≈78%, a piezoelectric response $|d33|$ of ≈22 $pC.N^{-1}$ and a magnetoelectric response of $\Delta|d33| \approx 6$ $pC.N^{-1}$ at a DC magnetic field of 220 mT. When the spheres were incorporated in the MAGG hydrogel, this hybrid material presented a 20 kPa Young's modulus and cell viability superior to 80%, thus showing suitability to support novel TE strategies based on magnetoelectric microenvironments.

PVDF was also processed into oriented and randomly-oriented fibers, by electrospinning, with different (5, 10 and 15 wt.%) loads of either Fe_3O_4 NPs or [Chol][TFSI] IL. These fillers did not result in significant differences in the morphology of the electrospun fibers or their degradation temperature. Their mean diameter varied between 0.8 and 2 μm, the crystallinity degree between 46 and 59% and the β-phase content between 73 and 88%. The NP content in the fibers had effective experimental yields between 93-97%, and the inclusion of the IL in PVDF matrix increased the conductivity of the polymer from 7.1×10^{-13} $S.cm^{-1}$ to 2.6×10^{-9} $S.cm^{-1}$. These fibers were tested for cytotoxicity and had cellular viability results of over 90%, indicating the cytocompatibility of these materials.

Further work on improving the conductivity of PVDF electrospun fibers was conducted by coating them with polyaniline (PVDF-PANI) and polypyrrole (PVDF-PPy). The surface electrical conductivity of the coatings reached values of σ = 1.19 $S.m^{-1}$ for PVDF-PPy and $\sigma = 3.84\times10^{-3}$ $S.m^{-1}$ for PVDF-PANI. After coating, the fibers became hydrophilic and remained biocompatible, resulting in a slight improvement in the metabolic activity of L929 fibroblasts.

In vivo TE often requires biodegradable materials. Therefore, biodegradable PHBV composites were prepared alongside similar PVDF ones. Electrospun oriented fiber mats, and films by doctor blading, were processed for both PVDF and PHBV and each polymer was blended with different wt.% of [Chol][Ac] (5, 10, 15%). Overall, the mean diameter of the fibers decreased, most noticeable in the case of PHBV fibers. For both polymer matrixes, an increase in the surface roughness of the films was observed, as well as a decrease of the thermal stability and surface wettability upon IL incorporation, regardless of IL content. Ionic conductivity was also increased, by about 3 orders of magnitude for the highest wt.% of IL. Cytocompatibility assays indicated that the wt.% of [Chol][Ac] had to be below 15% in order to use the samples as active scaffolds for TE applications.

Finally, a biodegradable magnetically and electrically active scaffold for TE applications was developed, by mixing the polymer PLGA (in a 50:50 monomer ratio) with Fe_3O_4 NP and [Chol][TFSI] IL. These materials were processed both in the form fiber mats and films, by electrospinning and doctor blading respectively.

Abstract

PLGA+IL fibers present diameters between 1.92-3.26 μm, with PLGA+Fe_3O_4 fibers ranging from 0.62 to 1.36 μm. PLGA membranes presented mean roughness of 3.84 nm, increasing with the inclusion of fillers to 6.58 nm (IL) and 5.07 nm (Fe_3O_4).

The effective NP content yield in the fiber samples varied between 52-78%, with that of the film samples varying between 77-97%. The ionic conductivity for PLGA+IL 15% fibers was 1.11×10^{-10} $S.cm^{-1}$, and 1.44×10^{-10} $S.cm^{-1}$ for PLGA+IL 15% films.

The fillers decreased the mechanical stiffness of the PLGA fibers, and increased that of the PLGA films. The elongation at yield of PLGA films was reduced by both fillers, while that of the PLGA fibers was reduced only by the IL.

Degradability assays under dynamic magnetic stimulation and static conditions were conducted in a bioreactor, with active conditions accelerating the degradation rate of the polymer. Finally, the potential of the materials for TE was evaluated, by analyzing their cytotoxicity for C2C12 myoblasts, with cell viability results of over 70% for the PLGA+Fe_3O_4 samples, in both morphologies, indicating the suitability of these materials for biomedical applications. Only PLGA+IL film samples presented an acceptable toxicity profile for biomedical applications, with all other PLGA+IL film and fiber mats presenting unsuitable results.

Thus, this work demonstrated the successful development, processing and characterization of a variety of composite materials, with electroactive and magnetoactive responses, showing promising properties for TE, particularly in skeletal muscle TE applications.

Resumen

Las matrices poliméricas desempeñan un papel cada vez más importante en la ingeniería de tejidos (TE), pero muchas veces su función es simplemente la de un soporte pasivo para el desarrollo celular y de los tejidos. De hecho, no toman en consideración los diversos estímulos requeridos por diferentes células y tejidos y, por lo tanto, no proporcionan una biomimetización precisa del microambiente vivo donde tiene lugar el crecimiento y desarrollo natural de las células. Esto tiene como consecuencia resultados subóptimos al aplicar estrategias de regeneración de tejidos. La demanda de mejora del biomimetismo de microambientes celulares basados en polímeros llevó a la introducción de los materiales inteligentes en aplicaciones de TE, resultando en avances relevantes en el conocimiento de las condiciones adecuadas para el desarrollo de tejidos y en los materiales y tecnologías adecuadas para proporcionar dichas condiciones. Las matrices activas capaces de proporcionar estímulos mecánicos, piezoeléctricos y eléctricos controlables han demostrado ser de gran importancia para el desarrollo de muchos tipos de tejidos, tales como tejido óseo y muscular, debido a su mayor biomimetismo.

En este contexto, la presente tesis se centra en el procesamiento y desarrollo de materiales a base de polímeros inteligentes, con diferentes cargas que les dan propiedades electroactivas y magnetoactivas, procesados en diversas morfologías para ser utilizados como matrices activas para aplicaciones de TE.

Se seleccionó fluoruro de polivinilideno (PVDF) como matriz de polímero piezoeléctrico para aplicaciones donde la biodegradabilidad no es una preocupación o requisito, y se combinó con nanopartículas (NP) de ferrita de cobalto ($CoFe_2O_4$) y NP de magnetita (Fe_3O_4), se recubrió con los polímeros conductores polianilina (PANI), y polipirrol (PPy), y se mezcló con líquidos iónicos (IL) conductores de bis(trifluorometilsulfonil)imida de colina ([Chol][TFSI]) y acetato de colina ([Chol][Ac]). El PVDF se procesó en tres morfologías diferentes, microesferas, mediante electropulverización, fibras mediante electrohilado y películas utilizando la técnica de la “doctor blade”. Para aplicaciones donde se requiere una degradación lenta de los materiales, se seleccionó poli(3-hidroxibutirato-co-3-hidroxivalerato) (PHBV), también un polímero piezoeléctrico, como matriz polimérica y se mezcló con [Chol][Ac] IL, y se lo ha procesado en fibras, por electrohilado, y como películas mediante “doctor blade”.

Finalmente, para cuando se requiere una degradación más rápida, ácido poli(láctico–co–glicólico) (PLGA), en una proporción de monómero 50:50, fue la matriz polimérica seleccionada, y se combinó con NP de Fe_3O_4 y con el IL [Chol][TFSI], se procesando el material en fibras por electrohilado, y películas mediante "doctor blade".

En este trabajo se utilizaron una serie de técnicas para caracterizar las muestras procesadas. La morfología se evaluó mediante Microscopía Electrónica de Barrido (SEM) y, cuando fue pertinente, mediante Microscopía Electrónica de Transmisión (TEM), Rayos-X de Dispersión de Energía (EDX) y Microscopía de Fuerza Atómica (AFM). Las propiedades magnéticas de las muestras fueron evaluadas por Magnetometría Vibrante de Muestras (VSM), y un análisis de posibles interacciones entre las matrices polimérica y su respectiva carga fue realizada Espectroscopía Infrarroja por Transformada de Fourier (FTIR), que también permitió la determinación de las fases electroactivas de PVDF. Los estudios térmicos se realizaron con Análisis Termogravimétrico (TGA) y Calorimetría Diferencial de Barrido (DSC), utilizándose DSC para determinar el grado de cristalinidad de los polímeros. Se utilizaron medidas de conductividad iónica para evaluar el efecto de las cargas de IL conductor en los polímeros, y se evaluó la mojabilidad de los polímeros, después de la inclusión de las diferentes cargas, mediante mediciones del ángulo de contacto de la superficie. Finalmente, se realizaron ensayos de citotoxicidad para evaluar la biocompatibilidad de las muestras.

Este trabajo empieza con el desarrollo y optimización de microesferas de PVDF con diferentes cargas de $CoFe_2O_4$ NP (20, 30 y 40% en peso), que luego se incorporaron en un hidrogel biodegradable de Goma Gellana Metacrilada (MAGG). Las esferas compuestas optimizadas con 20% en peso de carga de $CoFe_2O_4$ NP, presentaron un diámetro medio de ≈1 μm, contenido de fase β ≈78%, una respuesta piezoeléctrica $|d_{33}|$ de ≈22 $pC.N^{-1}$ y una respuesta magnetoeléctrica de $\Delta |d_{33}|$ ≈6 $pC.N^{-1}$ en un campo magnético de CC de 220 mT. Cuando se incorporaron las esferas en el hidrogel MAGG, este material híbrido presentó un módulo de Young de 20 kPa y una viabilidad celular superior al 80%, mostrando así su potencial para soportar nuevas estrategias de TE basadas en microambientes magnetoeléctricos.

PVDF también se procesó en fibras orientadas y no-orientadas, por electrohilado, con diferentes cargas (5, 10 y 15% en peso) de NP de Fe_3O_4 o de IL [Chol] [TFSI]. Estas cargas no dieron como resultado diferencias significativas en la morfología de las fibras electrohiladas o su temperatura de degradación. Su diámetro medio varió entre 0,8 y 2 μm, el grado de cristalinidad entre 46 y 59% y el contenido en fase β entre 73 y 88%. El contenido de NP en las fibras tuvo rendimientos experimentales efectivos entre 93-97%, y la inclusión de IL en la matriz de PVDF aumentó la conductividad iónica del polímero de 7.1×10^{-13} $S.cm^{-1}$ a 2.6×10^{-9} $S.cm^{-1}$. Estas fibras tuvieron resultados de viabilidad celular de más del 90%, lo que indica la biocompatibilidad de estos materiales.

Se realizó un trabajo adicional para mejorar la conductividad de las fibras electrohiladas de PVDF, recubriéndolas con polianilina (PVDF-PANI) y polipirrol (PVDF-PPy). La conductividad eléctrica superficial de los recubrimientos alcanzó valores de $\sigma = 1.19$ $S.m^{-1}$ para PVDF-PPy y $\sigma = 3.84\times10^{-3}$ $S.m^{-1}$ para PVDF-PANI. Después del recubrimiento, las fibras se volvieron hidrófilas y permanecieron biocompatibles, lo que resultó en una ligera mejora en la actividad metabólica de los fibroblastos L929.

La TE in vivo suele requerir materiales biodegradables. Por lo tanto, se prepararon compuestos de PHBV biodegradables junto con PVDF en condiciones similares. Así, se procesaron fibras orientadas, por electrohilado, y películas, mediante "doctor blade", tanto para PVDF como para PHBV, y cada polímero fue mezclado con diferente (5, 10, 15%) % en peso de [Chol] [Ac]. En general, el diámetro medio de las fibras disminuyó, siendo el diámetro de la fibra PHBV el más afectado por el % en peso de IL. Para ambas matrices de polímero, se observa un aumento en la rugosidad de la superficie de las películas, así como una disminución de la estabilidad térmica y la mojabilidad de la superficie tras la incorporación de IL, independientemente del contenido de IL, y su conductividad iónica aumentó en aproximadamente 3 órdenes de magnitud. Los ensayos de citotoxicidad indican que el % en peso de [Chol] [Ac] tiene que estar por debajo del 15% para utilizar las muestras como matrices activas para aplicaciones de TE.

Finalmente, se desarrollaron matrices biodegradables para aplicaciones de TE, mezclando PLGA (en una proporción de monómero 50:50) con NP de Fe_3O_4 y el IL [Chol][TFSI]. Estos materiales se procesaron en forma de fibras, por electrohilado, y películas por "doctor blade".

Las fibras de PLGA+IL presentan diámetros entre 1,92-3,26 μm, y las de PLGA+Fe_3O_4 van desde 0,62 a 1,36 μm. Las películas de PLGA presentaron una rugosidad media de 3,84 nm, aumentando con la inclusión de cargas a 6,58 nm (IL) y 5,07 nm (Fe_3O_4). El rendimiento de contenido de NP efectivo en las muestras de fibra varió entre 52-78%, y el de las muestras de película varió entre 77-97%. La conductividad iónica de las fibras de PLGA+IL 15% fue de 1.11×10^{-10} $S.cm^{-1}$, y de 1.44×10^{-10} $S.cm^{-1}$ para las películas de PLGA+IL 15%.

Los rellenos disminuyeron la rigidez mecánica de las fibras de PLGA y aumentaron la de las películas de PLGA. El alargamiento en el rendimiento de las películas de PLGA se redujo con ambos rellenos, mientras que el de las fibras de PLGA se redujo solo con el IL.

Los ensayos de degradabilidad bajo estimulación magnética dinámica y condiciones estáticas se realizaron en un biorreactor, con condiciones activas que aceleraban la tasa de degradación del polímero. Finalmente, se evaluó el potencial de los materiales para la TE, analizando su citotoxicidad para mioblastos C2C12, con resultados de viabilidad celular superiores al 70% para las muestras de PLGA+Fe_3O_4, en ambas morfologías, lo que indica la idoneidad de estos materiales para aplicaciones biomédicas. Solo las muestras de película de PLGA+IL presentaron un perfil de toxicidad aceptable para aplicaciones biomédicas, y todas las demás películas y fibras de PLGA+IL presentaron resultados inadecuados para TE.

Por lo tanto, este trabajo demostró con éxito el desarrollo, procesamiento y caracterización de una variedad de materiales composites, con respuestas electroactivas y magnetoactivas, mostrando propriedades prometedoras para TE, particularmente en aplicaciones de TE del músculo esquelético.

Laburpena

Matrize polimerikoek gero eta garrantzi handiagoa dute ehunen ingeniaritzan (TE), baina askotan haien funtzioa zelulen eta ehunen garapenerako euskarri pasiboa besterik ez da. Izan ere, ez dituzte kontuan hartzen zelula eta ehun ezberdinek behar dituzten hainbat estimulu eta, beraz, ez dute zelulen hazkuntza eta garapen naturala gertatzen den mikroingurune biziaren biomimetismo zehatzik ematen. Horrek ehunak birsortzeko estrategiak aplikatzean emaitza ez-optimoak eragiten ditu. Polimeroetan oinarritutako mikroingurune zelularren biomimetismoa hobetzeko eskariak, material adimendunak TE aplikazioetan sartzea ekarri zuen. Honek aurrerapen garrantzitsuak ekarri zituen ehunak garatzeko baldintza egokien ezagutzan eta baldintza egoki hauek sorrarazteko behar diren material eta teknologien ezagutzan. Estimulu mekaniko, piezoelektriko eta elektriko kontrolagarriak emateko gai diren matrize aktiboek garrantzi handia dutela frogatu dute ehun mota askoren garapenerako, hala nola hezur eta gihar ehunen, biomimetismo handiagoa baitute.

Testuinguru honetan, tesi honek polimeroetan oinarritutako material adimendunen prozesamenduan eta garapenean oinarritzen da, propietate elektroaktiboak eta magnetoaktiboak ematen dizkieten karga ezberdinekin, hainbat morfologiatan prozesatutako TE aplikazioetarako matrize aktibo gisa erabiltzeko.

Polibinilideno fluoruroa (PVDF) polimero-matrize piezoelektriko gisa hautatu zen biodegradagarritasuna kezka edo eskakizuna ez den aplikazioetarako. PVDF kobalto ferrita ($CoFe_2O_4$) eta magnetita (Fe_3O_4) NP-ekin konbinatu zen, eta polimero eroalez, polianilinaz (PANI) eta polipirrolaz (PPy) estali zue, eta kolin bis(trifluorometilsulfonil)imida ([Chol][TFSI]) eta kolina acetato ([Chol][Ac]) likido ionikoekin (IL) nahastu zen. PVDFa hiru morfologia ezberdinetan prozesatu zen, mikroesferak elektrospray bidez, zuntzak elektrospinning bidez eta filmak "doctor blade" teknika erabiliz. Materialen degradazio motela behar den aplikazioetarako, poli(3-hidroxibutirato-ko-3-hidroxivaleratoa) (PHBV), polimero piezoelektrikoa ere, matrize polimeriko gisa hautatu zen eta [Chol][Ac]IL-rekin nahastu zen, zuntzetan prozesatuz, elektrospinning bidez eta film gisa "doctor blade" bidez.

Azkenik, degradazio azkarragoa behar denean, azido poli(laktiko-ko-glikolikoa) (PLGA), 50:50 monomero proportzioan, hautatuzen matrize polimeriko bezala, eta Fe_3O_4 NP-ekin eta [Chol][TFSI], likido ionikoarekin konbinatu zen. Materiala elektrospinning bidez zuntz moduan prozesatu zen, eta film moduan "doctor blade" bidez.

Lan honetan, prozesatutako laginak karakterizatzeko hainbat teknika erabili dira. Morfologia, Ekorketa-Mikroskopia Elektronikoaren (SEM) eta, dagokionean, Transmisioko Mikroskopia Elektronikoaren (TEM), X Izpien Energia Dispertsioaren (EDX) eta Indar Atomikoaren Mikroskopiaren (AFM) bidez ebaluatu zen. Laginen propietate magnetikoak Langin Dardarkariaren Magnetometriaren (VSM) bidez ebaluatu ziren. Matrize polimerikoen eta dagozkien kargaren arteko elkarreraginaren azterketa Fourier-en eraldaketako Infragorrien Espektroskopiaren (FTIR) bidez egin zen, eta honek ere PVDF laginen fase elektroaktiboak zehaztea ahalbidetu zuen. Azterketa termikoak Analisi Termograbimetrikoarekin (TGA) eta Ekorketa-kalorimetria diferentzialarekin (DSC) egin ziren, azken hau polimeroen kristalinitate-maila zehazteko. Eroankortasun ionikoaren neurketak erabili ziren likido ionikoen karga eroaleek polimeroetan duten eragina ebaluatzeko. Polimeroen hezegarritasuna, karga desberdinak sartu ondoren, gainazaleko ukipen-angeluaren neurketen bidez ebaluatu zen. Azkenik, zitotoxikotasun probak egin ziren laginen biobateragarritasuna ebaluatzeko.

Lan hau $CoFe_2O_4$ NP karga desberdinak (%20, 30 eta 40 pisuan) dituzten PVDF mikroesferen garapenarekin eta optimizazioarekin hasten da, eta ondoren Metacrilate Gellana Goma (MAGG) hidrogel biodegradagarri batean sartu zirenak. $CoFe_2O_4$ NPren %20 pisuko kargarekin, optimizatutako esfera konposatuek, ≈1 μm-ko batez besteko diametroa aurkeztu zuten, β-fasearen edukia ≈78koa, erantzun piezoelektrikoa |d33| ≈22 $pC.N^{-1}$-koa eta Δ |d33| erantzun magnetoelektrikoa ≈6 $pC.N^{-1}$-koa 220 mT-ko DC eremu magnetiko batean. Esferak MAGG hidrogelean sartu zirenean, material hibrido honek 20 kPa-ko Young-en modulua eta % 80 baino handiagoko zelulen bideragarritasuna aurkeztu zuen, eta ondorioz, mikroingurune magnetoelektrikoetan oinarritutako ET estrategia berriak ahalbidetzeko gaitasuna erakutsi zuen.

PVDF zuntz orientatuetan eta ez-orientatuetan ere prozesatu zen, elektrospinning bidez, Fe_3O_4 NP edo [Chol][TFSI likido ionikoaren karga ezberdinekin (%5, 10 eta 15 pisuan). Karga hauek ez zuten elektro-irundako zuntzen morfologian edo haien degradazio-tenperaturan alde handirik eragin. Bere batez besteko diametroa 0.8 eta 2 μm artean aldatu zen, kristalinitate maila %46 eta %59 artean eta β-fasearen edukia %73 eta %88 artean. Zuntzetako NP edukiak %93-97 arteko etekin esperimental eraginkorra izan zuen, eta PVDF matrizean likido ionikoa sartzeak polimeroaren eroankortasun ionikoa 7.1×10^{-13} $S.cm^{-1}$-tik 2.6×10^{-9} $S.cm^{-1}$-era igo zuen. Zuntz hauek %90 baino handiagoko zelulen bideragarritasunak izan zituzten, material horien biobateragarritasuna adieraziz.

PVDF elektro-irundako zuntzen eroankortasuna hobetzeko lan osagarri bat egin zen, polianilinarekin (PVDF-PANI) eta polipirrolarekin (PVDF-PPy) estaliz. Estalduren gainazaleko eroankortasun elektrikoa $\sigma = 1.19$ $S.m^{-1}$ baliora iritsi zen PVDF-PPyrako eta $\sigma = 3.84\times10^{-3}$ $S.m^{-1}$ PVDF-PANIrako. Estaldu ondoren, zuntzak hidrofilo bihurtu ziren eta biobateragarriak izaten jarraitu zuten, L929 fibroblastoen jarduera metabolikoaren hobekuntza txiki bat eraginez.

In vivo TEek material biodegradagarriak behar ditu normalean. Hori dela eta, PHBV konposatu biodegradagarriak PVDFrekin batera prestatu ziren antzeko baldintzetan. Orientatutako zuntzak, elektrospinning bidez, eta filmak, "doctor blade", prozesatu ziren bai PVDFrako bai PHBVrako, polimero bakoitza [Chol] [Ac] ehuneko (%5, 10, 15 pisuan) desberdinekin nahastuta. Oro har, zuntzen batez besteko diametroa gutxitu egin zen, PHBV zuntzaren diametroa likido ionikoaren % pisuaren eraginpean gehien eragin zuena. Bi polimero-matrizei dagokienez, filmen gainazaleko zimurtasunaren igoera behatu zen, baita egonkortasun termikoaren eta gainazaleko hezegarritasunaren beherakada ere ikusi ziren likido ionikoa sartu ondoren, likido ionikoaren edukia edozein dela ere, eta bere eroankortasun ionikoa 3 magnitude ordenean inguru handitu zen. Zitotoxikotasunaren saiakuntzek adierazten zuten [Chol][Ac]-ren edukia %15etik beherakoa (pisuan) izan behar zela laginak TE aplikazioetarako matrize aktibo gisa erabili ahal izateko.

Azkenik, TE aplikazioetarako matrize biodegradagarriak garatu ziren PLGA (50:50 monomero proportzioan) Fe_3O_4 NP-ekin eta [Chol][TFSI] IL-rekin nahastuz. Material hauek zuntz moduan prozesatu ziren, elektrospinning bidez, eta filmak "doctor blade" bidez.

Laburpena

PLGA+IL zuntzek 1.92-3.26 μm arteko diametroak izan zituzten, eta PLGA+Fe_3O_4 zuntzek 0.62 eta 1.36 μm bitartekoak. PLGA filmek 3.84 nm-ko batez besteko zimurtasuna aurkeztu zuten, kargak sartzean 6.58 nm-tara (IL) eta 5.07 nm-tara (Fe_3O_4) handituz. Zuntz-laginetan NP eduki eraginkorra % 52-78 bitartekoa izan zen, eta film-laginena % 77-97 bitartekoa. PLGA+IL %15eko zuntzen eroankortasun ionikoa 1.11×10^{-10} $S.cm^{-1}$-koa izan zen, eta 1.44×10^{-10} $S.cm^{-1}$-koa PLGA+IL %15eko filmetan. Estimulazio magnetiko dinamikopeko eta baldintza estatikopeko degradagarritasun-probak bioerreaktore batean egin ziren, polimeroaren degradazio-tasa bizkortu zuten baldintza aktiboak ezarriz. Azkenik, materialek TErako duten potentziala ebaluatu zen, C2C12 mioblastoetarako duten zitotoxikotasuna aztertuz, PLGA+Fe_3O_4 laginetarako zelulen bideragarritasun emaitzek %70 baino handiagoak izanik, bi morfologietan, eta horrek material hauek aplikazio biomedikoetarako egokiak direla adierazten du. PLGA+IL film laginek soilik toxikotasun-profil onargarria aurkeztu zuten aplikazio biomedikoetarako, eta beste PLGA+IL filmek eta zuntzek emaitza desegokiak izan zituzten TErako.

Hori dela eta, lan honek arrakastaz frogatu du hainbat material konposatuen garapena, prozesaketa eta karakterizazioa, erantzun elektroaktibo eta magnetoaktiboekin, TErako proprietitate oparoak erakusten dute, bereziki muskulu hezurmamitsuetako TE aplikazioetan.

Table of Contents

Acknowledgements I

Abstract V

Resumen IX

Laburpena XIII

Table of Contents XVII

List of Figures XXIII

List of Tables XXXI

List of abbreviations, symbols and acronyms XXXIII

Chapter 1. Introduction 1

1.1. Materials and Mankind 3

1.2. Smart and multifunctional materials 8

1.2.1. Electroactive smart polymers 12

1.2.2. Challenge – biodegradability 13

1.3. Biomedical advancements - Tissue engineering 15

1.3.1. Skeletal muscle tissue engineering 18

1.3.2. Polymers for tissue engineering 20

1.3.2.1. Morphologies and processing 20

1.3.2.2. Poly(vinylidene fluoride) 23

1.3.2.3. Poly(hydroxybutyrate-co-hydroxyvalerate) 26

1.3.2.4. Poly(lactic-co-glycolide) 27

1.3.3. Composite smart materials for tissue engineering 28

1.3.3.1. Nanoparticle-based smart materials 29

1.3.3.2. Ionic liquid-based smart materials 32

1.4. General objectives and work plan 35

1.5. References 38

Chapter 2. Hydrogel-based magnetoelectric materials for tissue stimulation 61

2.1. Introduction 63

2.2. Experimental 65

2.2.1. Materials 65

2.2.2. Sample processing 66

2.2.3. Sample characterization 68

2.3. Results and discussion 71

2.3.1. Morphological features and vibrational spectra 71

2.3.1.1. Morphology 71

2.3.1.2. Vibrational spectra 73

2.3.2. Mechanical properties 74

2.3.3. Functional response 75

2.3.3.1. Magnetic properties 75

2.3.3.2. Cytotoxicity assay 76

2.4. Conclusions 78

2.5. References 79

Chapter 3. Tuning magnetic and ionic response of hybrid fibers 87

3.1. Introduction 89

3.2. Experimental 91

3.2.1. Materials 91

3.2.2. Sample processing 91

3.2.2.1. Solution preparation 91

3.2.2.2. Electrospinning 92

3.2.3. Sample characterization 93

3.2.3.1. *In vitro* cytotoxicity assay 94

3.3. Results and discussion 96

3.3.1. Morphological features and vibrational spectra 96

3.3.1.1. Morphology 96

3.3.1.2. Vibrational spectra 99

3.3.2. Thermal properties 101

3.3.3. Functional response 104

3.3.3.1. Ionic conductivity 104

3.3.3.2. Magnetic properties 105

3.3.3.3. Cytotoxicity assay 106

3.4. Conclusions 107

3.5. References 109

Chapter 4. Coated electrospun fiber mats for tissue regeneration applications 117

4.1. Introduction 119

4.2. Experimental 121

4.2.1. Materials 121

4.2.2. Sample processing 121

4.2.2.1. Electrospinning of PVDF 121

4.2.2.2. Coating of the PVDF fibers by PANI and PPy 122

4.2.3. Sample characterization 123

4.3. Results and discussion 125

4.3.1. Morphological features, Raman spectra and wettability 125

4.3.1.1. Morphology 125

4.3.1.2. Raman spectra 127

4.3.1.3. Wettability 128

4.3.2. Functional response 129

4.3.2.1. Conductivity 129

4.3.2.2. Cytotoxicity assay 130

4.4. Conclusions 131

4.5. References 132

Chapter 5. Ionic liquid modified microenvironments for biomedical applications 139

5.1. Introduction 141

5.2. Experimental 143

5.2.1. Materials 143

5.2.2. Sample processing 144

5.2.2.1. Solution preparation 144

5.2.2.2. Electrospun fiber processing 144

5.2.2.3. Film preparation 145

5.2.3. Sample characterization 145

5.2.3.1. Physico-chemical characterization 145

5.2.3.2. *In vitro* cytotoxicity Assay 147

5.3. Results and discussion 148

5.3.1. Morphological features, vibrational spectra and wettability 148

5.3.1.1. Morphology 148

5.3.1.2. Vibrational spectra 153

5.3.1.3. Surface wettability 154

5.3.2. Thermal properties 156

5.3.3. Functional response 160

5.3.3.1. Ionic conductivity 160

5.3.3.2. Cytotoxicity assay 162

5.4. Conclusions 163

5.5. References 164

Chapter 6. Advanced biodegradable microenvironments for tissue regeneration applications 173

6.1. Introduction 175

6.2. Experimental 177

6.2.1. Materials 177

6.2.2. Sample Processing 177

6.2.2.1. Pristine and composite films 177

6.2.2.2. Pristine and composite electrospun fibers 178

6.2.3. Sample characterization 180

6.3. Results and discussion 183

6.3.1. Morphological features, vibrational spectra and wettability 183

6.3.1.1. Morphology 183

6.3.1.2. Vibrational spectra 188

6.3.1.3. Wettability 189

6.3.2. Thermal and mechanical properties 190

6.3.2.1. Thermal properties 190

6.3.2.2. Mechanical Properties 193

6.3.3. Functional response 195

6.3.3.1. Ionic Conductivity 195

6.3.3.2. Magnetic properties 196

6.3.3.3. Cytotoxicity and degradability assays 198

6.4. Conclusions 202

6.5. References 203

Chapter 7. Conclusions and Future Work 213

7.1. Conclusions 215

7.2. Future work 217

Curriculum Vitae & Contributions 223

Copyright and Licencing information 233

List of Figures

Figure 1.1. Materials and the Ages, as Mankind discovers and evolves, supported by previous achievements and knowledge. 3

Figure 1.2. Examples of natural polymers: a) DNA, b) silk cocoons. Examples of synthetic polymers: c) nylon socks; d) polyvinyl chloride duck. 4

Figure 1.3. a) Copper statue of Pharaoh Pepi I (Cairo Museum); b) depiction of the Colossus of Rhodes (Maarten Heemskerck, Phillips Gale, 1572); c) Indonesian blacksmiths forging a blade. 6

Figure 1.4. Increase in surface-to-volume ratio, for increasingly smaller material sizes, an inevitability in nanotechnology. 7

Figure 1.5. The application of electric stimuli results in the exemplified deformation (bending) of a previously straight electroactive polymer. 12

Figure 1.6. Total tons of waste generated, per capita, in the EU and some of its member-states, per year. [33] 14

Figure 1.7. Scaffold strategy in tissue engineering: A) retrieval of donor cells from patient; B) *in vitro* cell culture; C) development of scaffold; D) encapsulation of cells in scaffold, for immediate use or *in vitro* development of tissue and E) implantation of scaffold, or *in vitro* developed tissue, in patient. 17

Figure 1.8. Schematic representation of the electrospinning process. 21

Figure 1.9. Photographs of a) Taylor cone and fiber formation during electrospinning; b) detail of the Taylor cone. 22

Figure 1.10. Photograph of a thickness-adjustable doctor blade. 22

Figure 1.11. Chemical representation of a PVDF monomer unit 23

Figure 1.12. Representation of the chain conformation for the three most studied phases of PVDF 24

Figure 1.13. Representation of the PHBV polymer 26

Figure 1.14. Representation of the PLGA copolymer, in the 50:50 formulation. 28

Figure 1.15. Crystallographic representation of the inverse spinel structure of $CoFe_2O_4$ and Fe_3O_4. 31

Figure 1.16. Application areas of IL/polymer-based multifunctional materials 33

Figure 1.17. Representation of the [Chol][Ac] IL. 34

Figure 1.18. Representation of the [Chol][TFSI] IL. 35

Figure 2.1. Schematic representation of the electrospraying process 67

Figure 2.2. Size distribution of: a) pure PVDF spheres with 3% w/v polymer solution; b) PVDF+$CoFe_2O_4$ 20%, c) PVDF+$CoFe_2O_4$ 40 wt.%. d) Tukey-style boxplot with the size distribution variations of the samples. 71

Figure 2.3. TEM images of the PVDF+$CoFe_2O_4$ 40 wt.% composite spheres, with the polymer in shades of grey and the magnetic NPs in black. 72

Figure 2.4. a) FTIR spectra of pure PVDF and PVDF+$CoFe_2O_4$ composites microspheres; b) Variation of β-phase content as a function of $CoFe_2O_4$ content. The values are presented as media ± standard deviation, n =3. 73

Figure 2.5. Stress/Strain curves of MAGG hydrogel, at a compression rate of 1.7% height.min^{-1}, with: a) 0, b) 1 and d) 2 wt.% of PVDF+$CoFe_2O_4$ 20% microspheres; and d) 1 wt.% of PVDF+$CoFe_2O_4$ 20 wt.% composite microspheres, between 0 % and 10 % strain, with linear fit and inset with associated data the fit. 74

Figure 2.6. a) RT hysteresis loops for the composite PVDF+$CoFe_2O_4$ spheres. Inset: RT hysteresis loop for the pure $CoFe_2O_4$ NPs; b) Relation between the wt.% of $CoFe_2O_4$ NPs in solution and those in the multiferroic spheres, with the blue dashed line indicating the ideal linear theoretical behavior. 76

Figure 2.7. Live/Dead fluorescence images for the initial test with the MC3T3-E1 cells: a) negative control, b) positive control and c) with PVDF+ $CoFe_2O_4$ 20 wt.% microspheres. d) Live/Dead results, in terms of average cell survivability. 77

Figure 3.1. During electrospinning the PVDF solution is stretched while the solvent evaporates, forming thin fibers 92

Figure 3.2. Preparation for cell culture prior to cytotoxicity assay _____ 95

Figure 3.3. Representative PVDF electrospun fiber mats: a) PVDF-O; b) PVDF-O+IL 15%; c) PVDF-R; d) PVDF-R+IL 15% (red arrows indicate fused fibers); e) PVDF-O+Fe_3O_4 5%; f) PVDF-O+Fe_3O_4 15%. _____ 97

Figure 3.4. Tukey-style boxplot with the diameters of the electrospun fibers (background: PVDF-R+IL 10%). _____ 98

Figure 3.5. a) Representative FTIR spectra of the samples, neat Fe_3O_4 and [Chol][TFSI]; b) Variation of the β-phase content of the samples as function of the filler content. _____ 99

Figure 3.6. a) Comparison of DSC thermographs of representative microfiber mats; b) Variation of the degree of crystallinity of the samples as function of filler content. _____ 101

Figure 3.7. a) Representative TGA thermographs of the different microfibers, with and without fillers; b) Variation of the onset temperature of the samples as function of their filler content. _____ 102

Figure 3.8. Remaining char after TGA analysis of a PVDF+Fe_3O_4 15% fiber sample. _____ 103

Figure 3.9. a) Nyquist plot of PVDF with 15% of IL at RT, and b) Arrhenius plots for the ionic conductivities of neat PVDF and PVDF with 15wt% of IL electrospun membranes. 104

Figure 3.10. a) RT hysteresis loops for the PVDF+Fe_3O_4 microfiber composites. Inset: RT hysteresis loop for pure Fe_3O_4 NP. b) Relation between the wt.% of Fe_3O_4 NP within the solution and those within the microfibers, with the blue dashed line indicating the linear theoretical behavior. _____ 105

Figure 3.11. Cytotoxicity assay of L929 fibroblast cells in contact with the as-prepared extraction media exposed to the different samples for 72 h. _____ 107

Figure 4.1. Chemical structures for: a) PANI; b) PVDF; c) PPy. _____ 122

Figure 4.2. Representative SEM images of the hybrid fibers: a, b) PVDF-PANI; c, d) PVDF-PPy. Representative EDX distribution maps of the coatings, indicated by the presence of the N element in fibers of: e) PVDF-PANI; f) PVDF-PPy. _____ 125

Figure 4.3. Tukey-style box plot with the diameters of the coated and uncoated fibers ___ 126

Figure 4.4. Raman spectra of PVDF-PANI and PVDF-PPy fibers: a) Spectra of PVDF, PET/ITO and PANI-salt included for comparison. Laser excitation line 633 nm. b) Spectra of PVDF, PET/ITO, PPy-salt and PANI-salt included for comparison. Laser excitation line 514 nm. 127

Figure 4.5. Absorption of a water droplet on a PVDF+PANI fiber mat, at 4 second intervals 128

Figure 4.6. IV-curves of PVDF-PPy and PVDF-PANI. 129

Figure 4.7. Cytotoxicity assay of L929 fibroblast cells in contact with the extraction media exposed to the different samples for 72 h (n = 4 ± standard deviation). 130

Figure 5.1. SEM images of PVDF and PHBV fiber and film samples: Electrospun fibers of a) PVDF; b) PVDF+IL 5%; c) PVDF+IL 15%; d) PHBV; e) PHBV+IL 5%; f) PHBV+IL 15%. Films of: g) PVDF; h) PVDF+IL 5%; i) PVDF+IL 15%; j) PHBV; k) PHBV+IL 5%; l) PHBV+IL 15%. 148

Figure 5.2. Tukey-style box plot with the diameters for PVDF+IL and PHBV+IL fibers, incorporating 5, 10 and 15 wt.% of IL [Chol][Ac] (background: PHBV+IL 5% fibers). 150

Figure 5.3. Representative EDX distribution maps of the IL in the processed samples, indicated by the presence of the N element for: PVDF+15% IL a) fibers and b) film; and for PHBV+15% IL c) fibers and d) film. 151

Figure 5.4. Representative AFM surface 3D images of the films: a) PVDF; b) PVDF+IL 15%; c) PHBV; d) PHBV+IL 15%. 152

Figure 5.5. FTIR spectra of IL, PVDF and PHBV and their IL based composites comprising 15 wt.% of [Chol][Ac]: a) PVDF and PHBV fibers; b) PVDF and PHBV films. Arrows indicate areas where the influence of the IL was detected. c) Variation of the β-phase content of the PVDF samples as function of IL content. 154

Figure 5.6. Comparison of CA measurements of a) PVDF; b) PHBV samples. 155

Figure 5.7. Representative DSC thermograms for neat PVDF and PHBV and the corresponding composites with 15 wt.% IL content: a) electrospun fibers; and b) films. Arrows indicate areas where IL influence was detected. c) Variation of the degree of crystallinity of the samples as function of IL content in the different samples. _____ 156

Figure 5.8. Representative TGA thermographs of PHBV and PVDF neat and the corresponding composites: a) fibers and b) films. Variation of the onset temperature, as function of IL filler content for c) fibers and d) films. _____ 159

Figure 5.9. a) Nyquist plot at RT for the PVDF and PHBV samples with 15% wt. [Chol][Ac] content (inset: detail of the plot for the PHBV electrospun mats). b) Arrhenius plots for the ionic conductivities of the different samples with 15% of [Chol][Ac]. _____ 161

Figure 5.10. Viability assay of C2C12 myoblast cells in contact with extraction media exposed to the different processed samples for 72 h: a) PHBV samples; and b) PVDF samples. (Relative cell activity presented as percentage of the negative control with n = 4 ± Standard Deviation). _____ 162

Figure 6.1. Effect of the solvent on the electrospinnability of PLGA. a) PLGA with 5 wt.% Fe_3O_4, in CF-DMF binary-solvent; b) PLGA with 5 wt.% Fe_3O_4, in DMF-THF binary-solvent. Note the scale and the absence of merged fibers in b). _____ 179

Figure 6.2. Magnetic bioreactor [30, 31] utilized to provide active magnetic stimuli to the processed samples _____ 183

Figure 6.3. Representative SEM images of the samples. Surface of electrospun fiber mats: a) PLGA1; b) PLGA1+IL 5%; c) PLGA1+IL 15%; d) PLGA2; e) PLGA2+Fe_3O_4 5%; f) PLGA2+Fe_3O_4 15%. Cross-section of the films: g) PLGA; h) PLGA+IL 5%; i) PLGA+IL 15%; j) PLGA+Fe_3O_4 5%; k) PLGA+Fe_3O_4 15%. _____ 184

Figure 6.4. Tukey-style box plot with the diameters of the processed fibers (background: PLGA2+Fe_3O_4 15% fibers). _____ 185

Figure 6.5. Representative EDX distribution maps of the fillers in samples of PLGA1+15% IL a) fibers and b) film; PLGA2+15% Fe_3O_4 c) fibers and d) film. _____ 186

Figure 6.6. 3D AFM topographic images of the surface of the films: a) PLGA; b) PLGA+IL 15%; c) PLGA+Fe_3O_4 15%. d) Phase-lift MFM of the PLGA+Fe_3O_4 15%. _____ 187

Figure 6.7. Representative FTIR-ATR spectra for PLGA+IL and PLGA+Fe_3O_4: a) electrospun fibers and b) films. [Chol][TFSI] and Fe_3O_4 spectra are provided as well. Arrows indicate areas where the influence of the fillers was detected_____ 188

Figure 6.8. CA measurements of neat PLGA (1 and 2), PLGA+IL and PLGA+Fe_3O_4 for a) electrospun fiber mats and b) films. _____ 189

Figure 6.9. Representative DSC thermograms for a) electrospun fiber mats, and b) films (inset, thermogram for [Chol][TFSI]). Representative TGA curves for: c) electrospun fiber mats (inset, for Fe_3O_4 NPs), and d) films. Variation of the onset temperature for polymer degradation as function of filler wt.% for: e) electrospun fiber mats and f) films._____ 191

Figure 6.10. Representative stress/strain curves for: a) fibers (inset, detail of curves at low strain), and b) films (detail of curves at low strain). Young Modulus as a function of filler wt.% for: c) fibers and d) films. Elongation at yield as a function of filler wt.% for e) fibers and f) films.194

Figure 6.11. a) Nyquist plot at RT and b) Arrhenius plots for the ionic conductivities of PLGA+IL electrospun membranes and films. _____ 195

Figure 6.12. RT hysteresis loops for: a) PLGA2+Fe_3O_4 fiber mats, and b) PLGA+Fe_3O_4 films; left inset: Detail of the respective hysteresis loops; right inset: RT hysteresis loop for pure Fe_3O_4 NP. Relation between the wt.% of Fe_3O_4 NP within the solution and those within: c) PLGA2+Fe_3O_4 fibers, and d) PLGA+Fe_3O_4 films. The blue dotted line indicates the linear theoretical behavior. _____ 197

Figure 6.13. Cell viability assay of C2C12 myoblast cells after 72 h for PLGA samples with: a) IL; b) Fe_3O_4 (Relative cell activity presented as percentage of the negative control with n = 4 ± SD). _____ 199

Figure 6.14. Mass loss from active and passive degradability assays for the PLGA samples. 200

Figure 6.15. a) Samples before the assay. Representative photos, after 14-day degradation assay, of: b) PLGA2 fibers with active stimuli; c) PLGA2 fibers; d) PLGA film with active stimuli; e) PLGA film; f) PLGA2+Fe_3O_4 15% fibers with active stimuli; g) PLGA2+Fe_3O_4 15% fibers; h) PLGA+Fe_3O_4 15% films af with active stimuli; i) PLGA+Fe_3O_4 15% films. _____ 201

List of Tables

Table 1.1. Some synthesis methods for preparing smart materials _____ 9

Table 1.2. Classification of smart materials according to the stimulus they are sensitive to and their response to said stimuli _____ 11

Table 3.1. Melting and onset temperatures for the different processed samples. The associated error is ± 2%. _____ 103

Table 3.2. NP yields in the PVDF-O Fe_3O_4 composite fibers. _____ 106

Table 5.1. Electrospinning conditions for the prepared PHBV and PVDF fiber mats and the corresponding composites with [Chol][Ac]. _____ 145

Table 5.2. Roughness data of representative samples. _____ 152

Table 5.3. Summary of the CA measurements for polymer samples. _____ 155

Table 5.4. T_m for PVDF and PHBV samples. Associated error of ± 2%. _____ 157

Table 5.5. Onset temperatures for the different samples. Associated error of ± 2%. _____ 160

Table 5.6. Ionic conductivity values (σ_i) and the corresponding apparent activation energy (E_a) at RT for the different composites. Associated error of ± 3%. _____ 161

Table 6.1. Electrospin conditions for the prepared fibers. _____ 179

Table 6.2. Properties of the solvents used in this study (η is the viscosity, ε is the dielectric constant, σ the conductivity and δ is the solubility parameter [27] _____ 180

Table 6.3. Roughness data of the representative samples (Sq is RMS roughness and Sa is Mean roughness) _____ 188

Table 6.4. Onset temperatures for the film samples. Associated error of ± 2% _____ 192

Table 6.8. NP yields in the PLGA Fe_3O_4 composite fibers. _____ 198

List of abbreviations, symbols and acronyms

[Ac]	Acetate anion
[Chol]	Choline cation
[Chol][Ac]	Choline Acetate
[Chol][TFSI]	Choline bis(trifluoromethylsulfonyl)imide
σ	Electric conductivity
σ_i	Ionic conductivity
0D	Zero-dimensional
1D	One-dimensional
2D	Two-dimensional
3D	Three-dimensional
AFM	Atomic Force microscope
ATR	Attenuated Total Reflection
CA	Surface contact angle
CF	Chloroform
cGG	Commercial gellan gum
DALY	Disability-adjusted life year
DMEM	Dulbecco's modified Eagle's medium
DMF	Dimethylformamide
DMSO	Dimethyl sulfoxide
DSC	Differential Scanning Calorimetry
DTGS	Deuterated triglycine sulfate
E_a	Apparent activation energy
ECM	Extracellular matrix

EDQM	European Directorate for the Quality of Medicines & HealthCare
EDS	Energy Dispersive Spectroscopy
EEAP	Electronic electroactive polymers
EHD	Electrohydrodynamic
EMA	European Medicines Agency
FBS	Fetal bovine serum
FDA	US Food and Drug Administration
FTIR	Fourier-Transform Infrared Spectroscopy
GBD	Global Burden of Diseases, Injuries and Risk Factors Study
IEAP	Ionic electroactive polymers
IL	Ionic liquid
MAGG	Methacrylated Gellan Gum
ME	Magnetoelectric effect
M_H	Magnetization along the direction of the magnetic field H
MOF	Metal-organic frameworks
M_S	Magnetization saturation
MSD	Musculoskeletal disorders
MTS	(3-(4-5-dimethylthiazol-2-yl)-5-(3-carboxymethoxyphenyl)-2-(4-sulfophenyl)-2H-tetrazolium)
Mw	Molecular weight
NM	Nanomaterial
NMP	N-methyl-2-pyrrolidone
NP	Nanoparticle
P/S	Penicillin/streptomycin
PANI	Polyaniline

PBS	Phosphate-buffered saline
PEDOT	Poly(3-4-ethylenedioxythiophene)
PET/ITO	Indium-tin-oxide-coated poly(ethylene terephthalate) foil
PGA	Poly(glycolic acid)
PHB	Polyhydroxybutyrate
PHBV	Poly(hydroxybutyrate-co-hydroxyvalerate)
PLA	Poly(lactic acid)
PLGA	Poly(lactide-co-glycolide)
PLGA1	Electrospun PLGA fibers prepared with 60:40 CF/DMF co-solvent system
PLGA2	Electrospun PLGA fibers prepared with 50:50 DMF/THF co-solvent system
PPy	Polypyrrole
PTFE	Polytetrafluoroethylene
PU	Polyurethane
PVDF	Poly(vinylidene fluoride)
PVDF-O	Oriented PVDF fibers
PVDF-PANI	PANI coated PVDF fibers
PVDF-PPy	PPy coated PVDF fibers
PVDF-R	Randomly-oriented PVDF fibers
PVDF-TrFE	Poly(vinylidene fluoride-co-trifluoroethylene)
RT	Room temperature
S_a	Mean roughness
SEM	Scanning Electron Microscope
S_q	RMS roughness
TE	Tissue Engineering

TEM	Transmission Electron Microscope
[TFSI]	Bis(trifluoromethylsulfonyl)imide anion
TGA	Thermogravimetric Analysis
THF	Tetrahydrofuran
T_m	Melting temperature
v/v	Volume/Volume
VLM	Volumetric muscle loss
VSM	Vibrating Sample Magnetometer
w/v	Weight/volume
wt.%	Weight percentage
X_C	Crystallinity content

Chapter 1

Introduction

Evolution of materials through History.

From the first arrowheads made by knapping or chipping stone, to the modern synthetic and composite materials used in cutting edge medicine, the evolution of materials has shaped and accompanied Human History. Nowadays, most of the evolution in science, society and lifestyle are related to new advancements in Materials Science. Micro- and nanostructured materials, in particular, allowed for unprecedented improvements in modern life.

1.1. Materials and Mankind

Materials, which can be defined as objects composed by one substance or a mixture of substances, can have many origins and classifications – they can be natural or synthetic, can be classified by their use (*e.g.*, refractory, building, nuclear, biomaterial), properties (*e.g.*, stiffness, thermal conductivity, magnetism, transparency, toxicity), or their structure (*e.g.*, ceramic, metallic, polymeric, crystalline).

However, one common element to all materials is their importance to the evolution of Mankind. So much so that our very Pre- and Proto-History is divided in Ages bearing the name of the most important materials used in those periods, such as the Stone Age, the Bronze Age or the Iron Age [1], a practice that is sometimes repeated when referring to later eras, with the naming of some particular periods after a specific material of great impact at the time (**Figure 1.1**), such as is the case of the Atomic Age or, the most recent, the Silicon Age or Electronic Materials Age [1].

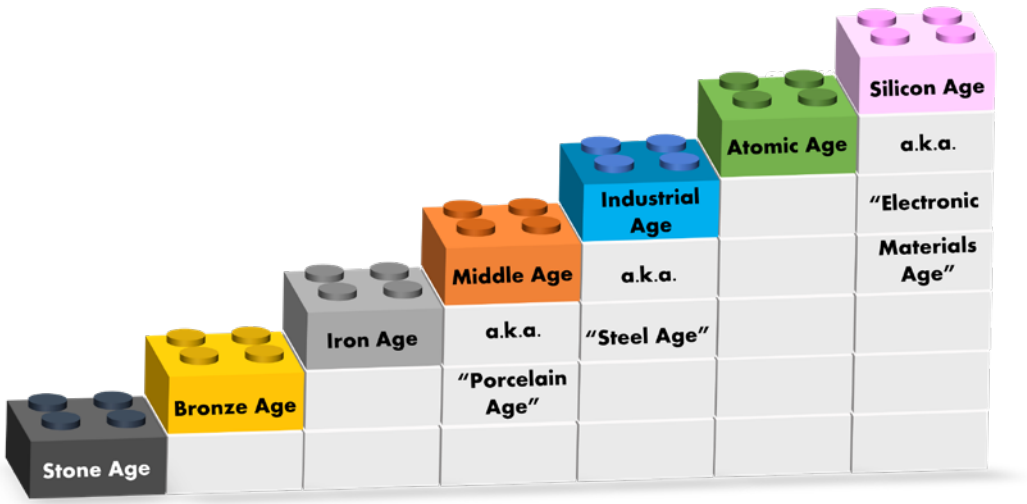

Figure 1.1. Materials and the Ages, as Mankind discovers and evolves, supported by previous achievements and knowledge.

It is therefore not surprising that Materials Science has expanded from classical subjects, such as metallurgy and ceramics, into new areas such as composite materials, polymers, biomaterials or optical materials, and even into fields that would be considered fictional a few centuries ago, such as intelligent materials, self-assembling materials, or auxetic materials [1].

Classes of materials can, themselves, be further divided into different categories. One of them, polymers, can be categorized in a multitude of ways, such as their origin (natural or synthetic) (**Figure 1.2**), their structure (linear, branched or crosslinked), or their synthesis process, to name just a few [2, 3].

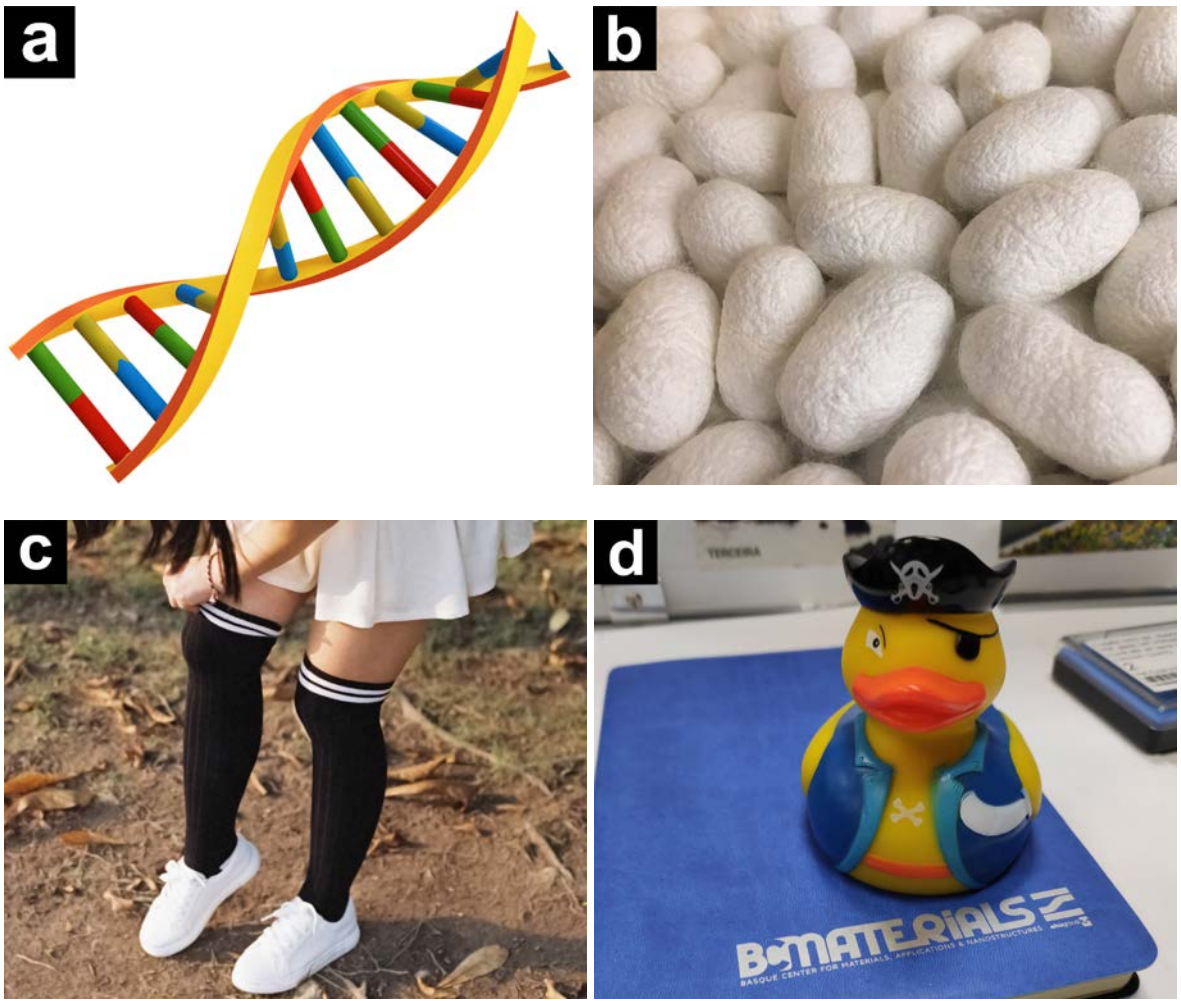

Figure 1.2. Examples of natural polymers: a) DNA, b) silk cocoons. Examples of synthetic polymers: c) nylon socks; d) polyvinyl chloride duck.

Polymers are defined as "a class of natural or synthetic substances composed of very large molecules, called macromolecules, that are multiples of simpler chemical units called monomers" [4]. They are one of the classes of materials that have seen the most advancement in recent decades, with the field of Polymer Science having gathered many accolades, such as Nobel Prizes [5], over the years.

However, the influence of polymers cannot be solely measured in accolades and awards. Life itself depends on polymers, and not in a metaphoric or allegoric fashion, for what are DNA, RNA, proteins or polysaccharides – the very building blocks of life on Earth – but the most basic and essential of polymers [2]. It is this fact, and the ubiquity of polymers in the modern world, that makes Polymer Science one of the most important areas of knowledge for Mankind.

One other important class of materials through History were metals – as mentioned, two of the pre-historic ages were named after humans discovered and began to use metals (bronze, an alloy of copper and tin, and iron) – with the knowledge of their use, manipulation and processing evolving, over thousands of years, from an art to a vast science [6].

From the early usage of gold, lead or iron in jewelry, tools and weaponry, to the aluminum, tungsten and titanium used in advanced medicine and in the aerospace industry, metals have been one of the most important and valuable materials for Mankind. Their rarity and beauty define wealth and currency, their strength and durability decide conflicts and warfare and their unique properties allow for incredible advances in science and knowledge.

The exponential advancements in the knowledge of metallurgy and metals are representative of the evolution in the knowledge of materials in general. The earliest known metal objects, dated at around 9000 B.C, may have been only wrought pieces of copper beaten into a rudimentary shape [6], and it took 7000 years for craftsmen to evolve from these simple copper objects to the life-size statue of Pharaoh Pepi I (2200 B.C.) [6], but less than 2000 years later the Colossus of Rhodes was built in iron and brass (280 B.C.), and circa 1122 A.D. Teophilus wrote his treatise "On Divers Arts" regarding artistic crafts, including knowledge in metals and advanced metalworking [6] (**Figure 1.3**).

Figure 1.3. a) Copper statue of Pharaoh Pepi I (Cairo Museum); b) depiction of the Colossus of Rhodes (Maarten Heemskerck, Phillips Gale, 1572); c) Indonesian blacksmiths forging a blade.

The rate of knowledge and advancement on metallurgy quickened considerable in the following centuries, culminating in the advanced metals and alloys used currently in automobile and the aerospace industries, as well those in medicine, computer and electronics industries.

In modern times, the knowledge and the field of Materials Science has been changing, refocusing and retesting the knowledge acquired over the millennia into a new realm, one of the very small, invisible to the naked eye, below the mili- and the micro-: the nanoscale. In the words of the late Nobel laureate, Richard P. Feynman, "there's plenty of room at the bottom".

His lecture on December 29, 1959, at Caltech, later transcribed and published [7], introduced many to the concept of nanotechnology, a word that would only be fully defined over a decade later, by Norio Taniguchi in 1974 [8].

Nanotechnology offers the possibility of manipulating matter at the smallest of scales in order to obtain new devices, solve problems both old and new, and makes Science and scientific knowledge advance by orders of magnitude. Manufacturing macroscale devices structured at the nanoscale, would allow the creation of devices with entirely new physical, chemical and even biological properties, as a result of the quantum effects that become more prominent as the dimensions of a material are shrunk to the nanometric scale [7].

One consequence of this miniaturization is the greatly increased surface reactivity of nanomaterials (NMs), as a result of their much greater surface-to-volume ratio (**Figure 1.4**).

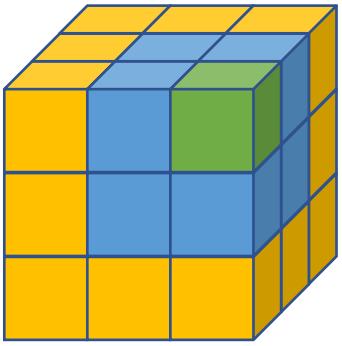

Area → $54x^2$
Volume → $27x^3$
Ratio → $\frac{2}{x}$

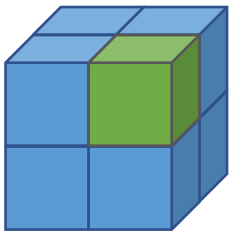

Area → $24x^2$
Volume → $8x^3$
Ratio → $\frac{3}{x}$

Area → $6x^2$
Volume → x^3
Ratio → $\frac{6}{x}$

Figure 1.4. Increase in surface-to-volume ratio, for increasingly smaller material sizes, an inevitability in nanotechnology.

This increase in reactivity, among many other interactions such as the Van der Waals forces, micro- and nanorugosity, intermolecular and electrostatic forces, all result in materials that present many new, often unheard, and usually exciting properties, for both Science and society in general. Over 60 years later, we are still discovering the wonderful world presented by Dr. Feynman in that Caltech lecture.

1.2. Smart and multifunctional materials

Research in the field of materials science is critical for the development of new technologies and the improvement of existing ones, in order to solve both new and existing problems. As mentioned, nanotechnology is an important venue to achieve this goal, due to its ability to both finely tune the properties of existing objects, and give them new ones, so as to apply them to new fields.

One of the strategies to provide new properties to a material involves the inclusion of nanomaterials in the host material, therefore creating a hybrid or a composite material with additional functionalities that the original did not possess. These "multifunctional materials" can have multiple applications, such as micro and nano devices, sensors and actuators, biomedicine, among others [9], and furthermore allowed for the creation of "intelligent" or "smart materials". A smart material can be defined as a material that can sense external stimuli, such as for example magnetic fields or humidity, and respond by altering one of its properties in a useable manner [10, 11].

There are many types of smart materials but, over the last decade, polymers have taken center stage as the basis for smart material development [10], being applied to the development of transparent electronics [12], tissue regeneration [13, 14], sensors [15-17], among others [18]. These materials can be synthesized using various processes, each with their own advantages and disadvantages. Some of these processes, detailed by Saleh et.al., with associated advantages and disadvantages, are presented in **Table 1.1** [10].

Table 1.1. Some synthesis methods for preparing smart materials

Synthesis methods	Advantages	Disadvantages
Hydrothermal	Low temperature, no calcination required, recycling of chemicals from synthesis	Selective crystallization, increased reaction kinetics, rapid heating process
Emulsion polymerization	Easily produces core-shell smart materials	Requires surfactant removal at the end of the reaction
Micro-emulsion polymerization	High kinetic reaction and average particle size	Requires stable thermodynamic conditions
Group transfer polymerization (GTP)	Ideal to control the molecular weight of polymers	Depend on the polydispersity of resulting polymers and discontinuous monomer
Reversible addition-fragmentation chain transfer (RAFT) polymerization	Controllable polymerization. Reduced number of radicals and termination reactions	Polymer chains include initiatior-produced radicals
Atom transfer radical polymerization (ATRP)	High grafting density and controlled polymer chain length	Required high concentration of usually toxic catalysts
One-pot greener (chemical oxidative polymerization)	Homogenous particle size and less waste produced	Required to control temperature and solvent during a process

Smart materials can also be processed from existing standard and conventional materials, using processes such as doctor blading [19], ionic and ultraviolet curing [20], electrospinning [21], printing [22], among others. This approach allows for some more flexibility in the materials used, and has the advantage of being able to take previously synthetized materials with interesting properties, such as nanomaterials with desirable quantum effects, and apply them in commonly used materials to give them highly useful properties for either their current applications, or completely new ones.

Smart materials are usually categorized into two different groups; active smart materials, capable of sensing a stimulus (*e.g.*, magnetic, thermal or electric,) and change their properties or geometry in response to it, allowing them to be used as actuators or transducers, and passive smart materials, which do not show an active response or generally just transfer energy [10, 18].

In addition to the two aforementioned categories, smart materials can be further classified according to the type of stimuli they are sensitive to, as well as their response to said stimuli. **Table 1.2** presents the main types of smart materials, according to the aforementioned classification.

One area where the importance of smart materials cannot be understated is that of biomedicine. The ability to structure a material at the nanoscale, giving it either new useful properties or reducing preexisting harmful ones, has found a home in the nascent field of biomedicine, which has had increasing demands for highly functionalized biomaterials since the early 2000s. The ability of smart materials provide a variety of stimuli on demand, and to do so using biocompatible and, in some cases, even biodegradable polymers, resulted in a natural and mutually beneficial partnership between these two areas [8]. Examples of this partnership are the development of a thermoresponsive polymer gels containing gold nanoparticles (NP) for smart topical antibacterial drug delivery systems [23], a composite poly(ethylene glycol) methacrylate–poly(propylene glycol) methacrylate/poly(lactide-co-glycolic acid) polymer platform for cell delivery in tissue engineering [24], or Fe_3O_4/methoxy poly(ethylene glycol)-poly(lactide) nanocapsules that are responsive to both ultrasounds and magnetic stimuli for use as contrast agents in ultrasonic/magnetic resonance imaging diagnostics [25], among many others [8].

Table 1.2. Classification of smart materials according to the stimulus they are sensitive to and their response to said stimuli

Stimuli \ Response	Electrical	Magnetic	Optical	Thermal	Mechanical	Chemical
Electrical		Magnetoelectric, spintronics	Electrochromic, electroluminescent, electro-optic, piezochromic, Kerr Effect, Pockels Effect	Thermoelectric (Peltier)	Piezoelectric, electrostrictive, electrorheological, electrokinetic	Electrolysis, electrochemical, bioelectric, electromigration
Magnetic	Magnetoelectric, spintronics, Hall Effect		Magneto-optic, piezochromic	Magnetothermal	Magnetostrictive, magneto-rheological	Nuclear magnetic resonance, magnetochemical
Optical	Photoconductive	Optomagnetic	Optical bi-stability	Photothermic	Optomechanical, photoacoustic	Photochemical, photosynthesis, photocatalyst
Thermal		Curie point	Thermocromic		Shape-memory	
Mechanical	Piezoelectric, electrostrictive	Magnetostrictive			Rheopexic, auxetic, shear-thinning, dilatants, non-Newtonian, pseudoplastic	
Chemical		Magnetochemical	Colourchange, litmus, luminiscence	Exothermic, endothermic		Catalysis

1.2.1. Electroactive smart polymers

Of particular interest for biomedical applications are polymer smart materials that have electroactive or magnetoactive properties. Electroactive materials can be defined as materials that can undergo structural deformations, such as swelling or bending, in response to an electrical field, or vice-versa [26] (**Figure 1.5**).

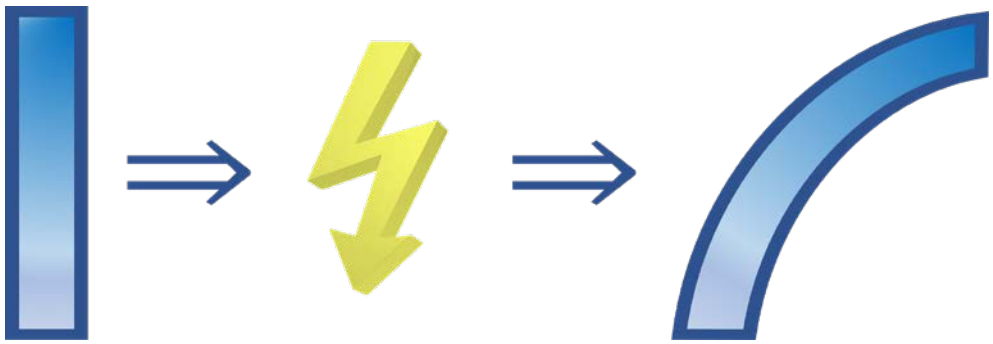

Figure 1.5. The application of electric stimuli results in the exemplified deformation (bending) of a previously straight electroactive polymer.

The application of an external electrical stimulus has the added advantage of allowing for very precise control of the mechanical deformation and behavior of the polymer, as a result of varying voltage, current and duration/interval of the stimulus [26]. And likewise, with the usage of modern, high-precision devices, it is also possible to use these materials to create very precise electrical signals as a response to a mechanical deformation. These properties make electroactive materials extremely interesting for biomedical applications where an electrical stimulus is an added value for the application, such as tissue engineering [13, 27, 28], sensing [29] and others [8, 26]. One of these applications is the work of Abidian *et al.*, who developed drug-loaded electrospun poly(lactide-co-glycolide) (PLGA) fibers, coated with a poly(3,4-ethylenedioxythiophene) (PEDOT) layer, as if it were a nanotube. Not only does the PEDOT nanotube significantly decrease the delivery rate of the drug, as a result of the hydrolytic degradation of PLGA that would quickly release the encapsulated drug, but it allows for the release rate of the drug to be controlled via the application of a positive charge that results in the shrinkage of the PEDOT nanotube, forcing more of the drug to be released from the material.

Other such examples are the development of polyurethane-zinc oxide (PU/ZnO) composites, for use as nerve guidance channels [30], or the work of Ribeiro *et al.*, coating poly(vinylidene fluoride) (PVDF) films with fibronectin, to assist in bone regeneration strategies [31].

Depending on their primary activation mechanism, electroactive polymers can be divided into two main categories: electronic electroactive polymers (EEAP) and ionic electroactive polymers (IEAP). The main difference between these polymer types lies in that EEAPs (such as piezoelectric polymers, electrostrictive polymers, and dielectric elastomers) are driven by external electric fields and by Coulomb forces, while IEAPs (such as ionic polymer–metal composites, polyelectrolyte gels, conducting polymers) are driven by the movement of ions or molecules [26]. The main advantages of EEAPs lie with their high efficiency, short response time, high durability, stability, and reliability, however they require very high electric fields. IEAPs, on the other hand, are activated by very low voltages, but typically can only be operated in an electrolyte medium [26]. Currently there is a number of studies on bridging the gap between these two categories, particularly with the use of ionic liquids (IL) paired with electroactive polymers in order to obtain large deformations with low applied voltages, and without surrounding the material with an electrolyte [32].

1.2.2. Challenge – biodegradability

Waste generation (**Figure 1.6**, [33]) is a growing concern in Europe, and accordingly, great efforts have been done to reduce it as much as possible.

Due to this situation, and on pair with the many properties that are directly relevant for their intended application, such as mechanical resistance, flexibility, electrical and ionic conductivity, magnetism or even biocompatibility, one specific property of materials has been gaining in importance in recent decades, particularly in the last few years: biodegradability [34].

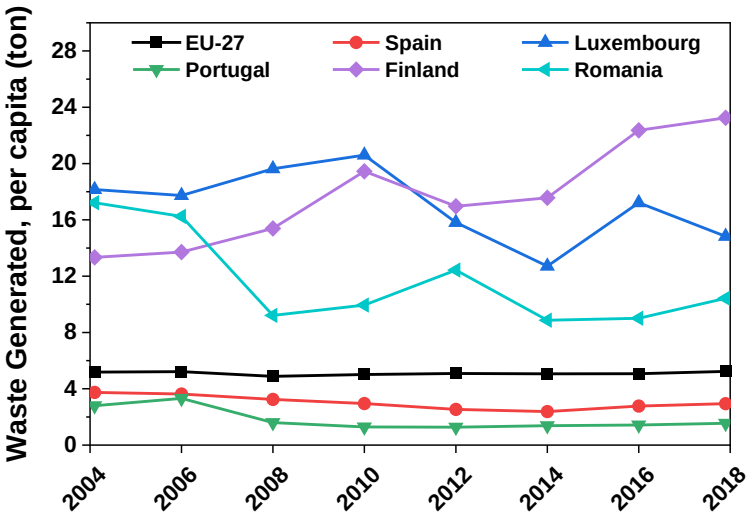

Figure 1.6. Total tons of waste generated, per capita, in the EU and some of its member-states, per year. [33]

Biodegradable materials, such as polymers, can be classified into environmentally degradable and physiologically degradable. Broadly speaking, they are defined as materials that can be degraded under natural environment or physiological condition by either of enzymatic degradation or spontaneous hydrolysis, and ultimately forming simpler by-products, non-toxic to living organisms [34, 35]. The process of polymer biodegradation consists of 4 major steps [36]:

I. Biodeterioration: biodegradable polymers break down into smaller components due to the action of decomposing organisms and/or abiotic degradation processes.

II. Depolymerization: catalytic reactions due to enzymes cause the biodegradable polymer chains to dissociate into smaller segments such as monomers, dimmers and oligomers. This results in a drastic reduction of the molecular weight of the material.

III. Assimilation: the previously generated segments are transported into microbial cells, for the production of energy, metabolites or biomass.

IV. Mineralization: previously generated metabolites and other by-products (such as water, CO_2 or CH_4) are discharged into the environment.

The EU has recently enacted two directives, on single-use plastics and on plastic bags, that aim to promote the reduction of non-degradable, polymer-based waste and encourage an economy that is both sustainable and environmentally-friendly. Furthermore, there are forthcoming policies and initiatives that aim to encourage the use of bio-based, biodegradable and compostable plastics, policies connected to the European Green Deal initiative [37].

In addition to the political and environmental desire to move away from synthetic and non-degradable materials wherever possible, the use of biodegradable materials in general is an added advantage for many applications, such as in the aforementioned case of biomedicine. Although there are biomedical scenarios that require the usage of non-degradable materials, such as sutures made from PU or PVDF [38], other situations greatly benefit from the usage of biodegradable materials, such as drug delivery or tissue regeneration [39].

It is therefore unsurprising to witness the current tendency and increasing interest in these types of materials, and there are numerous proposals for the replacement of existing biomedical devices based on polymers such as polytetrafluoroethylene (PTFE), PVDF and PU, into alternative polymers such as poly(lactic acid) (PLA) and its co-polymers [40], poly(hydroxybutyrate-co-hydroxyvalerate) (PHBV) [41, 42], among other biodegradable polymers [35, 39, 43].

1.3. Biomedical advancements - Tissue engineering

A current point of concern regarding modern healthcare service is the extremely high expenditure related to tissue damage or organ failure. The current increase in population ageing in European and Western countries means that this cost will inevitably grow as well [44-46], particularly in the case of musculoskeletal injuries and diseases as they are most prevalent in older individuals.

The Milliman Group reported in 2017 that the cost of the most common transplants in the US had reached a total of nearly US$34.7 billion (about €29.9 billion) [47]. Wu *et al.* reported that the total number of new fractures in 2019 was of 178 million new fractures worldwide, roughly translating to 5.6 new fractures every second [48].

Organ transplantation is also a concern. Although the COVID-19 pandemic resulted in a decrease of the number of transplants in the European Union, from ≈34 000 organs transplanted in each of 2018 and 2019 to ≈28 000 in 2020, the demand for organs and tissues remains high, with the total number of patients on waiting lists in Europe reaching nearly 150 000 [49-51].

To illustrate this, the European Directorate for the Quality of Medicines & HealthCare (EDQM) would often indicate how many aircraft would be needed to seat all these patients: in their standard 525 seat configuration, it would require 286 Airbus A380 airplanes.

Suffice to say, conventional therapies are already struggling with these numbers, and new strategies are required for the future. It is in this economical and medical context that a new approach develops: tissue engineering (TE).

The definition of TE by Langer *et al.* [52] is still widely used by most researchers: "an interdisciplinary field that applies the principles of engineering and the life sciences toward the development of biological substitutes that restore, maintain, or improve tissue function". And it is with this approach that TE promises future solutions for total organ replacement, on pair with more current benefits in the field of tissue repair. To achieve this, TE follows three general strategies [52]:

I. Isolated cells or cell substitutes. By only replacing the malfunctioning cells, it avoids complicated surgeries, but the infused cells can fail to maintain their function, and immunological rejection is a constant risk.

II. Tissue-inducing substances, or "growth factors". These signal molecules are delivered to the target tissue, encouraging cell multiplication.

III. Cell matrices or scaffolds. Constructed from biocompatible materials, they are able to carry cells and growth factors within their structure, and are permeable to nutrients and waste products.

Of these, the most relevant for this work is that of scaffolds, schematized in **Figure 1.7**. Scaffolds provide a temporary support for the cells to attach, grow, proliferate, and differentiate into specific tissue, facilitating their distribution within the region of desired tissue growth, supporting vascularization and neo-tissue formation, allowing for a faster recovery from surgery and consequently, lower socio-economic costs for both patients and healthcare systems [53-55].

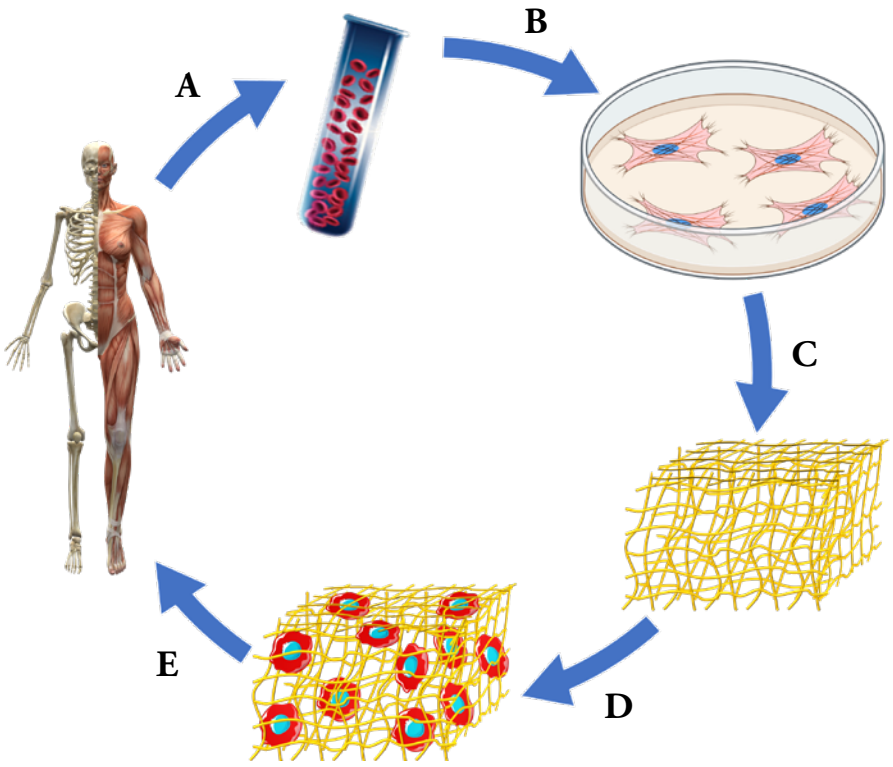

Figure 1.7. Scaffold strategy in tissue engineering: A) retrieval of donor cells from patient; B) *in vitro* cell culture; C) development of scaffold; D) encapsulation of cells in scaffold, for immediate use or *in vitro* development of tissue and E) implantation of scaffold, or *in vitro* developed tissue, in patient.

To achieve optimal results, the synthesis or processing parameters of scaffolds should be tailored [56], so that their mechanical and physico-chemical properties take in consideration both the specific tissue being repaired and the age of the patient as well, since the natural rate of tissue regeneration varies with age [46].

Scaffolds can be applied in a laboratory environment, in order to improve the accuracy of *in vitro* tests and assays, diminish the need of animal testing, or paired with other bioengineering and biomedical platforms in order to improve their efficiency. But they can also be applied directly *in vivo* [57], thus benefiting from processes that guide cell formation and development, such as chemical or biological signaling by the surrounding microenvironment, natural electrical stimuli by nearby organs and tissues, or mechanical stimuli given by the patient itself, as well as benefiting from processes responsible for cellular waste removal, such as the renal system, thus eliminating possible toxic byproducts of the degradation of the materials.

However, *in vivo* implantation of scaffolds requires these to be biocompatible and perfectly biodegradable, so as not to cause harm in the patient via tissue inflammation, presence of toxic by-products, or immunological reaction and rejection of the implanted material.

1.3.1. Skeletal muscle tissue engineering

Musculoskeletal disorders (MSDs) accounted for account for a large portion of current healthcare concerns and burden.

A common metric used to assess the burden of a particular condition is the "Disability-adjusted life year" metric (DALY), meaning the number of years lost due to ill-health, disability or early death. It is also used to compare overall health and life expectancy of different countries.

The Global Burden of Diseases, Injuries, and Risk Factors Study (GBD), a worldwide study that assesses all world data on incidence and impact of an exhaustive list of diseases and injuries, uses the DALY as a means to both compare healthcare systems worldwide, and measure the impact of each condition and disease on world healthcare systems [58]. According to the 2020 GBD, in 2019 MSDs had a total average worldwide impact, across all ages and in both sexes, of 150 000 000 DALY, or of 1 830 DALY per 100 000 individuals. [58].

Another metric is that of healthcare spending, although this is influenced by numerous other factors such as subsidized healthcare, inflation and location. Still, and taking these issues in consideration, some assessments can be made. Dieleman *et al.* found that, of the US $3.1 trillion (€2.7 trillion) spent on healthcare in 2016 (roughly 17.9% of the US GDP) [59]. This study accounted for 85.2% of this spending (US $3.1 trillion, or €2.7 trillion), and of this, 14.1% (US $380 billion, or €337 billion) was related to MSDs.

In the European Union it is difficult to assess the extent of the cost and burden of MSDs, due to the large number of countries and healthcare systems. However, at the level of individual Member States, some metrics were collected in a study by the European Risk Observatory [60]. In Austria, in 2006, MSDs were the most common cause of health-related retirement among men (34%) and the second most common on women (29.5%). In Germany, in 2016, it was reported that MSDs resulted in a loss of €30.4 billion of gross value (loss of labor productivity), or 1% of the German GDP, and the most common cause of days of incapacity to work among men (26% of total) and second-most common among women (22.5%). And in Spain, in 2007, MSDs were the leading cause of temporary work disability (18% of total), which translated into €1.7 billion in related costs.

It becomes therefore clear that new solutions, such as those provided by TE, are both a requirement and a necessity, for MSDs and their treatment are a worldwide problem, with a tendency to grow as the average age of the population increases. New solutions, that are not just for the benefit of the economy of a nation, but also for the sustainability of the healthcare systems and, most importantly, for the sake of the citizens as well.

TE pursues solutions for total organ replacement, but its main current benefit is the repair of tissues. And it can be applied to the repair and regeneration of musculoskeletal tissues that suffered injury, such as a tearing, disease or degeneration.

In order to treat these patients, TE offers an alternative approach to classical methods – it proposes to create new tissue, rather than implant allogenic (from living or dead donors) or autologous tissue (from the patient itself).

1.3.2. Polymers for tissue engineering

TE requires, in order to achieve its noble goals, both the repurposing of existing materials – providing they fulfill some strict requirements, such as in terms of biocompatibility – and the development of entirely new materials, with specific properties, tailored for the use in *in vitro* or *in vivo* tissue engineering.

Polymers are a key material to achieve this. Initially used for the ease of manipulating their surface and dimensions, to better simulate living structures, the ability of polymers to serve as carriers for multiple elements, such as drugs, NMs, or even other polymer structures, resulted in them becoming invaluable in the quest to perfectly mimic the extracellular matrix (ECM) and microenvironment conditions of living tissues and organs.

This is a complex task, as different organs require not only different types of structures and ECM (such as a multitude of oriented individual fibers to guide the development of fibrillar skeletal muscle tissue [57, 61, 62], or a smooth flat structure more appropriate for skin regeneration [63]), but also different – and sometimes multiple – types of stimuli, such as mechanical, electrical, piezoelectric, thermal, biochemical, or others [8].

In order to achieve the various required morphologies, and process polymers in the shape and dimensions most suitable for the specific tissue being healed, different techniques have been created and developed.

1.3.2.1. Morphologies and processing

Electrohydrodynamic techniques (EHD) are of particular interest for the processing of polymers for tissue engineering. EHDs are fabrication methods that produce particles, spheres (electrospray) or fibers (electrospin) of various dimensions by using electrostatic forces in a charged fluid with a constant flow; by varying the fluid or the process parameters, EHDs allow for the morphological characteristics of the fabricated materials to be customized for the intended application with high levels of precision.

Electrospray and electrospin follow the same general procedure: a constant pressure is applied to a container with a polymer solution, resulting in a constant flow of solution through a needle or a capillary, forming a small droplet at the tip (known as the Taylor cone).

By applying a strong electric charge to the solution, the electric charges accumulate at the surface of this droplet, and, at a critical point, the charge repulsion overcomes the surface tension of the droplet, pushing towards the collecting element, which is oppositely charged. The solvent is evaporated as the jet travels, with the resulting material gathered in the collector [64] (**Figure 1.8**).

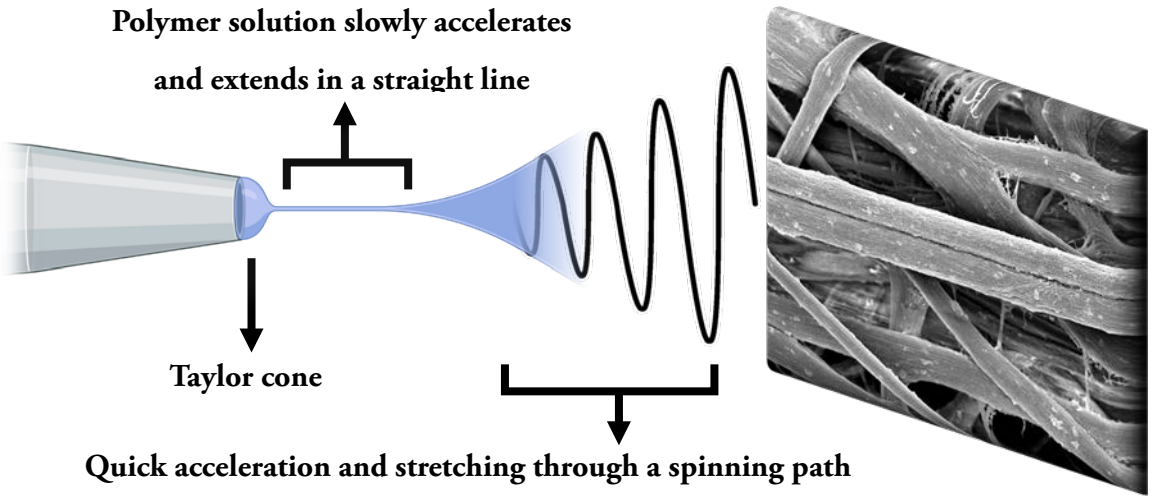

Figure 1.8. Schematic representation of the electrospinning process.

The main difference between electrospraying and electrospinning lies in the concentration of polymer in solution, and in the resulting structures obtained; with the low concentrations in electrospraying producing particle or sphere-like structures, while the higher concentrations of electrospinning produce fiber-like structures [64] (**Figure 1.9**).

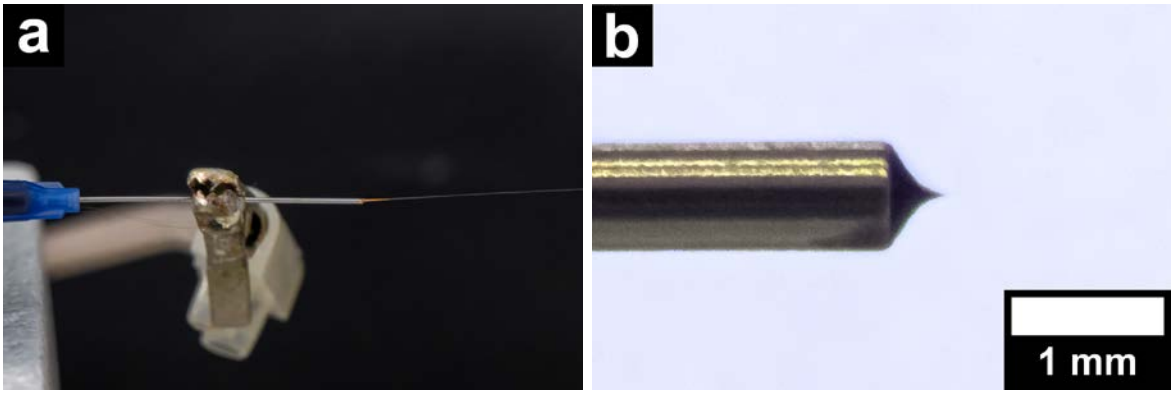

Figure 1.9. Photographs of a) Taylor cone and fiber formation during electrospinning; b) detail of the Taylor cone.

Doctor blading (**Figure 1.10**) is one of the most widely used techniques for the production of polymer thin films, first used in the 1940s [65]. The general procedure involves placing a well-mixed solution, of a pure polymer, a blend of polymers, or a polymer suspension of NPs or other substances (such as ILs or other chemicals), on a substrate. A blade, at a predetermined distance from the substrate, is then moved at a constant speed, spreading the solution on the substrate and forming a thin sheet with a constant thickness. After drying, the thin film is formed and can be detached from the substrate for usage [65].

Figure 1.10. Photograph of a thickness-adjustable doctor blade.

The final thickness of the film will always be lesser than that of the initial layer, due to evaporation of the solvent. The final wet thickness d will depend on multiple factors and is determined by the empirical **Equation 1.1** [66]:

$$d = \frac{1}{2} w \frac{c}{\rho} \qquad (1.1)$$

where w is the width of the gap, c is the concentration of all the solid material in the solution in $g.cm^{-3}$ and ρ the density of the material in the final film in $g.cm^{-3}$.

Other than its simplicity and scalability, doctor blading minimizes the waste of material during processing, making it an attractive method for many applications.

1.3.2.2. Poly(vinylidene fluoride)

PVDF (**Figure 1.11**) is a semi-crystalline polymer that has been receiving much interest over the last years. This polymer can present itself in five distinct phases, α, β, γ, δ and ε [67], with the most frequently studied ones being the non-polar α phase and the polar β and γ phases.

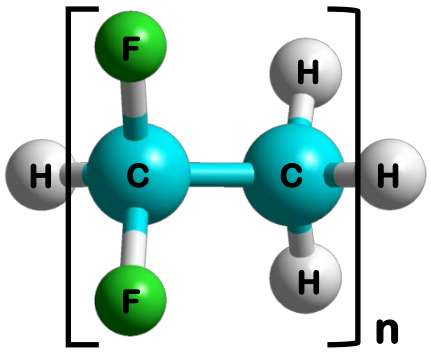

Figure 1.11. Chemical representation of a PVDF monomer unit

Among the various crystalline phases, the β-phase presents the highest dipolar moment per unit cell (8×10^{-30} C.m) [67], and, therefore, possesses the best piezoelectric response. The different chain conformations for the three most studied phases [67, 68] are represented in **Figure 1.12**.

Due to its high piezoelectric response, mainly related to the crystallization in the β-phase polymorph, and to its ability to incorporate different fillers, such as magnetic and metallic NP [69], carbon nanotubes and graphene [70], or ionic liquids [71], PVDF has been extensively studied and used in a variety of applications [66].

This includes applications on sensors and actuators [32], energy harvesting [72], cell culture [67, 73-75] and TE applications [76], as well as with silver particles grant it antimicrobial properties [77], and zeolites for controlled drug release [78].

Studies focused on the biocompatibility of PVDF showed it to be a promising material for biomedical applications, and that both the phase and polarization of PVDF influenced cellular response [73, 79].

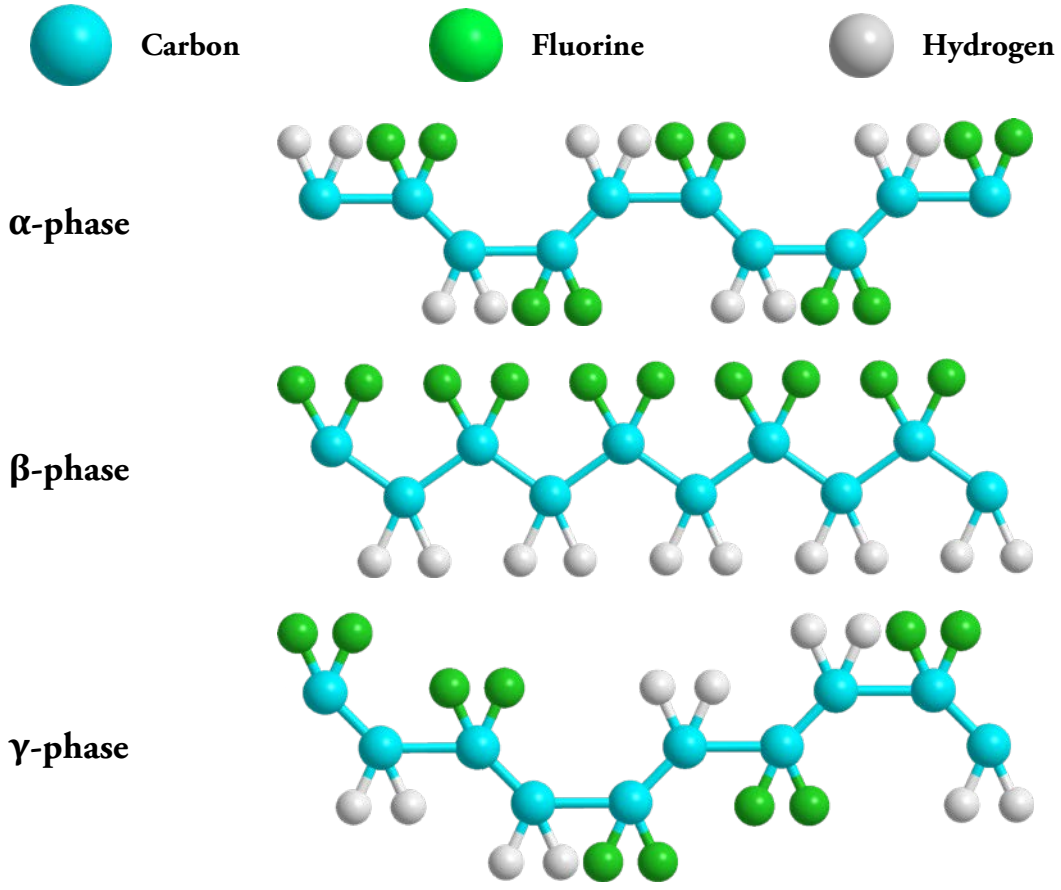

Figure 1.12. Representation of the chain conformation for the three most studied phases of PVDF

In particular for TE applications, PVDF and co-polymers have been used for bone, cardiac [80] and skeletal muscle regeneration [69, 76], among others. Ribeiro *et al.* [75] studying the influence of PVDF polarization with MC3T3-E1 pre-osteoblasts, concluding that positively charged PVDF films under dynamic stimulation promote higher osteoblast adhesion and proliferation. And, in order to be used in skeletal muscle TE, it has been combined with a multitude of materials, such as cobalt ferrite NP ($CoFe_2O_4$) [81], silica NP [82], and ILs [76], among others [83].

At the present, due to its long-time US Food and Drug Administration (FDA) approval, PVDF sees usage both in laboratory for research purposes and in multiple forms in the operating rooms of hospitals, such as surgical mesh for implants and surgery due to its stability, strength and biocompatibility [84].

However, and despite its many advantages, PVDF is not a biodegradable polymer, and its processing often relies on toxic solvents, such as dimethylformamide (DMF) or n-methyl-2-pyrrolidone (NMP), with obvious impact on human health.

Yadav et al. determined the health and environmental costs of hollow PVDF fiber membrane production [85], with some proposed solvent alternatives reducing the impact by up to 35%.

Unfortunately, this does not solve the issue of the non-biodegradability of the material. The properties, such as chemical stability and strength, that make PVDF an attractive material for so many applications, result in that it can be decomposed only at high temperatures (500 ºC), which is the preferred method in the industry [86]. However, such decomposition results in the release of hydrogen fluoride gas, which causes not only acute health issues, but also atmospheric pollution and rain acidification [86].

However, the strict requirements of some applications, namely biomedical, mean that not all bio-friendly alternative polymers are viable replacements for PVDF, and therefore it becomes a necessity to determine which ones present the adequate properties for specific biomedical application that currently rely on PVDF.

1.3.2.3. Poly(hydroxybutyrate-co-hydroxyvalerate)

PHBV (**Figure 1.13**) is a thermoplastic bio-polyester that is structurally originated from the insertion of a 3HV unit into the PHB polymer structure.

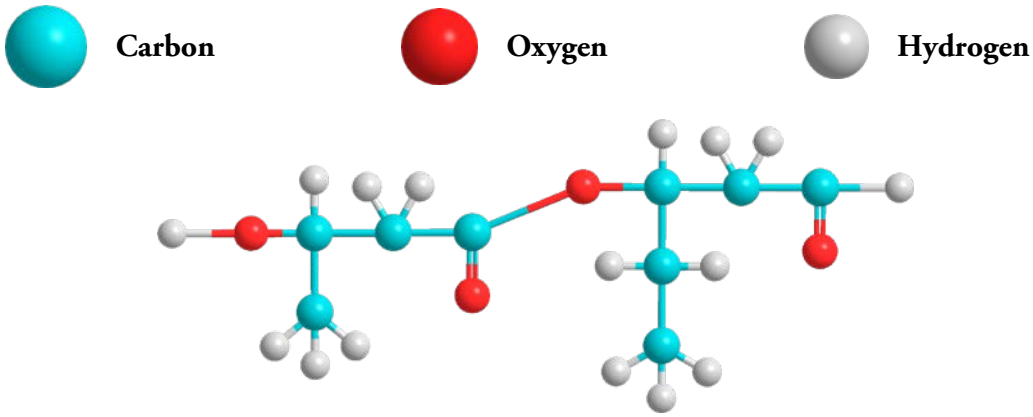

Figure 1.13. Representation of the PHBV polymer

The polymer is commonly produced by bacteria [36, 87] via fermentation processes, but recently it became possible, through genetic engineering, to synthetize PHBV from green plants [36]. It is a biocompatible and biodegradable co-polymer of polyhydroxybutyrate (PHB) [88], with good bioactivity and piezoelectric properties [42].

PHBV has been processed into different morphologies, including films, fibers and microspheres [89], presenting better mechanical properties than pure PHB [42], and is a possible replacement for synthetic, non-degradable polymers in many applications [36].

Composite materials based of PHBV have been used in combination with ILs and graphene oxide-ZnO for barriers for packaging [90], or, particularly for TE [41, 42], where biodegradability is either a requirement (for *in vivo* applications) or desirable (for health and environmental concerns), where is has been combined with $CoFe_2O_4$ [42] and iron oxide-graphene oxide [91], as well as silver nanoparticles, graphene or other polymers [89].

However, PHBV presents some problems when compared to other polymers, namely a high production cost, low processing window and inferior mechanical properties, particularly its brittleness (attributed to factors such as low nucleation density, slow crystallization causing the formation of large spherulites, increase in its crystallinity with aging and presence of micro and nanofractures inside the spherulites), as well as low impact resistance and low elongation at break [36].

In order to overcome these problems, PHBV has been blended with other materials, such as other polymers, natural fibers [36], organic and inorganic nanomaterials [41, 42, 92] and ionic liquids [90], among others [93].

1.3.2.4. Poly(lactic-co-glycolide)

Some of the most common polymers used in TE are poly(α-hydroxy esters), such as PLA, poly(glycolic acid) (PGA), and the PLGA copolymer (**Figure 1.14**) in its various formulations [94], often identified by the PLA:PGA monomer ratio.

Approved for medical use by both the FDA and the European Medicines Agency (EMA) [95, 96], and first used for biomedical purposes in the early 1970s, PLGA is one of the most extensively used. The blend between PLA and PGA monomers allows to more finely tune the properties of PLGA to the desired application, by varying not only the molecular weight of the polymers, but also their ratio in the co-polymer. Recent advances in nanotechnology and nanomaterial processing have increased the interest in PLGA for TE applications, such as for cardiac tissue engineering [97], bone tissue engineering [94], wound dressing [98] and the treatment of chronic wounds [99].

This polymer is both biocompatible and biodegradable. Its degradation occurs by chain scissions due to hydrolysis in aqueous environments, and its byproducts are lactic acid and glycolic acid, which are removed from living organisms via the renal system [96].

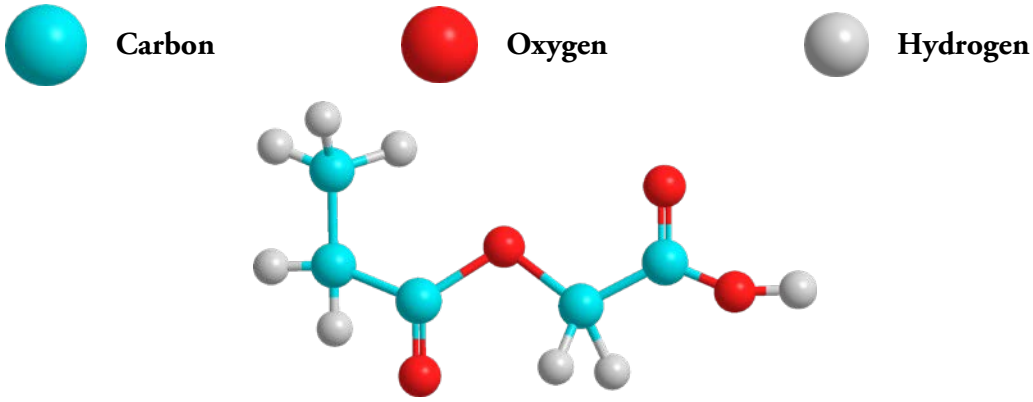

Figure 1.14. Representation of the PLGA copolymer, in the 50:50 formulation.

PLGA has been processed as micro and NPs (for use in drug delivery, vaccines, contrast agents, and TE), 3D scaffolds and fibers (for TE) [96], macroscale hydrogels and foams (for TE and long-term drug-delivery) [100], and others [101].

As mentioned, the constituent monomers of PLGA can be present in various ratios, from 5:95 to 95:5 PLA:PGA ratio. These different ratios have a profound impact on the exact properties of the copolymer, such as the degradation rate, that can vary from a few weeks to months [102], or the degree of crystallinity of the copolymer, that can either be semi-crystalline or, more often, completely amorphous [103]. Interestingly, there is no linear relation between the monomer ratio and the properties of the copolymer: a study reports that oral implants composed of a 50:50 formulation of PLGA present a half-life of just a single week, while formulations with either 75% PLA or 75% PGA presented a half-life of about 3 weeks [104]. *In vitro* degradation studies presented similar conclusions, reporting 2 weeks of half-life for PLGA 50:50 and 6 weeks for PLGA 75:25 [105]. These outcomes can further be tuned by the specific molecular weight (Mw) of the polymer, with low Mw PLGA presenting a much faster degradation rate than high Mw PLGA [106]

1.3.3. Composite smart materials for tissue engineering

The advantageous properties of smart materials and their composites have already been mentioned briefly, but their benefits for TE cannot be understated.

It is known that cells and tissues require more than just a suitable biochemical environment in order to successfully develop and differentiate - in fact, most of the major functions in cells and organs are controlled by small electrical signals [107]. Likewise, mechanical stimuli are a constant reality in living organisms, from the smallest and involuntary ones (such as those resulting from respiration, heartbeat or interaction with the surrounding environment), to major voluntary movements such as those related to locomotion.

Therefore, mechanical and electrical stimuli at the nanoscale are of great interest to scientists currently studying the development and differentiation of cells, such as in the creation of TE solutions and applications [84, 108]. Likewise, the ability to create devices that can target specific elements in cells or tissues allows the creation of new medical solutions to both old and new diseases, and other healthcare problems, as well as improving existing therapies.

Composite smart materials offer the possibility of combining the properties of various different materials in order to create an integrated solution that can offer therapeutical benefits, with the ability to respond to external stimuli and apply the therapy at specific moments and/or dosages. Furthermore, when regenerating tissues, they also offer the possibility of delivering specific stimuli at the nanoscale, in order to greatly improve the regenerative process [8, 13, 108].

1.3.3.1. Nanoparticle-based smart materials

One of the most common methods to develop polymer-based smart materials involves the use of NMs, by embedding them in a suitable polymer matrix in order to give it new properties, such as giving magnetic properties to an existing piezoelectric polymer, thus transforming it into a magnetoelectric material [69, 109, 110].

NMs can be two-dimensional (2D) sheets, such as graphene-oxide sheets [111], one-dimensional (1D), such as nanowires, nanotubes, nanorods, or nanofibers [8, 111], made of materials as varied as gold, silver, or even other polymers, or even zero-dimensional (0D), such as NPs made of similar materials as those previously mentioned [8, 111].

One of the properties of NM that is of particular interest is magnetism. Briefly, magnetic effects result of particles that have charge, mass, and spin, such as electrons, protons, or subatomic particles. These spinning charged particles create a magnetic dipole, which associate in groups. The volume of magnetic material in which all magnetic dipoles share the same orientation is known as a magnetic domain, and how these domains distribute within any given material will determine the strength and magnetic behavior of the material itself [112]. Most materials are multi-domain materials, even those with magnetic properties, with the final magnetic properties resulting from the vectorial sum of all the domains.

However, when the size of a material is reduced past a critical value, into the nanoscale, it becomes a single-domain structure, with all of its internal magnetization oriented in the same direction. Naturally, this results in that the material will have the largest possible magnetic moment for its size and composition. Furthermore, at even smaller sizes, some materials present superparamagnetic characteristics, meaning that (in the absence of an external field) thermal fluctuations will spontaneously change the direction of the magnetic field. For biomedical purposes, NM with magnetic and, particularly, superparamagnetic properties are of particular interest, as they open possibilities of using magnetic effects for diagnostics and therapies, as well as to enhance existing materials by controlling them at a distance.

For its purpose, this work shall focus on 0D NMs, NPs. Even in this category, the variety of existing NPs is immense, as they can be metallic or oxides [8, 69, 111], mineral [113, 114], polymeric, ceramic [115], and even metal-organic frameworks (MOF) [116, 117]. The discussion of all of these would fall far beyond the scope of this thesis. Therefore, this work will focus only on the studied NPs, cobalt ferrite ($CoFe_2O_4$) and magnetite (Fe_3O_4).

Both $CoFe_2O_4$ and Fe_3O_4 present an inverse spinel crystalline structure [118, 119] (**Figure 1.15**). A spinel is a face-centered cubic crystallographic structure that, in most cases, follows the formula XY_2Z_4, with X being a divalent cation, Y a trivalent cation and Z a divalent anion. In the case of ferrites, this formula can be rewritten as MFe_2O_4, with M being a metal ion.

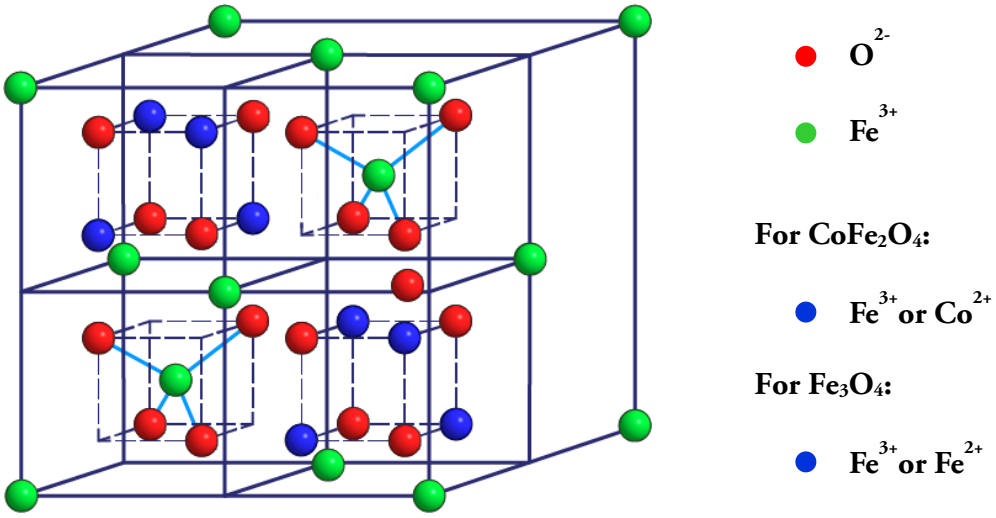

Figure 1.15. Crystallographic representation of the inverse spinel structure of $CoFe_2O_4$ and Fe_3O_4.

These structures have two different crystallographic sites, tetrahedral A-sites and octahedral B-sites, and both of them can be occupied by either divalent M^{2+} ions or trivalent Fe^{3+} ions (represented in blue in **Figure 1.15**).

There are 8 tetrahedral A-sites and 16 octahedral B-sites, causing the typical local asymmetry of spinels. When Fe^{3+} cations occupy all octahedral B-sites, and M^{2+} cations occupy all tetrahedral A-sites, the spinel structure is called "normal". When Fe^{3+} cations occupy all tetrahedral A-sites, and half of the Fe^{3+} cations and all the M^{2+} cations occupy the octahedral B-sites, the structure is called "inverse" [120].

Both $CoFe_2O_4$ and Fe_3O_4 have good thermal and chemical stability, good mechanical hardness and wear resistance, as well as moderate saturation magnetization (M_S) [109, 121], with some of their differences being a different magnetic profile ($CoFe_2O_4$ presents a magnetic anisotropy of 380 $kJ.m^{-3}$ while that of Fe_3O_4 is 14 $kJ.m^{-3}$ [119]), and the cytotoxicity of $CoFe_2O_4$, versus the well-known biocompatibility of Fe_3O_4 [122, 123]. Indeed, it has been reported that $CoFe_2O_4$ NPs present severe genotoxicity [124], which can lead to cell mutation and resulting in cancerous growths, and cytotoxicity, by arresting cell cycle, causing apoptosis and decreased metabolism [125, 126].

Studies on $CoFe_2O_4$ report that it presents superparamagnetic behavior under ≈10 nm and ferromagnetic between 10-100 nm [127], while Fe_3O_4 has been reported to present superparamagnetic behavior at sizes under 20 nm and ferrimagnetic between 20-300 nm [128].

These properties make both materials interesting options for use in smart material applications, as a way to remotely move the material, or to apply mechanical and/or electromechanical stimuli from polymer base scaffolds. In the field of biomedicine in particular, magnetic NPs such as $CoFe_2O_4$ and Fe_3O_4 have been increasingly used in a great number of applications [129, 130] such as hyperthermia treatment for tumors [130-132], accurate drug and gene transport and delivery [133-136], contrast agents for MRI [137-139], analysis and detection of specific elements and cells [140-143], among others. However, the cytotoxic nature of some of them, such as $CoFe_2O_4$ [126], requires that these NPs be coated with a non-degradable biocompatible material, before they can be used in biomedical applications. This, in conjunction with the fact that many types of NPs are not biodegradable, means that alternatives to NPs are desirable.

1.3.3.2. Ionic liquid-based smart materials

Hybrid materials based on polymers and ILs have been extensively explored and implemented in different areas (**Figure 1.16**), from sensors and actuators to the biomedical field, and have been gaining increasing attention for TE due to their interesting properties and functionalities.

ILs are defined as salts with a low melting point (under 100 ºC) whose main properties are determined by their specific anions and cations, and an interplay between their hydrogen bonds, coulombic and van der Waals interactions. They present negligible vapor pressure, often have ionic conductivities in the range of 10^{-3} to 10^{-2} $S.cm^{-1}$, as well as viscosities much higher than organic solvents. Due to their solubility and miscibility parameters, they also can replace common organic solvents in many different processes, thus encouraging the development of cleaner, greener, chemical technologies, and their high chemical, electrochemical, and thermal stability make them interesting for applications in batteries, actuators, biosensors and biomedical devices [71]. Furthermore, their non-volatility and non-flammability makes them interesting for increasing security in laboratory and industrial applications.

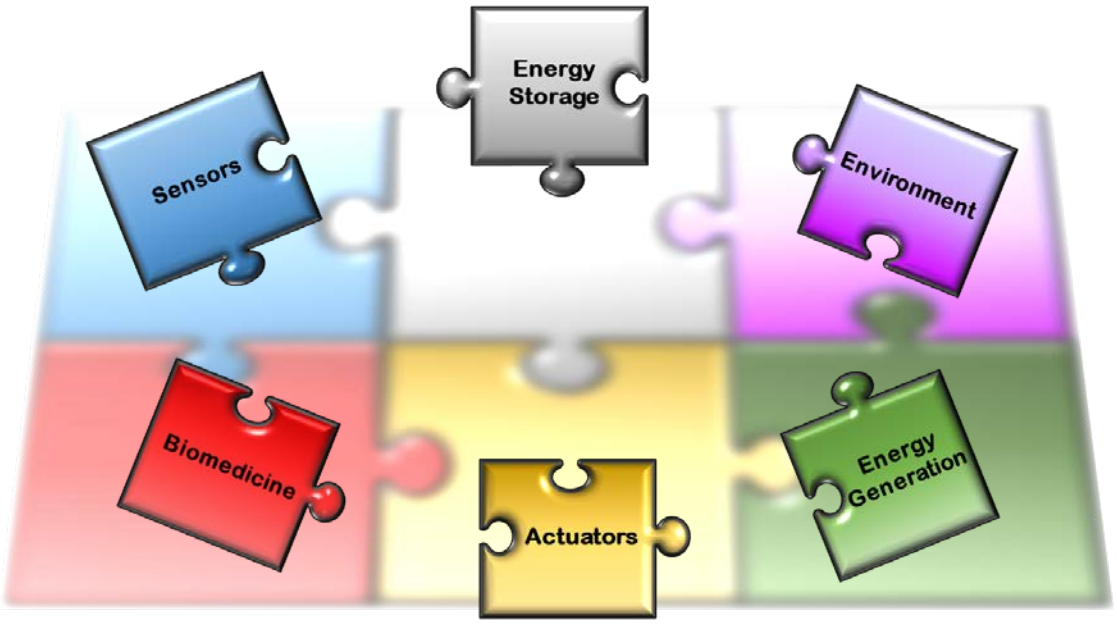

Figure 1.16. Application areas of IL/polymer-based multifunctional materials

Due to the biocompatibility and biodegradability of many ILs, these are starting to be used for TE applications, such as 1-butyl-3-methylimidazolium chloride and 2-hydroxyethyl-trimethylammonium dihydrogen phosphate for muscle tissue engineering [76], 1-butyl-3-methylimidazolium acetate for skin regeneration [144], or 1-ethyl-3-methylimidazolium acetate for neural TE [144], combined with polymers such as PVDF [76, 145] or cellulose blends[146]. Additionally, the functionalities of ILs can be further tailored by the introduction of functional groups linked to either (or both) of the ions, further increasing their effectiveness towards specific tasks and applications [71]. With about $\approx 10^{18}$ different ILs having been reported [71], with their specific properties (viscosity, size of constituent ions, density, among others) and functionalities (magnetic, luminescent, catalytic, conductive), and ability to tune the response of a material to specific stimuli (light, heat, magnetic fields, among others), it is no surprise that they have been applied in fields as diverse as batteries, CO2 capture, catalysis, lubricants, fuels and medicine [71].

For its purpose, this work shall focus only on applications of ILs for TE, and particularly, choline-based ILs.

Choline ([Chol]), also known as vitamin B4 and considered an essential micronutrient for cells [144], is a biocompatible cation that is growing in popularity in recent years. As it is a chemical readily used by cells and tissues, it is a precursor of the neurotransmitter acetylcholine and is part of the phospholipids that are abundant in cell membranes [144]. Consequently, its use often results in ILs with a good profile of both biocompatibility and biodegradability, encouraging traits for biomedical applications such as TE.

However, for a fully biodegradable and biocompatible IL, the choice of anion is equally important, in order to avoid toxicity of the material [147]. Examples of [Chol]-based ILs in biomedical applications are the use of [Chol]-L-phenylalaninate and [Chol]-L-glutaminate, that have been paired with PLGA 50:50 and PLGA 75:25, for the development of drug delivery systems [144], and of [Chol]-dihydrogen phosphate for developing electroactive films for muscle TE [76].

This work is focused on two specific [Chol]-based ILs, [Chol]-acetate ([Chol][Ac]) and [Chol]-bis(trifluoromethylsulfonyl)imide ([Chol][TFSI]). [Chol][Ac] (**Figure 1.17**) is a conductive, biodegradable, and biocompatible IL [148-150], that has been applied as an electrolyte [150], as part of hybrid polymer actuators [148], and in certain biomedical applications [149].

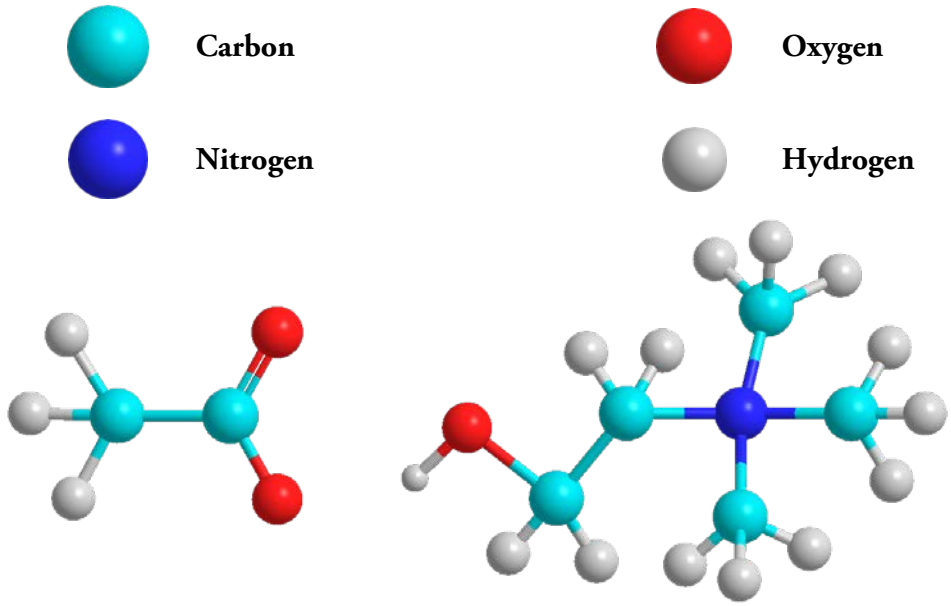

Figure 1.17. Representation of the [Chol][Ac] IL.

[Chol][TFSI] (**Figure 1.18**) presents higher ionic conductivity than [Chol][Ac], and has also been used as an electrolyte [151], as well as for biocatalysis and microbial fuel cells [152] applications. However, [Chol][TFSI] may present some toxicity in large contents, due to the effects of the bis(trifluoromethylsulfonyl)imide anion ([TFSI]) [147], so it requires additional care when used for biomedical or TE applications.

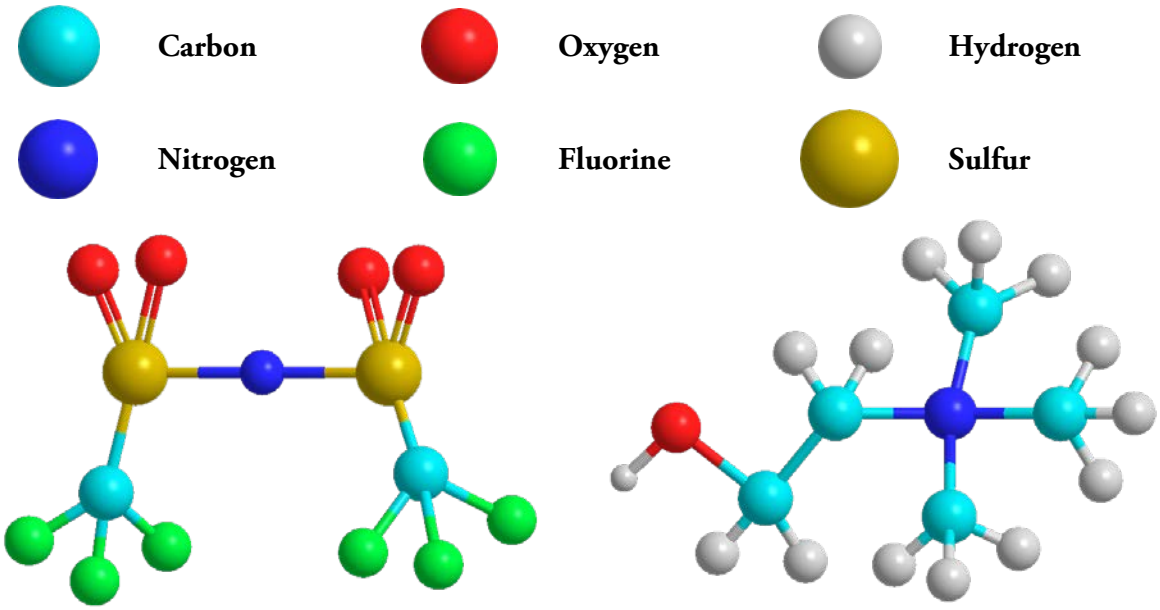

Figure 1.18. Representation of the [Chol][TFSI] IL.

1.4. General objectives and work plan

The current trend in population ageing will result in an increasing demand for tissue repair treatments, with more patients entering waiting lists. This will in turn put added pressure in healthcare systems which, as the COVID-19 pandemic revealed, often exist in a delicate balancing act of human resources, medical supplies, and patient demand – and if this act can easily be disrupted with a sudden change, such as a pandemic, it can also be slowly and surely eroded by the predicted growing demand for tissue repair treatments. New therapies are required, and TE presents itself as an answer to this situation.

For the development of TE strategies, and as it has been the case through History whenever societies faced a new challenge, the development of new or advanced materials takes particular importance, namely the development of smart materials tuned and targeted for both *in vitro* and *in vivo* tissue regeneration therapies.

In this context, the objective of the thesis is to provide a new generation of electroactive and magnetoactive polymer-based materials suitable for tissue engineering applications and, in particular for muscle tissue engineering.

The structure of this thesis document follows the sequential development of the different composite materials through the course of this doctorate. Thus, **Chapter 1** presented a short historical context of the importance of materials through History, and how their development invariably results in great benefits to society. Furthermore, it presented the main concepts that are explored, and a general overview of the state of the art in the area.

Chapter 2 of this document focuses on the possibility of combining piezoelectric polymers with magnetic NP, and embedding this magnetoelectric material on a hydrogel matrix, testing its biocompatibility and bioactivity. Specifically, magnetic $CoFe_2O_4$ nanoparticles were included in PVDF microspheres, and the process was optimized in terms of polymer quantity and NP load. The resulting composite microspheres were characterized, and later embedded in a biocompatible and biodegradable hydrogel. This hybrid material was also tested for any possible toxicity and for osteoblast response, with the goal of being applied in bone tissue regeneration.

In addition to NPs, which present some problems regarding disposal and possible environmental impact, ILs are a hot topic of research in many fields, namely in TE, being able to grant new properties for existing materials. With that in mind, **Chapter 3** explores the possibility of optimizing the magnetic response, as well as the ionic conductivity, of piezoelectric PVDF fibers processed by electrospinning in random and aligned orientation, with magnetic Fe_3O_4 and a conductive [Chol][TFSI] IL, so as to develop hybrid magnetoelectric and conductive PVDF fibers, ideally suited for *in vitro* muscle tissue engineering.

Although electrospinning is still the prime method for obtaining nano- and microfibers, a coating procedure can further enhance pre-processed fibers and either improve their properties or provide them new ones. Furthermore, it allows for different types of materials to be used, not being restricted to the nanoscale. **Chapter 4** presents this approach, of coating electrospun, randomly-oriented, PVDF fibers with two different conducting polymers – polyaniline and polypyrrole – in order to create conductive microfibers suitable for muscle tissue regeneration.

The need of biodegradable solutions for many tissue regeneration applications is the motivation for **Chapter 5**, where both the non-degradable PVDF and the degradable PHBV, as electrospun fibers and films prepared via doctor blade, are functionalized with a conductive [Chol][Ac] IL, with the intent of both making these materials more conductive and, therefore, improve their biomimicry for biomedical applications, and allowing the comparison of both polymers under similar processing conditions and functionalization process.

Finally, **Chapter 6** focuses on a fully biodegradable polymer, PLGA, functionalized with both a conductive [Chol][TFSI] IL, to improve its conductivity, and magnetic Fe_3O_4 NPs in order to allow for the material to be controllable at a distance. These hybrid materials were prepared both as electrospun fibers and as films, via doctor blade, and not only were their physical, mechanical, and chemical properties studied, but their toxicity and degradation profile as well.

The final chapter of this thesis is dedicated to the overall conclusions of the work, as well as some final remarks and consideration for future works.

1.5. References

1. Hummel, R.E., *Understanding materials science: History - Properties - Applications*. 2005: Springer New York. 1-440. DOI: 10.1007/b137957

2. Young, R.J. and P.A. Lovell, *Introduction to Polymers*. 2011, CRC Press. DOI: 10.1201/9781439894156

3. Ebewele, R.O., *Polymer Science and Technology*. 2000, CRC Press. DOI: 10.1201/9781420057805

4. Britannica, T.E.o.E. *polymer*. 2021 22 October 2021 [cited 2021 25 November]; Available from: https://www.britannica.com/science/polymer.

5. NobelPrize.org. *All Nobel Prizes*. 2021 [cited 2021 25 November]; Available from: https://www.nobelprize.org/prizes/lists/all-nobel-prizes.

6. *Discovering Metals—A Historical Overview*, in *Metallurgy for the Non-Metallurgist*, A.C. Reardon, Editor. 2011, ASM International. p. 0. DOI: 10.31399/asm.tb.mnm2.t53060073

7. Feynman, R.P., *There's Plenty of Room at the Bottom.* Engineering and Science, 1960. **23**(5): p. 22-36. Available from: https://resolver.caltech.edu/CaltechES:23.5.1960Bottom.

8. Aflori, M., *Smart Nanomaterials for Biomedical Applications-A Review.* Nanomaterials (Basel, Switzerland), 2021. **11**(2): p. 396. DOI: 10.3390/nano11020396

9. Ferreira, A.D.B.L., P.R.O. Nóvoa, and A.T. Marques, *Multifunctional Material Systems: A state-of-the-art review.* Composite Structures, 2016. **151**: p. 3-35. DOI: 10.1016/j.compstruct.2016.01.028

10. Saleh, T.A., G. Fadillah, and E. Ciptawati, *Smart advanced responsive materials, synthesis methods and classifications: from Lab to applications.* Journal of Polymer Research, 2021. **28**(6). DOI: 10.1007/s10965-021-02541-x

11. Bogue, R., *Smart materials: a review of capabilities and applications.* Assembly Automation, 2014. **34**(1): p. 16-22. DOI: 10.1108/aa-10-2013-094

12. Polícia, R., A.C. Lima, N. Pereira, E. Calle, M. Vázquez, S. Lanceros-Mendez, and P. Martins, *Transparent Magnetoelectric Materials for Advanced Invisible Electronic Applications.* Advanced Electronic Materials, 2019. **5**(12): p. 1900280. DOI: 10.1002/aelm.201900280

13. Pinho, T.S., C.B. Cunha, S. Lanceros-Méndez, and A.J. Salgado, *Electroactive Smart Materials for Neural Tissue Regeneration.* ACS Applied Bio Materials, 2021. **4**(9): p. 6604-6618. DOI: 10.1021/acsabm.1c00567

14. Li, Y., C. Liao, and S.C. Tjong, *Electrospun Polyvinylidene Fluoride-Based Fibrous Scaffolds with Piezoelectric Characteristics for Bone and Neural Tissue Engineering.* Nanomaterials (Basel, Switzerland), 2019. **9**(7): p. 952. DOI: 10.3390/nano9070952

15. Hou, X., Y. Zhou, Y. Liu, L. Wang, and J. Wang, *Coaxial electrospun flexible PANI//PU fibers as highly sensitive pH wearable sensor.* Journal of Materials Science, 2020. **55**(33): p. 16033-16047. DOI: 10.1007/s10853-020-05110-7

16. Merlini, C., R.d.S. Almeida, M.A. D'Ávila, W.H. Schreiner, and G.M.d.O. Barra, *Development of a novel pressure sensing material based on polypyrrole-coated electrospun poly(vinylidene fluoride) fibers.* Materials Science and Engineering: B, 2014. **179**: p. 52-59. DOI: 10.1016/j.mseb.2013.10.003

17. Costa, P., S. Gonçalves, H. Mora, S.A.C. Carabineiro, J.C. Viana, and S. Lanceros-Mendez, *Highly Sensitive Piezoresistive Graphene-Based Stretchable Composites for Sensing Applications.* ACS Applied Materials & Interfaces, 2019. **11**(49): p. 46286-46295. DOI: 10.1021/acsami.9b19294

18. Oliveira, J., V. Correia, H. Castro, P. Martins, and S. Lanceros-Mendez, *Polymer-based smart materials by printing technologies: Improving application and integration.* Additive Manufacturing, 2018. **21**: p. 269-283. DOI: 10.1016/j.addma.2018.03.012

19. Rincón-Iglesias, M., E. Lizundia, and S. Lanceros-Méndez, *Water-Soluble Cellulose Derivatives as Suitable Matrices for Multifunctional Materials.* Biomacromolecules, 2019. **20**(7): p. 2786-2795. DOI: 10.1021/acs.biomac.9b00574

20. Mendes-Felipe, C., J. Oliveira, I. Etxebarria, J.L. Vilas-Vilela, and S. Lanceros-Mendez, *State-of-the-Art and Future Challenges of UV Curable Polymer-Based Smart Materials for Printing Technologies.* Advanced Materials Technologies, 2019. **4**(3): p. 1800618. DOI: 10.1002/admt.201800618

21. Hermenegildo, B., C. Ribeiro, N. Peřinka, P. Martins, M. Trchová, M. Hajná, J. Stejskal, and S. Lanceros-Méndez, *Electroactive poly(vinylidene fluoride) electrospun fiber mats coated with polyaniline and polypyrrole for tissue regeneration applications.* Reactive and Functional Polymers, 2022. **170**: p. 105118. DOI: 10.1016/j.reactfunctpolym.2021.105118

22. Fernandes, L.C., D.M. Correia, C. García-Astrain, N. Pereira, M. Tariq, J.M.S.S. Esperança, and S. Lanceros-Méndez, *Ionic-Liquid-Based Printable Materials for Thermochromic and Thermoresistive Applications.* ACS Applied Materials & Interfaces, 2019. **11**(22): p. 20316-20324. DOI: 10.1021/acsami.9b00645

23. Arafa, M.G., R.F. El-Kased, and M.M. Elmazar, *Thermoresponsive gels containing gold nanoparticles as smart antibacterial and wound healing agents.* Scientific reports, 2018. **8**(1): p. 13674-13674. DOI: 10.1038/s41598-018-31895-4

24. Wang, W., H. Liang, R. Cheikh Al Ghanami, L. Hamilton, M. Fraylich, K.M. Shakesheff, B. Saunders, and C. Alexander, *Biodegradable Thermoresponsive Microparticle Dispersions for Injectable Cell Delivery Prepared Using a Single-Step Process.* Advanced Materials, 2009. **21**(18): p. 1809-1813. DOI: 10.1002/adma.200800382

25. Xu, B., H. Dou, K. Tao, K. Sun, J. Ding, W. Shi, X. Guo, J. Li, D. Zhang, and K. Sun, *"Two-in-One" Fabrication of Fe3O4/MePEG-PLA Composite Nanocapsules as a Potential Ultrasonic/MRI Dual Contrast Agent.* Langmuir, 2011. **27**(19): p. 12134-12142. DOI: 10.1021/la202096x

26. Cardoso, V.F., C. Ribeiro, and S. Lanceros-Mendez, *3 - Metamorphic biomaterials*, in *Bioinspired Materials for Medical Applications*, L. Rodrigues and M. Mota, Editors. 2017, Woodhead Publishing. p. 69-99. DOI: 10.1016/B978-0-08-100741-9.00003-6

27. Verbrugghe, P., J. Verhoeven, W. Coudyzer, E. Verbeken, P. Dubruel, E. Mendes, F. Stam, B. Meuris, and P. Herijgers, *An electro-responsive hydrogel for intravascular applications: an in vitro and in vivo evaluation.* Journal of materials science. Materials in medicine, 2015. **26**(11): p. 264-264. DOI: 10.1007/s10856-015-5598-9

28. Ribeiro, C., V. Sencadas, D.M. Correia, and S. Lanceros-Méndez, *Piezoelectric polymers as biomaterials for tissue engineering applications.* Colloids and Surfaces B: Biointerfaces, 2015. **136**: p. 46-55. DOI: 10.1016/j.colsurfb.2015.08.043

29. Wallace, G.G., M. Smyth, and H. Zhao, *Conducting electroactive polymer-based biosensors.* TrAC Trends in Analytical Chemistry, 1999. **18**(4): p. 245-251. DOI: 10.1016/s0165-9936(98)00113-7

30. Seil, J.T. and T.J. Webster, *Decreased astroglial cell adhesion and proliferation on zinc oxide nanoparticle polyurethane composites.* International journal of nanomedicine, 2008. **3**(4): p. 523-531. DOI: 10.2147/ijn.s4346

31. Ribeiro, C., J. Pärssinen, V. Sencadas, V. Correia, S. Miettinen, V.P. Hytönen, and S. Lanceros-Méndez, *Dynamic piezoelectric stimulation enhances osteogenic differentiation of human adipose stem cells.* Journal of Biomedical Materials Research Part A, 2014. **103**(6): p. 2172-2175. DOI: 10.1002/jbm.a.35368

32. Fernandes, L.C., D.M. Correia, E. Fernández, M. Tariq, J.M.S.S. Esperança, and S. Lanceros-Méndez, *Design of Ionic-Liquid-Based Hybrid Polymer Materials with a Magnetoactive and Electroactive Multifunctional Response.* ACS Applied Materials & Interfaces, 2020. **12**(37): p. 42089-42098. DOI: 10.1021/acsami.0c10746

33. Eurostat, *Generation of waste by waste category, hazardousness and NACE Rev. 2 activity*. 2021. Available from: https://ec.europa.eu/eurostat/databrowser/view/env_wasgen/default/table?lang=en.

34. Larrañaga, A. and E. Lizundia, *A review on the thermomechanical properties and biodegradation behaviour of polyesters.* European Polymer Journal, 2019. **121**: p. 109296. DOI: 10.1016/j.eurpolymj.2019.109296

35. Ohya, Y., *Biodegradable Materials*, in *Encyclopedia of Polymeric Nanomaterials*, S. Kobayashi and K. Müllen, Editors. 2021, Springer Berlin Heidelberg: Berlin, Heidelberg. p. 1-8. DOI: 10.1007/978-3-642-36199-9_232-1

36. Javadi, A., S. Pilla, S. Gong, and L.-S. Turng, *Biobased and Biodegradable PHBV-Based Polymer Blends and Biocomposites: Properties and Applications*, in *Handbook of Bioplastics and Biocomposites Engineering Applications*. 2011. p. 372-396. DOI: 10.1002/9781118203699.ch14

37. Comission, E. *Bio-based, biodegradable and compostable plastics*. 2021; Available from: https://ec.europa.eu/environment/topics/plastics/bio-based-biodegradable-and-compostable-plastics_en.

38. Dennis, C., S. Sethu, S. Nayak, L. Mohan, Y.Y. Morsi, and G. Manivasagam, *Suture materials - Current and emerging trends.* Journal of Biomedical Materials Research Part A, 2016. **104**(6): p. 1544-1559. DOI: 10.1002/jbm.a.35683

39. Song, R., M. Murphy, C. Li, K. Ting, C. Soo, and Z. Zheng, *Current development of biodegradable polymeric materials for biomedical applications.* Drug design, development and therapy, 2018. **12**: p. 3117-3145. DOI: 10.2147/DDDT.S165440

40. Lopes, M.S., A.L. Jardini, and R.M. Filho, *Poly (Lactic Acid) Production for Tissue Engineering Applications.* Procedia Engineering, 2012. **42**: p. 1402-1413. DOI: 10.1016/j.proeng.2012.07.534

41. Amaro, L., D.M. Correia, P.M. Martins, G. Botelho, S.A.C. Carabineiro, C. Ribeiro, and S. Lanceros-Mendez, *Morphology Dependence Degradation of Electro- and Magnetoactive Poly(3-hydroxybutyrate-co-hydroxyvalerate) for Tissue Engineering Applications.* Polymers, 2020. **12**(4): p. 953. DOI: 10.3390/polym12040953

42. Amaro, L., D.M. Correia, T. Marques-Almeida, P.M. Martins, L. Pérez, J.L. Vilas, G. Botelho, S. Lanceros-Mendez, and C. Ribeiro, *Tailored Biodegradable and Electroactive Poly(Hydroxybutyrate-Co-Hydroxyvalerate) Based Morphologies for Tissue Engineering Applications.* International journal of molecular sciences, 2018. **19**(8): p. 2149. DOI: 10.3390/ijms19082149

43. Palza, H., P.A. Zapata, and C. Angulo-Pineda, *Electroactive Smart Polymers for Biomedical Applications.* Materials, 2019. **12**(2): p. 277. DOI: 10.3390/ma12020277

44. Research, Z.M., *Soft Tissue Repair Market (Mesh/Tissue Patch, Soft Tissue Fixation Devices, Laparoscopic Instruments and Others) for Skin Repair, Orthopedic, Hernia Repair, Dental, Breast Reconstruction Repair and Other Applications: Global Industry Perspective, Comprehensive Analysis, Size, Share, Growth, Segment, Trends and Forecast, 2015 – 2021*. 2016, Zion Market Research. Available from: https://www.zionmarketresearch.com/report/soft-tissue-repair-market.

45. Research, T.M., *U.S., Europe and Japan Orthopedic Soft Tissue Surgical Procedures Market (Rotator Cuff Repair, Vaginal Prolapse, Lateral Epicondylitis, Achilles Tendinosis Repair, Gluteal Tendon/Trochanteric Bursitis Repair and Anterior Cruciate Ligament (ACL) Reconstruction): Industry Analysis, Size, Share, Growth, Trends and Forecast 2014 - 2020*. 2015, Transparency Market Research. Available from: http://www.transparencymarketresearch.com/soft-tissue-repair-sports-medicine.html.

46. Atala, A., F.K. Kasper, and A.G. Mikos, *Engineering Complex Tissues.* Science Translational Medicine, 2012. **4**(160): p. 160rv12. DOI: 10.1126/scitranslmed.3004890

47. Bentley, T.S. and S.J. Phillips, *2017 US organ and tissue transplant cost estimates and discussion*, S.G. Hanson, Editor. 2017, Milliman. Available from: http://www.milliman.com/uploadedFiles/insight/2017/2017-Transplant-Report.pdf.

48. Wu, A.-M., C. Bisignano, S.L. James, G.G. Abady, A. Abedi, E. Abu-Gharbieh, R.K. Alhassan, V. Alipour, J. Arabloo, M. Asaad, W.N. Asmare, A.F. Awedew, M. Banach, S.K. Banerjee, A. Bijani, T.T.M. Birhanu, S.R. Bolla, L.A. Cámera, J.-C. Chang, D.Y. Cho, et al., *Global, regional, and national burden of bone fractures in 204 countries and territories, 1990–2019: a systematic analysis from the Global Burden of Disease Study 2019.* The Lancet Healthy Longevity, 2021. **2**(9): p. e580-e592. DOI: 10.1016/S2666-7568(21)00172-0

49. *Newsletter Transplant: International figures on donation and transplantation 2018*. Vol. 24. 2019: European Directorate for the Quality of Medicines, HealthCare of the Council of Europe. Available from: https://freepub.edqm.eu/publications/NT-archive/detail.

50. *Newsletter Transplant: International figures on donation and transplantation 2019*. Vol. 25. 2020: European Directorate for the Quality of Medicines, HealthCare of the Council of Europe. Available from: https://freepub.edqm.eu/publications/NT-archive/detail.

51. *Newsletter Transplant: International figures on donation and transplantation 2020*. Vol. 26. 2021: European Directorate for the Quality of Medicines, HealthCare of the Council of Europe. Available from: https://freepub.edqm.eu/publications/PUBSD-87/detail.

52. Langer, R. and J.P. Vacanti, *Tissue Engineering*. Science, 1993. **260**(5110): p. 920-926. DOI: 10.1126/science.8493529

53. Hogan, M.V., Y. Kawakami, C.D. Murawski, and F.H. Fu, *Tissue engineering of ligaments for reconstructive surgery*. Arthroscopy: The Journal of Arthroscopic & Related Surgery, 2015. **31**(5): p. 971-979. DOI: 10.1016/j.arthro.2014.11.026

54. Chaudhari, A.A., K. Vig, D.R. Baganizi, R. Sahu, S. Dixit, V. Dennis, S.R. Singh, and S.R. Pillai, *Future Prospects for Scaffolding Methods and Biomaterials in Skin Tissue Engineering: A Review.* International Journal of Molecular Sciences, 2016. **17**(12): p. 1974-2004. DOI: 10.3390/ijms17121974

55. Bose, S., M. Roy, and A. Bandyopadhyay, *Recent advances in bone tissue engineering scaffolds.* Trends in Biotechnology, 2012. **30**(10): p. 546-554. DOI: 10.1016/j.tibtech.2012.07.005

56. Correia, D.M., C. Ribeiro, V. Sencadas, L. Vikingsson, M.O. Gasch, J.L.G. Ribelles, G. Botelho, and S. Lanceros-Mendez, *Strategies for the development of three dimensional scaffolds from piezoelectric poly(vinylidene fluoride)*. Materials & Design, 2016. **92**: p. 674-681. DOI: 10.1016/j.matdes.2015.12.043

57. Zhu, M., W. Li, X. Dong, X. Yuan, A.C. Midgley, H. Chang, Y. Wang, H. Wang, K. Wang, P.X. Ma, H. Wang, and D. Kong, *In vivo engineered extracellular matrix scaffolds with instructive niches for oriented tissue regeneration.* Nature communications, 2019. **10**(1): p. 4620-4620. DOI: 10.1038/s41467-019-12545-3

58. Vos, T., S.S. Lim, C. Abbafati, K.M. Abbas, M. Abbasi, M. Abbasifard, M. Abbasi-Kangevari, H. Abbastabar, F. Abd-Allah, A. Abdelalim, M. Abdollahi, I. Abdollahpour, H. Abolhassani, V. Aboyans, E.M. Abrams, L.G. Abreu, M.R.M. Abrigo, L.J. Abu-Raddad, A.I. Abushouk, A. Acebedo, et al., *Global burden of 369 diseases and injuries in 204 countries and territories, 1990–2019: a systematic analysis for the Global Burden of Disease Study 2019.* The Lancet, 2020. **396**(10258): p. 1204-1222. DOI: 10.1016/S0140-6736(20)30925-9

59. Dieleman, J.L., J. Cao, A. Chapin, C. Chen, Z. Li, A. Liu, C. Horst, A. Kaldjian, T. Matyasz, K.W. Scott, A.L. Bui, M. Campbell, H.C. Duber, A.C. Dunn, A.D. Flaxman, C. Fitzmaurice, M. Naghavi, N. Sadat, P. Shieh, E. Squires, et al., *US Health Care Spending by Payer and Health Condition, 1996-2016.* JAMA, 2020. **323**(9): p. 863-884. DOI: 10.1001/jama.2020.0734

60. Jan de Kok, P.V., Jacqueline Snijders, Georgios Roullis, Martin Clarke (Panteia), Kees Peereboom, Pim van Dorst, Iñigo Isusi, *Work-related musculoskeletal disorders: prevalence, costs and demographics in the EU*. 2019, European Risk Observatory. DOI: 10.2802/66947

61. Jana, S., S.K.L. Levengood, and M. Zhang, *Anisotropic Materials for Skeletal-Muscle-Tissue Engineering.* Advanced materials (Deerfield Beach, Fla.), 2016. **28**(48): p. 10588-10612. DOI: 10.1002/adma.201600240

62. Martins, P.M., S. Ribeiro, C. Ribeiro, V. Sencadas, A.C. Gomes, F.M. Gama, and S. Lanceros-Méndez, *Effect of poling state and morphology of piezoelectric poly(vinylidene fluoride) membranes for skeletal muscle tissue engineering.* RSC Advances, 2013. **3**(39): p. 17938-17944. DOI: 10.1039/c3ra43499k

63. Chaudhari, A.A., K. Vig, D.R. Baganizi, R. Sahu, S. Dixit, V. Dennis, S.R. Singh, and S.R. Pillai, *Future Prospects for Scaffolding Methods and Biomaterials in Skin Tissue Engineering: A Review.* International journal of molecular sciences, 2016. **17**(12): p. 1974. DOI: 10.3390/ijms17121974

64. Seeram, R., M. Zamani, and P.P. Molamma, *Advances in drug delivery via electrospun and electrosprayed nanomaterials.* International Journal of Nanomedicine, 2013. **8**(1): p. 2997-3017. DOI: 10.2147/ijn.s43575

65. Berni, A., M. Mennig, and H. Schmidt, *Doctor Blade*, in *Sol-Gel Technologies for Glass Producers and Users*, M.A. Aegerter and M. Mennig, Editors. 2004, Springer US: Boston, MA. p. 89-92. DOI: 10.1007/978-0-387-88953-5_10

66. Ribeiro, C., C.M. Costa, D.M. Correia, J. Nunes-Pereira, J. Oliveira, P. Martins, R. Gonçalves, V.F. Cardoso, and S. Lanceros-Méndez, *Electroactive poly(vinylidene fluoride)-based structures for advanced applications.* Nature Protocols, 2018. **13**(4): p. 681-704. DOI: 10.1038/nprot.2017.157

67. Martins, P., A.C. Lopes, and S. Lanceros-Mendez, *Electroactive phases of poly(vinylidene fluoride): Determination, processing and applications.* Progress in Polymer Science, 2014. **39**(4): p. 683-706. DOI: 10.1016/j.progpolymsci.2013.07.006

68. Wang, X., F. Sun, G. Yin, Y. Wang, B. Liu, and M. Dong, *Tactile-Sensing Based on Flexible PVDF Nanofibers via Electrospinning: A Review.* Sensors, 2018. **18**(2): p. 330-345. DOI: 10.3390/s18020330

69. Hermenegildo, B., C. Ribeiro, L. Pérez-Álvarez, J.L. Vilas, D.A. Learmonth, R.A. Sousa, P. Martins, and S. Lanceros-Méndez, *Hydrogel-based magnetoelectric microenvironments for tissue stimulation.* Colloids and Surfaces B: Biointerfaces, 2019. **181**: p. 1041-1047. DOI: 10.1016/j.colsurfb.2019.06.023

70. Li, Y., C. Liao, and S.C. Tjong, *Electrospun Polyvinylidene Fluoride-Based Fibrous Scaffolds with Piezoelectric Characteristics for Bone and Neural Tissue Engineering.* Nanomaterials, 2019. **9**(7): p. 952. DOI: 10.3390/nano9070952

71. Correia, D.M., L.C. Fernandes, P.M. Martins, C. García-Astrain, C.M. Costa, J. Reguera, and S. Lanceros-Méndez, *Ionic Liquid-Polymer Composites: A New Platform for Multifunctional Applications.* Advanced Functional Materials, 2020: p. 1909736. DOI: 10.1002/adfm.201909736

72. Rodrigues-Marinho, T., N. Castro, V. Correia, P. Costa, and S. Lanceros-Méndez, *Triboelectric Energy Harvesting Response of Different Polymer-Based Materials.* Materials, 2020. **13**(21): p. 4980. DOI: 10.3390/ma13214980

73. Ribeiro, C., J.A. Panadero, V. Sencadas, S. Lanceros-Méndez, M.N. Tamaño, D. Moratal, M. Salmerón-Sánchez, and J.L. Gómez Ribelles, *Fibronectin adsorption and cell response on electroactive poly(vinylidene fluoride) films.* Biomedical Materials, 2012. **7**(3): p. 035004-035013. DOI: 10.1088/1748-6041/7/3/035004

74. Lee, H. and B. Bhushan, *Nanotribology of polyvinylidene difluoride (PVDF) in the presence of electric field.* Journal of Colloid and Interface Science, 2011. **360**(2): p. 777-784. DOI: 10.1016/j.jcis.2011.04.087

75. Ribeiro, C., S. Moreira, V. Correia, V. Sencadas, J.G. Rocha, F.M. Gama, J.L.G. Ribelles, and S. Lanceros-Mendez, *Enhanced proliferation of pre-osteoblastic cells by dynamic piezoelectric stimulation.* RSC Advances, 2012. **2**(30): p. 11504-11509. DOI: 10.1039/c2ra21841k

76. Meira, R.M., D.M. Correia, S. Ribeiro, P. Costa, A.C. Gomes, F.M. Gama, S. Lanceros-Méndez, and C. Ribeiro, *Ionic-Liquid-Based Electroactive Polymer Composites for Muscle Tissue Engineering.* ACS Applied Polymer Materials, 2019. **1**(10): p. 2649-2658. DOI: 10.1021/acsapm.9b00566

77. Sharma, V.K., R.A. Yngard, and Y. Lin, *Silver nanoparticles: Green synthesis and their antimicrobial activities.* Advances in Colloid and Interface Science, 2009. **145**(1-2): p. 83-96. DOI: 10.1016/j.cis.2008.09.002

78. Lopes, A.C., C. Caparros, J.L. Gómez Ribelles, I.C. Neves, and S. Lanceros-Mendez, *Electrical and thermal behavior of γ-phase poly(vinylidene fluoride)/NaY zeolite composites.* Microporous and Mesoporous Materials, 2012. **161**: p. 98-105. DOI: 10.1016/j.micromeso.2012.05.019

79. Costa, R., C. Ribeiro, A.C. Lopes, P. Martins, V. Sencadas, R. Soares, and S. Lanceros-Mendez, *Osteoblast, fibroblast and in vivo biological response to poly(vinylidene fluoride) based composite materials.* Journal of Materials Science: Materials in Medicine, 2012. **24**(2): p. 395-403. DOI: 10.1007/s10856-012-4808-y

80. Adadi, N., M. Yadid, I. Gal, M. Asulin, R. Feiner, R. Edri, and T. Dvir, *Electrospun Fibrous PVDF-TrFe Scaffolds for Cardiac Tissue Engineering, Differentiation, and Maturation.* Advanced Materials Technologies, 2020. **5**(3): p. 1900820. DOI: 10.1002/admt.201900820

81. Ribeiro, S., C. Ribeiro, E.O. Carvalho, C.R. Tubio, N. Castro, N. Pereira, V. Correia, A.C. Gomes, and S. Lanceros-Méndez, *Magnetically Activated Electroactive Microenvironments for Skeletal Muscle Tissue Regeneration.* ACS Applied Bio Materials, 2020. **3**(7): p. 4239-4252. DOI: 10.1021/acsabm.0c00315

82. Ribeiro, S., T. Ribeiro, C. Ribeiro, D.M. Correia, J.P.S. Farinha, A.C. Gomes, C. Baleizão, and S. Lanceros-Méndez, *Multifunctional Platform Based on Electroactive Polymers and Silica Nanoparticles for Tissue Engineering Applications.* Nanomaterials (Basel, Switzerland), 2018. **8**(11): p. 933. DOI: 10.3390/nano8110933

83. Kapat, K., Q.T.H. Shubhra, M. Zhou, and S. Leeuwenburgh, *Piezoelectric Nano-Biomaterials for Biomedicine and Tissue Regeneration.* Advanced Functional Materials, 2020. **30**(44): p. 1909045. DOI: 10.1002/adfm.201909045

84. Yildirim, T., *Stimuli-responsive polymeric nanoparticles biomedical applications*, in *Chemisch-Geowissenschaftliche Fakultät*. 2017, Friedrich-Schiller-Universität Jena. p. 324. Available from: https://www.db-thueringen.de/receive/dbt_mods_00033094.

85. Yadav, P., N. Ismail, M. Essalhi, M. Tysklind, D. Athanassiadis, and N. Tavajohi, *Assessment of the environmental impact of polymeric membrane production.* Journal of Membrane Science, 2021. **622**: p. 118987. DOI: 10.1016/j.memsci.2020.118987

86. Wang, M., Q. Tan, L. Liu, and J. Li, *A Facile, Environmentally Friendly, and Low-Temperature Approach for Decomposition of Polyvinylidene Fluoride from the Cathode Electrode of Spent Lithium-ion Batteries.* ACS Sustainable Chemistry & Engineering, 2019. **7**(15): p. 12799-12806. DOI: 10.1021/acssuschemeng.9b01546

87. Slater, S., T. Gallaher, and D. Dennis, *Production of poly-(3-hydroxybutyrate-co-3-hydroxyvalerate) in a recombinant Escherichia coli strain.* Applied and Environmental Microbiology, 1992. **58**(4): p. 1089-1094. DOI: 10.1128/aem.58.4.1089-1094.1992

88. Doi, Y., Y. Kanesawa, M. Kunioka, and T. Saito, *Biodegradation of microbial copolyesters: poly(3-hydroxybutyrate-co-3-hydroxyvalerate) and poly(3-hydroxybutyrate-co-4-hydroxybutyrate).* Macromolecules, 1990. **23**(1): p. 26-31. DOI: 10.1021/ma00203a006

89. Rivera-Briso, A.L. and Á. Serrano-Aroca, *Poly(3-Hydroxybutyrate-co-3-Hydroxyvalerate): Enhancement Strategies for Advanced Applications.* Polymers, 2018. **10**(7): p. 732. DOI: 10.3390/polym10070732

90. Gouvêa, R.F. and C.T. Andrade, *Testing the effect of imidazolium ionic liquid and citrate derivative on the properties of graphene-based PHBV/EVA immiscible blend.* Polymer Testing, 2020. **89**: p. 106615. DOI: 10.1016/j.polymertesting.2020.106615

91. Pramanik, N., S. Bhattacharya, T. Rath, J. De, A. Adhikary, R.K. Basu, and P.P. Kundu, *Polyhydroxybutyrate-co-hydroxyvalerate copolymer modified graphite oxide based 3D scaffold for tissue engineering application.* Materials Science and Engineering: C, 2019. **94**: p. 534-546. DOI: 10.1016/j.msec.2018.10.009

92. Antunes, A., A. Popelka, O. Aljarod, M.K. Hassan, P. Kasak, and A.S. Luyt, *Accelerated Weathering Effects on Poly(3-hydroxybutyrate-co-3-hydroxyvalerate) (PHBV) and PHBV/TiO(2) Nanocomposites.* Polymers, 2020. **12**(8): p. 1743. DOI: 10.3390/polym12081743

93. Turco, R., G. Santagata, I. Corrado, C. Pezzella, and M. Di Serio, *In vivo and Post-synthesis Strategies to Enhance the Properties of PHB-Based Materials: A Review.* Frontiers in bioengineering and biotechnology, 2021. **8**: p. 619266-619266. DOI: 10.3389/fbioe.2020.619266

94. Gentile, P., V. Chiono, I. Carmagnola, and P.V. Hatton, *An overview of poly(lactic-co-glycolic) acid (PLGA)-based biomaterials for bone tissue engineering.* International journal of molecular sciences, 2014. **15**(3): p. 3640-3659. DOI: 10.3390/ijms15033640

95. Chereddy, K.K., G. Vandermeulen, and V. Préat, *PLGA based drug delivery systems: Promising carriers for wound healing activity.* Wound Repair and Regeneration, 2016. **24**(2): p. 223-236. DOI: 10.1111/wrr.12404

96. Martins, C., F. Sousa, F. Araújo, and B. Sarmento, *Functionalizing PLGA and PLGA Derivatives for Drug Delivery and Tissue Regeneration Applications.* Advanced Healthcare Materials, 2017. **7**(1): p. 1701035. DOI: 10.1002/adhm.201701035

97. Gelmi, A., J. Zhang, A. Cieslar-Pobuda, M.K. Ljunngren, M.J. Los, M. Rafat, and E.W.H. Jager, *Electroactive 3D materials for cardiac tissue engineering*, in *Electroactive Polymer Actuators and Devices (EAPAD) 2015*. 2015, SPIE. DOI: 10.1117/12.2084165

98. Liu, S.-J., Y.-C. Kau, C.-Y. Chou, J.-K. Chen, R.-C. Wu, and W.-L. Yeh, *Electrospun PLGA/collagen nanofibrous membrane as early-stage wound dressing.* Journal of Membrane Science, 2010. **355**(1-2): p. 53-59. DOI: 10.1016/j.memsci.2010.03.012

99. Garcia-Orue, I., G. Gainza, P. Garcia-Garcia, F.B. Gutierrez, J.J. Aguirre, R.M. Hernandez, A. Delgado, and M. Igartua, *Composite nanofibrous membranes of PLGA/Aloe vera containing lipid nanoparticles for wound dressing applications.* International Journal of Pharmaceutics, 2019. **556**: p. 320-329. DOI: 10.1016/j.ijpharm.2018.12.010

100. Phua, K.K.L., E.R.H. Roberts, and K.W. Leong, *Degradable Polymers*, in *Comprehensive Biomaterials*. 2011, Elsevier. p. 381-415. DOI: 10.1016/b978-0-08-055294-1.00253-1

101. Lü, J.-M., X. Wang, C. Marin-Muller, H. Wang, P.H. Lin, Q. Yao, and C. Chen, *Current advances in research and clinical applications of PLGA-based nanotechnology.* Expert review of molecular diagnostics, 2009. **9**(4): p. 325-341. DOI: 10.1586/erm.09.15

102. Middleton, J.C. and A.J. Tipton, *Synthetic biodegradable polymers as orthopedic devices.* Biomaterials, 2000. **21**(23): p. 2335-2346. DOI: 10.1016/s0142-9612(00)00101-0

103. Blasi, P., *Poly(lactic acid)/poly(lactic-co-glycolic acid)-based microparticles: an overview.* Journal of Pharmaceutical Investigation, 2019. **49**(4): p. 337-346. DOI: 10.1007/s40005-019-00453-z

104. Miller, R.A., J.M. Brady, and D.E. Cutright, *Degradation rates of oral resorbable implants (polylactates and polyglycolates): Rate modification with changes in PLA/PGA copolymer ratios.* Journal of Biomedical Materials Research, 1977. **11**(5): p. 711-719. DOI: 10.1002/jbm.820110507

105. Lu, L., C.A. Garcia, and A.G. Mikos, *In vitro degradation of thin poly(DL-lactic-co-glycolic acid) films.* Journal of Biomedical Materials Research, 1999. **46**(2): p. 236-244. DOI: 10.1002/(sici)1097-4636(199908)46:2<236::aid-jbm13>3.0.co;2-f

106. Machatschek, R. and A. Lendlein, *Fundamental insights in PLGA degradation from thin film studies.* Journal of Controlled Release, 2020. **319**: p. 276-284. DOI: 10.1016/j.jconrel.2019.12.044

107. Gajendiran, M., J. Choi, S.-J. Kim, K. Kim, H. Shin, H.-J. Koo, and K. Kim, *Conductive biomaterials for tissue engineering applications.* Journal of Industrial and Engineering Chemistry, 2017. **51**: p. 12-26. DOI: 10.1016/j.jiec.2017.02.031

108. Ribeiro, C., V. Correia, P. Martins, F.M. Gama, and S. Lanceros-Mendez, *Proving the suitability of magnetoelectric stimuli for tissue engineering applications.* Colloids and Surfaces B: Biointerfaces, 2016. **140**: p. 430-436. DOI: 10.1016/j.colsurfb.2015.12.055

109. Goncalves, R., P. Martins, D.M. Correia, V. Sencadas, J.L. Vilas, L.M. Leon, G. Botelho, and S. Lanceros-Mendez, *Development of magnetoelectric CoFe2O4/poly(vinylidene fluoride) microspheres.* RSC Advances, 2015. **5**(45): p. 35852-35857. DOI: 10.1039/c5ra04409j

110. Martins, P., A. Lasheras, J. Gutierrez, J.M. Barandiaran, I. Orue, and S. Lanceros-Mendez, *Optimizing piezoelectric and magnetoelectric responses on CoFe2O4/P(VDF-TrFE) nanocomposites.* Journal of Physics D: Applied Physics, 2011. **44**(49): p. 495303-495310. DOI: 10.1088/0022-3727/44/49/495303

111. Dong, R., P.X. Ma, and B. Guo, *Conductive biomaterials for muscle tissue engineering.* Biomaterials, 2020. **229**: p. 119584. DOI: 10.1016/j.biomaterials.2019.119584

112. Akbarzadeh, A., M. Samiei, and S. Davaran, *Magnetic nanoparticles: preparation, physical properties, and applications in biomedicine.* Nanoscale research letters, 2012. **7**(1): p. 144-144. DOI: 10.1186/1556-276X-7-144

113. Sridharan, R., K.J. Genoud, D.J. Kelly, and F.J. O'Brien, *Hydroxyapatite Particle Shape and Size Influence MSC Osteogenesis by Directing the Macrophage Phenotype in Collagen-Hydroxyapatite Scaffolds.* ACS Applied Bio Materials, 2020. **3**(11): p. 7562-7574. DOI: 10.1021/acsabm.0c00801

114. Roohani-Esfahani, S.-I., S. Nouri-Khorasani, Z. Lu, R. Appleyard, and H. Zreiqat, *The influence hydroxyapatite nanoparticle shape and size on the properties of biphasic calcium phosphate scaffolds coated with hydroxyapatite–PCL composites.* Biomaterials, 2010. **31**(21): p. 5498-5509. DOI: 10.1016/j.biomaterials.2010.03.058

115. Wu, Y., W. Jiang, X. Wen, B. He, X. Zeng, G. Wang, and Z. Gu, *A novel calcium phosphate ceramic–magnetic nanoparticle composite as a potential bone substitute.* Biomedical Materials, 2010. **5**(1): p. 015001. DOI: 10.1088/1748-6041/5/1/015001

116. Busquets, M.A. and J. Estelrich, *Prussian blue nanoparticles: synthesis, surface modification, and biomedical applications.* Drug Discovery Today, 2020. **25**(8): p. 1431-1443. DOI: 10.1016/j.drudis.2020.05.014

117. Han, D., Y. Li, X. Liu, B. Li, Y. Han, Y. Zheng, K.W.K. Yeung, C. Li, Z. Cui, Y. Liang, Z. Li, S. Zhu, X. Wang, and S. Wu, *Rapid bacteria trapping and killing of metal-organic frameworks strengthened photo-responsive hydrogel for rapid tissue repair of bacterial infected wounds.* Chemical Engineering Journal, 2020. **396**: p. 125194. DOI: 10.1016/j.cej.2020.125194

118. Tsais, P.J. and L.I. Chan, *Nickel-based batteries: materials and chemistry*, in *Electricity Transmission, Distribution and Storage Systems*. 2013, Elsevier. p. 309-397. DOI: 10.1533/9780857097378.3.309

119. Yuliantika, D., A. Taufiq, A. Hidayat, Sunaryono, N. Hidayat, and S. Soontaranon, *Exploring Structural Properties of Cobalt Ferrite Nanoparticles from Natural Sand.* IOP Conference Series: Materials Science and Engineering, 2019. **515**: p. 012047. DOI: 10.1088/1757-899x/515/1/012047

120. Zeng, X., J. Zhang, S. Zhu, X. Deng, H. Ma, J. Zhang, Q. Zhang, P. Li, D. Xue, N.J. Mellors, X. Zhang, and Y. Peng, *Direct observation of cation distributions of ideal inverse spinel $CoFe_2O_4$ nanofibres and correlated magnetic properties.* Nanoscale, 2017. **9**(22): p. 7493-7500. DOI: 10.1039/c7nr02013a

121. Sivakumar, N., A. Narayanasamy, K. Shinoda, C.N. Chinnasamy, B. Jeyadevan, and J.M. Greneche, *Electrical and magnetic properties of chemically derived nanocrystalline cobalt ferrite.* Journal of Applied Physics, 2007. **102**(1): p. 013916-013923. DOI: 10.1063/1.2752098

122. Bagheri, S. and N.M. Julkapli, *Modified iron oxide nanomaterials: Functionalization and application.* Journal of Magnetism and Magnetic Materials, 2016. **416**: p. 117-133. DOI: 10.1016/j.jmmm.2016.05.042

123. Ankamwar, B., T.C. Lai, J.H. Huang, R.S. Liu, M. Hsiao, C.H. Chen, and Y.K. Hwu, *Biocompatibility of Fe3O4 nanoparticles evaluated by in vitro cytotoxicity assays using normal, glia and breast cancer cells.* Nanotechnology, 2010. **21**(7): p. 075102. DOI: 10.1088/0957-4484/21/7/075102

124. Hwang, D.W., D.S. Lee, and S. Kim, *Gene Expression Profiles for Genotoxic Effects of Silica-Free and Silica-Coated Cobalt Ferrite Nanoparticles.* Journal of Nuclear Medicine, 2011. **53**(1): p. 106-112. DOI: 10.2967/jnumed.111.088443

125. Ahmad, F., X. Liu, Y. Zhou, and H. Yao, *An in vivo evaluation of acute toxicity of cobalt ferrite (CoFe2O4) nanoparticles in larval-embryo Zebrafish (Danio rerio).* Aquatic Toxicology, 2015. **166**: p. 21-28. DOI: 10.1016/j.aquatox.2015.07.003

126. Kumar Prabhakar, P., S. Vijayaraghavan, J. Philip, and M. Doble, *Biocompatibility Studies of Functionalized $CoFe_2O_4$ Magnetic Nanoparticles.* Current Nanoscience, 2011. **7**(3): p. 371-376. DOI: 10.2174/157341311795542435

127. Nguyen, D.T. and K.-S. Kim, *Controlled Magnetic Properties of Iron Oxide-Based Nanoparticles for Smart Therapy.* KONA Powder and Particle Journal, 2016. **33**(0): p. 33-47. DOI: 10.14356/kona.2016010

128. Li, Q., C.W. Kartikowati, S. Horie, T. Ogi, T. Iwaki, and K. Okuyama, *Correlation between particle size/domain structure and magnetic properties of highly crystalline Fe(3)O(4) nanoparticles.* Scientific reports, 2017. **7**(1): p. 9894-9894. DOI: 10.1038/s41598-017-09897-5

129. Issa, B., I. Obaidat, B. Albiss, and Y. Haik, *Magnetic Nanoparticles: Surface Effects and Properties Related to Biomedicine Applications.* International Journal of Molecular Sciences, 2013. **14**(12): p. 21266-21305. DOI: 10.3390/ijms141121266

130. Pankhurst, Q.A., J. Connolly, S.K. Jones, and J. Dobson, *Applications of magnetic nanoparticles in biomedicine.* Journal of Physics D: Applied Physics, 2003. **36**(13): p. R167-R181. DOI: 10.1088/0022-3727/36/13/201

131. Christophi, C., A. Winkworth, V. Muralihdaran, and P. Evans, *The treatment of malignancy by hyperthermia.* Surgical Oncology, 1998. **7**(1-2): p. 83-90. DOI: 10.1016/s0960-7404(99)00007-9

132. Fortin, J.-P., F. Gazeau, and C. Wilhelm, *Intracellular heating of living cells through Néel relaxation of magnetic nanoparticles.* European Biophysics Journal, 2007. **37**(2): p. 223-228. DOI: 10.1007/s00249-007-0197-4

133. Senyei, A., K. Widder, and G. Czerlinski, *Magnetic guidance of drug-carrying microspheres.* Journal of Applied Physics, 1978. **49**(6): p. 3578-3583. DOI: 10.1063/1.325219

134. Koneracká, M., P. Kopčanský, M. Antalík, M. Timko, C.N. Ramchand, D. Lobo, R.V. Mehta, and R.V. Upadhyay, *Immobilization of proteins and enzymes to fine magnetic particles.* Journal of Magnetism and Magnetic Materials, 1999. **201**(1-3): p. 427-430. DOI: 10.1016/s0304-8853(99)00005-0

135. Koneracká, M., P. Kopčanský, M. Timko, C.N. Ramchand, A. de Sequeira, and M. Trevan, *Direct binding procedure of proteins and enzymes to fine magnetic particles.* Journal of Molecular Catalysis B: Enzymatic, 2002. **18**(1-3): p. 13-18. DOI: 10.1016/s1381-1177(02)00016-4

136. Hutchins, B.M., M. Platt, W.O. Hancock, and M.E. Williams, *Directing Transport of $CoFe_2O_4$-Functionalized Microtubules with Magnetic Fields.* Small, 2007. **3**(1): p. 126-131. DOI: 10.1002/smll.200600410

137. Pouliquen, D., H. Perroud, F. Calza, P. Jallet, and J.J. Le Jeune, *Investigation of the magnetic properties of iron oxide nanoparticles used as contrast agent for MRI.* Magnetic Resonance in Medicine, 1992. **24**(1): p. 75-84. DOI: 10.1002/mrm.1910240108

138. Wang, Y.-X.J., S.M. Hussain, and G.P. Krestin, *Superparamagnetic iron oxide contrast agents: physicochemical characteristics and applications in MR imaging.* European Radiology, 2001. **11**(11): p. 2319-2331. DOI: 10.1007/s003300100908

139. Rohrer, M., H. Bauer, J. Mintorovitch, M. Requardt, and H.-J. Weinmann, *Comparison of Magnetic Properties of MRI Contrast Media Solutions at Different Magnetic Field Strengths.* Investigative Radiology, 2005. **40**(11): p. 715-724. DOI: 10.1097/01.rli.0000184756.66360.d3

140. Terstappen, L.W.M.M., A.G.J. Tibbe, B.G.d. Grooth, J. Greve, P.A. Liberti, and G.J. Dolan, *Optical tracking and detection of immunomagnetically selected and aligned cells.* Nature Biotechnology, 1999. **17**(12): p. 1210-1213. DOI: 10.1038/70761

141. Kularatne, B.Y., P. Lorigan, S. Browne, S.K. Suvarna, M.O. Smith, and J. Lawry, *Monitoring tumour cells in the peripheral blood of small cell lung cancer patients.* Cytometry Part A, 2002. **50**(3): p. 160-167. DOI: 10.1002/cyto.10071

142. Morisada, S., N. Miyata, and K. Iwahori, *Immunomagnetic separation of scum-forming bacteria using polyclonal antibody that recognizes mycolic acids.* Journal of Microbiological Methods, 2002. **51**(2): p. 141-148. DOI: 10.1016/s0167-7012(02)00046-5

143. Zigeuner, R.E., R. Riesenberg, H. Pohla, A. Hofstetter, and R. Oberneder, *Isolation of circulating cancer cells from whole blood by immunomagnetic cell enrichment and unenriched immunocytochemistry in vitro.* The Journal of Urology, 2003. **169**(2): p. 701-705. DOI: 10.1016/s0022-5347(05)63996-1

144. Correia, D.M., L.C. Fernandes, M.M. Fernandes, B. Hermenegildo, R.M. Meira, C. Ribeiro, S. Ribeiro, J. Reguera, and S. Lanceros-Méndez, *Ionic Liquid-Based Materials for Biomedical Applications.* Nanomaterials (Basel, Switzerland), 2021. **11**(9): p. 2401. DOI: 10.3390/nano11092401

145. Dias, J.C., D.C. Correia, A.C. Lopes, S. Ribeiro, C. Ribeiro, V. Sencadas, G. Botelho, J.M.S.S. Esperança, J.M. Laza, J.L. Vilas, L.M. León, and S. Lanceros-Méndez, *Development of poly(vinylidene fluoride)/ionic liquid electrospun fibers for tissue engineering applications.* Journal of Materials Science, 2016. **51**(9): p. 4442-4450. DOI: 10.1007/s10853-016-9756-3

146. Kim, M.H., S. An, K. Won, H.J. Kim, and S.H. Lee, *Entrapment of enzymes into cellulose–biopolymer composite hydrogel beads using biocompatible ionic liquid.* Journal of Molecular Catalysis B: Enzymatic, 2012. **75**: p. 68-72. DOI: 10.1016/j.molcatb.2011.11.011

147. Mena, I.F., E. Diaz, J. Palomar, J.J. Rodriguez, and A.F. Mohedano, *Cation and anion effect on the biodegradability and toxicity of imidazolium– and choline–based ionic liquids.* Chemosphere, 2020. **240**: p. 124947. DOI: 10.1016/j.chemosphere.2019.124947

148. Elhi, F., H. Priks, P. Rinne, N. Kaldalu, E. Žusinaite, U. Johanson, A. Aabloo, T. Tamm, and K. Põhako-Esko, *Electromechanically active polymer actuators based on biofriendly choline ionic liquids.* Smart Materials and Structures, 2020. **29**(5): p. 055021. DOI: 10.1088/1361-665x/ab7f24

149. Gomes, J.M., S.S. Silva, and R.L. Reis, *Exploring the Use of Choline Acetate on the Sustainable Development of α-Chitin-Based Sponges.* ACS Sustainable Chemistry & Engineering, 2020. **8**(35): p. 13507-13516. DOI: 10.1021/acssuschemeng.0c05076

150. Sakthivel, M., S.P. Batchu, A.A. Shah, K. Kim, W. Peters, and J.-F. Drillet, *An Electrically Rechargeable Zinc/Air Cell with an Aqueous Choline Acetate Electrolyte.* Materials (Basel, Switzerland), 2020. **13**(13): p. 2975. DOI: 10.3390/ma13132975

151. Suominen, M., S. Lehtimäki, R. Yewale, P. Damlin, S. Tuukkanen, and C. Kvarnström, *Electropolymerized polyazulene as active material in flexible supercapacitors.* Journal of Power Sources, 2017. **356**: p. 181-190. DOI: 10.1016/j.jpowsour.2017.04.082

152. Haj Kacem, S., S. Galai, A. Pérez de los Ríos, F.J. Hernández Fernández, and I. Smaali, *New efficient laccase immobilization strategy using ionic liquids for biocatalysis and microbial fuel cells applications.* Journal of Chemical Technology & Biotechnology, 2017. **93**(1): p. 174-183. DOI: 10.1002/jctb.5337

Chapter 2

Hydrogel-based magnetoelectric materials for tissue stimulation

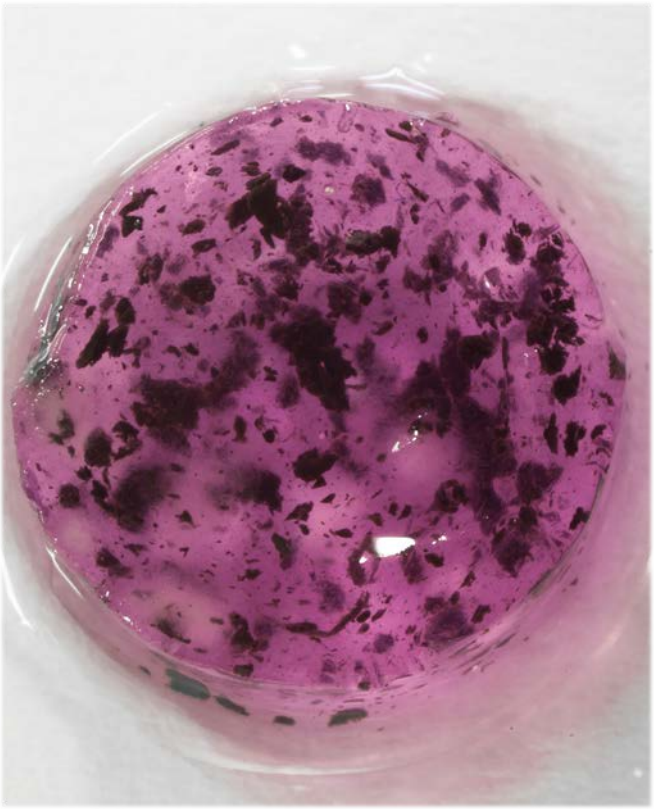

Hydrogel disk with magnetoelectric microspheres.

Hydrogels are scaffolds that can mimic the natural environment of tissues, and can carry nanomaterials that give them new properties. Adding magnetoelectric materials to hydrogel-based scaffolds is a promising approach for tissue engineering, as the hybrid hydrogel becomes capable of delivering active stimuli to the tissues, further improving the biomimicry of an ex-vivo approach. This chapter details the development of a novel, biocompatible, Methacrylated Gellan Gum/poly(vinylidene fluoride)/$CoFe_2O_4$ hydrogel-based scaffold, that can be controlled by an external magnetic field in order to apply active stimuli to cells and tissues.

2.1. Introduction

The transplantation of organs remains the ultimate approach to treat end-stage failures and injuries [1]. However, this strategy is invasive, costly, and with a low number of organs/tissues available for transplantation.

Therefore, new TE strategies are needed to treat the increasing number of patients with tissue problems [2]. Aiming to support the replacement of damaged regions and to promote tissue redevelopment, TE has become one of the most investigated methods for tissue reconstruction and/or regeneration [3].

Generally, an engineered tissue is composed of cells, growth factors and scaffolds. In this approach, it is essential to find an appropriate scaffold material to meet the specific/precise physical, chemical, mass transport, and biological design variables inherent to each engineered tissue [4], i.e. to develop the suitable microenvironment for each tissue. To ensure a successful tissue reconstruction and/or regeneration, the selected scaffold should have the following features [5]:

I. Interconnected three-dimensional (3D) porous structure (to ensure cell growth and flow transport of chemicals and metabolic waste);

II. Biocompatibility and, in most cases, bioresorbability with a controllable degradation and resorption rate (to meet *in vitro* and/or *in vivo* environments);

III. Appropriate surface physico-chemical characteristics (to allow cell attachment, proliferation, and differentiation);

IV. Tailored and precise mechanical properties (to mimic the ones exhibited by tissues at the site of implantation).

In addition to those characteristics, hydrogel-based matrices add numerous advantages over traditional scaffolds, namely [6-8]:

I. The flowable material can fill any space, shape or defect;

II. The hydrogel can be loaded agents of therapeutic interest; and finally,

III. Its implantation does not require invasive surgical techniques in case of injectable hydrogels.

The incorporation of magnetic nanoparticles into hydrogel-based scaffolds represents a promising approach for TE applications, as it can promote not only the tissue regeneration, but also the external control of the scaffold, mainly magnetically induced mechanical movements and electromagnetically induced thermal variations [9-11]. In fact, the enhancing effect of magnetic fields on bone-inductive properties of demineralized bone matrix has been proven through the stimulation of osteoblast differentiation and by the effectiveness of magnetic fields in regulating the orientation of adherent cells [9]. Further, electroactive microenvironments, mainly based on piezoelectric materials, are being increasingly investigated for different TE strategies of bone, muscle and neurons (among others) due to the proven relevance of electrical signals on cell development and function [12].

In some cases, the application of the electrical signals can be remotely triggered through the application of a magnetic field, making use of the magnetoelectric (ME) effect [13], which has been used for TE applications [14]. ME composites composed of Terfenol-D and poly(vinylidene fluoride-co-trifluoroethylene) (PVDF-TrFE) were able to provide electrical and mechanical stimuli to MC3T3-E1 pre-osteoblast cells by the application of an external magnetic fields. Cell proliferation was enhanced by up to ≈ 25% when cells were cultured under mechanical (up to 110 ppm) and electrical stimulation (up to 0.115 mV) [14].

ME scaffolds are usually composed of piezoelectric and magnetostrictive phases [15] and, when a magnetic field is applied, the magnetostrictive phase suffers a mechanical deformation that is transmitted to the piezoelectric phase which in turn generates a voltage/polarization due to the strain [13]. In this way, a ME scaffold can remotely induce three types of stimuli: magnetic, mechanical and electric.

Despite the appealing properties of ME materials, to the best of our knowledge there are no previous reports on the use of ME materials for TE applications.

In this study, ME PVDF+$CoFe_2O_4$ composite spheres were introduced in Methacrylated Gellan Gum (MAGG) gel to obtain a composite hydrogel capable of providing magnetic, electric and mechanical stimuli to specific cells.

The spherical geometry of the ME composite was selected as scaffolds due to the several advantages when compared with traditional monolithic scaffolds [16], namely improved control over sustained delivery of therapeutic agents, stimulus-sensitive drug delivery for triggered release, the formation of porous structures and/or improved mechanical properties of the matrix, as well as the possibility of preparing injectable and/or moldable formulations to be applied by minimally invasive surgery [17].

Additionally, PVDF+$CoFe_2O_4$ spheres have been already suggested for TE [18]. MAGG was selected as a matrix as it is non-immunogenic, easy to handle, supports long term cell encapsulation (at least 21 days) either *in vitro* or *in vivo* and is compatible with multiple cell characterization protocols and histological procedures.

2.2. Experimental

2.2.1. Materials

PVDF (Solef 1010) was purchased from Solvay. Cobalt ferrite ($CoFe_2O_4$) nanoparticles (NPs), with ≈ 35–55 nm, were purchased from Nanoamor. Analytical grade tetrahydrofuran (THF) and DMF were purchased from Macron Fine Chemicals; absolute ethanol was purchased from Panreac Applichem and laboratory grade Triton X-100 was acquired from Sigma-Aldrich.

MAGG was prepared from commercial gellan gum (cGG) (Gelzan TM, Sigma-Aldrich), with a degree of substitution with methacrylate groups between 1.5 and 5%. Briefly, cGG was dissolved in distilled water at 90 ºC into a solution of 1 % w/v concentration. Heating was stopped and the pH of the solution was adjusted to 8.5 by the addition of 1 M aqueous sodium hydroxide solution. Excess glycidyl methacrylate was added in one portion and the methacrylation reaction was allowed to proceed for 24 hours whilst pH was maintained at 8.5. Acetone was then added to the reaction mixture and allowed to stand for 2 hours.

The precipitate was recovered by filtration, dissolved in distilled water and then placed in a cellulose dialysis membrane (MWCO 12 KDa) and dialysed with distilled water for 7 days. The dialysed solution was then frozen at -20 ºC and subsequently freeze-dried to give MAGG as an amorphous white solid.

For hydrogel preparation, MAGG powder was added to deionized water at 1.25 % w/V and 2.5 % w/v, in a water-bath at 37 ºC, with 100 rpm agitation.

LIVE/DEAD™ Viability/Cytotoxicity Kit (reference L3224) was acquired from Molecular Probes. MC3T3-E1 pre-osteoblast cells were obtained from Riken Bank (Japan). Phosphate-buffered saline (PBS) and Dulbecco's modified Eagle's medium (DMEM) were acquired from Gibco. Fetal bovine serum (FBS), trypsin and penicillin/streptomycin (P/S) were obtained from Biochrom. Formaldehyde was acquired from Merck and dimethyl sulfoxide (DMSO) from Sigma-Aldrich.

2.2.2. Sample processing

The preparation of the pure PVDF spheres followed the procedure proposed in the work of Correia *et al.* [19] and detailed in the following protocol [16].

Polymer concentrations of 3, 4, 5 and 6% weight/volume (w/v) in the solution with DMF were evaluated in order to optimize the polymer concentration required to obtain spheres by electrospraying.

PVDF+$CoFe_2O_4$ spheres with NP contents of 10, 40 and 70% weight percentage (wt.%) in solution have been previously prepared [18], showing that the maximum NP content within the spheres was 40 wt.%. Thus, PVDF+$CoFe_2O_4$ composite solutions with NP contents of 20, 30 and 40 wt.% were prepared in this work.

$CoFe_2O_4$ was dispersed for 30 minutes in a solution of DMF and Triton X-100, with a IKA ULTRA-TURRAX S25 Basic with a S25N-10G dispersing tool, at 6500 rpm.

Then, PVDF and THF were added and the composite solution was further dispersed for 1 hour. After dispersion, the composite solution was placed in a 5 mL Braun Inkjet plastic syringe, fitted with a steel needle with an inner diameter of 0,41 mm.

Electrospraying (**Figure 2.1**) was conducted by applying 1 $kV.cm^{-1}$ with a HiTek Power OL400/303 power supply, while a syringe pump (Syringe Pump NE300) lead to a constant flow of 1 $mL.h^{-1}$ through a needle of 0.41mm internal diameter. The resulting spheres were collected on static collector placed at 24 cm from the syringe tip.

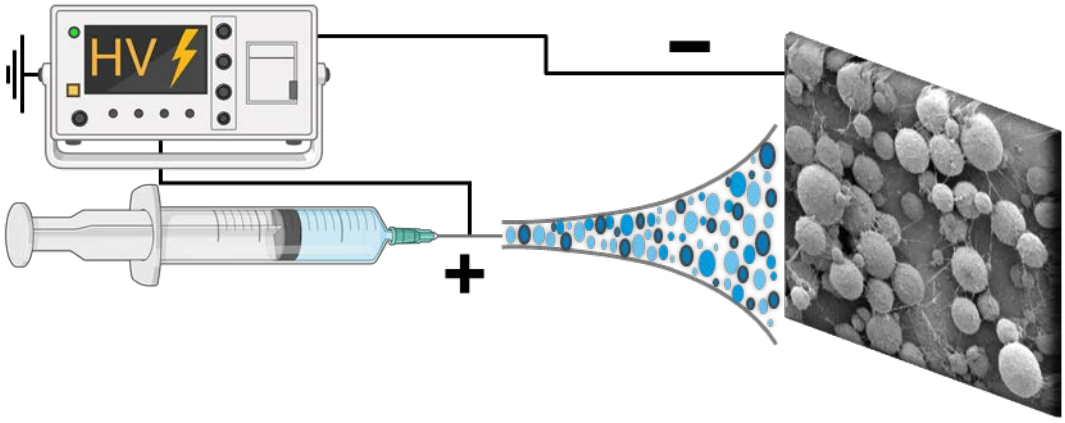

Figure 2.1. Schematic representation of the electrospraying process

Hydrogel disks were prepared following an optimized protocol, using a final concentration of 1% w/v [20]. The polymer was weighed into a vial and the appropriate quantity of ultrapure water added, with the solution left under slow agitation overnight.

Once the polymer was completely dissolved, a small quantity of the polymer solution and DMEM, acting as an ionic crosslinker, was pipetted to an eppendorf in a 9:1 ratio, to achieve the required volume and concentration. The prepared liquid hydrogel was vortexed, to adequately mix the crosslinker and the polymer solution, and 120 µl of the prepared hydrogel pipetted into silicone molds placed in the wells of a 48-well plate, and allowed to rest for 60 minutes to achieve the complete gelation.

PVDF+$CoFe_2O_4$ microspheres with 20 wt.% of $CoFe_2O_4$ in solution were incorporated into the hydrogel, by firstly suspending them in the ionic crosslinker. The polymer solution was then added to the suspension and lightly vortexed for dispersing the composite microspheres, and, finally, pipetted into the silicon molds.

2.2.3. Sample characterization

The morphology of the samples was evaluated with a Hitachi S4800 Field Emission Scanning Electron Microscope (SEM), with an accelerating voltage of 10 kV. Microsphere diameter distribution was calculated by measuring 60 microspheres at a magnification of 5.0 kX with the ImageJ software. Before microscopic characterization, samples were coated with a ≈15 nm thick layer of gold with a Quorum Emitech K550 Sputter Coater using the Film Thickness Monitor option.

The proper incorporation of the NPs in the polymer was evaluated with a JEOL JEM-1400 Transmission Electron Microscope (TEM), with an accelerating voltage of 120 kV.

The magnetic properties of the PVDF+$CoFe_2O_4$ spheres were evaluated by measuring the magnetization loops up to 22 kOe using a Microsense 2.2 Tesla Vibrating Sample Magnetometer (VSM). The Law of Approach to Saturation, as described by **Equation 2.1**, was then applied to determine the saturation magnetization (M_S) [21, 22].

$$M_H = M_S\left(1 - \frac{a}{H} - \frac{b}{H^2}\right) + cH \qquad \textbf{(2.1)}$$

where M_H is the magnetization along the direction of the magnetic field H, and a, b and c are constants. Given the magnetic NP are homogeneous and the magnitude of the applied field, both a/H and cH can be considered null [21, 22], and as such, **Equation 2.1** can be simplified into **Equation 2.2**.

$$M_H = M_S\left(1 - \frac{b}{H^2}\right) \qquad \textbf{(2.2)}$$

As M_H equals M_S when the $1/H^2$ factor is zero, M_S is determined by plotting M_H in function of $1/H^2$ for each of the composite samples, and extrapolating the linear part of the curve to intersect where $1/H^2 = 0$. There will be where M_H equals M_S.

Once M_H is known for all the samples, **Equation 2.3** can be used to determine the effective NP content in the composite PVDF+Fe_3O_4 microfibers [23].

$$CoFe_2O_4 \text{ wt.\% in spheres} = \frac{\text{Saturation Magnetization}_{\text{Spheres}} \times 100}{\text{Saturation Magnetization}_{\text{Pure } CoFe_2O_4}} \qquad \textbf{(2.3)}$$

The piezoelectric and magnetoelectric response of the spheres was confirmed for the PVDF+$CoFe_2O_4$ microspheres with 20 wt.% of NPs in solution, as a quality control, following the procedures indicated in [15]. In short, after 30 minutes of corona poling at 10 kV and 120 ºC in a home-made chamber, the piezoelectric response (d_{33}) of the samples was measured with a wide range d_{33}-meter (model 8000, APC Int Ltd). The ME response was confirmed by the variation of the piezoelectric response with and without applying a 220 Oe DC magnetic field.

A PerkinElmer Spectrum Two FT-IR coupled with a PerkinElmer UATR Two was used for the Fourier-Transform Infrared Spectroscopy (FTIR) measurements. The samples were placed in the deuterated triglycine sulfate (DTGS) sensor and their transmittance measured at room temperature (RT) in Attenuated Total Reflection (ATR) mode, between 4000 and 400 cm^{-1} using 64 scans at a resolution of 4 cm^{-1}.

According to [24], the β-phase fraction present in a sample containing α and β-phase PVDF can be determined by applying **Equation 2.4**.

$$F_\beta = \frac{A_\beta}{\left(K_\beta / K_\alpha\right) A_\alpha + A_\beta} \qquad \textbf{(2.4)}$$

where F_β is the fraction of β-phase, A_α and A_β are the absorbance values of the α and β phases, and with K_α and K_β being the absorption coefficients at the respective wavenumber. The wavenumbers selected for the α and β phases were 763 cm^{-1} and 840 cm^{-1} respectively, with K_α = $6{,}1\times10^4$ $cm^2.mol^{-1}$ and K_β = $7{,}7\times10^4$ $cm^2.mol^{-1}$ [24].

Hydrogel unconfined compression tests followed the general guidelines of the compression protocol developed by DeKosky *et al.* [25]. In this way, hydrogel discs were placed between two glass slides, and both the height and diameter of the discs were measured using calipers. Disks were placed in a Shimadzu AG-IS autograph and tested under unconfined uniaxial compression with a 50 N load cell. Measurements were performed on discs swollen to equilibrium in DMEM. As the hydrogel would gradually lose liquid during compression, there was no need to apply additional lubrication to the glass slides.

A stress-strain curve was generated by compressing each sample at a rate of 1.7% height.min^{-1}, in order to reduce any viscoelastic (i.e., a time-dependent) response.

In order to assess the viability of a MAGG hydrogel loaded with the prepared ME microspheres, *in vitro* trials with MC3T3-E1 cells were performed, with the culture following an established protocol [14]. The MC3T3-E1 cells were grown in DMEM containing 1 $g.L^{-1}$ glucose, 10% FBS and 1% P/S, at 37 °C in an incubator with 95% humidified air containing 5% carbon dioxide (CO_2).

For all assays, cells were seeded on each well, diluted from the original concentration to achieve a concentration of 3×10^4 cells mL^{-1}. For each study, 4 replicates were prepared per studied condition.

Live/Dead assays were conducted in order to evaluate the cytotoxicity of the PVDF+$CoFe_2O_4$ microspheres, together with the corresponding positive and negative controls. Previous studies demonstrated that PVDF microspheres and MAGG hydrogels are not considered toxic to cells [19, 26]. The negative control corresponds to the DMEM and the positive control refers to the DMEM with 20% volume/volume (v/v) of DMSO to induce cell death. The Live/Dead solution was prepared according to the Fluorescence Microscopy Protocol of the LIVE/DEAD™ Viability/Cytotoxicity Kit manual [27].

A Leica DMI3000 B Inverted Microscope with an attached Leica DFC450 C camera and the Leica Application Suite software were used for image acquisition, and the ImageJ software was used for data analysis.

Following the cytotoxicity assay, a fluorescence study was conducted with the MC3T3-E1 cells, using the DAPI and TRITC fluorophores, in order to assess cell cytoskeleton morphology and adhesion to the hydrogel when reinforced with PVDF+$CoFe_2O_4$ 20% microspheres. Hydrogel disc preparation followed the method previously detailed.

The hydrogels were placed in a 24-well cell culture plate. The MC3T3-E1 cells were prepared as previously described, and carefully deposited on the surface of the hydrogel discs. After 3 hours of cell seeding, samples were fixed with 4% formaldehyde, for 10 minutes at 37 °C in a 5% CO_2 incubator.

2.3. Results and discussion

2.3.1. Morphological features and vibrational spectra

2.3.1.1. Morphology

The morphology of the different produced microspheres was analyzed by SEM with magnifications of 1.5 kX and 5.0 kX for pure PVDF spheres, and 1.5 kX, 5.0 kX and 20.0 kX for the PVDF+$CoFe_2O_4$ composite spheres. The SEM images of the pure PVDF spheres with 3% w/v polymer solution and PVDF+$CoFe_2O_4$ composite spheres with 20 and 40 wt.% of NPs are presented in **Figure 2.2**.

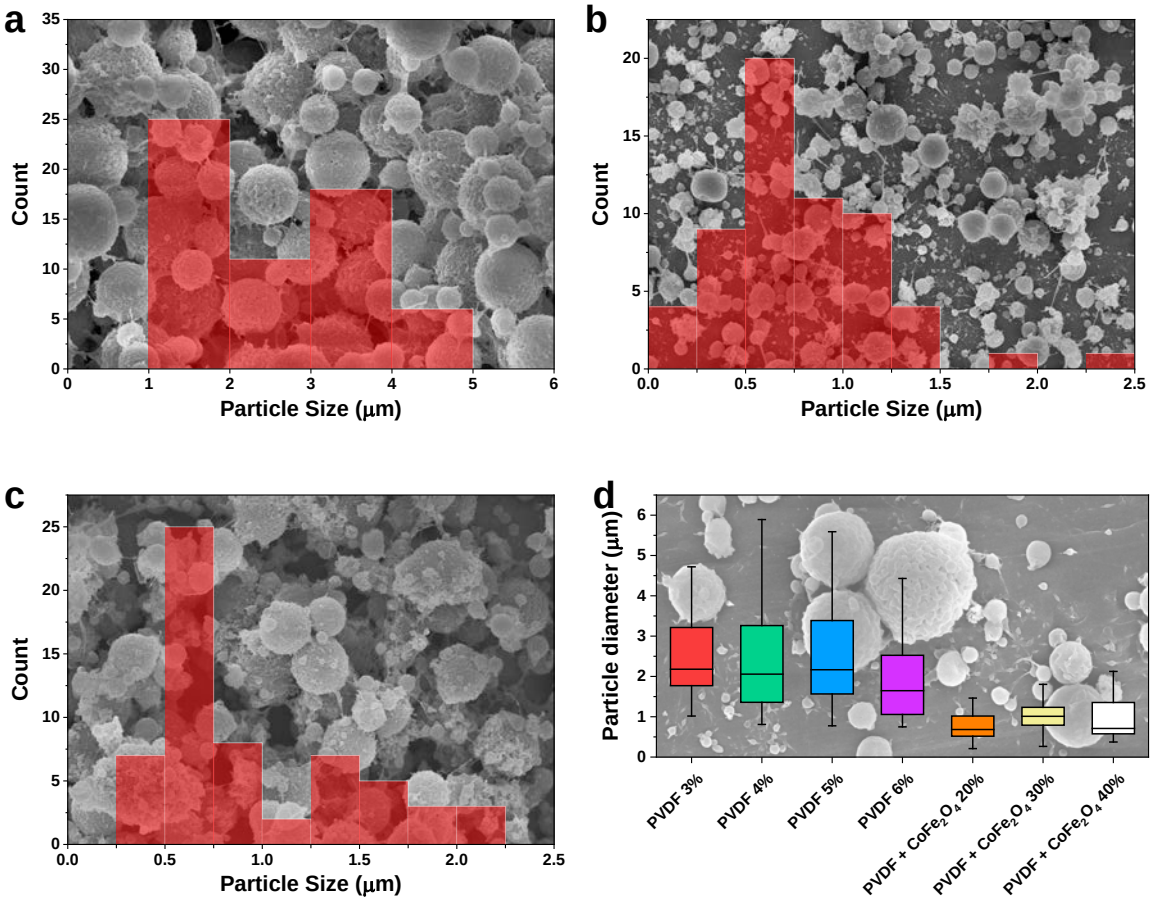

Figure 2.2. Size distribution of: a) pure PVDF spheres with 3% w/v polymer solution; b) PVDF+$CoFe_2O_4$ 20%, c) PVDF+$CoFe_2O_4$ 40 wt.%. d) Tukey-style boxplot with the size distribution variations of the samples.

Independently of the polymer concentration, most of the spheres present diameters between 1 μm and 3 μm. As the 3% w/v concentration (PVDF 3%) allowed the formation of spheres with well-defined spherical structure (**Figure 2.2-a**) and low standard deviation in the diameters, this was the selected polymer concentration for all subsequent tests with the inclusion of $CoFe_2O_4$ NPs, in order to develop the composite spheres.

It should be noted that, although some microspheres may seem connected by polymer links, these links are quite soft and just occur for high particle concentrations. In fact, the microspheres can be even properly separated by size by centrifugation [18, 28], if required for a specific application.

It is observed that the introduction of $CoFe_2O_4$ NPs within the PVDF polymer spheres causes a slight decrease in the sphere diameter from 2.4 μm to 1.0 μm [18]. This decrease is due to the higher density of ferrite nanoparticles, causing less polymer to be electrospun from the needle for the same weight of ejected material.

The TEM analysis of the composite microspheres reveals a proper encapsulation of the ferrite nanoparticles, as presented in **Figure 2.3**.

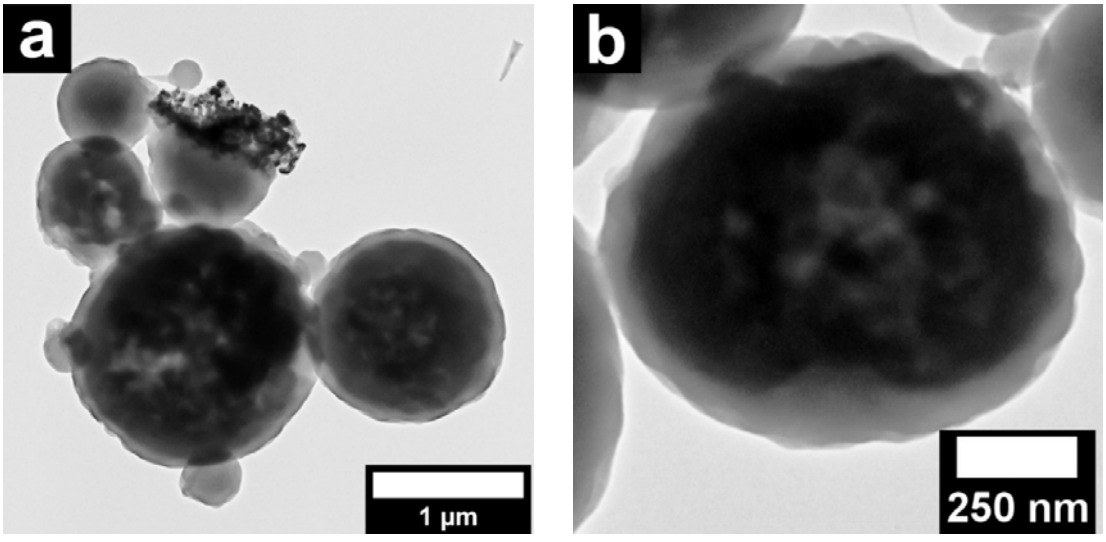

Figure 2.3. TEM images of the PVDF+$CoFe_2O_4$ 40 wt.% composite spheres, with the polymer in shades of grey and the magnetic NPs in black.

2.3.1.2. Vibrational spectra

As the β-phase of PVDF is essential for obtaining proper piezoelectric and, therefore, ME response in the composite, FTIR was used to identify and quantify the β-phase of both pure and composite samples (**Figure 2.4-a**).

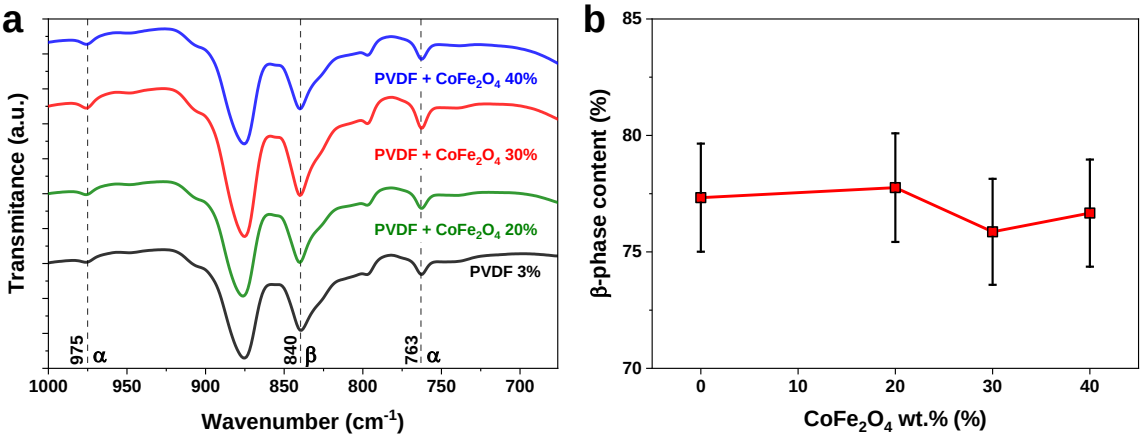

Figure 2.4. a) FTIR spectra of pure PVDF and PVDF+$CoFe_2O_4$ composites microspheres; b) Variation of β-phase content as a function of $CoFe_2O_4$ content. The values are presented as media ± standard deviation, n =3.

The β-phase content of the samples was calculated as per **Equation 2.4**. The results are presented in **Figure 2.4-b**. All samples exhibit β-phase contents ≈ 78% independently of the filler content, being therefore the low solvent evaporation temperatures (≤ 60°C) and the electric field from the electrospinning process the origin of the crystallization of the polymer mainly in the β-phase [16, 32, 33].

The piezoelectric and ME response of the microspheres was verified for the PVDF+$CoFe_2O_4$ 20% samples, obtaining a piezoelectric response $|d_{33}|$ of ≈ 22 $pC.N^{-1}$ and a magnetoelectric response of $\Delta|d_{33}|$ ≈ 6 $pC.N^{-1}$ at a DC magnetic field of 220 mT, confirming the results obtained in [15].

2.3.2. Mechanical properties

Being the mechanical properties one of the most important characteristics of the implementation of scaffolds [5], compression tests (up to a strain of 90%) were conducted and results presented in **Figure 2.5**.

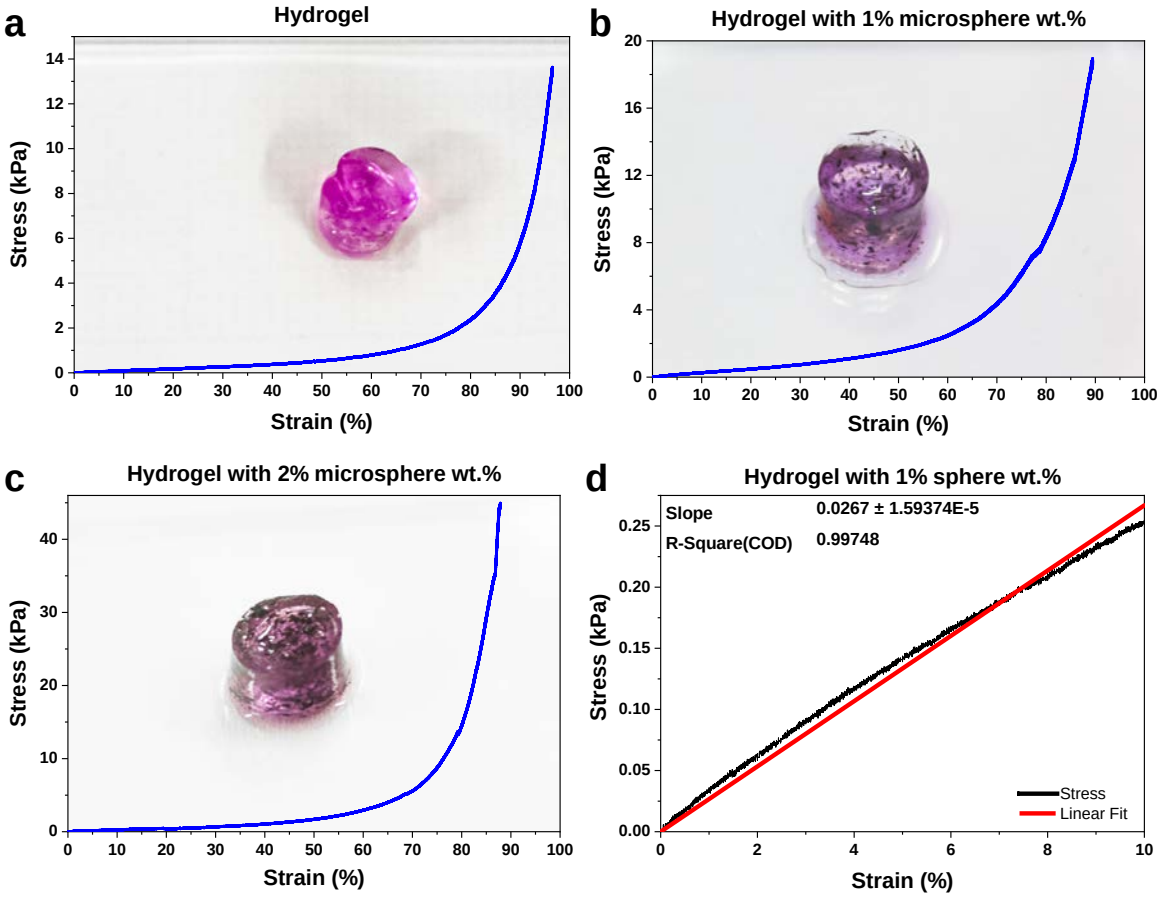

Figure 2.5. Stress/Strain curves of MAGG hydrogel, at a compression rate of 1.7% height.min^{-1}, with: a) 0, b) 1 and d) 2 wt.% of PVDF+$CoFe_2O_4$ 20% microspheres; and d) 1 wt.% of PVDF+$CoFe_2O_4$ 20 wt.% composite microspheres, between 0 % and 10 % strain, with linear fit and inset with associated data the fit.

It shows that the general response of the hydrogel is not affected by the introduction of the microspheres, although its strength is greatly improved. The Strain/Stress curves are similar to other hydrogels [34], and are characterized by both elastic and plastic regions.

Determining the elastic modulus on a given section of the curve provides further insight on this improvement. The elastic modulus was determined by choosing a section of the curve, and calculating the most accurate linear adjustment to it.

For biomedical applications, the stress-strain region of larger interest [35] is between 0 and 10% strain, and, so, this was the selected section for determining the elastic modulus. An average of three tests was used, and the resulting curve and linear fit are presented in **Figure 2.5-d**, for the sample with 1 wt.% of microspheres. The hydrogel without particles presents an elastic modulus of 9.39 kPa (R^2 = 0.997). With the introduction of the microspheres, the mechanical resistance of the hydrogel is improved, presenting elastic modulus of 20.33 kPa (R^2 = 0.9997), 26.70 kPa (R^2 = 0.998) and 28.69 kPa (R^2 = 0.996), with 0.5 wt.%, 1 wt.% and 2 wt.%, respectively. These results indicate that this improvement reaches a plateau at microsphere wt.% of about 1.

2.3.3. Functional response

2.3.3.1. Magnetic properties

By measuring the hysteresis curves obtained by the VSM technique, the magnetic NP content present in the composite samples can be determined [29-31]. Thus, this technique was used to assess the effective content of $CoFe_2O_4$ NPs in the composite spheres. **Figure 2.6-a** presents the obtained curves.

From the magnetization measurements it was determined that all spheres exhibited 2.7 kOe coercivity at RT, consistent with their ferromagnetic behaviour. The saturation magnetization at 25 kOe increased with increasing ferrite content (from 20% to 40% in solution), from 9.8 emu/g to 18.9 emu/g.

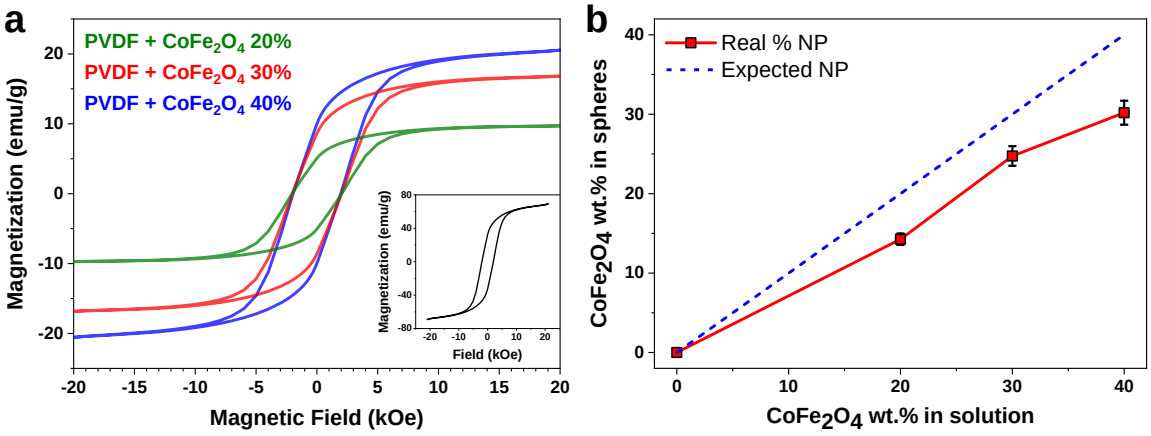

Figure 2.6. a) RT hysteresis loops for the composite PVDF+$CoFe_2O_4$ spheres. Inset: RT hysteresis loop for the pure $CoFe_2O_4$ NPs; b) Relation between the wt.% of $CoFe_2O_4$ NPs in solution and those in the multiferroic spheres, with the blue dashed line indicating the ideal linear theoretical behavior.

Figure 2.6-b shows that the maximum NP content in the composite spheres (calculated by **Equation 2.3**) increases almost linearly with NP content in the solution [18]. Additionally, the NP weight content in the resulting spheres is ≈ 20% lower than the one formulated from the initial solutions. This can be explained by the higher density of the $CoFe_2O_4$ NPs (when compared to the polymer matrix) that causes the settling of some NPs on the bottom of the syringe during the electrospinning, and also from partial blockage of the needle hole by agglomeration of NPs, due to the flow funneling towards the needle [18].

2.3.3.2. Cytotoxicity assay

In order to determine if the prepared microspheres were toxic to the target cells, Live/Dead assay (**Figure 2.7 a-c**) was conducted, and various images were obtained of the cells with contrasting fluorescent dyes, by counting and averaging the number of living and dead cells in each image. These results, together with representative images of the Live/Dead assays, are presented in the **Figure 2.7-d**, showing the viability of the MC3T3-E1 cells in the proposed scaffolds.

Previous studies have demonstrated that the implementation of scaffolds capable of providing mechanical and/or electrical stimuli to the cells represent a promising platform for tissue engineering [12]. These preliminary results demonstrate the potential of scaffolds based on MAGG loaded with PVDF+$CoFe_2O_4$ microspheres for tissue engineering applications, as they the components are non-cytotoxic and could be used to support cell culture under magnetomechanical [14] (with non-poled samples) and ME [14] (with poled samples) stimuli.

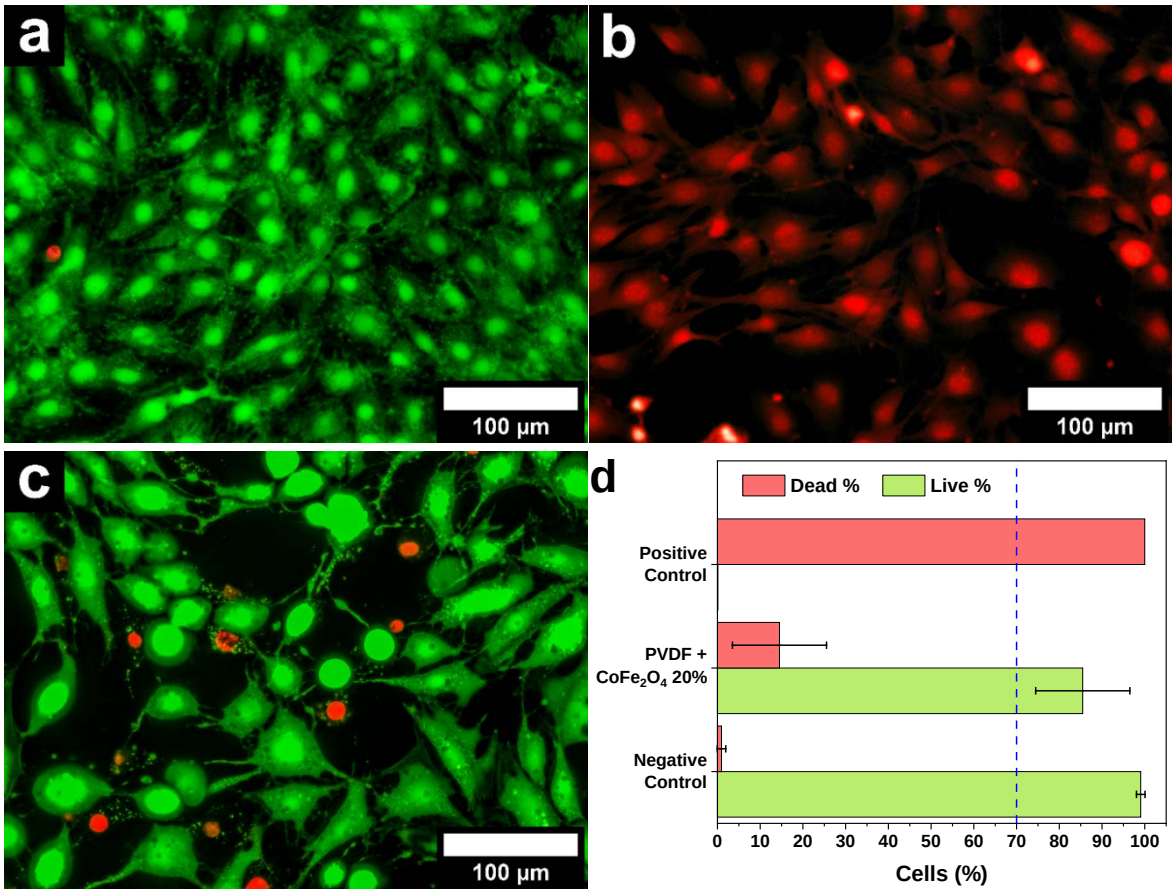

Figure 2.7. Live/Dead fluorescence images for the initial test with the MC3T3-E1 cells: a) negative control, b) positive control and c) with PVDF+ $CoFe_2O_4$ 20 wt.% microspheres. d) Live/Dead results, in terms of average cell survivability.

In this way, such scaffolds could be used to effectively mimic complex electromechanical microenvironments in the human body, using *ex vivo* dynamic bioreactors [12, 14, 36], allowing to improve cell regeneration through mechano-electrical stimulation.

2.4. Conclusions

Injectable magneto-sensitive MAGG-based hydrogels have been developed to support novel tissue engineering strategies based on magnetoelectric microenvironments. Composite hydrogels were prepared by mixing MAGG with 1 μm $CoFe_2O_4$/PVDF composite spheres, showing promising features such as cell viability superior to 80%. The novel developed hydrogels will allow in cell culture under dynamic magnetically controlled mechanical and electrical clues.

2.5. References

1. Saidi, R.F. and S.K. Hejazii Kenari, *Challenges of organ shortage for transplantation: solutions and opportunities.* International journal of organ transplantation medicine, 2014. **5**(3): p. 87-96. Available from: https://www.ncbi.nlm.nih.gov/pmc/PMC4149736/.

2. Attalla, R., C. Ling, and P. Selvaganapathy, *Fabrication and characterization of gels with integrated channels using 3D printing with microfluidic nozzle for tissue engineering applications.* Biomedical Microdevices, 2016. **18**(1): p. 1-12. DOI: 10.1007/s10544-016-0042-6

3. Liu, M., X. Zeng, C. Ma, H. Yi, Z. Ali, X. Mou, S. Li, Y. Deng, and N. He, *Injectable hydrogels for cartilage and bone tissue engineering.* Bone Research, 2017. **5**. DOI: 10.1038/boneres.2017.14

4. Drury, J.L. and D.J. Mooney, *Hydrogels for tissue engineering: Scaffold design variables and applications.* Biomaterials, 2003. **24**(24): p. 4337-4351. DOI: 10.1016/S0142-9612(03)00340-5

5. Hutmacher, D.W., *Scaffolds in tissue engineering bone and cartilage.* Biomaterials, 2000. **21**(24): p. 2529-2543. DOI: 10.1016/S0142-9612(00)00121-6

6. Gutowska, A., B. Jeong, and M. Jasionowski, *Injectable gels for tissue engineering.* Anatomical Record, 2001. **263**(4): p. 342-349. DOI: 10.1002/ar.1115

7. Zhang, Y.S. and A. Khademhosseini, *Advances in engineering hydrogels.* Science, 2017. **356**(6337). DOI: 10.1126/science.aaf3627

8. Lee, J.H. and H.W. Kim, *Emerging properties of hydrogels in tissue engineering.* Journal of Tissue Engineering, 2018. **9**. DOI: 10.1177/2041731418768285

9. Karahaliloglu, Z., E. Yalçln, M. Demirbilek, and E.B. Denkbas, *Magnetic silk fibroin e-gel scaffolds for bone tissue engineering applications.* Journal of Bioactive and Compatible Polymers, 2017. **32**(6): p. 596-614. DOI: 10.1177/0883911517693635

10. Cardoso, V.F., A. Francesko, C. Ribeiro, M. Bañobre-López, P. Martins, and S. Lanceros-Mendez, *Advances in Magnetic Nanoparticles for Biomedical Applications.* Advanced Healthcare Materials, 2018. **7**(5). DOI: 10.1002/adhm.201700845

11. Li, Y., G. Huang, X. Zhang, B. Li, Y. Chen, T. Lu, T.J. Lu, and F. Xu, *Magnetic hydrogels and their potential biomedical applications.* Advanced Functional Materials, 2013. **23**(6): p. 660-672. DOI: 10.1002/adfm.201201708

12. Ribeiro, C., V. Sencadas, D.M. Correia, and S. Lanceros-Méndez, *Piezoelectric polymers as biomaterials for tissue engineering applications.* Colloids and Surfaces B: Biointerfaces, 2015. **136**: p. 46-55. DOI: 10.1016/j.colsurfb.2015.08.043

13. Martins, P. and S. Lanceros-Méndez, *Polymer-based magnetoelectric materials.* Advanced Functional Materials, 2013. **23**(27): p. 3371-3385. DOI: 10.1002/adfm.201202780

14. Ribeiro, C., V. Correia, P. Martins, F.M. Gama, and S. Lanceros-Mendez, *Proving the suitability of magnetoelectric stimuli for tissue engineering applications.* Colloids and Surfaces B: Biointerfaces, 2016. **140**: p. 430-436. DOI: 10.1016/j.colsurfb.2015.12.055

15. Martins, P., Y.V. Kolen'Ko, J. Rivas, and S. Lanceros-Mendez, *Tailored Magnetic and Magnetoelectric Responses of Polymer-Based Composites.* ACS Applied Materials and Interfaces, 2015. **7**(27): p. 15017-15022. DOI: 10.1021/acsami.5b04102

16. Ribeiro, C., C.M. Costa, D.M. Correia, J. Nunes-Pereira, J. Oliveira, P. Martins, R. Gonçalves, V.F. Cardoso, and S. Lanceros-Méndez, *Electroactive poly(vinylidene fluoride)-based structures for advanced applications.* Nature Protocols, 2018. **13**(4): p. 681-704. DOI: 10.1038/nprot.2017.157

17. Wang, H., S.C.G. Leeuwenburgh, Y. Li, and J.A. Jansen, *The use of micro-and nanospheres as functional components for bone tissue regeneration.* Tissue Engineering - Part B: Reviews, 2012. **18**(1): p. 24-39. DOI: 10.1089/ten.teb.2011.0184

18. Goncalves, R., P. Martins, D.M. Correia, V. Sencadas, J.L. Vilas, L.M. Leon, G. Botelho, and S. Lanceros-Mendez, *Development of magnetoelectric CoFe2O4/poly(vinylidene fluoride) microspheres.* RSC Advances, 2015. **5**(45): p. 35852-35857. DOI: 10.1039/c5ra04409j

19. Correia, D.M., R. Goncalves, C. Ribeiro, V. Sencadas, G. Botelho, J.L.G. Ribelles, and S. Lanceros-Mendez, *Electrosprayed poly(vinylidene fluoride) microparticles for tissue engineering applications.* RSC Advances, 2014. **4**(62): p. 33013-33021. DOI: 10.1039/c4ra04581e

20. Carvalho, E.M.O., *Desenvolvimento de hidrogéis biodegradáveis carregados com microsferas eletroativas para aplicação em Engenharia de Tecidos*, in *School of Sciences*. 2017, University of Minho. p. 74. Available from.

21. Morrish, A.H., *The Analysis of the Magnetization Curves of Bulk Material*, in *The Physical Principles of Magnetism*, R.J. Herrick, Editor. 2001, IEEE Press: USA. p. 382.403. DOI: 10.1109/9780470546581

22. Grössinger, R., *A critical examination of the law of approach to saturation. I. Fit procedure.* Physica Status Solidi (a), 1981. **66**(2): p. 665-674. DOI: 10.1002/pssa.2210660231

23. Hermenegildo, B., C. Ribeiro, L. Pérez-Álvarez, J.L. Vilas, D.A. Learmonth, R.A. Sousa, P. Martins, and S. Lanceros-Méndez, *Hydrogel-based magnetoelectric microenvironments for tissue stimulation.* Colloids and Surfaces B: Biointerfaces, 2019. **181**: p. 1041-1047. DOI: 10.1016/j.colsurfb.2019.06.023

24. Martins, P., A.C. Lopes, and S. Lanceros-Mendez, *Electroactive phases of poly(vinylidene fluoride): Determination, processing and applications.* Progress in Polymer Science, 2014. **39**(4): p. 683-706. DOI: 10.1016/j.progpolymsci.2013.07.006

25. DeKosky, B.J., N.H. Dormer, G.C. Ingavle, C.H. Roatch, J. Lomakin, M.S. Detamore, and S.H. Gehrke, *Hierarchically Designed Agarose and Poly(Ethylene Glycol) Interpenetrating Network Hydrogels for Cartilage Tissue Engineering.* Tissue Engineering Part C: Methods, 2010. **16**(6): p. 1533-1542. DOI: 10.1089/ten.tec.2009.0761

26. Silva-Correia, J., V. Miranda-Gonçalves, A.J. Salgado, N. Sousa, J.M. Oliveira, R.M. Reis, and R.L. Reis, *Angiogenic Potential of Gellan-Gum-Based Hydrogels for Application in Nucleus Pulposus Regeneration:In VivoStudy.* Tissue Engineering Part A, 2012. **18**(11-12): p. 1203-1212. DOI: 10.1089/ten.tea.2011.0632

27. Probes, M., *LIVE/DEAD Viability/Cytotoxicity Kit for mammalian cells*. 2005, Invitrogen. Available from: https://assets.thermofisher.com/TFS-Assets/LSG/manuals/mp03224.pdf.

28. Correia, D.M., V. Sencadas, C. Ribeiro, P.M. Martins, P. Martins, F.M. Gama, G. Botelho, and S. Lanceros-Méndez, *Processing and size range separation of pristine and magnetic poly(l-lactic acid) based microspheres for biomedical applications.* Journal of Colloid and Interface Science, 2016. **476**: p. 79-86. DOI: 10.1016/j.jcis.2016.05.012

29. Wei, L., M. Yinping, Z. Hao, L. Bo, L. Yange, S. Binbin, and W. Jixuan, *Two-Dimensional Magnetic Field Vector Sensor Based on Tilted Fiber Bragg Grating and Magnetic Fluid.* Journal of Lightwave Technology, 2013. **31**(15): p. 2599-2605. DOI: 10.1109/jlt.2013.2271635

30. Valan, M.F., A. Manikandan, and S.A. Antony, *Microwave Combustion Synthesis and Characterization Studies of Magnetic Zn1–x Cd x Fe2O4 (0 ≤ x ≤ 0.5) Nanoparticles.* Journal of Nanoscience and Nanotechnology, 2015. **15**(6): p. 4543-4551. DOI: 10.1166/jnn.2015.9801

31. Martins, P., A. Lasheras, J. Gutierrez, J.M. Barandiaran, I. Orue, and S. Lanceros-Mendez, *Optimizing piezoelectric and magnetoelectric responses on CoFe2O4/P(VDF-TrFE) nanocomposites.* Journal of Physics D: Applied Physics, 2011. **44**(49): p. 495303-495310. DOI: 10.1088/0022-3727/44/49/495303

32. Luo, C.J., T. Okubo, M. Nangrejo, and M. Edirisinghe, *Preparation of polymeric nanoparticles by novel electrospray nanoprecipitation.* Polymer International, 2014. **64**(2): p. 183-187. DOI: 10.1002/pi.4822

33. Martins, P., C.M. Costa, M. Benelmekki, G. Botelho, and S. Lanceros-Mendez, *On the origin of the electroactive poly(vinylidene fluoride) β-phase nucleation by ferrite nanoparticles via surface electrostatic interactions.* CrystEngComm, 2012. **14**(8): p. 2807–2811. DOI: 10.1039/c2ce06654h

34. Czerner, M., L.S. Fellay, M.P. Suárez, P.M. Frontini, and L.A. Fasce, *Determination of Elastic Modulus of Gelatin Gels by Indentation Experiments.* Procedia Materials Science, 2015. **8**: p. 287-296. DOI: 10.1016/j.mspro.2015.04.075

35. Panadero, J.A., S. Lanceros-Mendez, and J.L.G. Ribelles, *Differentiation of mesenchymal stem cells for cartilage tissue engineering: Individual and synergetic effects of three-dimensional environment and mechanical loading.* Acta Biomaterialia, 2016. **33**: p. 1-12. DOI: 10.1016/j.actbio.2016.01.037

36. Ghafar-Zadeh, E., J.R. Waldeisen, and L.P. Lee, *Engineered approaches to the stem cell microenvironment for cardiac tissue regeneration.* Lab on a Chip, 2011. **11**(18): p. 3031-3048. DOI: 10.1039/c1lc20284g

Chapter 3

Tuning magnetic and ionic response of hybrid fibers

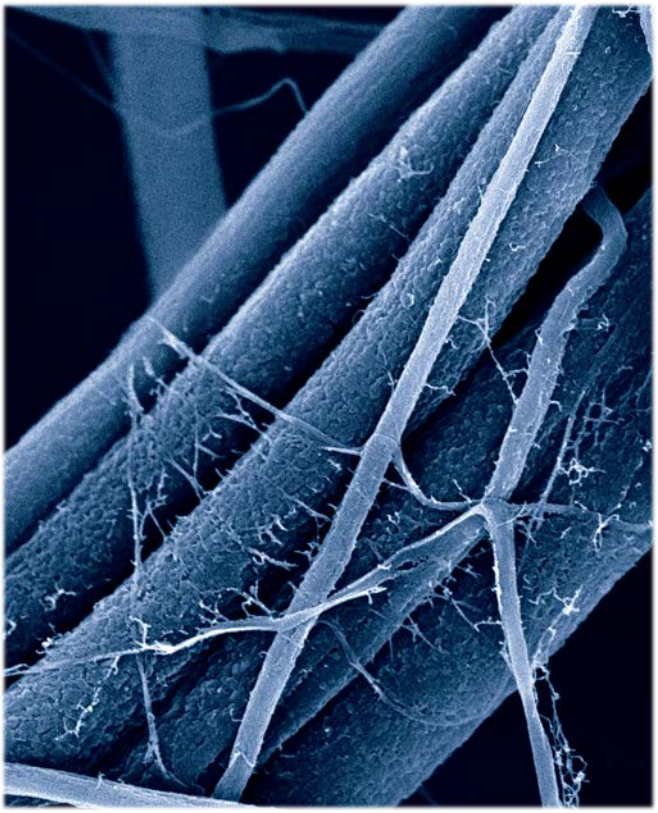

Hybrid electrospun polymer-ionic liquid microfibers.

Tissue engineering aims to solve the lack of tissue donors by creating new tissue in in-vitro conditions. This requires microenvironments that are capable of delivering specific stimuli to cells and tissues, in a controlled manner. Electroactive materials, such as polymer fibers produced via electrospinning, can be finely tuned to specific tissues and applications, making them capable of delivering said controlled stimuli, opening the door to new and improved therapies. This chapter details the development of hybrid magnetoelectric and conductive poly(vinylidene fluoride) fibers, aimed at assisting in muscle tissue regeneration.

3.1. Introduction

The increasing number of patients with tissue damage or degenerative diseases is a growing problem worldwide, related both to recreational and work-related accidents, as well as to the improvements to life expectancy [1]. The 1988 to 2020 U.S. Department of health and human services data indicates that more than 50% of all transplant procedures have been performed in patients with more than 50 years of age [2]. A particularly complex case is that of volumetric muscle loss (VLM), in which a large portion of skeletal muscle is removed due to disease or serious trauma, something particularly common in high-level athletes or military personnel. This is a type of tissue that hardly regenerates after such a serious injury and, consequently, patients that suffer from VLM often need to undergo complicated surgeries for tissue transplant and long periods of therapy, with only limited benefits [3].

Tissue engineering (TE), as defined by Langer *et al.* [4], aims to become a possible solution to this problem, proposing, among other approaches, muscle tissue to be grown *in vitro* from cells of the patient, and then implanted in the patient as required, bypassing the need of compatible donors or waiting lists.

This approach requires physically active microenvironments based on electroactive materials, relevant for applications for different tissues such as bone [5], cardiac [6], and skeletal muscle. Electroactive materials composed of oriented fibers with an active behavior, including magnetically induced mechano-transduction or mechanically induced electroactivity, have already been proven to be suitable for muscle tissue regeneration, based on the specific electro-mechanical characteristics of this tissue during its functional response [7].

Electroactive materials have been processed into different morphologies such as films, fibers, and microspheres [8]. For muscle TE strategies, fibers obtained by electrospinning are of particularly interest due to various advantages such as high surface-to-volume ratio and tunable porosity [9].

Electrospinning also allows a fine control of micro- and nanofiber properties, so that they can be tuned according to the morphological microenvironment of specific cells and tissues, improving their development and regeneration [10]. Furthermore, this technique allows the production of hybrid and composite materials, such as polymer fibers with embedded nanoparticles (NPs) [11, 12].

Among the different electroactive polymers, poly(vinylidene fluoride) (PVDF) has been extensively studied for TE applications. PVDF is a biocompatible material that, due to its high piezoelectric coefficient, mainly related to the crystallization in the β-phase polymorph, can be used to develop scaffolds that assist and improve muscle tissue regeneration [13]. PVDF is a versatile material, that can be processed in up to five polymorphs, being the non-polar α and the polar β phases the most commonly used for applications, and in a wide variety of morphologies [8]. Additionally, PVDF is also able to incorporate different fillers, such as magnetic and metallic nanoparticles [5], carbon nanotubes and graphene [11], or ionic liquids (ILs) [14], allowing to tune the active response of the material. This makes PVDF an extremely suitable and interesting material for TE applications.

On the specific case of muscle TE, it has been described that the process is greatly benefited by giving the cells not only a passive morphological stimuli – by means of a scaffold comprised of oriented fibers – but also an active stimuli, namely in the form of mechanical and electric stimuli, in a way that mimics the natural conditions of muscle tissues [13]. Adding these functionalities to otherwise passive polymer scaffolds, is a subject of great interest, particularly if they allow the development of smart scaffolds that not only are capable of delivering the stimuli, but also of controlling when, where, and the magnitude of its application.

Recently, ILs have gained special attention for biomedical and TE applications [13, 14]. ILs are defined as salts with a low melting point (under 100 ºC), and their main properties are determined by their specific anions and cations, including a high electrochemical and thermal stability that makes them interesting for a large variety of applications including actuators, sensors and biomedical devices [14]. Furthermore, the high ionic conductivity and biocompatibility/biodegradability of some ILs makes them attractive for muscle TE [15]. Choline bis(trifluoromethylsulfonyl)imide ([Chol][TFSI]) is an IL that presents ionic conductivity values of 3.98 $mS.cm^{-1}$, and has been previously evaluated for electrolyte [16], biocatalysis and microbial fuel cells [17] applications. The choline cation ([Chol]) of this IL is reported as both biodegradable and biocompatible, as it is a molecule that supports various biological functions [18]. However, [Chol][TFSI] may present some toxicity in large contents, due to the effects of the bis(trifluoromethylsulfonyl)imide anion ([TFSI]) [19]. There have been no previous reports on attempts to incorporate this IL type into polymer fibers for TE.

In the last twenty years, the interest in the application of nanomaterials (NMs) in the biomedical or medical areas has strongly grown with applications ranging from contrast agents in medical imaging [20, 21] and drug delivery [22, 23], to wound healing [24, 25] and TE [5, 26].

Iron(II,III) oxide (Fe_3O_4) is a biocompatible material that has been extensively studied for a variety of applications, ranging from sensors and actuators to biomedicine and environmental remediation [27, 28]. Fe_3O_4, in the NP form, has been reported to present superparamagnetic behavior at sizes under 20 nm and ferrimagnetic between 20-300 nm [29], making it an interesting material to be used in smart material applications, and as a way to remotely control the application of mechanical and/or electromechanical stimuli from polymer base scaffolds.

In this work, oriented PVDF-O and randomly oriented PVDF-R fibers incorporating different amounts of IL (5, 10 and 15 wt.%) and Fe_3O_4 (5, 10 and 15 wt.%) have been produced by electrospinning. Their morphology, physico-chemical and thermal properties were evaluated, as well as the ionic and magnetic properties of the PVDF+Fe_3O_4 fibers. The potential of these materials for TE applications was confirmed by cytotoxicity assays.

3.2. Experimental

3.2.1. Materials

N,N-Dimethylformamide (DMF, 99.9% GLR) was purchased from Labkem. PVDF, reference Solef 5130, was purchased from Solvay. Choline bis(trifluoromethylsulfonyl) imide ([Chol][TFSI], 99%) IL was acquired from Iolitec. Iron (II,III) oxide nanopowder (Fe_3O_4, 99%, 30 nm), was purchased from Nanostructured & Amorphous Materials.

3.2.2. Sample processing

3.2.2.1. Solution preparation

For the pure polymer solution, PVDF was dissolved in DMF, with a concentration of 15% weight percentage (wt.%) [30], and the solution was kept under agitation with a magnetic stirrer at room temperature (RT) until complete dissolution of the polymer.

For the PVDF+IL solutions with different IL content (5, 10 and 15 wt.%), [Chol][TFSI] was added to DMF and mixed with a magnetic stirrer for 20 minutes. PVDF (15 wt.%) was then slowly added to the solution under agitation until complete dissolution of the polymer.

For the solutions with magnetic NP, Fe_3O_4 NPs (5, 10 and 15 wt.%) were dispersed in DMF in an ultrasound bath for 4 h to ensure good dispersion and prevent nanoparticle agglomeration. Then, PVDF was slowly added, and the solution placed in a Teflon mechanical stirrer until complete dissolution of the polymer.

3.2.2.2. Electrospinning

For all samples, the polymer solution was placed in a 5 mL Terumo plastic syringe fitted with a steel needle with 0.41 mm inner diameter. Electrospinning (**Figure 3.1**) was conducted by applying a voltage of 15 kV with a HiTek Power OL400/303 power supply. A syringe pump (Syringepump NE-300) provided a constant polymer solution flow at a rate of 0.4 $mL.h^{-1}$.

The electrospun PVDF-R fibers were collected on a grounded collecting plate 20 cm away from the needle, while in the case of the PVDF-O fibers, they were collected on a grounded drum of 80 mm diameter, rotating at 1500 rpm, and 20 cm away from the needle. For all samples, temperature was kept between 20-25 ºC, and ambient humidity values were kept between 40-60%. After 24 h of room-temperature drying, the fiber mats were detached from the collectors for characterization.

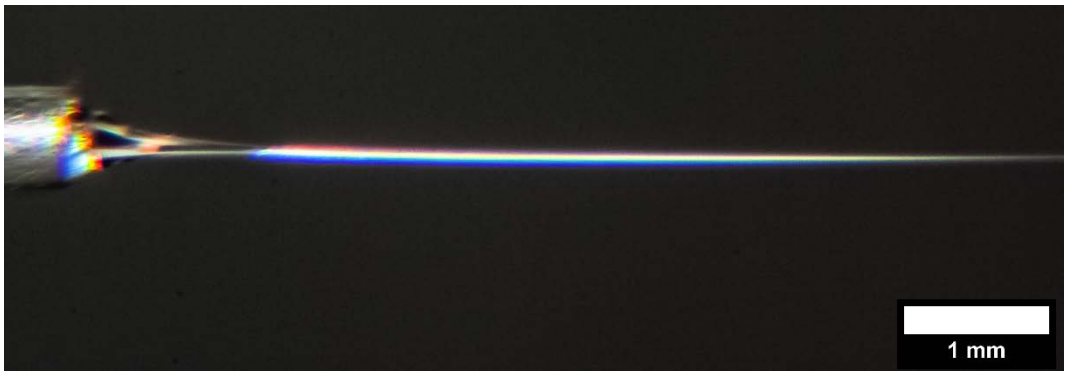

Figure 3.1. During electrospinning the PVDF solution is stretched while the solvent evaporates, forming thin fibers

3.2.3. Sample characterization

The morphology of the pristine PVDF and PVDF+IL fibers was evaluated by Scanning Electron Microscopy (SEM), using a Hitachi S-4800 field emission SEM, in SE mode at an accelerating voltage of 10 kV. The fibers without NP were coated with a ≈ 15 nm thick layer of gold using a Quorum Emitech K550 Sputter Coater with the Film Thickness Monitor option, at 25 mA and a pressure of 0.09 mbar. For all samples, fiber diameter and distribution were calculated by randomly measuring 40 fibers, at magnifications of 1.5 kX and 10.0 kX, using the ImageJ software.

Fourier Transform Infrared Spectroscopy (FTIR) was performed at RT with a JASCO FT/IR-6100 in ATR mode, using 64 scans between 2000 and 600 cm^{-1} with a resolution of 4 cm^{-1}. The β-phase content of the samples was evaluated by using **Equation 2.4**, described in **Chapter 2**.

The thermal behavior of the samples was evaluated by Differential Scanning Calorimetry (DSC) and by Thermogravimetric Analysis (TGA). DSC measurements were acquired with a Mettler Toledo DSC822e, equipped with a sample robot, at a heating rate of 10 °C.min^{-1} under nitrogen flow of 50 mL.min^{-1}. STAR software was used to retrieve and analyze the data.

The crystallinity content (X_C) of the PVDF samples was calculated by applying **Equation 3.1**.

$$X_C = \frac{\Delta H}{\%_{polymer}\left(x\Delta H_\alpha + y\Delta H_\beta\right)} \qquad (\mathbf{3.1})$$

where ΔH is the melting enthalpy of the sample, ΔH_α and ΔH_β are the melting enthalpies of a 100% crystalline sample in the α- and β-phase, respectively. The mass fraction of PVDF within the membranes is represented by $\%_{polymer}$. The amount of the α- and β-phase present in the sample are represented, respectively, by x and y, and were previously determined by FTIR analysis. Finally, the values attributed to melting enthalpies of a 100% crystalline sample of PVDF were ΔH_α = 93.07 J.g^{-1} and ΔH_β = 103.4 J.g^{-1} [31].

For TGA, samples were placed in an open ceramic crucible and analyzed in a Mettler Toledo TGA/SDTA851 equipped with a thermobalance. The samples were heated from 25 to 800 ºC, at a rate of 10 ºC.min^{-1} and a nitrogen flow rate of 50 mL.min^{-1}.

The ionic conductivity value (σ_i) of the electrospun membranes was measured by impedance analyses (real and impedance imaginary) in an Autolab PGSTAT-12 (Eco Chemie) at frequencies between 500 mHz and 65 kHz and a temperature range from 20 to 100 °C, using a constant volume support equipped with gold blocking electrodes placed within a Buchi TO 50 oven.

The sample temperature was evaluated by means of a type K thermocouple placed close to the electrolyte membrane. **Equation 3.2** can be used to determine σ_i:

$$\sigma_i = \frac{t}{A * R_b} \quad \textbf{(3.2)}$$

where t is the thickness, A is the area and R_b is sample bulk resistivity, obtained by interception of the imaginary impedance (minimum value of Z'') with the slanted line in the real impedance (Z').

The magnetic properties of the PVDF+Fe_3O_4 fiber mats were evaluated by measuring the magnetization loops (M_H) of up to 18 kOe, using a Microsense 2.2 Tesla Vibrating Sample Magnetometer (VSM). The Law of Approach to Saturation, as described by **Equations 2.1** and **2.2** (described in Chapter 2), was then applied to determine the saturation magnetization (M_S) [32, 33].

Once M_S is known for all the samples, **Equation 3.3** can be used to determine the effective NP content in the composite PVDF+Fe_3O_4 microfibers [5].

$$Fe_3O_4 \text{ wt.\% in fibers} = \frac{\text{Saturation Magnetization}_{\text{Fibers}} \times 100}{\text{Saturation Magnetization}_{\text{Pure } Fe_3O_4}} \quad \textbf{(3.3)}$$

3.2.3.1. *In vitro* cytotoxicity assay

Indirect cytotoxicity evaluation of the prepared samples was performed by adapting the ISO 10993-5 standard test method. L929 cells were cultured in 75 cm^2 cell culture flask at 37 °C in a humidified environment with 5% CO_2, using Dulbecco's modified Eagle's medium (DMEM, Biochrom) containing 4.5 $g.L^{-1}$ glucose, 10% fetal bovine serum (FBS, Biochrom) and 1% Volume/Volume (v/v) penicillin/streptomycin solution (P/S, Biochrom) (**Figure 3.2**).

The samples were cut to approximately 1 cm^2. The sterilization was conducted by exposure to ultraviolet radiation for 1 h on each side of the samples and afterwards washed with a sterile phosphate-buffered saline solution (PBS, pH 7.4).

Then, a suspension of 2×10^4 $cell.mL^{-1}$ was seeded in 96-well tissue culture polystyrene plates and incubated for 24 h at the same conditions described above to ensure cell attachment on the plate. Simultaneously, each sample was incubated for 24 h in a 24-well tissue culture polystyrene plate.

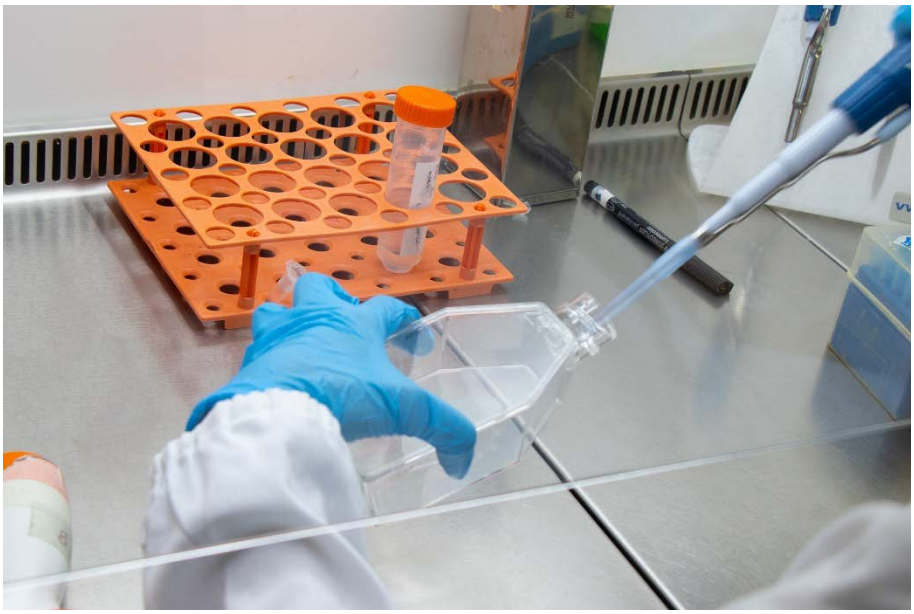

Figure 3.2. Preparation for cell culture prior to cytotoxicity assay

Then, the cell culture medium in the 96-well plates was removed, and 100 µL of culture medium (that was in contact with the different samples) was added to each well and allowed to incubate for 72 h in standardized culture conditions as mentioned above.

A solution of 20% dimethyl sulfoxide (DMSO) was used for positive control. The metabolic activity was then evaluated after 72 h of incubation using (3-(4,5-dimethylthiazol-2-yl)-5-(3-carboxymethoxyphenyl)-2-(4-sulfophenyl)-2H-tetrazolium) (MTS, Promega). Briefly, the medium of every well was removed, and fresh medium containing MTS solution (in a 1:5 ratio) was added to each well and incubated for 2 h. After this incubation time, the optical density was measured at 490 nm with a spectrophotometric plate reader (Biotech Synergy HT).

The results are presented as the average of viability ± standard deviation. The percentage of metabolic activity was calculated according to **Equation 3.4**.

$$\text{Metabolic activity (\%)} = \frac{\text{Absorbance of sample}}{\text{Absorbance of negative control}} \times 100 \qquad \textbf{(3.4)}$$

3.3. Results and discussion

3.3.1. Morphological features and vibrational spectra

3.3.1.1. Morphology

The morphology of neat PVDF, PVDF+IL and PVDF+Fe_3O_4 fiber mats with different IL and NP contents was analyzed by SEM. Representative SEM images of the different hybrid materials are shown in **Figure 3.3**.

Overall, it has been observed that the inclusion of the filler slightly influences the mean fiber diameter and standard deviation, and that the effect of the rotating cylinder, used for the fabrication of the oriented fiber mats, has the largest effect on fiber diameter due to fiber stretching [34].

Indeed, there are no significant differences between the PVDF-O fibers with varying IL content, as demonstrated by the representative images for PVDF-O and PVDF-O+IL 15%. (**Figure 3.3-a** and **Figure 3.3-b**), with similar results verified for the intermediate concentrations of IL.

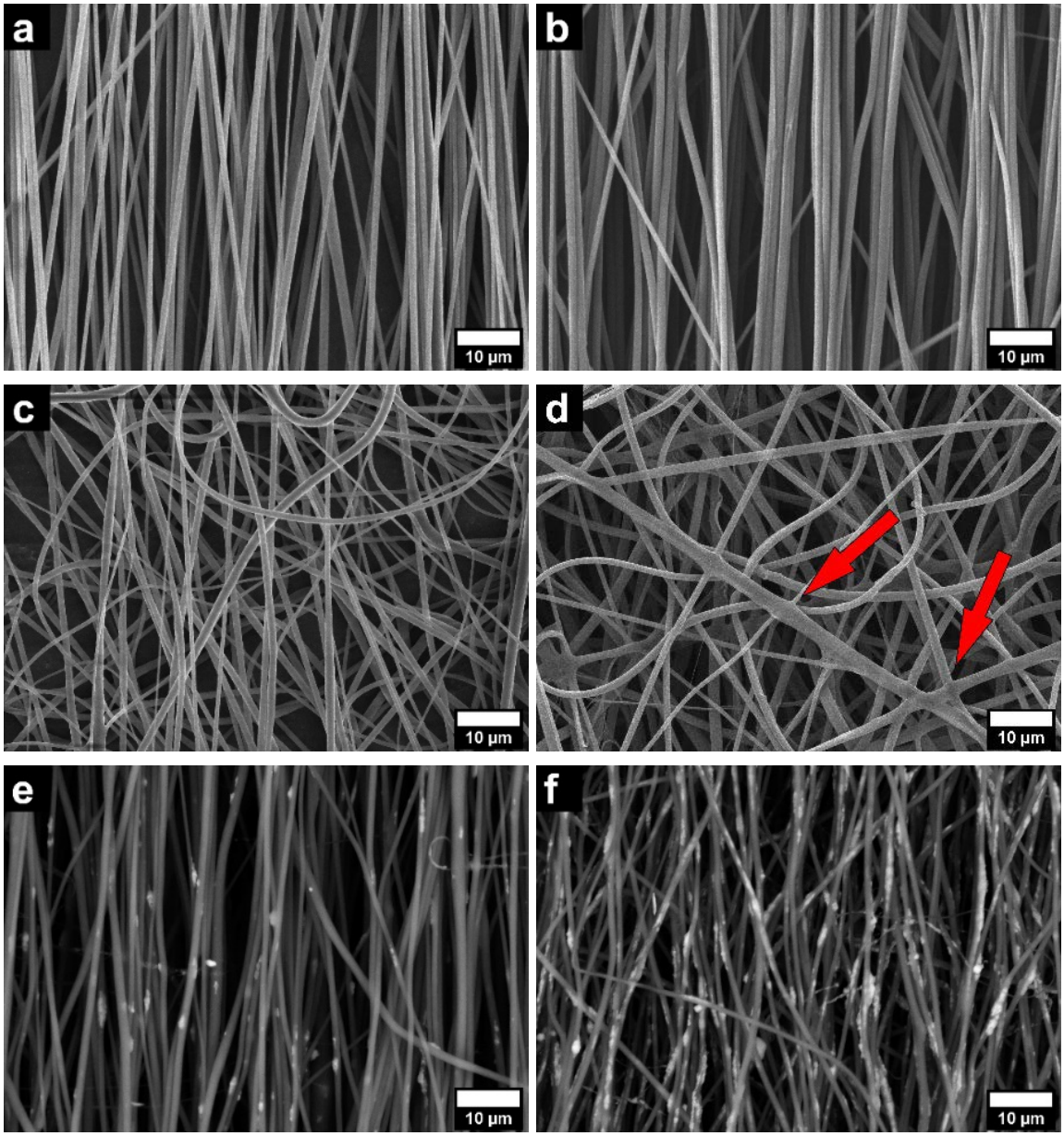

Figure 3.3. Representative PVDF electrospun fiber mats: a) PVDF-O; b) PVDF-O+IL 15%; c) PVDF-R; d) PVDF-R+IL 15% (red arrows indicate fused fibers); e) PVDF-O+Fe_3O_4 5%; f) PVDF-O+Fe_3O_4 15%.

The mean diameter increases slightly with increasing IL wt.% content, from 0.98 ± 0.19 µm for PVDF-O up to 1.28 ± 0.15 µm for PVDF-O+IL 15% (**Figure 3.4).**

PVDF-R and PVDF-R+IL fiber mats (**Figure 3.3-c** and **Figure 3.3-d**) show no significant morphological differences upon the incorporation of 15 wt.% IL into the PVDF matrix, being the randomly oriented fibers characterized by a smooth surface.

The presence of some fiber fusion (red arrows in **Figure 3.3-d**) leads to the observed difference in the average mean diameters. Similar results are observed for the PVDF-R+IL fibers containing 5 and 10 wt.%

Nevertheless, all randomly oriented fibers show similar average diameters, within experimental error with average diameters ranging from 1.29 ± 0.25 μm for PVDF-R fibers, 1.97 ± 0.60 μm for PVDF-R+IL 5%, 1.54 ± 0.33 μm for PVDF-R+IL 10% and 1.36 ± 0.28 μm for PVDF-R+IL 15% (**Figure 3.4).**

The observed slight diameters variations are related to the varying electrical conductivity of the solution due to the increasing ionic content. As for the PVDF-O +IL fibers, the stretching effect of the rotating cylinder has the largest influence in determining the decrease in average fiber diameter, as it is also observed for the PVDF-O+Fe_3O_4 fibers (**Figure 3.3-e** and **Figure 3.3-f**).

The PVDF-O fibers with NP content (**Figure 3.3-e and Figure 3.3-f**) displayed some NP agglomerates present both within the microfibers and at their surface. A slight diameter variation is also observed as a result of the introduction of the NP (attributed to the increase in solution viscosity), that nonetheless remained within the standard deviation. Due to the presence of the NP on the surface, the microfibers displayed increasing roughness with increasing filler wt.%.

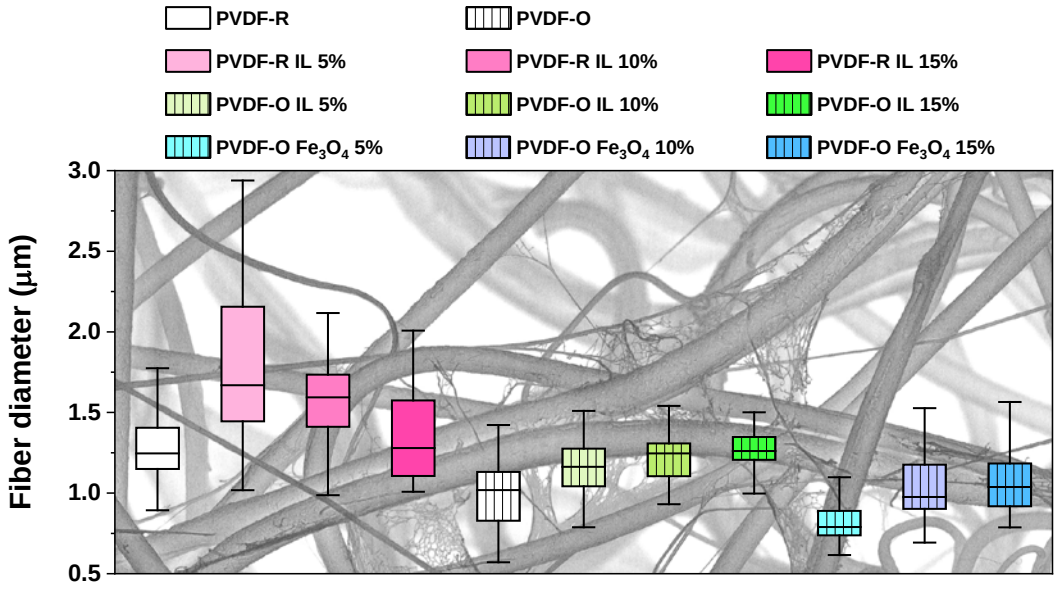

Figure 3.4. Tukey-style boxplot with the diameters of the electrospun fibers (background: PVDF-R+IL 10%).

The mean diameter remains basically constant within experimental error for the different samples: PVDF-O: 0.98 ± 0.19 μm; PVDF-O+Fe_3O_4 5%: 0.82 ± 0.13 μm; PVDF-O+Fe_3O_4 15%: 1.07 ± 0.20 μm. A more detailed comparison of the obtained results is presented in the boxplot in **Figure 3.4** as per the method detailed by Krzywinski and Altman [35].

3.3.1.2. Vibrational spectra

The polymer phase identification and phase content quantification of the electrospun fiber mats were performed after FTIR-ATR measurements (**Figure 3.5**). The presence of the α-phase of PVDF is identified by the 763 and 976 cm^{-1} bands, with the β-phase being identified by the 840 and 1277 cm^{-1} bands.

No chemical changes (new bands or energy shifts) are observed due to the incorporation of the IL and Fe_3O_4 NPs into the PVDF matrix, beyond the specific bands of the different fillers, with the [Chol][TFSI] identified at the 1349, 1132 and 740 cm^{-1} bands. The band at 740 cm^{-1} is due to the cis [TFSI]– conformation, while the bands at 1132 and 1349 cm^{-1} are assigned to a symmetric and asymmetric stretching vibration of the SO_2 group [36]. For the composites comprising the Fe_3O_4 NPs an absorption band at 618 cm^{-1} is observed, being attributed to Fe–O stretching, characteristic of the Fe_3O_4 [37].

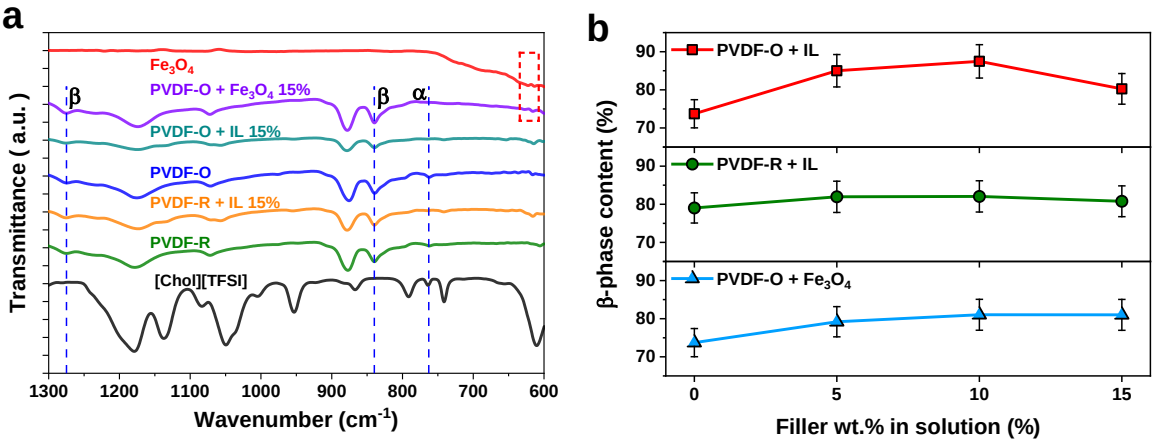

Figure 3.5. a) Representative FTIR spectra of the samples, neat Fe_3O_4 and [Chol][TFSI]; b) Variation of the β-phase content of the samples as function of the filler content.

FTIR-ATR spectra (**Figure 3.5-a**) and **Equation 2.4** have been used to evaluate the β-phase content of the processed samples, as presented in **Figure 3.5-b.**

The β-phase content increased with the incorporation of IL and NPs into the PVDF matrix, ranging from 73% to 88% (**Figure 3.5-b**), with this increase being more pronounced in the PVDF-O+IL fibers.

Due to the electrospinning conditions (solvent evaporation at RT and jet stretching [34]), PVDF crystallizes manly in the electroactive β-phase (73.7 ± 3% for PVDF-O) [30]. Upon IL incorporation and independently of the IL content, no significant changes occur in the electroactive phase content, displaying the PVDF-O+IL 15% samples a β-phase content of 80.2 ± 3%. Similarly, no significant differences are observed for PVDF-R+IL fibers, ranging the β-phase content from 79.0 ± 3% for PVDF-R to 80.8 ± 3% for the PVDF-R+IL 15% sample [38].

The small increase in the electroactive β-phase content present in the PVDF+IL fibers results from the interactions between IL and polymer, namely the positive CH_2 groups with the negative IL charge and also between the CF_2 groups with the IL positive charge [36]. The highest β-phase contents obtained with the oriented electrospun fibers is the result of the stretching process that further promotes crystallization in the electroactive phase [34].

The incorporation of Fe_3O_4 NPs also promotes an increase in the β-phase content [31]. As it is shown in **Figure 3.5-b**, the β-phase content increased from 73.7 ± 4% for PVDF-O to 79.2 ± 4% for PVDF-O+Fe_3O_4 5%, and to 81.0 ± 4% for both PVDF-O+Fe_3O_4 10% and PVDF-O+Fe_3O_4 15%, as a result of the electrostatic interactions between the polymer and the NPs. These results are compatible with previously reported ones [34]. The results confirm that low temperature solvent evaporation temperatures (≤ 60 °C) and the stretching of the jet solution leads to the crystallization of the polymer mainly in the β-phase, an effect reinforced by electrostatic interactions between the NP and the polar polymer chains [34].

3.3.2. Thermal properties

In order to determine the degree of crystallinity of the polymer, the melting enthalpy of the samples was evaluated by DSC analysis.

The DSC curves of neat PVDF-O and PVDF-R, and those of PVDF+IL and PVDF+Fe_3O_4 comprising the maximum amount of IL and NP are shown in **Figure 3.6-a**. A single melting peak, corresponding to the melting of PVDF is observed at ≈165 ºC, and, for both PVDF-O and PVDF-R, the higher concentration of IL results in a decrease of the melting temperature and a wider melting peak, both indicating a destabilization of the crystalline phase. The inclusion of Fe_3O_4 NP has no significant influence on the thermal response of the polymer.

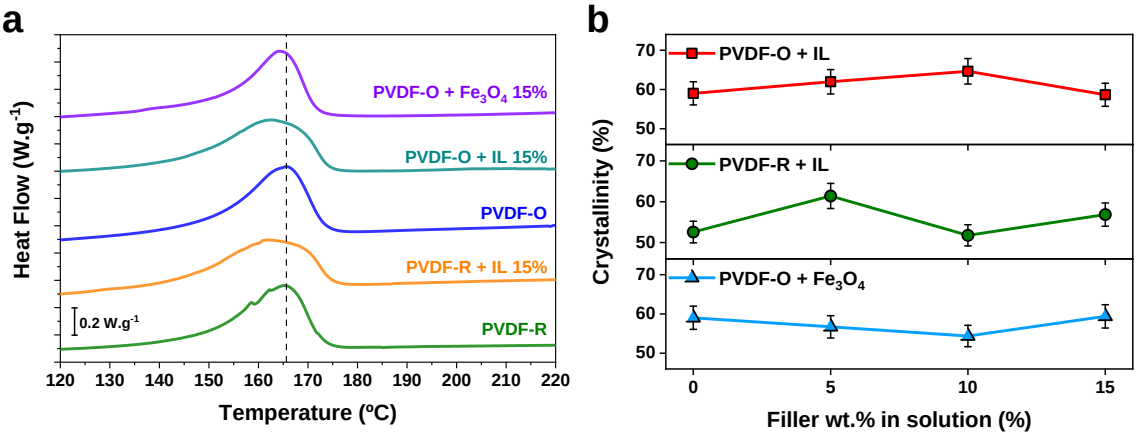

Figure 3.6. a) Comparison of DSC thermographs of representative microfiber mats; b) Variation of the degree of crystallinity of the samples as function of filler content.

The degree of crystallinity of the samples was evaluated by applying **Equation 3.1**. The results presented in **Figure 3.6-b** show a degree of crystallinity ranging between 51% and 64%. For the PVDF-O+IL fibers, the degree of crystallinity ranges between 58% and 64%, with the PVDF-O presenting a crystallinity of 59% (**Figure 3.6-b**). The observed variations are attributed to the ionic species acting as initial nucleation sites for the crystallization process but, with the higher concentrations, they seem to act as defects, preventing or even inhibiting crystallite formation.

The PVDF-R+IL fiber mats show crystallinity values between 51% and 61%, with 53% for PVDF-R, and the PVDF-O+Fe_3O_4 fibers presented crystallinity between 54-59%. Thus, the overall effect of different fillers on the degree of crystallinity are slight variations due to the filler-polymer interactions, which are larger in the case of the ILs due to the ion-dipole interactions [36]. TGA measurements evaluated the thermal stability of the samples (**Figure 3.7**).

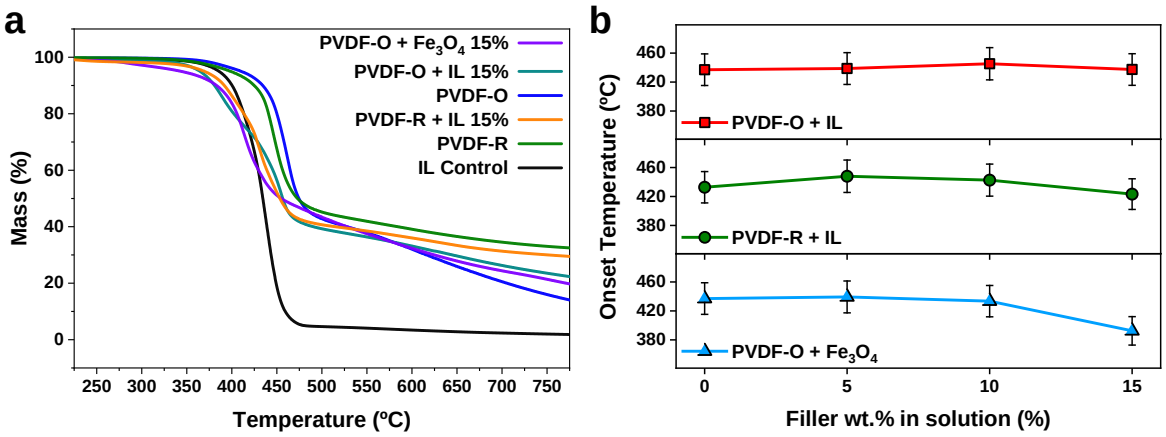

Figure 3.7. a) Representative TGA thermographs of the different microfibers, with and without fillers; b) Variation of the onset temperature of the samples as function of their filler content.

PVDF presents a single degradation step corresponding to the C-H and C-F scissions of the PVDF chain, displaying a T_{onset} at ≈432 ºC (**Figure 3.7-b**) [36]. Independently of the fiber orientation two degradation steps are observed, attributed to degradation of IL (starting at ≈360 ºC) followed by the one of PVDF (**Figure 3.7-a**). Independently of fiber orientation, an increase in the thermal stability is observed, with the T_{onset} of PVDF+IL increasing from ≈412 ºC (PVDF-R) and 414ºC (PVDF-O) to 437 and 423 ºC respectively, for an IL content of 15 wt.% (**Figure 3.7-b** and **Table 3.1**).

For PVDF-O+Fe_3O_4 fibers, only a single degradation step is observed (**Figure 3.7-a**), decreasing the thermal stability with increasing NPs content from 5 to 15 wt.%, and respectively decreasing of the T_{onset} from 439 ºC to 392 ºC, while a greater quantity of char, when compared to the neat samples, was observed (**Figure 3.8**).

Figure 3.8. Remaining char after TGA analysis of a PVDF+Fe_3O_4 15% fiber sample.

Similar results [39] are reported as indicating interactions between the magnetic NPs and the PVDF macromolecular chains, affecting the thermal stability of the fibers.

Table 3.1. Melting and onset temperatures for the different processed samples. The associated error is ± 2%.

	PVDF-O+IL			**PVDF-R+IL**			**PVDF-O+Fe_3O_4**		
	Melting temp. (ºC)	**First onset (ºC)**	**Second onset (ºC)**	**Melting temp. (ºC)**	**First onset (ºC)**	**Second onset (ºC)**	**Melting temp. (ºC)**	**First onset (ºC)**	**Second onset (ºC)**
0%	166	437	-	165	433	-	166	437	-
5%	165	360	439	166	332	448	167	275	439
10%	165	351	445	166	360	443	164	269	433
15%	163	362	437	162	377	423	164	248	392

3.3.3. Functional response

3.3.3.1. Ionic conductivity

Figure 3.9-a shows the Nyquist plot of PVDF+IL electrospun membranes at RT. It is observed that Nyquist plot contains two different regions characterized by a semi-circle located in the high frequency range that corresponds to charge transfer process and a straight line at lower frequencies in which is defined by charge diffusion process.

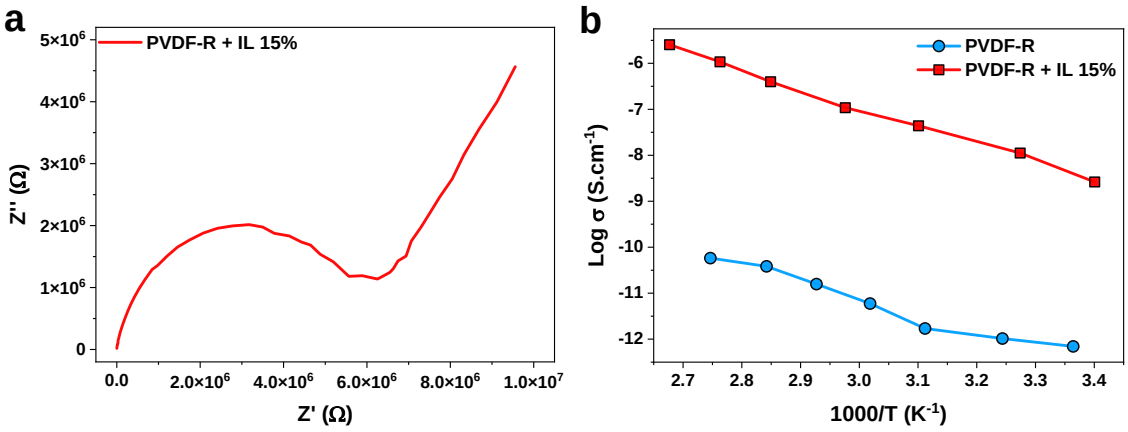

Figure 3.9. a) Nyquist plot of PVDF with 15% of IL at RT, and b) Arrhenius plots for the ionic conductivities of neat PVDF and PVDF with 15wt% of IL electrospun membranes.

The temperature dependence of the ionic conductivity for both electrospun membranes is represented in **Figure 3.9-b**. Regardless of electrospun membranes, it is observed that the ionic conductivity values increase with increasing temperature as a result of the polymer chains that acquire thermally induced faster internal modes leading to intra-chain ion movements.

Independently of the temperature, it is observed that the inclusion of 15 wt.% IL content into PVDF matrix leads to an increase of the RT ionic conductivity from 7.1×10^{-13} S.cm^{-1} for PVDF to 2.6×10^{-9} S.cm^{-1} as a result of the inclusion of IL charges (cations and anions) and their mobility in the PVDF matrix.

3.3.3.2. Magnetic properties

Measuring of the hysteresis curves allows to accurately determine the magnetic NP content present in samples of the composite microfibers. Thus, VSM was used to assess the effective content of Fe_3O_4 NPs in the fibers. **Figure 3.10-a** shows the room-temperature hysteresis curves with the expected ferrimagnetic behavior of the PVDF+Fe_3O_4 fibers [29].

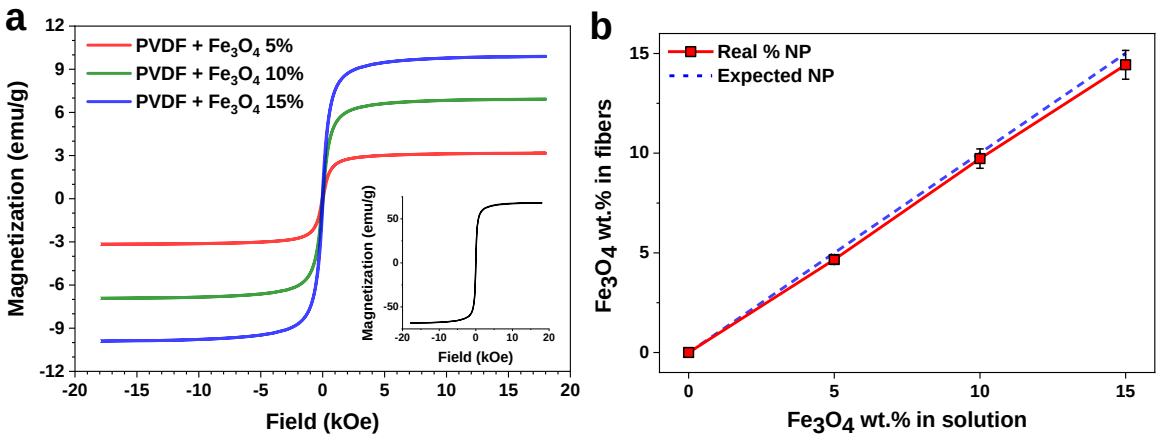

Figure 3.10. a) RT hysteresis loops for the PVDF+Fe_3O_4 microfiber composites. Inset: RT hysteresis loop for pure Fe_3O_4 NP. b) Relation between the wt.% of Fe_3O_4 NP within the solution and those within the microfibers, with the blue dashed line indicating the linear theoretical behavior.

For all samples, the magnetization saturates at ≈10kOe, and increases with NP content. From the inset presented in **Figure 3.10-a**, it is possible to observe that Fe_3O_4 NPs present a maximum magnetization of ≈68 emu.g^{-1} at an applied magnetic field of 18 kOe. As mentioned, the magnetic saturation of PVDF-O+Fe_3O_4 fibers increased as the NP content increases from 5 to 15 wt.%, from 3.2 emu.g^{-1} for PVDF-O+Fe_3O_4 5% fibers to 9.8 emu.g^{-1} for PVDF-O+Fe_3O_4 15% fibers.

Table 3.2. NP yields in the PVDF-O Fe_3O_4 composite fibers.

Sample	Magnetization (emu/g)	wt.% Fe_3O_4 in sample (%)	Experimental Yield (%)
Pure Fe_3O_4 NPs	68.21	100.00	-
PVDF-O+5% Fe_3O_4	3.18	4.66	93.26
PVDF-O+10% Fe_3O_4	6.64	9.73	97.27
PVDF-O+15% Fe_3O_4	9.85	14.43	96.22

The effective NP content within the electrospun PVDF fiber, was evaluated using **Equation 3.3**. The obtained results are presented in **Figure 3.10-b** and **Table 3.2**. It is shown that the electrospinning conditions result in experimental yields of NP content in the fibers above 93%. The loss of NPs is attributed to sedimentation in solution during the electrospinning process.

3.3.3.3. Cytotoxicity assay

A key issue for the development and use of materials for biomedical applications is their eventual cytotoxic behaviour. It has been shown that PVDF fibers present no cytotoxicity and are biocompatible [40]. However, the introduction of different fillers in the matrix can lead to cytotoxic effects. In this way, the cytotoxicity of the different PVDF fibers with IL and with magnetic particles were evaluated. The study of metabolic activity of the L929 fibroblast, assessed with MTS assay, was applied to all the samples and the results of representative samples after 72 h are presented in **Figure 3.11**.

According to the ISO standard 10993-5, the samples are considered cytotoxic when cells suffer a viability reduction larger than 30%. The measured cell viability values are all higher than 70%, confirming the cytocompatibility of all the samples.

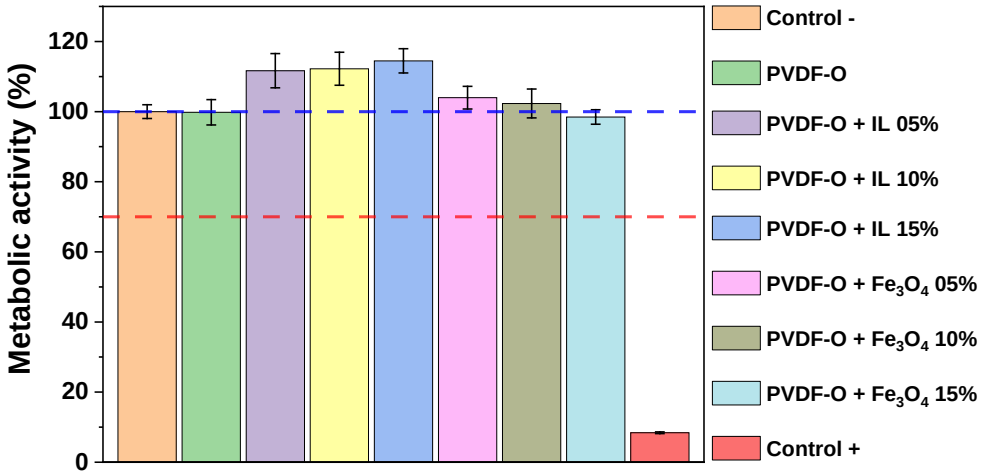

Figure 3.11. Cytotoxicity assay of L929 fibroblast cells in contact with the as-prepared extraction media exposed to the different samples for 72 h.

Thus, the introduction of the different fillers (IL and Fe_3O_4) does not cause cytotoxicity to the composite samples. Furthermore, it was verified an increase of the metabolic activity of the cells with the samples containing IL, which is a similar behaviour to that verified in previous studies focusing on ILs with the same anion [15]. Therefore, it is proven that the processed samples can be used for biomedical applications.

3.4. Conclusions

Composite polymeric electrospun microfiber mats were developed to support novel tissue engineering approaches for muscle tissue repair and regeneration, by embedding either magnetic Fe_3O_4 NP or the [Chol][TFSI] IL in a PVDF polymer matrix. Randomly oriented and oriented fibers comprising different IL and NP content (5, 10 and 15 wt.%) were produced.

The morphology, physico-chemical and thermal properties of the electrospun samples were evaluated. PVDF-O+IL and PVDF-R+IL fibers were successfully obtained, increasing the fiber diameter with the IL content increase from 0.98 ± 0.19 μm to 1.28 ± 0.15 μm (PVDF-O+IL), and 1.29 ± 0.25 μm to 1.36 ± 0.28 μm (PVDF-R+IL). The PVDF-O+Fe_3O_4 fiber diameter presented an even lower variation, from 0.98 ± 0.19 μm to 1.07 ± 0.20 μm.

The inclusion of both the IL and Fe_3O_4 has a small influence in the degree of crystallinity of the polymer, varying between 51-61% (PVDF-R+IL), 58-64% (PVDF-O+IL) and 54-59% (PVDF-O+Fe_3O_4), and in the β-phase content, ranging between 79-82% (PVDF-R+IL), 73-87% (PVDF-O+IL) and 73-81% (PVDF-O+Fe_3O_4).

Other than the appearance of an additional degradation step at ≈360 ºC, no significant differences were observed in the thermal behavior of the composite fibers, with the thermal stability of the samples increasing with higher IL content, and decreasing with increasing NP content.

The incorporation efficiency of the magnetic NPs in the electrospun fibers was above 93%, independently of the NP content and the ionic conductivity increased from 7.1×10^{-13} $S.cm^{-1}$ for PVDF to 2.6×10^{-9} $S.cm^{-1}$ for the PVDF sample with 15% IL content. The composite fibers demonstrated to be highly compatible with L929 fibroblasts, showing their suitability for biomedical applications.

3.5. References

1. Brown, G.C., *Living too long.* EMBO reports, 2014. **16**(2): p. 137-141. DOI: 10.15252/embr.201439518

2. Network, O.P.a.T., *Transplant : Transplant Year by Recipient Age: U.S. Transplants Performed: January 1, 1988 - August 31, 2020*. 2020, U.S. Department of Health & Human Services. Available from: https://optn.transplant.hrsa.gov/data/view-data-reports/build-advanced/.

3. Greising, S.M., B.T. Corona, C. McGann, J.K. Frankum, and G.L. Warren, *Therapeutic Approaches for Volumetric Muscle Loss Injury: A Systematic Review and Meta-Analysis.* Tissue Engineering Part B: Reviews, 2019. **25**(6): p. 510-525. DOI: 10.1089/ten.teb.2019.0207

4. Langer, R. and J.P. Vacanti, *Tissue Engineering.* Science, 1993. **260**(5110): p. 920-926. DOI: 10.1126/science.8493529

5. Hermenegildo, B., C. Ribeiro, L. Pérez-Álvarez, J.L. Vilas, D.A. Learmonth, R.A. Sousa, P. Martins, and S. Lanceros-Méndez, *Hydrogel-based magnetoelectric microenvironments for tissue stimulation.* Colloids and Surfaces B: Biointerfaces, 2019. **181**: p. 1041-1047. DOI: 10.1016/j.colsurfb.2019.06.023

6. Hitscherich, P., A. Aphale, R. Gordan, R. Whitaker, P. Singh, L.-h. Xie, P. Patra, and E.J. Lee, *Electroactive graphene composite scaffolds for cardiac tissue engineering.* Journal of Biomedical Materials Research Part A, 2018. **106**(11): p. 2923-2933. DOI: 10.1002/jbm.a.36481

7. Ribeiro, S., C. Ribeiro, E.O. Carvalho, C.R. Tubio, N. Castro, N. Pereira, V. Correia, A.C. Gomes, and S. Lanceros-Méndez, *Magnetically Activated Electroactive Microenvironments for Skeletal Muscle Tissue Regeneration.* ACS Applied Bio Materials, 2020. **3**(7): p. 4239-4252. DOI: 10.1021/acsabm.0c00315

8. Ribeiro, C., C.M. Costa, D.M. Correia, J. Nunes-Pereira, J. Oliveira, P. Martins, R. Gonçalves, V.F. Cardoso, and S. Lanceros-Méndez, *Electroactive poly(vinylidene fluoride)-based structures for advanced applications.* Nature Protocols, 2018. **13**(4): p. 681-704. DOI: 10.1038/nprot.2017.157

9. Goh, Y.-F., I. Shakir, and R. Hussain, *Electrospun fibers for tissue engineering, drug delivery, and wound dressing.* Journal of Materials Science, 2013. **48**(8): p. 3027-3054. DOI: 10.1007/s10853-013-7145-8

10. Jana, S., S.K.L. Levengood, and M. Zhang, *Anisotropic Materials for Skeletal-Muscle-Tissue Engineering.* Advanced materials (Deerfield Beach, Fla.), 2016. **28**(48): p. 10588-10612. DOI: 10.1002/adma.201600240

11. Li, Y., C. Liao, and S.C. Tjong, *Electrospun Polyvinylidene Fluoride-Based Fibrous Scaffolds with Piezoelectric Characteristics for Bone and Neural Tissue Engineering.* Nanomaterials (Basel, Switzerland), 2019. **9**(7): p. 952. DOI: 10.3390/nano9070952

12. Ramakrishna, S., K. Fujihara, W.-E. Teo, T.-C. Lim, and Z. Ma, *An Introduction to Electrospinning and Nanofibers*. 2005: WORLD SCIENTIFIC. DOI: 10.1142/5894

13. Meira, R.M., D.M. Correia, S. Ribeiro, P. Costa, A.C. Gomes, F.M. Gama, S. Lanceros-Méndez, and C. Ribeiro, *Ionic-Liquid-Based Electroactive Polymer Composites for Muscle Tissue Engineering.* ACS Applied Polymer Materials, 2019. **1**(10): p. 2649-2658. DOI: 10.1021/acsapm.9b00566

14. Correia, D.M., L.C. Fernandes, P.M. Martins, C. García-Astrain, C.M. Costa, J. Reguera, and S. Lanceros-Méndez, *Ionic Liquid-Polymer Composites: A New Platform for Multifunctional Applications.* Advanced Functional Materials, 2020: p. 1909736. DOI: 10.1002/adfm.201909736

15. Dias, J.C., D.C. Correia, A.C. Lopes, S. Ribeiro, C. Ribeiro, V. Sencadas, G. Botelho, J.M.S.S. Esperança, J.M. Laza, J.L. Vilas, L.M. León, and S. Lanceros-Méndez, *Development of poly(vinylidene fluoride)/ionic liquid electrospun fibers for tissue engineering applications.* Journal of Materials Science, 2016. **51**(9): p. 4442-4450. DOI: 10.1007/s10853-016-9756-3

16. Suominen, M., S. Lehtimäki, R. Yewale, P. Damlin, S. Tuukkanen, and C. Kvarnström, *Electropolymerized polyazulene as active material in flexible supercapacitors.* Journal of Power Sources, 2017. **356**: p. 181-190. DOI: 10.1016/j.jpowsour.2017.04.082

17. Haj Kacem, S., S. Galai, A. Pérez de los Ríos, F.J. Hernández Fernández, and I. Smaali, *New efficient laccase immobilization strategy using ionic liquids for biocatalysis and microbial fuel cells applications.* Journal of Chemical Technology & Biotechnology, 2017. **93**(1): p. 174-183. DOI: 10.1002/jctb.5337

18. Niesyto, K. and D. Neugebauer, *Synthesis and Characterization of Ionic Graft Copolymers: Introduction and In Vitro Release of Antibacterial Drug by Anion Exchange.* Polymers, 2020. **12**(9): p. 2159. DOI: 10.3390/polym12092159

19. Mena, I.F., E. Diaz, J. Palomar, J.J. Rodriguez, and A.F. Mohedano, *Cation and anion effect on the biodegradability and toxicity of imidazolium– and choline–based ionic liquids.* Chemosphere, 2020. **240**: p. 124947. DOI: 10.1016/j.chemosphere.2019.124947

20. Fu, S., Z. Cai, and H. Ai, *Stimulus-Responsive Nanoparticle Magnetic Resonance Imaging Contrast Agents: Design Considerations and Applications.* Advanced Healthcare Materials, 2020: p. 2001091. DOI: 10.1002/adhm.202001091

21. Busquets, M.A. and J. Estelrich, *Prussian blue nanoparticles: synthesis, surface modification, and biomedical applications.* Drug Discovery Today, 2020. **25**(8): p. 1431-1443. DOI: 10.1016/j.drudis.2020.05.014

22. Ekladious, I., Y.L. Colson, and M.W. Grinstaff, *Polymer–drug conjugate therapeutics: advances, insights and prospects.* Nature Reviews Drug Discovery, 2018. **18**(4): p. 273-294. DOI: 10.1038/s41573-018-0005-0

23. Patra, J.K., G. Das, L.F. Fraceto, E.V.R. Campos, M.D.P. Rodriguez-Torres, L.S. Acosta-Torres, L.A. Diaz-Torres, R. Grillo, M.K. Swamy, S. Sharma, S. Habtemariam, and H.-S. Shin, *Nano based drug delivery systems: recent developments and future prospects.* Journal of nanobiotechnology, 2018. **16**(1): p. 71-71. DOI: 10.1186/s12951-018-0392-8

24. Francesko, A., P. Petkova, and T. Tzanov, *Hydrogel Dressings for Advanced Wound Management.* Current Medicinal Chemistry, 2019. **25**(41): p. 5782-5797. DOI: 10.2174/0929867324666170920161246

25. Wang, L., C. Hu, and L. Shao, *The antimicrobial activity of nanoparticles: present situation and prospects for the future.* International journal of nanomedicine, 2017. **12**: p. 1227-1249. DOI: 10.2147/IJN.S121956

26. Machado, R., A. da Costa, V. Sencadas, C. Garcia-Arévalo, C.M. Costa, J. Padrão, A. Gomes, S. Lanceros-Méndez, J.C. Rodríguez-Cabello, and M. Casal, *Electrospun silk-elastin-like fibre mats for tissue engineering applications.* Biomedical Materials, 2013. **8**(6): p. 065009. DOI: 10.1088/1748-6041/8/6/065009

27. Wang, Y., Y. Miao, G. Li, M. Su, X. Chen, H. Zhang, Y. Zhang, W. Jiao, Y. He, J. Yi, X. Liu, and H. Fan, *Engineering ferrite nanoparticles with enhanced magnetic response for advanced biomedical applications.* Materials Today Advances, 2020. **8**: p. 100119. DOI: 10.1016/j.mtadv.2020.100119

28. Shen, Y., B. Jiang, and Y. Xing, *Recent advances in the application of magnetic Fe3O4 nanomaterials for the removal of emerging contaminants.* Environmental Science and Pollution Research, 2021. DOI: 10.1007/s11356-020-11877-8

29. Li, Q., C.W. Kartikowati, S. Horie, T. Ogi, T. Iwaki, and K. Okuyama, *Correlation between particle size/domain structure and magnetic properties of highly crystalline Fe(3)O(4) nanoparticles.* Scientific reports, 2017. **7**(1): p. 9894-9894. DOI: 10.1038/s41598-017-09897-5

30. Maciel, M.M., S. Ribeiro, C. Ribeiro, A. Francesko, A. Maceiras, J.L. Vilas, and S. Lanceros-Méndez, *Relation between fiber orientation and mechanical properties of nano-engineered poly(vinylidene fluoride) electrospun composite fiber mats.* Composites Part B: Engineering, 2018. **139**: p. 146-154. DOI: 10.1016/j.compositesb.2017.11.065

31. Goncalves, R., P. Martins, D.M. Correia, V. Sencadas, J.L. Vilas, L.M. Leon, G. Botelho, and S. Lanceros-Mendez, *Development of magnetoelectric CoFe2O4/poly(vinylidene fluoride) microspheres.* RSC Advances, 2015. **5**(45): p. 35852-35857. DOI: 10.1039/c5ra04409j

32. Morrish, A.H., *The Analysis of the Magnetization Curves of Bulk Material*, in *The Physical Principles of Magnetism*, R.J. Herrick, Editor. 2001, IEEE Press: USA. p. 382.403. DOI: 10.1109/9780470546581

33. Grössinger, R., *A critical examination of the law of approach to saturation. I. Fit procedure.* Physica Status Solidi (a), 1981. **66**(2): p. 665-674. DOI: 10.1002/pssa.2210660231

34. He, Z., F. Rault, M. Lewandowski, E. Mohsenzadeh, and F. Salaün, *Electrospun PVDF Nanofibers for Piezoelectric Applications: A Review of the Influence of Electrospinning Parameters on the β Phase and Crystallinity Enhancement.* Polymers, 2021. **13**(2): p. 174. DOI: 10.3390/polym13020174

35. Krzywinski, M. and N. Altman, *Visualizing samples with box plots.* Nature Methods, 2014. **11**(2): p. 119-120. DOI: 10.1038/nmeth.2813

36. Correia, D.M., J.C. Barbosa, C.M. Costa, P.M. Reis, J.M.S.S. Esperança, V. de Zea Bermudez, and S. Lanceros-Méndez, *Ionic Liquid Cation Size-Dependent Electromechanical Response of Ionic Liquid/Poly(vinylidene fluoride)-Based Soft Actuators.* The Journal of Physical Chemistry C, 2019. DOI: 10.1021/acs.jpcc.9b00868

37. Roacho-Pérez, J.A., F.G. Ruiz-Hernandez, C. Chapa-Gonzalez, H.G. Martínez-Rodríguez, I.A. Flores-Urquizo, F.E. Pedroza-Montoya, E.N. Garza-Treviño, M. Bautista-Villareal, P.E. García-Casillas, and C.N. Sánchez-Domínguez, *Magnetite Nanoparticles Coated with PEG 3350-Tween 80: In Vitro Characterization Using Primary Cell Cultures.* Polymers, 2020. **12**(2): p. 300. DOI: 10.3390/polym12020300

38. Barbosa, J.C., D.M. Correia, R. Gonçalves, V. de Zea Bermudez, M.M. Silva, S. Lanceros-Mendez, and C.M. Costa, *Enhanced ionic conductivity in poly(vinylidene fluoride) electrospun separator membranes blended with different ionic liquids for lithium ion batteries.* Journal of Colloid and Interface Science, 2021. **582**: p. 376-386. DOI: 10.1016/j.jcis.2020.08.046

39. Li, Y., Y. Zhao, X. Lu, Y. Zhu, and L. Jiang, *Self-healing superhydrophobic polyvinylidene fluoride/Fe3O4@polypyrrole fiber with core–sheath structures for superior microwave absorption.* Nano Research, 2016. **9**(7): p. 2034-2045. DOI: 10.1007/s12274-016-1094-x

40. Martins, P.M., S. Ribeiro, C. Ribeiro, V. Sencadas, A.C. Gomes, F.M. Gama, and S. Lanceros-Méndez, *Effect of poling state and morphology of piezoelectric poly(vinylidene fluoride) membranes for skeletal muscle tissue engineering.* RSC Advances, 2013. **3**(39): p. 17938-17944. DOI: 10.1039/c3ra43499k

Chapter 4

Coated electrospun fiber mats for tissue regeneration applications

Conductive polymer coating on white electrospun polymer microfibers.

Some cells and tissues, due either to their nature or function, benefit greatly from the application of electrical stimuli when attempting their regeneration or stimulating their natural healing processes. Electrically conductive smart materials are particularly sought after for these applications, as they can provide such stimuli in a controllable, on-demand, manner. This chapter details the development of electrospun fibers with piezoelectric properties, coated afterwards with conductive polymers, aimed at tissue regeneration applications.

4.1. Introduction

Tissue engineering (TE) represents an interesting approach to address the growing problem of tissue and organ availability for medical treatment of tissue damage or disease, as well as for the problems often associated with these procedures, such as donor tissue rejection by the host patient. The approach of TE, to grow the required tissue *in vivo* or *in vitro* from cells and tissues of the patient, allows to avoid the majority of these issues [1].

Smart and multifunctional materials aim to become a cornerstone of this strategy, as they are able to provide a more specific biomimicry of the cellular microenvironment than what is possible by using only traditional materials that are typically just used as support [2, 3]. In order to achieve this goal, it becomes necessary to fabricate smart and multifunctional materials at the micro- and nanoscale level, the same dimensions of the cellular microenvironment they wish to emulate, while preserving their functional response. There are several methods for achieving this, but many of them are either material-specific, cannot be upscaled, or suffer some limitation on the possible morphologies that can be achieved in the processed material [4]. One of the most versatile is electrospinning, a technique that allows to obtain fiber mats with tailored fiber properties, including size and alignment, so that they can be tuned for the specific microenvironment of target cells and tissues, improving their development and regeneration [5].

Piezoelectric fluorinated polymers have been shown as suitable materials for biomedical applications and can be processed by a variety of techniques, in order to obtain specific morphologies [6]. Among the different fluorinated polymers, poly(vinylidene fluoride) (PVDF) is a biocompatible and versatile material that can be processed in up to five polymorphs, being the non-polar α and the polar β phases the most commonly used for applications [2]. Due to its high piezoelectric response, mainly related to the crystallization in the β-phase polymorph, and to its ability to incorporate different fillers, such as magnetic and metallic nanoparticles [7], carbon nanotubes and graphene [8], or ionic liquids [9], PVDF has been extensively studied and used in a variety of applications [2], including sensors and actuators [10], energy harvesting [11] and TE applications [12]. In particular for TE applications, PVDF and their copolymers have been used for bone and skeletal muscle regeneration [7, 12], cardiac muscle regeneration [13], to name just a few.

Among the different morphologies in which PVDF and co-polymers have been processed, electrospun fiber mats stand out among the most suitable for tissue regeneration. Aligned and randomly oriented fiber mats have been obtained [13, 14] and the effect of electrospun processing parameters has been studied [4, 14], and it was determined that one of the most desirable characteristics of electrospun mats is that PVDF mostly crystallizes in the electroactive β-phase, due to the low temperature solvent-based processing [15]. Furthermore, the fiber mats are self-poled due to the processing under a strong electric field and, therefore, piezoelectrically active, generating a surface charge variation upon mechanical solicitation [15]. As a piezoelectric material, PVDF is dielectric and, for specific applications, a conductive layer is required to properly transduce the mechano-electrical stimuli homogeneously along the materials surface.

Polyaniline (PANI) and polypyrrole (PPy) represent the main types of conducting polymers [16]. The main characteristics and properties of these polymers are their intrinsic electronic conductivity, mechanical flexibility, low density, transparency to visible light and their potential biocompatibility [17-19]. These properties make them suitable for applications where conductive flexible nanostructures need to be produced [20]. Both PANI and PPy have been used to coat different nanostructures by oxidative polymerization in the presence of water-soluble stabilizing polymers [21, 22]. Furthermore, their electrical conductivity and flexibility are particularly interesting properties for TE applications, where they have been used for neural [23, 24], cardiac [25], dental pulp [26], and bone TE [24].

In this work, PVDF fibers have been produced by electrospinning and coated with either a thin PANI or PPy film. Their morphology and physico-chemical properties were evaluated, and the potential of the developed hybrid fiber composites to be applied as scaffolds for TE was confirmed by cytotoxicity assays.

4.2. Experimental

4.2.1. Materials

PVDF, reference Solef 5130, was purchased from Solvay. Ammonium peroxydisulfate and aniline hydrochloride were acquired from Penta, Czech Republic. *N*,*N*-dimethylformamide (DMF, 99.9% GLR) was purchased from Labkem. Poly(*N*-vinylpyrrolidone) (molecular weight 360000), pyrrole, iron(III) chloride hexahydrate and indium-tin-oxide-coated poly(ethylene terephthalate) foil (PET/ITO, reference 639303) were acquired from Sigma-Aldrich. Hydrochloric acid was purchased from Lach-Ner, Czech Republic.

4.2.2. Sample processing

4.2.2.1. Electrospinning of PVDF

The electrospun membranes were processed following the general guidelines presented in [2]: PVDF was first dissolved in DMF in a concentration of 15% weight percentage (wt.%) and the solution was kept under agitation with a magnetic stirrer at room temperature (RT) until complete dissolution of the polymer. The polymer solution was then placed in a 10 mL plastic syringe fitted with a steel needle with 0.41 mm inner diameter.

Electrospinning was conducted by applying a voltage of 15 kV with a HiTek Power OL400/303 power supply. A syringe pump (Syringepump) fed the polymer solution into the needle tip at a rate of 0.4 $mL.h^{-1}$. The electrospun fibers were collected on a grounded PET/ITO sheet placed 20 cm from the needle tip. PET/ITO was selected due to its transparency and conductivity, allowing both for the electrospinning process and for a better evaluation of the coating results.

PVDF fiber mats with average fiber diameter of 0.90 ± 0.19 μm, electroactive phase content of 79.0 ± 3% and degree of crystallinity of 53% were obtained, as evaluated by scanning electron microscopy, Fourier transform infrared spectroscopy and differential scanning calorimetry [2, 5], respectively.

4.2.2.2. Coating of the PVDF fibers by PANI and PPy

PVDF fibers were coated with a thin PANI film by the oxidative polymerization of aniline hydrochloride (0.2 M) with ammonium peroxydisulfate (0.25 M), in 2 wt.% aqueous solution of poly(*N*-vinylpyrrolidone) [27].

Both solutions, aniline hydrochloride monomer and peroxydisulfate oxidant, were mixed at RT and subsequently spread over the surface of the PVDF fibers. Such procedure results in a smooth PANI coating of submicrometric thickness without any of the adhering polymer precipitating.

The analogous coating of PVDF fibers by a PPy film was realized by oxidative polymerization of pyrrole (0.2 M) with iron(III) chloride hexahydrate (0.5 M) in 2 wt.% aqueous solution of poly(*N*-vinylpyrrolidone). Both solutions of pyrrole and of the oxidant were mixed again at RT and spread over the surface of the PVDF fibers.

In both cases, the coated substrates were rinsed for 1 hour with an aqueous solution of hydrochloric acid (0.2 M) and then with ethanol. Finally, the coated PVDF fibers were dried in air at RT. **Figure 4.1** presents the chemical structures of PVDF, PANI [22] and PPy [28].

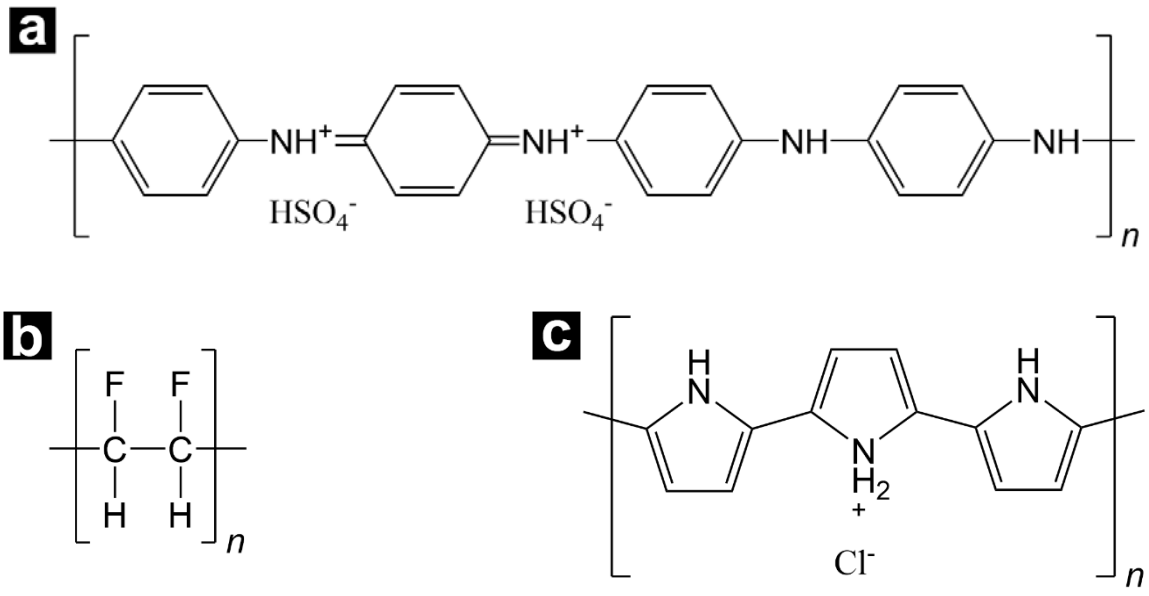

Figure 4.1. Chemical structures for: a) PANI; b) PVDF; c) PPy.

4.2.3. Sample characterization

The morphology of the coated PVDF fibers was evaluated by scanning electron microscopy (SEM), using a scanning ultra-high-resolution electron microscope MAIA3 Tescan, at an accelerating voltage of 3 kV. A Carl Zeiss EVO-40 Scanning Electron Microscope equipped with an Oxford Instruments X-Max Microanalysis EDS-Detector was also used at an accelerating voltage of 20 kV.

Raman spectra of PVDF nanofibers deposited on the ITO/PET support and coated with PANI or PPy were obtained with a Renishaw InVia Reflex Raman microspectrometer using an Ar-ion 514 nm and HeNe 633 nm lasers for excitation. A research-grade Leica DM LM microscope with an objective magnification 50× was used to focus the laser beam on the sample. The scattered light was analyzed by the spectrograph with holographic gratings of 2400 and 1800 lines mm^{-1} for the individual lasers, respectively.

The surface contact angle (CA) of the samples was measured using a Data-Physics Contact Angle System OCA 15EC and the SCA20 software, by depositing 3 µL drops of ultrapure water on the surface of the membranes, and averaging the mean value of the CA on each side of the drop.

The DC surface electrical conductivity of the samples was obtained by measuring the characteristic IV curves at RT with a Keithley 6487 picoammeter/voltage source. Previously, two rectangular electrodes (4 mm length with spacing of 3 mm) were deposited using a Polaron, model SC502 sputter coater. From the IV characteristics of the samples, the resistivity (ρ) was calculated, taking into account the geometrical factors according to **Equation 4.1**:

$$\rho = R \times \frac{w.t}{l} \qquad (\mathbf{4.1})$$

where R is the film resistance, calculated by the inverse of the slope of the I (V) function, l is the distance between electrodes, w the length of the electrodes, and t the film thickness, measured with a Digimatic Micrometer MDC-25PX.

The conductivity σ has been determined as a reciprocal value ρ^{-1}. Indirect cytotoxicity evaluation of the different samples was performed by adapting the ISO 10993-5 standard test method. L929 cells were cultured in 75 cm^2 cell culture flask at 37 °C in a humidified environment and 5% CO_2, using Dulbecco's modified Eagle's medium (DMEM, Biochrom, Berlin, Germany) containing 4.5 $g.L^{-1}$ glucose, 10% fetal bovine serum (FBS, Biochrom, Berlin, Germany) and 1% (v/v) penicillin/streptomycin solution (P/S, Biochrom). Different samples were cut with 2.5 cm^2. Their sterilization was carried out by exposition to ultraviolet radiation for 1 h each side of the samples and washing with sterile phosphate-buffered saline solution (PBS 1x, pH 7.4).

A suspension of 3×10^4 $cell.mL^{-1}$ was seeded in 96-well tissue culture polystyrene plates and incubated for 24 h at the same conditions described above to ensure cell attachment on the plate. Simultaneously, each sample was incubated for 24 h in a 24-well tissue culture polystyrene plate with DMEM. After this time, the cell culture medium in the 96-well plates was removed, and 100 µL of culture medium (that was in contact with the different samples) was added to each well and allowed to incubate for 72 h in standardized culture conditions as mentioned above. A solution of 20% dimethyl sulfoxide was used for positive control. The metabolic activity was then evaluated after 72 h of incubation using the [3-(4,5-dimethylthiazol-2-yl)-5-(3-carboxymethoxyphenyl)-2-(4-sulfophenyl)-2H-tetrazolium] (MTS, Promega). Briefly, the medium of every well was removed, and fresh medium containing MTS solution (in a 1:5 volume ratio) was added to each well and incubated for 2 h.

After this incubation time, the optical density was measured at 490 nm with a spectrophotometric plate reader (Biotech Synergy HT). The results are presented as the average of viability ± standard deviation. The percentage of metabolic activity was calculated according to **Equation 3.4**, as described in **Chapter 3**.

4.3. Results and discussion

4.3.1. Morphological features, Raman spectra and wettability

4.3.1.1. Morphology

The morphology of the PVDF fiber mats coated with PANI (PVDF-PANI) and PPy (PVDF-PPy) was analyzed by SEM, and representative images are presented in **Figure 4.2 a-d.**

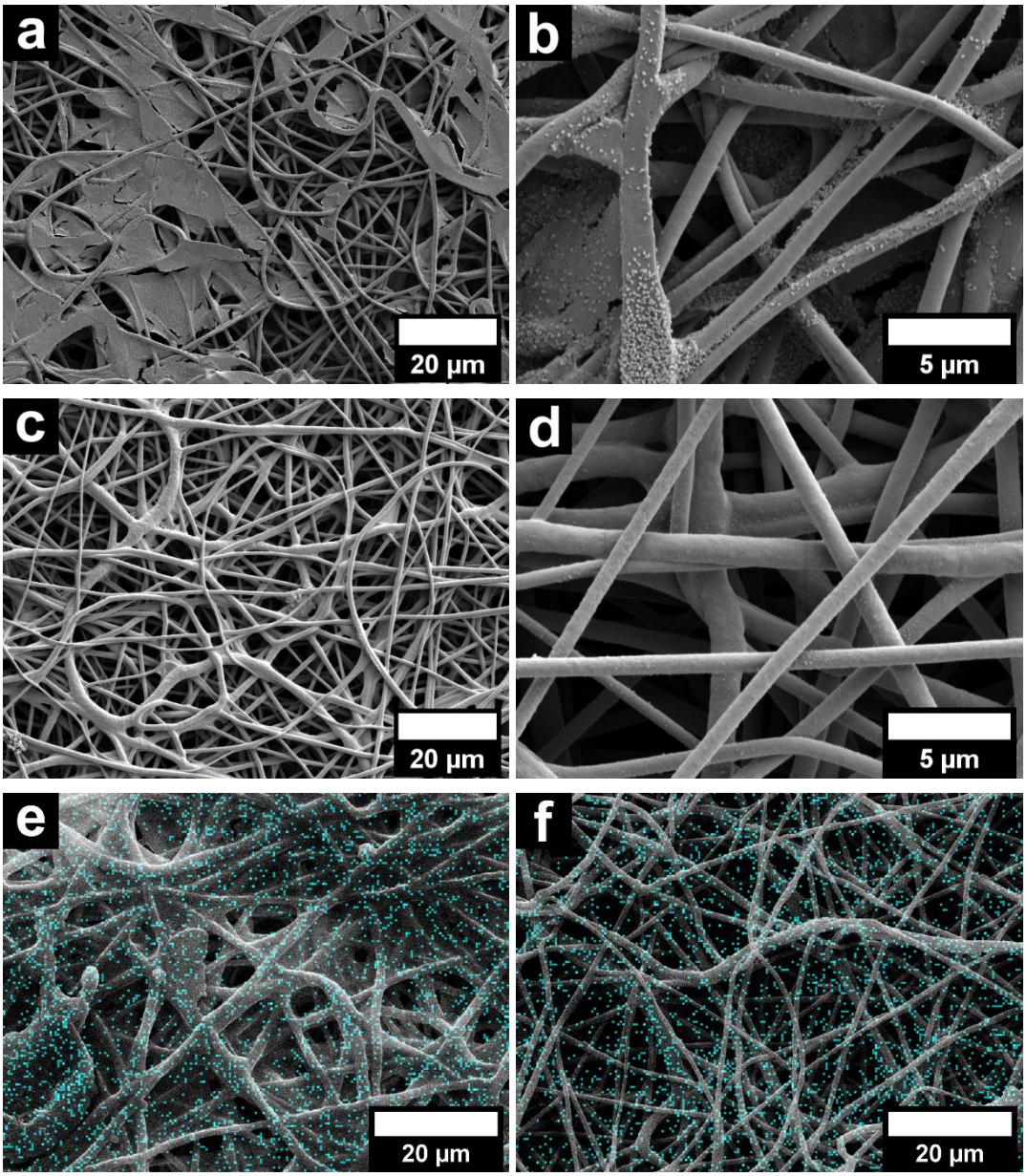

Figure 4.2. Representative SEM images of the hybrid fibers: a, b) PVDF-PANI; c, d) PVDF-PPy. Representative EDX distribution maps of the coatings, indicated by the presence of the N element in fibers of: e) PVDF-PANI; f) PVDF-PPy.

Additionally, **Figure 4.3** presents a boxplot, elaborated as per Krzywinski and Altman [29], with the fiber diameter distribution.

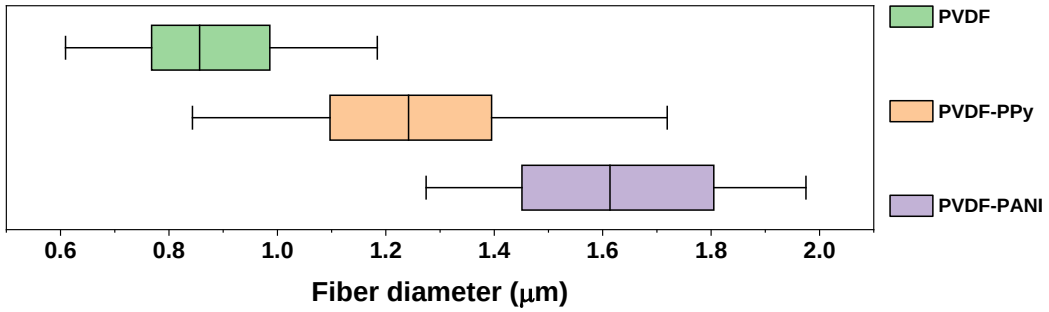

Figure 4.3. Tukey-style box plot with the diameters of the coated and uncoated fibers

Overall, it has been observed that a good coating of the fibers was achieved, although with some morphological alterations. In the case of PVDF-PANI, the coating easily bridges the gaps between multiple fibers into a single uniform composite layer. In the PVDF-PPy fibers, on the other hand, this phenomenon was rarely observed and only in the smallest of gaps, with the vast majority of fibers being individually coated. Furthermore, and as expected, a small increase in fiber diameter was observed, although it should not impede the applicability of these materials in different tissue engineering strategies.

In order to confirm the uniform coating of the PVDF fibers, further analysis was performed by SEM-EDX, aimed at detecting the presence of nitrogen, (present in the both PANI and PPy, but not in PVDF) (**Figure 4.2 e-f**). The relatively uniform distribution of nitrogen indicates that both PANI and PPy completely coated the PVDF fibers.

4.3.1.2. Raman spectra

A Raman spectroscopic analysis was conducted at first with a laser excitation line of 633 nm (**Figure 4.4-a**). The spectra shows polyaniline hydrochloride (PANI-salt) peaks in the PVDF-PANI fibers, at 1590 cm^{-1} (C=C stretching vibrations in a quinonoid ring), 1513 cm^{-1} (N–H deformation vibrations associated with the semiquinonoid structures), 1334 cm^{-1} (C-N vibrations of delocalized polaronic structures), 1164 cm^{-1} (C–H in-plane bending vibrations of the semi-quinonoid or benzenoid rings), 811 cm^{-1} (benzene-ring deformations), 584 cm^{-1} (amine in-plane deformation vibrations of the emeraldine salt) and 519 and 514 cm^{-1} (out-of-plane deformations of the ring) [30].

Peaks corresponding to PVDF or PET/ITO were not observed in the PVDF-PANI spectrum, indicating that the energy of laser excitation 633 nm is in resonance with the energy of the electronic transition in PANI and that the PANI coating is thicker than the penetration depth of a laser excitation at this energy [31].

In the PVDF-PPy spectrum only a strong fluorescence was observed. Consequently, a second analysis was then conducted with a laser excitation line of 514 nm (**Figure 4.4-b**), and in this, the PVDF-PPy spectra presented multiple peaks, although peaks of the PVDF-PANI spectra resulted less clear than with the excitation line of 633 nm.

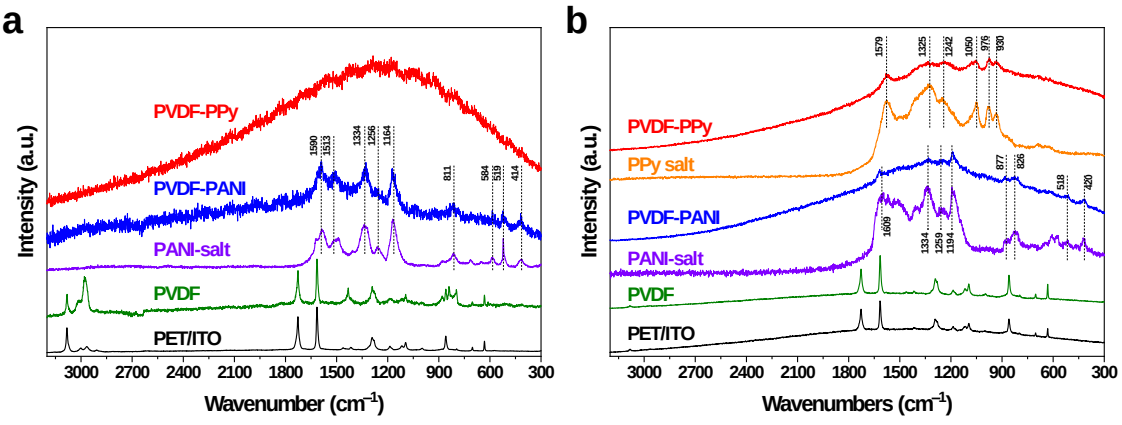

Figure 4.4. Raman spectra of PVDF-PANI and PVDF-PPy fibers: a) Spectra of PVDF, PET/ITO and PANI-salt included for comparison. Laser excitation line 633 nm. b) Spectra of PVDF, PET/ITO, PPy-salt and PANI-salt included for comparison. Laser excitation line 514 nm.

In the Raman spectrum of PVDF-PPy, peaks of PPy salt (PPy-salt) were detected at 1579 cm^{-1} (C=C stretching vibrations of PPy backbone), 1325 cm^{-1} (ring-stretching vibrations in protonated PPy), 1242 cm^{-1} (antisymmetric C–H deformation vibrations), 1050 cm^{-1} (C–H out-of-plane deformation vibrations), 976 and 930 cm^{-1} (ring-deformation vibrations) [32]. In the Raman spectrum of PVDF-PANI, peaks of PANI-salt were detected at 1609, 1334, 1259, 1194, 877, 826, 518 and 420 cm^{-1}, which are identified in the spectrum of PANI-salt as well.

In the case of the PVDF spectrum, only the peaks corresponding to the substrate (PET/ITO) were detected, and, as was the case with the laser excitation line of 633 nm, the peaks of the PET/ITO spectrum were not observed in either the PVDF-PANI or the PVDF-PPy spectra.

4.3.1.3. Wettability

Contact angle measurements were carried out on the PVDF fibers, which presented the typical hydrophobic nature of fluorinated polymers [37] with an initial contact angle of 141.3±2º.

When the fibers were coated with either PPy or PANI, it was observed that both coatings lead to hydrophilic membranes, with the PVDF+PANI fiber mat absorbing the water drop in ≈11 seconds (**Figure 4.5**), while the PVDF+PPy fiber mat does so in ≈1 second.

Figure 4.5. Absorption of a water droplet on a PVDF+PANI fiber mat, at 4 second intervals

4.3.2. Functional response

4.3.2.1. Conductivity

Figure 4.6-a shows characteristic IV curves for coated fiber mat samples at RT.

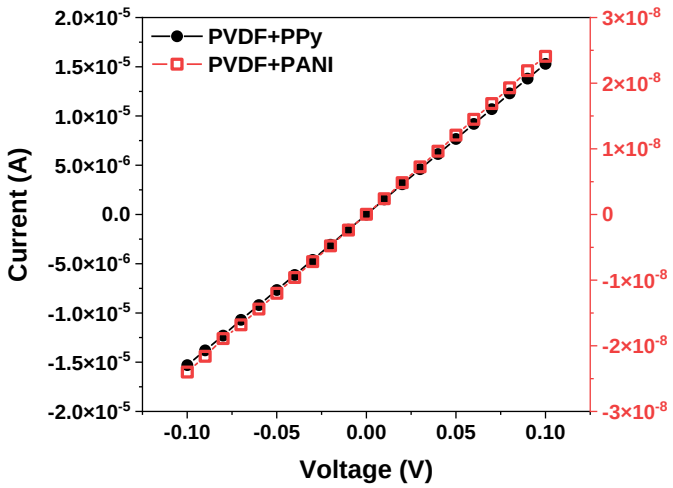

Figure 4.6. IV-curves of PVDF-PPy and PVDF-PANI.

The PVDF+PPy sample presents the highest conductivity, σ = 1.19 $S.m^{-1}$, while the PVDF+PANI sample shows a conductivity of 3.84×10^{-3} $S.m^{-1}$. As a comparison, neat PANI electrospun fibers have been reported to have a conductivity of 0.45 $S.m^{-1}$ [33], while PVDF fibers coated in PANI by an immersion process presented conductivity between 2.6×10^{-3} $S.m^{-1}$ and 330 $S.m^{-1}$ [34].

Taking the work of Merlini *et al.* [34] as a guide, it could be argued that the coating of PVDF fibers by PANI was not perfectly homogeneous, which would result in the lower conductivity obtained. As for PPy, electrospun membranes of PVDF coated with PPy by immersion, provide conductivities up to 70 $S.m^{-1}$ [35]. Merlini *et al.*, using a similar procedure to that of the previously cited work, obtained conductivity up to 160 $S.m^{-1}$ [36]. These two works indicate that the method used in this work, focusing on coating just one side of the membranes, results in homogeneous thinner PPy coatings.

4.3.2.2. Cytotoxicity assay

A key issue for the development and use of materials for biomedical applications is their eventual cytotoxic behavior. It has been shown that PVDF fibers present no cytotoxicity and are biocompatible [38].

However, the introduction of different fillers or coating in the matrix can lead to cytotoxic effects. In this way, the cytotoxicity of the different PVDF fibers with PPy and PANI coating were evaluated. The study of metabolic activity of the L929 fibroblast, assessed with MTS assay, was applied to all the samples and the results after 72 h are presented in **Figure 4.7**.

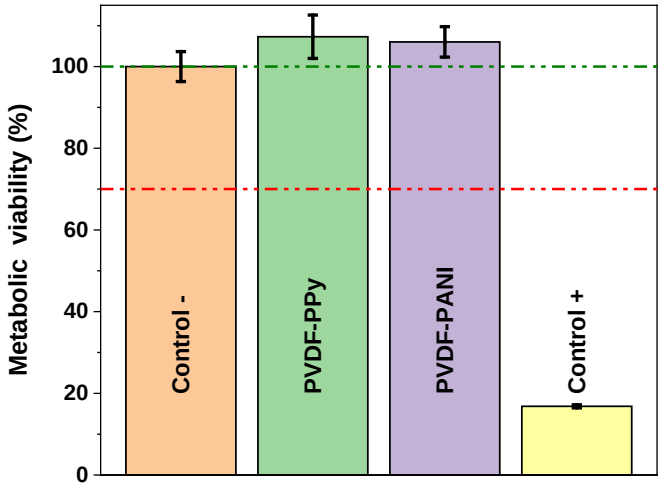

Figure 4.7. Cytotoxicity assay of L929 fibroblast cells in contact with the extraction media exposed to the different samples for 72 h (n = 4 ± standard deviation).

According to the ISO standard 10993-5, the samples are considered cytotoxic when cells suffer a viability reduction larger than 30%. The measured cell viability values are all higher than 70%, confirming the cytocompatibility of the samples.

Therefore, the coating of PVDF fibers with PANI or PPy does not cause cytotoxicity to the composite samples, but rather results in a slight increase in metabolic activity of the cells, a result that is more evident in the PVDF-PPy sample. Thus, it is proven that the fiber mats surface-modified with conducting polymers can be used for biomedical applications.

4.4. Conclusions

Hybrid polymeric electrospun microfiber mats were developed for advanced tissue regeneration strategies, by coating an electroactive PVDF matrix with conductive PANI or PPy.

The morphology, physico-chemical and electrical properties of the fiber mats were evaluated. While the PANI coating often bridged the gaps between fibers, creating small portions more similar to a film or membrane, and thus slightly reducing the porosity of the samples coated with PANI, PPy allows to coat more easily and consistently each fiber individually. Although the porosity, due to the nature of the fibrous membranes, is still very high, if needed this phenomenon could be avoided by adding a surfactant, which would modify the surface tension of the polymerization media. Coating with both conductive polymers lead the hydrophobic PVDF membranes to become hydrophilic, the fiber mats completely absorbing the water drop after few seconds. The electrical conductivity of the hybrid samples shows a value of σ = 1.19 $S.m^{-1}$ for the PVDF+PPy samples and $\sigma = 3.84 \times 10^{-3}$ $S.m^{-1}$ for the PVDF+PANI ones. Further, both hybrid membranes are not cytotoxic, proving their suitability for biomedical applications.

4.5. References

1. Langer, R. and J.P. Vacanti, *Tissue Engineering*. Science, 1993. **260**(5110): p. 920-926. DOI: 10.1126/science.8493529

2. Ribeiro, C., C.M. Costa, D.M. Correia, J. Nunes-Pereira, J. Oliveira, P. Martins, R. Gonçalves, V.F. Cardoso, and S. Lanceros-Méndez, *Electroactive poly(vinylidene fluoride)-based structures for advanced applications.* Nature Protocols, 2018. **13**(4): p. 681-704. DOI: 10.1038/nprot.2017.157

3. Lu, Y., A.A. Aimetti, R. Langer, and Z. Gu, *Bioresponsive materials.* Nature Reviews Materials, 2016. **2**(1). DOI: 10.1038/natrevmats.2016.75

4. Ramakrishna, S., K. Fujihara, W.-E. Teo, T.-C. Lim, and Z. Ma, *An Introduction to Electrospinning and Nanofibers*. 2005: WORLD SCIENTIFIC. DOI: 10.1142/5894

5. Jana, S., S.K.L. Levengood, and M. Zhang, *Anisotropic Materials for Skeletal-Muscle-Tissue Engineering.* Advanced Materials, 2016. **28**(48): p. 10588-10612. DOI: 10.1002/adma.201600240

6. Cardoso, V.F., D.M. Correia, C. Ribeiro, M.M. Fernandes, and S. Lanceros-Méndez, *Fluorinated Polymers as Smart Materials for Advanced Biomedical Applications.* Polymers, 2018. **10**(2): p. 161. DOI: 10.3390/polym10020161

7. Hermenegildo, B., C. Ribeiro, L. Pérez-Álvarez, J.L. Vilas, D.A. Learmonth, R.A. Sousa, P. Martins, and S. Lanceros-Méndez, *Hydrogel-based magnetoelectric microenvironments for tissue stimulation.* Colloids and Surfaces B: Biointerfaces, 2019. **181**: p. 1041-1047. DOI: 10.1016/j.colsurfb.2019.06.023

8. Li, Y., C. Liao, and S.C. Tjong, *Electrospun Polyvinylidene Fluoride-Based Fibrous Scaffolds with Piezoelectric Characteristics for Bone and Neural Tissue Engineering.* Nanomaterials, 2019. **9**(7): p. 952. DOI: 10.3390/nano9070952

9. Correia, D.M., L.C. Fernandes, P.M. Martins, C. García-Astrain, C.M. Costa, J. Reguera, and S. Lanceros-Méndez, *Ionic Liquid-Polymer Composites: A New Platform for Multifunctional Applications.* Advanced Functional Materials, 2020: p. 1909736. DOI: 10.1002/adfm.201909736

10. Fernandes, L.C., D.M. Correia, E. Fernández, M. Tariq, J.M.S.S. Esperança, and S. Lanceros-Méndez, *Design of Ionic-Liquid-Based Hybrid Polymer Materials with a Magnetoactive and Electroactive Multifunctional Response.* ACS Applied Materials & Interfaces, 2020. **12**(37): p. 42089-42098. DOI: 10.1021/acsami.0c10746

11. Rodrigues-Marinho, T., N. Castro, V. Correia, P. Costa, and S. Lanceros-Méndez, *Triboelectric Energy Harvesting Response of Different Polymer-Based Materials.* Materials, 2020. **13**(21): p. 4980. DOI: 10.3390/ma13214980

12. Meira, R.M., D.M. Correia, S. Ribeiro, P. Costa, A.C. Gomes, F.M. Gama, S. Lanceros-Méndez, and C. Ribeiro, *Ionic-Liquid-Based Electroactive Polymer Composites for Muscle Tissue Engineering.* ACS Applied Polymer Materials, 2019. **1**(10): p. 2649-2658. DOI: 10.1021/acsapm.9b00566

13. Adadi, N., M. Yadid, I. Gal, M. Asulin, R. Feiner, R. Edri, and T. Dvir, *Electrospun Fibrous PVDF-TrFe Scaffolds for Cardiac Tissue Engineering, Differentiation, and Maturation.* Advanced Materials Technologies, 2020. **5**(3): p. 1900820. DOI: 10.1002/admt.201900820

14. Ding, J., J. Zhang, J. Li, D. Li, C. Xiao, H. Xiao, H. Yang, X. Zhuang, and X. Chen, *Electrospun polymer biomaterials.* Progress in Polymer Science, 2019. **90**: p. 1-34. DOI: 10.1016/j.progpolymsci.2019.01.002

15. He, Z., F. Rault, M. Lewandowski, E. Mohsenzadeh, and F. Salaün, *Electrospun PVDF Nanofibers for Piezoelectric Applications: A Review of the Influence of Electrospinning Parameters on the β Phase and Crystallinity Enhancement.* Polymers, 2021. **13**(2): p. 174. DOI: 10.3390/polym13020174

16. Inzelt, G., *Introduction*, in *Monographs in Electrochemistry*. 2012, Springer Berlin Heidelberg. p. 1-6. DOI: 10.1007/978-3-642-27621-7_1

17. Le, T.-H., Y. Kim, and H. Yoon, *Electrical and Electrochemical Properties of Conducting Polymers.* Polymers, 2017. **9**(4): p. 150. DOI: 10.3390/polym9040150

18. Barbero, C.A., D.F. Acevedo, E. Yslas, M. Broglia, D.O. Peralta, E. Frontera, R. Rivero, C.R. Rivarola, M. Bertuzzi, V. Rivarola, and M.C. Miras, *Synthesis, Properties and Applications of Conducting Polymer Nano-Objects.* Molecular Crystals and Liquid Crystals, 2010. **521**(1): p. 214-228. DOI: 10.1080/15421401003720074

19. Capáková, Z., K.A. Radaszkiewicz, U. Acharya, T.H. Truong, J. Pacherník, P. Bober, V. Kašpárková, J. Stejskal, J. Pfleger, M. Lehocký, and P. Humpolíček, *The biocompatibility of polyaniline and polypyrrole 2 : Doping with organic phosphonates.* Materials Science and Engineering: C, 2020. **113**: p. 110986. DOI: 10.1016/j.msec.2020.110986

20. Riaz, U. and S.M. Ashraf, *Nanostructured Conducting Polymers and their Nanocomposites: Classification, Properties, Fabrication and Applications*. Nanotechnology Science and Technology. 2010: NOVA Science Publishers. 193. Available from.

21. Stejskal, J. and I. Sapurina, *Polyaniline: Thin films and colloidal dispersions (IUPAC Technical Report).* Pure and Applied Chemistry, 2005. **77**(5): p. 815-826. DOI: 10.1351/pac200577050815

22. Stejskal, J., I. Sapurina, and M. Trchová, *Polyaniline nanostructures and the role of aniline oligomers in their formation.* Progress in Polymer Science, 2010. **35**(12): p. 1420-1481. DOI: 10.1016/j.progpolymsci.2010.07.006

23. Castagna, R., M. Tunesi, B. Saglio, C. Della Pina, A. Sironi, D. Albani, C. Bertarelli, and E. Falletta, *Ultrathin electrospun PANI nanofibers for neuronal tissue engineering.* Journal of Applied Polymer Science, 2016. **133**(35). DOI: 10.1002/app.43885

24. Huang, Z.-B., G.-F. Yin, X.-M. Liao, and J.-W. Gu, *Conducting polypyrrole in tissue engineering applications.* Frontiers of Materials Science, 2014. **8**(1): p. 39-45. DOI: 10.1007/s11706-014-0238-8

25. Qazi, T.H., R. Rai, and A.R. Boccaccini, *Tissue engineering of electrically responsive tissues using polyaniline based polymers: A review.* Biomaterials, 2014. **35**(33): p. 9068-9086. DOI: 10.1016/j.biomaterials.2014.07.020

26. Mirzaei, A., E. Saburi, S.E. Enderami, M. Barati Bagherabad, S.E. Enderami, M. Chokami, A. Shapouri Moghadam, R. Salarinia, A. Ardeshirylajimi, V. Mansouri, and F. Soleimanifar, *Synergistic effects of polyaniline and pulsed electromagnetic field to stem cells osteogenic differentiation on polyvinylidene fluoride scaffold.* Artificial Cells, Nanomedicine, and Biotechnology, 2019. **47**(1): p. 3058-3066. DOI: 10.1080/21691401.2019.1645154

27. Riede, A., M. Helmstedt, I. Sapurina, and J. Stejskal, *In Situ Polymerized Polyaniline Films: 4. Film Formation in Dispersion Polymerization of Aniline.* Journal of Colloid and Interface Science, 2002. **248**(2): p. 413-418. DOI: 10.1006/jcis.2001.8197

28. Omastová, M., M. Trchová, J. Kovářová, and J. Stejskal, *Synthesis and structural study of polypyrroles prepared in the presence of surfactants.* Synthetic Metals, 2003. **138**(3): p. 447-455. DOI: 10.1016/s0379-6779(02)00498-8

29. Krzywinski, M. and N. Altman, *Visualizing samples with box plots.* Nature Methods, 2014. **11**(2): p. 119-120. DOI: 10.1038/nmeth.2813

30. Stejskal, J., M. Trchová, P. Bober, P. Humpolíček, V. Kašpárková, I. Sapurina, M.A. Shishov, and M. Varga, *Conducting Polymers: Polyaniline*, in *Encyclopedia of Polymer Science and Technology*. 2015, John Wiley & Sons, Inc. p. 1-44. DOI: 10.1002/0471440264.pst640

31. Trchová, M. and J. Stejskal, *Resonance Raman Spectroscopy of Conducting Polypyrrole Nanotubes: Disordered Surface versus Ordered Body.* The Journal of Physical Chemistry A, 2018. **122**(48): p. 9298-9306. DOI: 10.1021/acs.jpca.8b09794

32. Stejskal, J. and M. Trchová, *Conducting polypyrrole nanotubes: a review.* Chemical Papers, 2018. **72**(7): p. 1563-1595. DOI: 10.1007/s11696-018-0394-x

33. Hou, X., Y. Zhou, Y. Liu, L. Wang, and J. Wang, *Coaxial electrospun flexible PANI//PU fibers as highly sensitive pH wearable sensor.* Journal of Materials Science, 2020. **55**(33): p. 16033-16047. DOI: 10.1007/s10853-020-05110-7

34. Merlini, C., G.M.d.O. Barra, S.D.A.d.S. Ramôa, G. Contri, R.d.S. Almeida, M.A. d'Ávila, and B.G. Soares, *Electrically Conductive Polyaniline-Coated Electrospun Poly(Vinylidene Fluoride) Mats.* Frontiers in Materials, 2015. **2**(14). DOI: 10.3389/fmats.2015.00014

35. Dias, J.C., D.M. Correia, G. Botelho, S. Lanceros-Méndez, and V. Sencadas, *Electrical properties of intrinsically conductive core–shell polypyrrole/poly(vinylidene fluoride) electrospun fibers.* Synthetic Metals, 2014. **197**: p. 198-203. DOI: 10.1016/j.synthmet.2014.09.013

36. Merlini, C., R.d.S. Almeida, M.A. D'Ávila, W.H. Schreiner, and G.M.d.O. Barra, *Development of a novel pressure sensing material based on polypyrrole-coated electrospun poly(vinylidene fluoride) fibers.* Materials Science and Engineering: B, 2014. **179**: p. 52-59. DOI: 10.1016/j.mseb.2013.10.003

37. Huang, F.L., Q.Q. Wang, Q.F. Wei, W.D. Gao, H.Y. Shou, and S.D. Jiang, *Dynamic wettability and contact angles of poly(vinylidene fluoride) nanofiber membranes grafted with acrylic acid.* Express Polymer Letters, 2010. **4**(9): p. 551-558. DOI: 10.3144/expresspolymlett.2010.69

38. Martins, P.M., S. Ribeiro, C. Ribeiro, V. Sencadas, A.C. Gomes, F.M. Gama, and S. Lanceros-Méndez, *Effect of poling state and morphology of piezoelectric poly(vinylidene fluoride) membranes for skeletal muscle tissue engineering.* RSC Advances, 2013. **3**(39): p. 17938-17944. DOI: 10.1039/c3ra43499k

Chapter 5

Ionic liquid modified microenvironments for biomedical applications

Cytotoxicity assay for new ionic liquid modified materials.

Ionic liquids have been extensively explored and implemented in different areas, including the biomedical. In this, they have been used both to assist the preparation of new materials, as well as in the development of new hybrid materials with specific properties. Their usage in tissue engineering is still scarce and, therefore, their ability to grant conductive, sensing or magnetic properties to materials that lacked them should be explored. This chapter details the development of new polymer-based, ionic liquid modified, biodegradable materials for biomedical applications.

5.1. Introduction

Muscle loss is a particularly serious case of tissue damage, due to the low regenerability of muscle tissue in the case of large volumetric loss, and the complexity of the tissue itself, rendering many therapies ineffective or with less-than-desirable results [1]. In this scope, tissue engineering (TE) emerges as an effective approach to muscle repair. TE proposes, among other strategies, to grow new tissue *in vitro* from samples taken from the patient itself, to be implanted afterwards in the patient as required, without rejection issues nor the need of compatible donors [2]. However, the specific tissue growth and development requirements of skeletal muscle fibers mean that, to our knowledge, no suitable solutions have yet been developed.

One of the main challenges relies on the fact that muscle cell growth and development is greatly enhanced by active stimuli of cells, such as mechanical and/or electric, by means of scaffolds based on oriented fibers [3, 4] mimicking the natural growth conditions of muscle tissue [5]. For this, muscle TE requires the use of biocompatible materials with a controllable mechanic- and electroactive response, being also desirable materials that are biodegradable as well, degrading as the new functional tissue is generated. This will minimize possible long-term health issues, related to the implantation of permanent extrinsic materials within the body.

Electroactive smart materials can be processed into different shapes and morphologies such as fibers, films, and microspheres [6], and have demonstrated potential applicability in a variety of TE applications including bone [7], cardiac [8], and skeletal muscle tissues [3, 4, 9], where it has verified that an active scaffold with a specific morphology resembling the morphology of the tissue to be regenerated is a suitable approach for functional tissue regeneration.

In particular, electrospinning is a method for obtaining oriented polymer fibers that allows a fine control of fiber properties, and can tune them to the individual needs of specific tissues and microenvironments, such as skeletal muscle tissue, improving both biomimicry and cellular development and regeneration [4].

Among the different electroactive polymers, poly(vinylidene fluoride) (PVDF) has been extensively studied as scaffold for TE applications, due to its biocompatibility, processing versatility and high piezoelectric response associated to the presence of the β-crystalline phase [10, 11]. In order to be used in skeletal muscle TE, it has been combined with different organic and inorganic materials, such as cobalt ferrite ($CoFe_2O_4$) nanoparticles (NP) [9], silica NPs [5], and ionic liquids (ILs) [11], among others [12]. However, it is a non-biodegradable material, which restricts its applicability. For this reason, electroactive and biodegradable polymers such as polyhydroxybutyrate-co-hydroxyvalerate (PHBV) are of increasing interest.

PHBV is a biocompatible and biodegradable co-polymer of polyhydroxybutyrate (PHB), with good bioactivity and piezoelectric properties [13], and is an excellent candidate to replace PVDF for TE applications where biodegradability is an *in vivo* requirement. PHBV has also been processed into different morphologies, including films, fibers and microspheres [14], and presents improved mechanical properties when compared to PHB [13]. PHBV has been used as polymer matrix for the development of composite materials, with tailored functional properties, in combination with ILs and graphene oxide-ZnO for selective barriers in advanced packaging [15], or for TE, combined with $CoFe_2O_4$ [13] and iron oxide-graphene oxide [16], as well as silver NPs, graphene or other polymers [14].

As a material for tailoring the functional response of polymer matrices, ILs have been gaining attention for TE [17, 18]. ILs are defined as salts with a low melting temperature (under 100 ºC), high electrochemical and thermal stability and their main properties can be tailored by the proper selection of anions and cations. Thus, ILs and IL based polymer hybrid materials have been explored for batteries, actuators, biosensors and biomedical devices [18]. Furthermore, due to the biocompatibility and biodegradability of many ILs, these have been used for different TE applications [17]. This is the case of 1-butyl-3-methylimidazolium chloride and 2-hydroxyethyl-trimethylammonium dihydrogen phosphate for muscle tissue engineering [11], 1-butyl-3-methylimidazolium acetate for skin regeneration [17], or 1-ethyl-3-methylimidazolium acetate for neural TE [17], combined with polymers such as PVDF [11, 19] or cellulose blends[20].

One of these biodegradable and biocompatible ILs is choline acetate ([Chol][Ac]), that displays high ionic conductivity [21-23] and has previously been evaluated as an electrolyte in Zn/air rechargeable batteries [23], as an actuator in combination with polypyrrole-PVDF [21], and for biomedical applications when combined with α-chitin [22]. However, the overall research on the combination of ILs and PHBV is limited, and to the best of our knowledge, there are no reports about ILs being used with PHBV polymeric scaffolds for TE applications, nor on the use of [Chol][Ac] for TE applications. It is to notice that, together with the intrinsic characteristics of each of the components of the hybrid materials, IL-polymer composites show, for specific filler concentrations, piezo-ionic effect particularly suitable for the mimicking of muscle tissue [11, 17].

In this context, the present work focuses on the development of PVDF and PHBV electrospun fibers and films to be applied as scaffolds for tissue engineering applications, in order to study the possibilities of both as biostable and biodegradable platforms, respectively. The morphology, physico-chemical, thermal and conductive properties of the PVDF and PHBV hybrid fibers and films with the IL [Chol][Ac] were comparatively studied and their potential to be applied as scaffolds for muscle TE assessed.

5.2. Experimental

5.2.1. Materials

PHBV (Mw = 460,64 $g.mol^{-1}$; HV = 3%, mole fraction), 99% purity, was supplied from Natureplast. PVDF with different molecular weights (PVDF 5130 (Mw = 1000-1100 kDa) and PVDF 6010 (Mw=300-320 kDa)) purchased from Solef and Solvay, respectively, were used. PVDF 5130 was selected for electrospun fiber mats preparation, as high PVDF molecular weights favors the production of homogeneous fibers without the presence of beads [24]. [Chol][Ac] was acquired from Iolitec. Chloroform (Chromasolv 99.8%) (CF) was purchased from Honeywell and N,N-dimethylformamide (DMF) from Merck.

5.2.2. Sample processing

5.2.2.1. Solution preparation

For the preparation of the polymer solutions, PHBV was dissolved in CF, with a concentration of 15% weight/volume (w/v), and the solution was kept under agitation with a magnetic stirrer at 50 ºC for 2 h. PVDF was dissolved in DMF, at 15% w/v concentration, and kept under magnetic agitation at 35 ºC until complete dissolution of the polymer.

Independently of the polymer matrix, IL contents of 5, 10 and 15 weight percentage (wt.%) were incorporated into the polymer matrix. For the PHBV+IL hybrid materials, the IL was first dispersed in CF under magnetic stirring for 30 min. PHBV (15% w/v) was then added and magnetically stirred at 50 ºC until complete polymer dissolution. For the development of the PVDF+IL hybrid materials, after IL dispersing in DMF for 30 min, PVDF (15% w/v) was added, and the mixture stirred until complete polymer dissolution.

5.2.2.2. Electrospun fiber processing

PHBV and PVDF, neat and IL [Chol][Ac] containing, aligned fibers were produced by electrospinning following the general guidelines presented in previous studies [13, 19]. The polymer solution was placed in a 10 mL plastic syringe fitted with a steel needle with 0.41 mm inner diameter.

Electrospinning was conducted by applying high voltage with a Matsusada AU-30P1-L power supply. A Syringepump NE-300 fed a constant flow of polymer solution into the needle tip. The electrospun fibers were collected on a grounded drum of 80 mm diameter, rotating at 1500 rpm.

The specific conditions for each polymer and concentration are detailed in **Table 5.1**. PVDF revealed to be more sensitive to the inclusion of the IL than PHBV, with increasing wt.% of IL requiring adjustments to parameters in order to obtain fiber mats.

Table 5.1. Electrospinning conditions for the prepared PHBV and PVDF fiber mats and the corresponding composites with [Chol][Ac].

	Flow Rate ($mL.h^{-1}$)	Voltage Applied (kV)	Collector distance (cm)
PVDF	0.3	14.1	20
PVDF+IL 5%	0.3	15.1	18
PVDF+IL 10%	0.3	15.8	12
PVDF+IL 15%	0.3	15.8	12
PHBV	1	15	15
PHBV+IL 5%	1	15	15
PHBV+IL 10%	1	15	15
PHBV+IL 15%	1	15	15

5.2.2.3. Film preparation

The solutions were prepared as previously described. The PVDF polymer solutions were poured onto a glass substrate and spread with a film applicator with a 450 μm thickness, and the solvent was evaporated at 120 ºC for 30 min. The PHBV solution was poured on a Petri dish, covered, and allowed to slowly evaporate for 48 h at room temperature (RT).

5.2.3. Sample characterization

5.2.3.1. Physico-chemical characterization

Scanning Electron Microscopy (SEM) was used to assess the morphology of both fibers and films, using a Hitachi S-4800 field emission SEM at an accelerating voltage of 5 kV. Prior to the analysis, the samples were coated with a 15 nm thick layer of gold using a Quorum Emitech K550 Sputter Coater at 25 mA and a pressure of 0.09 mbar. Microfiber diameter and distribution in the electrospun fiber mats were calculated by measuring 45 fibers, at magnifications of x1.5 kX, 5.0 kX and 20kX, using the ImageJ software.

Energy-dispersive X-ray (EDX) analysis was performed with a Carl Zeiss EVO-40 Scanning Electron Microscope equipped with an Oxford Instruments X-Max Microanalysis EDS-Detector, at an accelerating voltage of 20 kV and x2.5 kX magnification.

Surface characterization was performed with a CSI Nano-Observer Atomic Force Microscope, with AppNano ANSCM-PT tips. Data was then analyzed with the Gwyddion software.

Fourier Transform Infrared Spectroscopy (FTIR) measurements were conducted at room temperature with a JASCO FT/IR-6100 in ATR mode, using 64 scans between 4000 and 500 cm-1 with a resolution of 4 cm^{-1}. The β-phase content of the PVDF samples was evaluated with the previously described **Equation 2.4** (**Chapter 2**).

The thermal behavior of the samples was evaluated by Thermogravimetric Analysis (TGA) and by Differential Scanning Calorimetry (DSC). TGA measurements were carried out with a Mettler Toledo TGA/SDTA851 equipped with a thermobalance and with the samples in an open ceramic crucible. The samples were heated from 25 to 900 ºC, at a rate of 10 $ºC.min^{-1}$ and a nitrogen flow rate of 50 $mL.min^{-1}$.

The DSC measurements were performed with a Mettler Toledo DSC822e, equipped with a sample robot, at a heating rate of 10 $°C.min^{-1}$ under nitrogen flow of 50 $mL.min^{-1}$. STAR software was used to retrieve and analyze the data.

The crystallinity degree (X_C) of the PHBV samples was calculated by applying **Equation 5.1**

$$X_C = \frac{\Delta H}{\%_{polymer}\ \Delta H_{100}} \qquad \textbf{(5.1)}$$

where ΔH is the melting enthalpy of the sample, ΔH_{100} is the melting enthalpy of a 100% crystalline sample of the polymer, with ΔH_{100} = 146.6 $J.mol^{-1}$ in the case of PHBV [13], and the mass fraction of polymer within the samples is represented by $\%_{polymer}$.

In the case of the PVDF polymer, due to the coexistence of polymer phases, **Equation 3.1**, previously described in **Chapter 3**, was used instead.

Impedance measurements were measured using an Autolab PGSTAT-12, varying the frequencies between 500 mHz and 50 kHz, and the ionic conductivity (σ_i) was calculated with **Equation 3.2**.

The contact angle (CA) of the polymer samples was measured using a Data-Physics Contact Angle System OCA 15EC and the SCA20 software, by depositing five 3 μL of ultrapure water drops on the surface of the samples and averaging the mean value of the CA on each side of the drop.

5.2.3.2. *In vitro* cytotoxicity Assay

Indirect cytotoxicity evaluation of the samples was performed by adapting the ISO 10993-5 standard test method. C2C12 cells were cultured in 75 cm^2 cell culture flask, at 37 °C, in a humidified environment with 5% CO_2, using Dulbecco's modified Eagle's medium (DMEM, Biochrom) containing 4.5 $g.L^{-1}$ glucose, 10% fetal bovine serum (FBS, Biochrom) and 1% (v/v) penicillin/streptomycin solution (P/S, Biochrom).

The different samples were cut to pieces of approximately 1 cm^2, sterilized by exposure to ultraviolet radiation for 1 h on each side of the samples, and washed with a sterile phosphate-buffered saline solution (PBS, pH 7.4).

A suspension of 2×10^4 $cell.mL^{-1}$ was then seeded in 96-well tissue culture polystyrene plates and incubated for 24 h at the previously described conditions to ensure cell attachment. Simultaneously, each sample was incubated with DMEM for 24 h in a 24-well tissue culture polystyrene plate. After this time, the cell culture medium in the 96-well plates was then removed, and 100 μL of culture medium (previously in contact with the different samples) was added to each well and allowed to incubate in standardized culture conditions for 72 h as mentioned above.

The cell activity was then evaluated using (3-(4,5-dimethylthiazol-2-yl)-5-(3-carboxymethoxyphenyl)-2-(4-sulfophenyl)-2H-tetrazolium) (MTS, Promega). Briefly, the medium of every well was removed, and fresh medium containing MTS solution (in a 1:5 ratio) was added to each well and incubated for 2 h. After the incubation time, the optical density was measured at 490 nm with a spectrophotometric plate reader (Biotech Synergy HT).

The results are presented as the average of viability ± standard deviation. The percentage of cell activity was calculated according to **Equation 3.4**.

5.3. Results and discussion

5.3.1. Morphological features, vibrational spectra and wettability

5.3.1.1. Morphology

The morphology of the PVDF and PHBV samples with different contents of IL was analyzed by SEM. **Figure 5.1 a-f** presents representative SEM images of PVDF and PHBV electrospun and film samples.

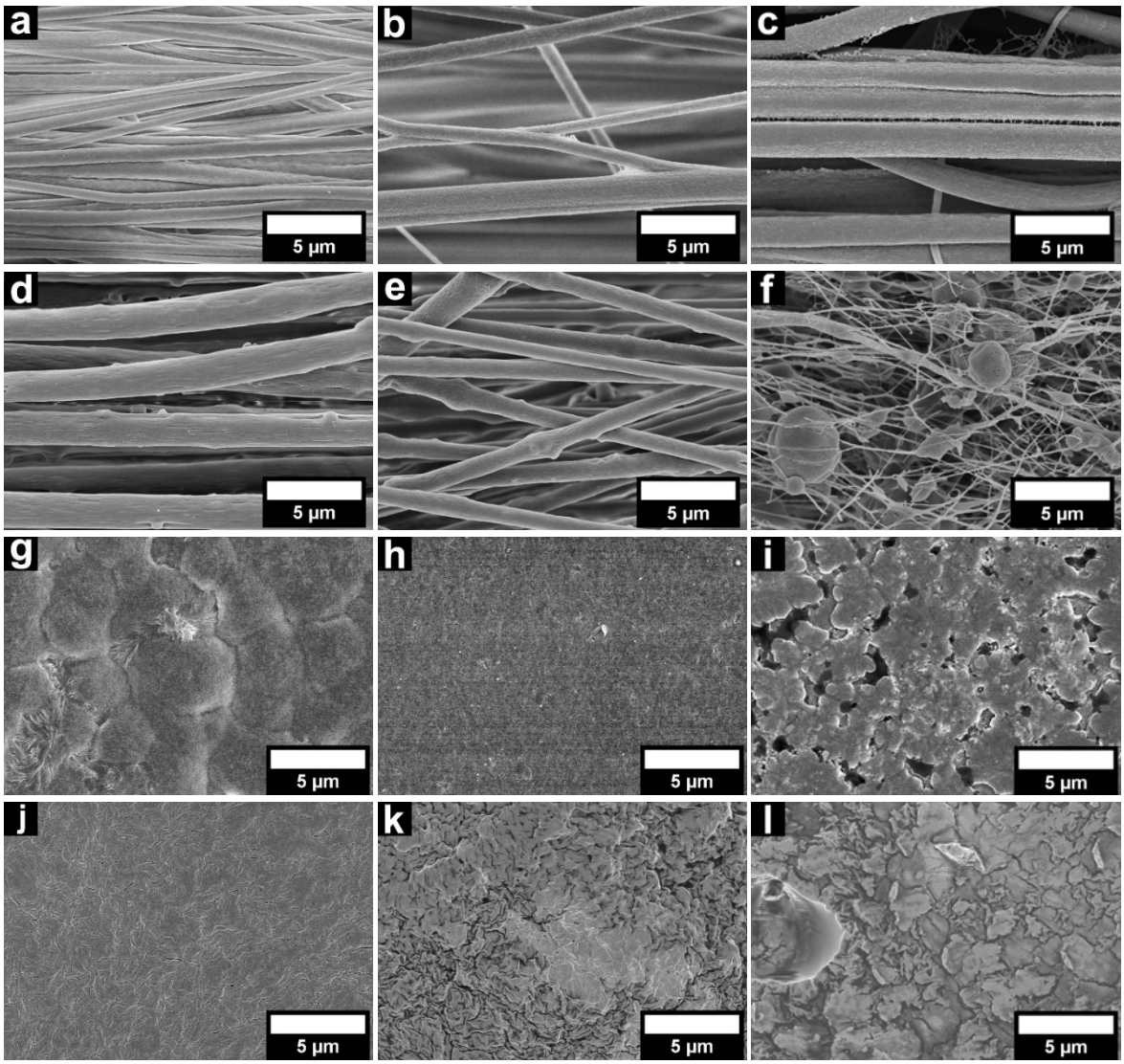

Figure 5.1. SEM images of PVDF and PHBV fiber and film samples: Electrospun fibers of a) PVDF; b) PVDF+IL 5%; c) PVDF+IL 15%; d) PHBV; e) PHBV+IL 5%; f) PHBV+IL 15%. Films of: g) PVDF; h) PVDF+IL 5%; i) PVDF+IL 15%; j) PHBV; k) PHBV+IL 5%; l) PHBV+IL 15%.

Regardless of polymer type, and for the same processing conditions, the inclusion of IL into the polymer matrix induces an increase in the randomness of the fiber orientation (**Figure 5.1 a-f**), with this effect being more noticeable for the PHBV+IL electrospun fibers, an effect already reported in the literature [25].

For PVDF+IL fibers, no significant morphological differences are observed upon the IL incorporation into the PVDF matrix, with smooth surface fibers and small variations in fiber diameter (**Figure 5.1 a-c**). As it can be seen in the box plot (obtained after the methodology by Krzywinski and Altman [28]) presented in **Figure 5.2**, no significant differences are observed in the fiber diameter of PVDF fibers (0.98 ± 0.19 μm) upon the inclusion of 5 wt.% of IL (1.06 ± 0.29 μm) and 10 wt.% (0.83 ± 0.13 μm). However, incorporating 15 wt.% of IL promotes a small increase in fiber diameter, up to 1.31 ± 0.25 μm, with morphology remaining otherwise similar. The initially observed fiber-thinning effect related to the incorporation of ILs has been previously reported, being attributed to the presence of ionic charges from the IL, that lead to a higher jet stretching comparatively to pristine PVDF [19, 26]. The thicker and self-bundled fibers observed at a higher wt.% of IL (**Figure 5.1-c**) are attributed to the interaction of the ionic charges with the charged solution during the electrospinning process, which, after a critical concentration, leads to jet instabilities and to the formation of bundles and thicker PVDF fibers, as it is verified (**Figure 5.1-c**) [27].

For the PHBV based samples, it is observed that the increase in IL content promotes significant changes in the fiber morphology and fiber diameter, with fibers becoming thinner with the increase in IL content from 5 to 10 wt.% (**Figure 5.1 d-f**). Higher IL contents of 15 wt.% (**Figure 5.1-f**) do not allow fiber formation, with some thin fibers with large particles observed. These results indicate that a higher number of ionic charges in the PHBV+IL solution leads to jet instability, causing jet sputtering.

The diameter of PHBV fibers decreased with increasing IL content from 1.73 ± 0.21 μm for neat PHBV to 1.00 ± 0.17 μm for PHBV+IL 5% and 0.22 ± 0.05 μm for PHBV+IL 10% (**Figure 5.2**).

These results indicate that a higher number of ionic charges in the PHBV+IL solution leads to jet instability, causing jet sputtering. The diameter of PHBV fibers decreased with IL content increase from 1.73 ± 0.21 μm for neat PHBV to 1.00 ± 0.17 μm for PHBV+IL 5% and 0.22 ± 0.05 μm for PHBV+IL 10% (**Figure 5.2**).

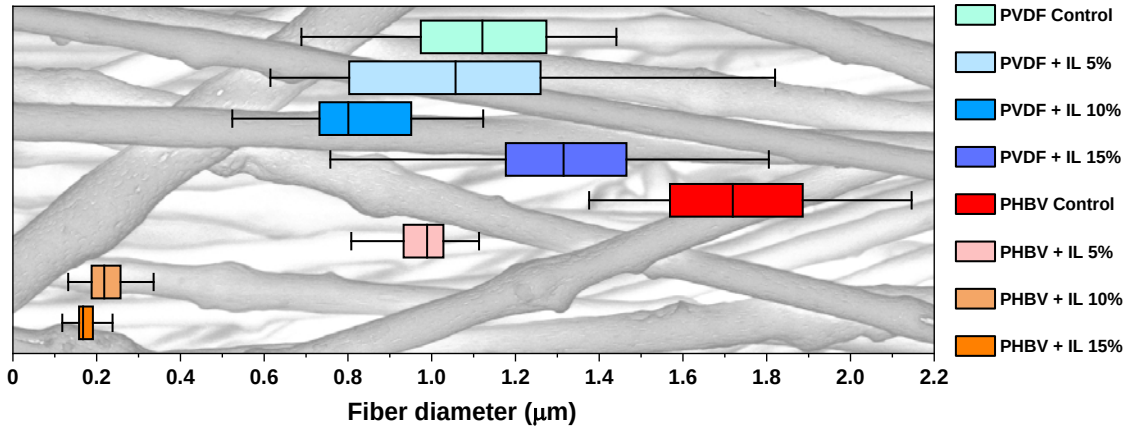

Figure 5.2. Tukey-style box plot with the diameters for PVDF+IL and PHBV+IL fibers, incorporating 5, 10 and 15 wt.% of IL [Chol][Ac] (background: PHBV+IL 5% fibers).

The morphology of the films was also evaluated by SEM. The surface of PVDF films (**Figure 5.1-g**) shows the typical spherulitic structure [28], that disappear when the IL is added (**Figure 5.1-h**) promoting the formation of small pores, more evident at higher wt.% of IL (**Figure 5.1-i**). PHBV films also appear to increase in roughness with increasing wt.% of IL (**Figure 5.1 j-l**) and form much larger pores (**Figure 5.1-l**) than PVDF (**Figure 5.1-i**).

The presence of pores, in both polymeric composite films, results from a polymer liquid-liquid phase separation, as well as the physical interactions that occurs between the IL and the different polymer solvents previous to both PVDF and PHBV crystallization. Both phenomena promote IL encapsulation within the pores once the solvent evaporates [29].

The presence of IL in electrospun fibers and films of PVDF+IL and PHBV+IL was assessed by SEM-EDX (**Figure 5.3**). The IL was effectively incorporated into the polymer matrix as indicated by the presence of nitrogen (N), present in the IL but not in either of the polymers.

The relatively uniform distribution of N indicates that the IL is homogeneously distributed in the polymers, regardless of the processing conditions and the resulting film morphology.

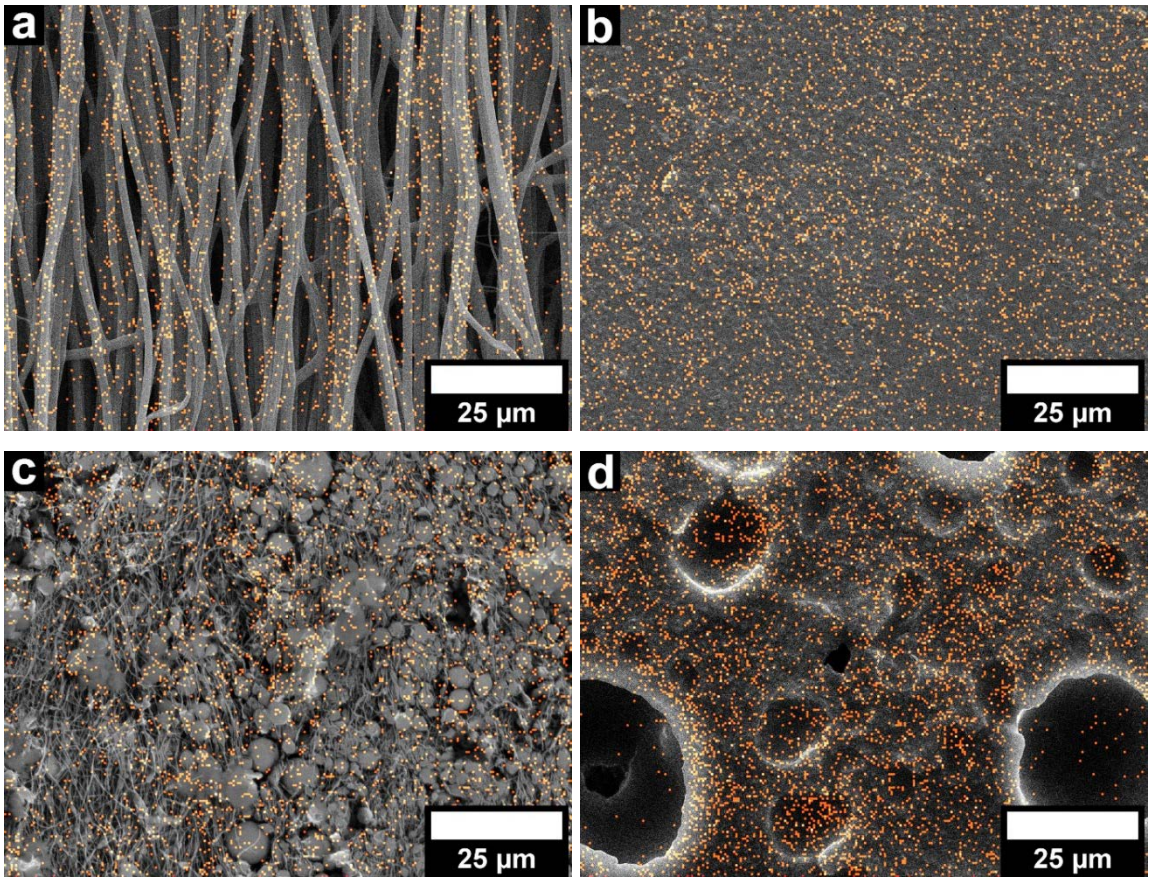

Figure 5.3. Representative EDX distribution maps of the IL in the processed samples, indicated by the presence of the N element for: PVDF+15% IL a) fibers and b) film; and for PHBV+15% IL c) fibers and d) film.

The influence of the IL content into the surface roughness of PVDF and PHBV was further evaluated by AFM. **Figure 5.4** shows the AFM images for neat PVDF and PHBV and their composites for an IL content of 15 wt.% Independently of the polymer matrix, the inclusion of IL into both polymer matrixes leads to changes in the surface topography of the materials.

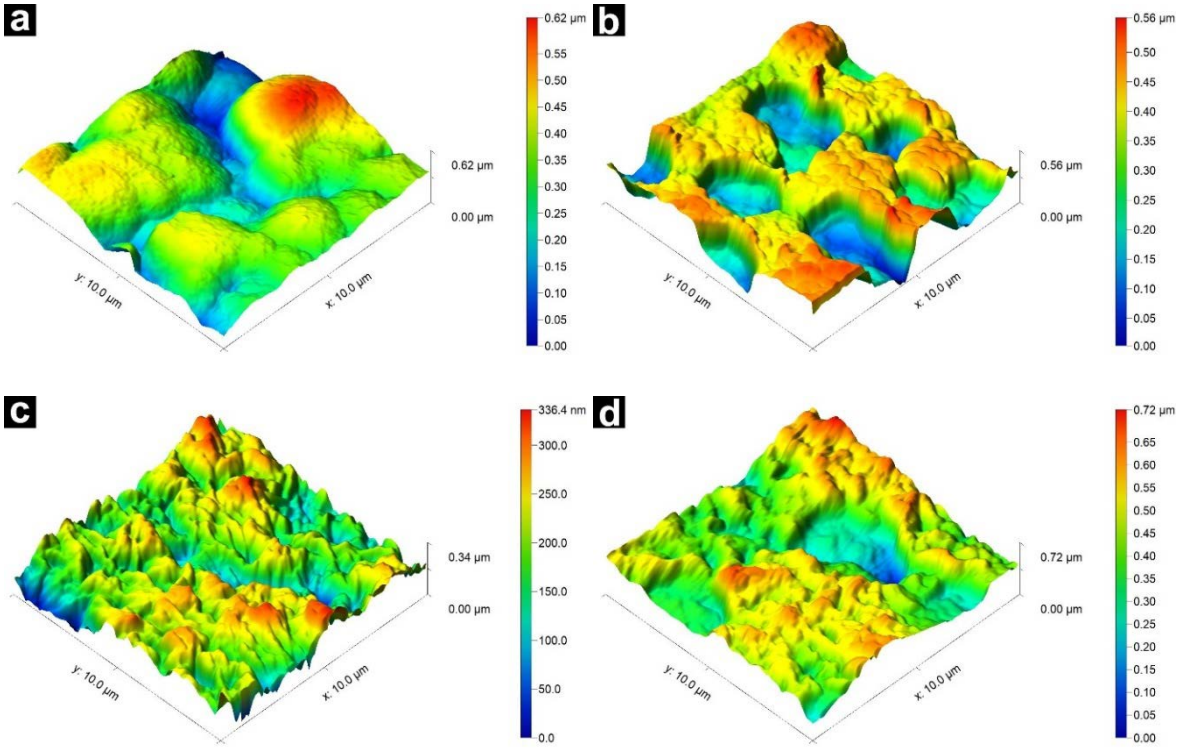

Figure 5.4. Representative AFM surface 3D images of the films: a) PVDF; b) PVDF+IL 15%; c) PHBV; d) PHBV+IL 15%.

For PVDF, the surface roughness increases upon IL incorporation (**Figure 5.4 a-b**), from 87 nm to 108 nm, respectively. Similar increase in roughness occurs for PHBV+15% IL (**Figure 5.4 c-d**), with a surface roughness increase from 41 to 86 nm. **Table 5.2** summarizes this data.

This increase is attributed to the presence of the IL, as it promotes the appearance of pores and the formation of smaller spherulites and crystals.

Table 5.2. Roughness data of representative samples.

Film Sample	RMS roughness (Sq) (nm)	Mean roughness (Sa) (nm)
PHBV	52.16	41.63
PHBV+IL 15%	105.10	85.50
PVDF	110.80	87.30
PVDF+IL 15%	123.70	108.40

5.3.1.2. Vibrational spectra

The influence of IL content in the vibration spectra of PHBV and PVDF electrospun fibers and films was evaluated by FTIR-ATR (**Figure 5.5**).

The presence of the IL in both PHBV and PVDF hybrid materials is identified by the presence of specific characteristic bands of [Chol][Ac] [30] (**Figure 5.5**). In particular, the following bands are observed in both morphologies of PVDF and PHBV based composites with IL: the absorption band at 1572 cm^{-1}, attributed to the antisymmetric stretching vibration of the COO^- group present in the acetate anion ([Ac]); the absorption band at 1485 cm^{-1}, associated to the twisting vibration of CH_3 groups in the choline cation ([Chol]); and the absorption band at 1011 cm^{-1}, ascribed to a wagging vibration of the OH group. Furthermore, the following IL-related bands are observed: in the PVDF fibers and films, bands at 962 and 952 cm^{-1}, related to the stretching vibrations of the CH_3 groups; in PVDF and PHBV fibers, an absorption band at 761 cm^{-1} is related to the symmetric stretching vibration of $N(CH_3)$ group [30].

The main absorption bands of the CH_2 and CF_2 groups of PVDF are identified in PVDF+IL fibers and films [31]. For the PVDF fibers and films, the absorption bands characteristic of the α-PVDF phase appear at 762 and 876 cm^{-1}, and the β-phase is identified by the bands appearing at 840 and 1275 cm^{-1}.

No changes occur on the characteristic bands of PHBV upon the IL incorporation into the matrix. From the FTIR spectra of both PHBV films and fibers, characteristic bands are observed in the regions of 826–979 cm^{-1} and 1227–1478 cm^{-1}, related to a C-H stretching vibration, and those at 1057, 1133, and 1183 cm^{-1} associated to a C-O stretching [13].

The amount of electroactive β-phase of PVDF of both fibers and films was evaluated from the FTIR-ATR spectra using **Equation 2.4** (**Figure 5.5-c**). In the case of PVDF fibers processed by electrospinning, it crystallizes mainly in the electroactive β-phase (80 ± 2%), with no significant variation in the β-phase content upon the incorporation of the IL up to 15 wt.% IL content.

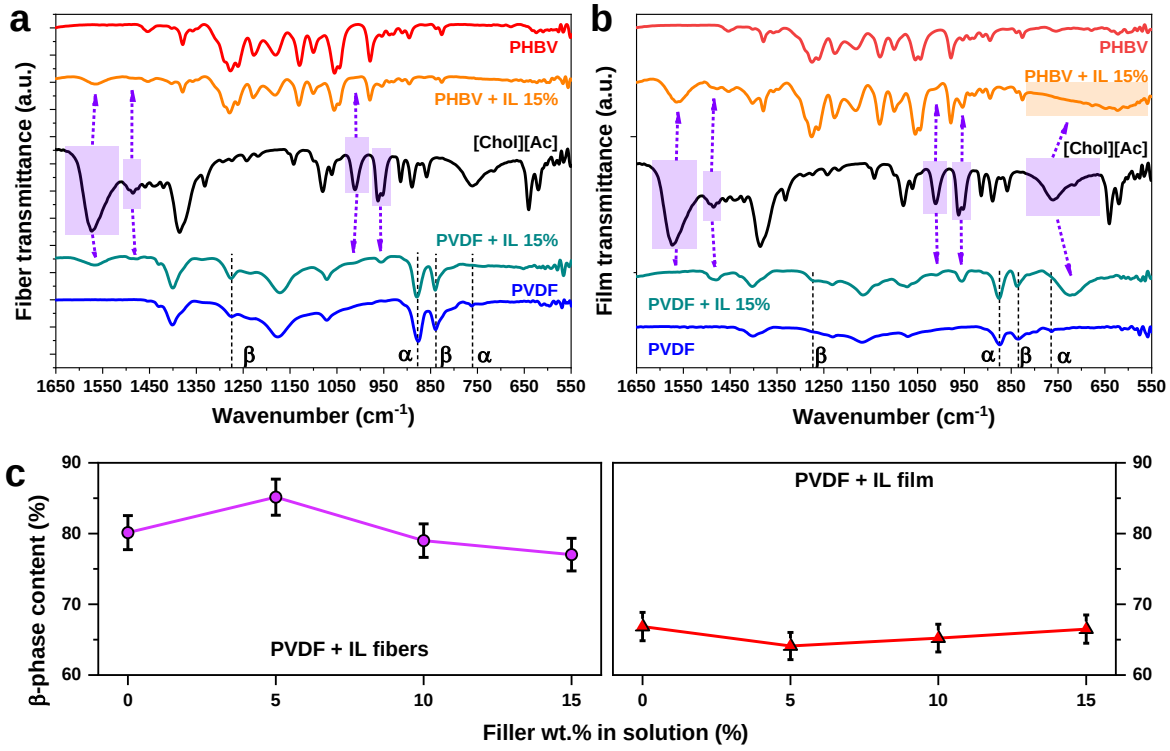

Figure 5.5. FTIR spectra of IL, PVDF and PHBV and their IL based composites comprising 15 wt.% of [Chol][Ac]: a) PVDF and PHBV fibers; b) PVDF and PHBV films. Arrows indicate areas where the influence of the IL was detected. c) Variation of the β-phase content of the PVDF samples as function of IL content.

Regarding the PVDF films, the β-phase content for the pristine films is 67 ± 2%, and again no relevant variations are observed upon IL incorporation. Thus, the processing conditions and in particular the solvent evaporation temperature is the driving factor determining the crystallization process and the polymer phase content [6].

5.3.1.3. Surface wettability

CA measurements show that the addition of the IL to PVDF (**Figure 5.6-a**), in both morphologies, leads to the decrease of the wettability of the fibers from ≈140º (neat PVDF) to 87º (PVDF+IL 15%), and from ≈85º (PVDF neat) to ≈71º (PVDF+IL 15%) for the films, as a result of the hygroscopic nature of ILs, the polymer–IL interactions [40], and the increase in porosity identified in the films with IL filler.

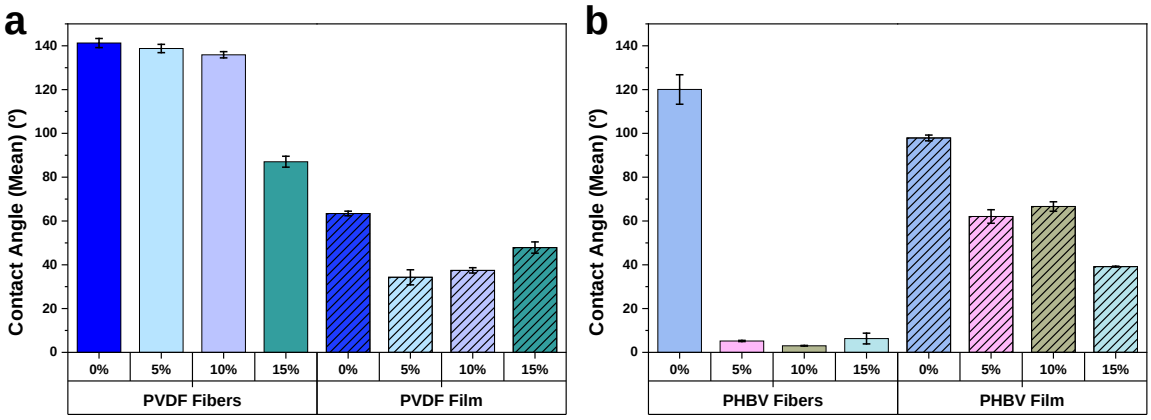

Figure 5.6. Comparison of CA measurements of a) PVDF; b) PHBV samples.

In relation to PHBV electrospun fibers, the contact angle is greatly reduced with the increase of IL content, the PHBV composite fibers absorbing the water droplet: for PHBV+IL 5% fiber mats, the water absorption process begins about 11 s after contact with the droplet, and takes around 1 s for full droplet absorption. For PHBV+IL 10% fiber mats, the process begins about 0.5 s after contact with the droplet, and the droplet is absorbed after around 0.5 s. As for PHBV+IL 15% fibers, the water droplet absorption is completed in 1 s after contact with the droplet. The contact angle decrease is also observed for PHBV+IL films, although less pronounced (**Figure 5.6-b**). **Table 5.3** summarizes the CA results.

Table 5.3. Summary of the CA measurements for polymer samples.

IL wt.% (%)	PVDF+IL Fiber CA (°)	PVDF+IL Film CA (°)	PHBV+IL Fiber CA (°)	PHBV+IL Film CA (°)
0	141.25 ± 2.06	84.97 ± 0.90	120.05 ± 6.73	97.91 ± 1.32
5	138.76 ± 1.86	59.71 ± 2.99	5.20 ± 0.26	62.05 ± 3.10
10	135.89 ± 1.43	62.44 ± 1.05	3.02 ± 0.15	66.61 ± 2.16
15	87.06 ± 2.49	71.47 ± 2.23	6.32 ± 2.46	39.15 ± 0.21

5.3.2. Thermal properties

The DSC thermograms of both PVDF and PHBV electrospun fiber mats and films comprising the maximum amount of IL (15 wt.%) are shown in **Figure 5.7 a-b**.

The IL presents a wide melting peak at ≈76 ºC, as it can be observed in **Figure 5.7**. Independently of the processing conditions and sample morphology, the inclusion of [Chol][Ac] in PVDF does not induce significant changes in the melting temperature (T_m).

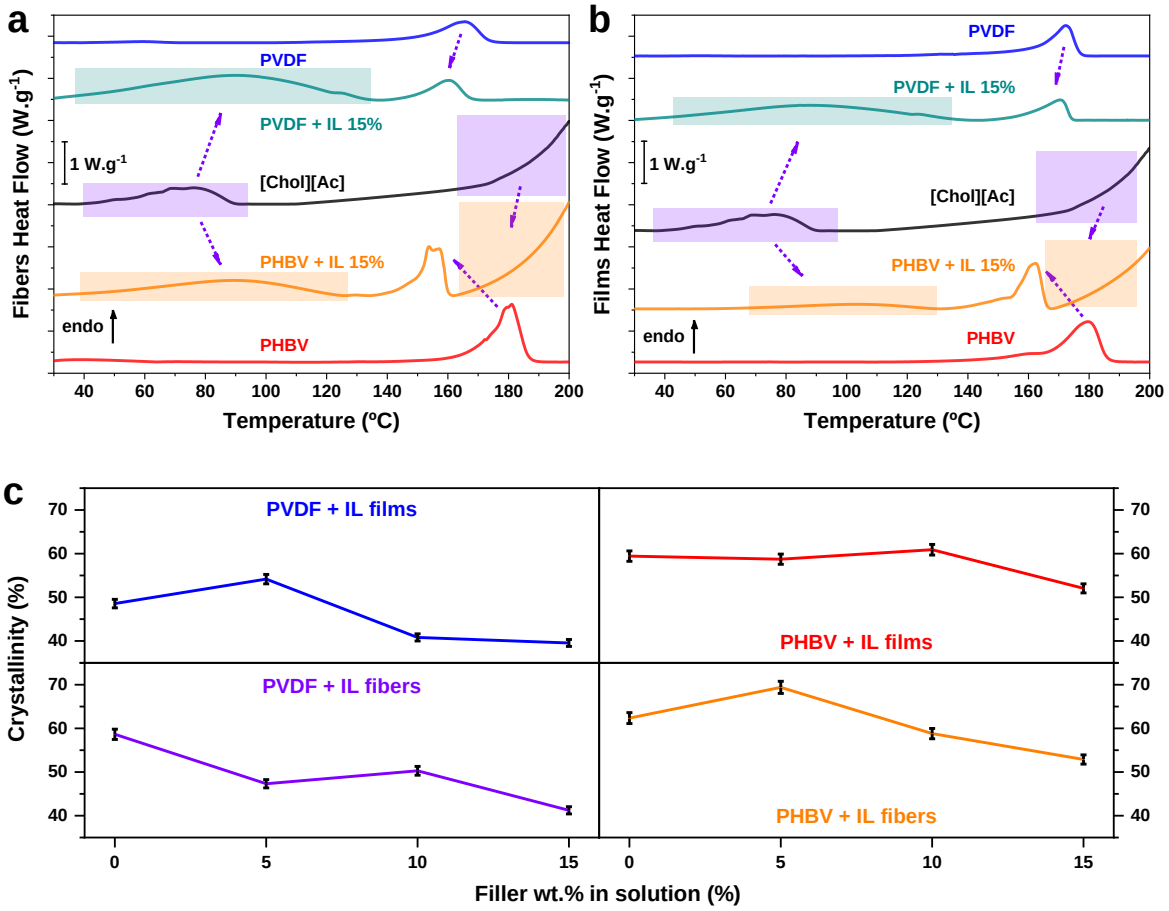

Figure 5.7. Representative DSC thermograms for neat PVDF and PHBV and the corresponding composites with 15 wt.% IL content: a) electrospun fibers; and b) films. Arrows indicate areas where IL influence was detected. c) Variation of the degree of crystallinity of the samples as function of IL content in the different samples.

For neat PVDF, the T_m occurs at ≈166 ºC for the electrospun fibers and at ≈172 ºC for the films, similarly to previously published works [5]. Upon the IL incorporation, a slight decrease down to ≈160 ºC is observed for PVDF+IL 15% fiber mats and to 170 ºC for PVDF+IL 15% films. These results indicate that the incorporation of IL into both matrixes promotes changes in the crystallization process, acting the IL as a nucleating agent, influencing the kinetics of crystallization [29]. Further, the decrease in T_m is also indicative of the formation of PVDF crystals from a liquid phase containing the IL [32].

Both neat PHBV film and electrospun fibers show a T_m of ≈180 ºC in agreement with previous works [13]. Upon the IL incorporation, and regardless of the processing procedure and sample morphology, a decrease to 154 ºC for PHBV+IL 15% fibers and 163 ºC for PHBV+IL 15% films is observed. All these values are summarized in **Table 5.4**.

Independently of the morphology of the sample, all composite samples show an endothermic peak at ≈85 ºC indicative of the melting of the IL.

Table 5.4. T_m for PVDF and PHBV samples. Associated error of ± 2%.

	PVDF+IL				PHBV+IL			
IL wt.% (%)	**0**	**5**	**10**	**15**	**0**	**5**	**10**	**15**
Fiber T_m (ºC)	166	167	163	160	181	159	155	154
Film T_m (ºC)	172	173	171	170	180	163	160	163

The degree of crystallinity of PHBV and PVDF electrospun fibers and films was calculated by applying **Equation 3.1** and **Equation 5.1**, with the results presented in **Figure 5.7-c**.

Neat PVDF fibers present a degree of crystallinity of 59%, which decreases as the IL content increases from 5 (47%) to 15 wt.% (41%), as a result of the IL hindering the formation and growth of PVDF crystals [29]. For PVDF films, presenting a crystallinity of 49%, an increase in crystallinity to 54% is observed for the PVDF+IL 5% sample.

This increase reveals that, for films, the IL acts as a nucleating agent, favoring the formation of small nucleation centers during the crystallization process [11]. However, IL contents higher than 5 wt.% have the opposite effect, with IL hindering the PVDF crystallization process, resulting in a decrease in crystallinity to ≈40% at 15 wt.% of IL.

A 5 wt.% concentration of IL also acts as a nucleating agent for the PHBV fibers, resulting in a crystallinity degree increase from ≈62% to ≈69%. IL concentrations higher than 5 wt.% hinder the PHBV crystallization, promoting a decrease in the degree of crystallinity to 53% for PHBV+IL 15% fibers. As for the PHBV films, their crystallinity remains rather constant at ≈60% for the neat and both 5 and 10 wt.% IL containing samples, decreasing to 52% for the PHBV+IL 15% film.

The thermal stability of the PVDF and PHBV electrospun fibers and films was evaluated by TGA measurements (**Figure 5.8 a-b**).

For both morphologies, neat PVDF presents a single degradation step, at ≈437 ºC for fibers and ≈452 ºC for films (**Figure 5.8 c-d**), corresponding to the C-H and C-F scissions of the PVDF chain, with char being the final thermal degradation product [33]. The IL presents a single degradation step, at ≈196 ºC.

Upon the inclusion of IL into PVDF, additional degradation steps are observed. In all samples and morphologies, solvent evaporation is observed between 35-55 ºC. In the case of PVDF fibers, for the 10 and 15 wt.% IL content, water loss is observed at ≈133 ºC as a result of the hygroscopic nature of [Chol][Ac]. In all samples and morphologies, between ≈190-200 ºC, the thermal degradation of the IL in the samples is observed. Between ≈320-450 ºC begins the degradation of PVDF, by scission of its carbon–hydrogen bonds [34].

Independently of IL content and morphology, a decrease in the thermal stability is observed as revealed by the decrease on the degradation temperatures of PVDF with the IL content increase.

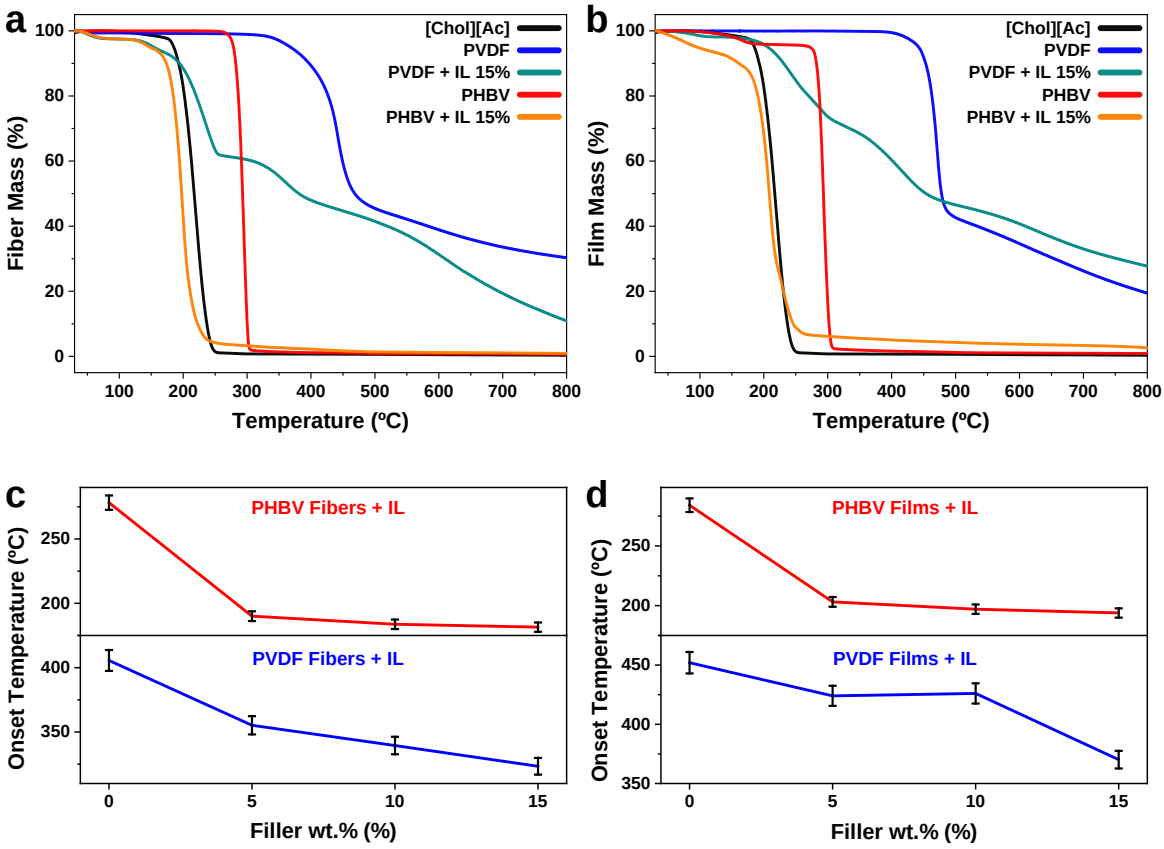

Figure 5.8. Representative TGA thermographs of PHBV and PVDF neat and the corresponding composites: a) fibers and b) films. Variation of the onset temperature, as function of IL filler content for c) fibers and d) films.

Neat PHBV presents a single degradation step, at ≈278 ºC, and two for films, at ≈132 and ≈284 ºC. In the case of the earlier step detected on PHBV films, it is attributed to water loss, while the main step is attributed to a random chain scission process, with CO_2 and H_2O being the final volatile degradation products [35]. Upon the IL incorporation (**Figure 5.8 a-b**), two more degradation steps are observed for fibers, corresponding the first step to evaporation of small quantities of solvent remaining in the fibers, and the second to water loss, as previously described due to the hygroscopic nature of the IL. A third degradation step starting at ≈190 ºC corresponds to PHBV and IL degradation. The PHBV films display only one additional degradation step for both 5 and 10 wt.% samples, attributed to both solvent evaporation and water loss, while the PHBV+IL 15% displays two additional steps, similarly to the fiber samples. These results are summarized in **Table 5.5**.

Table 5.5. Onset temperatures for the different samples. Associated error of ± 2%.

	PVDF				PHBV		
Sample, IL wt.% (%)	**1st onset (ºC)**	**2nd onset (ºC)**	**3rd onset (ºC)**	**4th onset (ºC)**	**1st onset (ºC)**	**2nd onset (ºC)**	**3rd onset (ºC)**
Fiber, 0	437	-	-	-	278	-	-
Fiber, 5	38	193	355	-	40	130	190
Fiber, 10	40	134	207	340	36	130	184
Fiber, 15	39	133	200	323	39	128	181
Film, 0	452	-	-	-	132	284	-
Film, 5	44	189	424	-	113	203	-
Film, 10	44	196	426	-	114	197	-
Film, 15	55	201	370	-	40	144	194

5.3.3. Functional response

5.3.3.1. Ionic conductivity

Figure 5.9-a shows the Nyquist plots of PVDF+IL films and fibers, and PHBV+IL fibers at RT. It should be noticed that the PHBV+IL films show a very brittle behaviour, not suitable for the conductivity measurements. **Figure 5.9-a** shows that the PVDF samples are characterized by a semi-circle, related to the charge transfer processes, while the PHBV sample presents a quarter-circle as well as a linear zone that corresponds to the charge diffusion processes [36].

The variation of the ionic conductivity of the PHBV and PVDF composites with 15 wt.% IL content is shown in **Figure 5.9-b**. Increasing temperature leads to an increase of the electrical conductivity, attributed to the increase of the segmental motion of the polymer chains [37]. The same figure shows that the PHBV sample is the one with the higher electrical conductivity, as shown in **Table 5.6**.

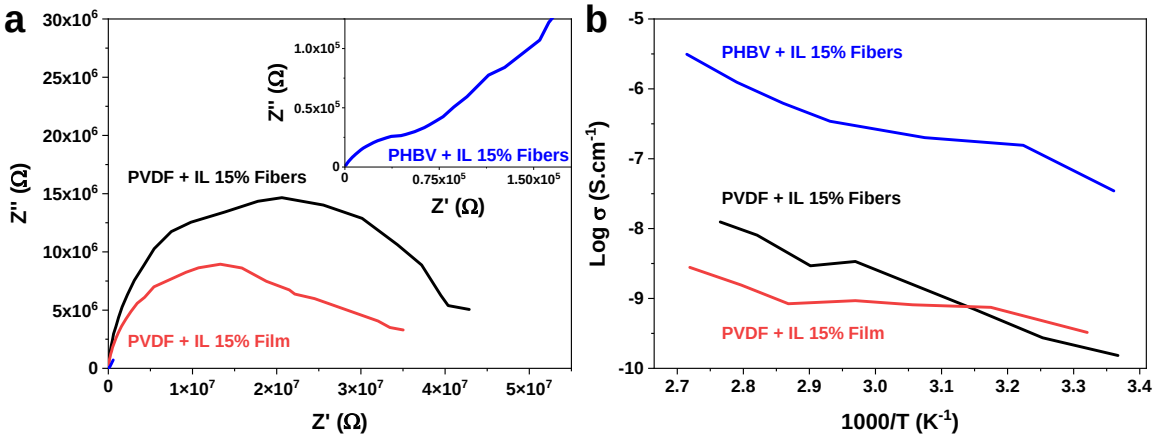

Figure 5.9. a) Nyquist plot at RT for the PVDF and PHBV samples with 15% wt. [Chol][Ac] content (inset: detail of the plot for the PHBV electrospun mats). b) Arrhenius plots for the ionic conductivities of the different samples with 15% of [Chol][Ac].

PVDF+IL 15% fibers present an ionic conductivity of 1.53×10^{-10} S.cm^{-1}, compared to 7×10^{-13} S.cm^{-1} for neat PVDF fibers [26], while the ionic conductivity of PVDF+IL 15% films is 3.27×10^{-10} S.cm^{-1}, compared to 9.7×10^{-13} S.cm^{-1} for the pristine polymer [38]. PHBV+IL 15% fibers show an ionic conductivity of 3.46×10^{-8} S.cm^{-1}, compared to 8.46×10^{-11} S.cm^{-1} for pristine PHBV [39]. Overall, the IL improved the conductivity of the samples in about 3 orders of magnitude (**Table 5.6**), due to the increase in the number of mobile charged species provided by the incorporation of the IL.

Table 5.6. Ionic conductivity values (σ_i) and the corresponding apparent activation energy (E_a) at RT for the different composites. Associated error of ± 3%.

Sample	σ_i / mS.cm^{-1}	E_a / kJ.mol^{-1}
PVDF+IL 15% Fibers	1.53×10^{-10}	26.52
PVDF+IL 15% Films	3.27×10^{-10}	10.28
PHBV+IL 15% Fibers	3.46×10^{-8}	21.81

5.3.3.2. Cytotoxicity assay

Regarding the cytotoxicity of the samples, PHBV presents no cytotoxicity behavior [14], as well as PVDF [41] and [Chol][Ac] [22], all being biocompatible. However, as interactions between the polymeric matrix and the IL can modify this behavior, the cytotoxicity of the hybrid materials was evaluated. The viability of C2C12 myoblasts for the different samples is presented in **Figure 5.10**.

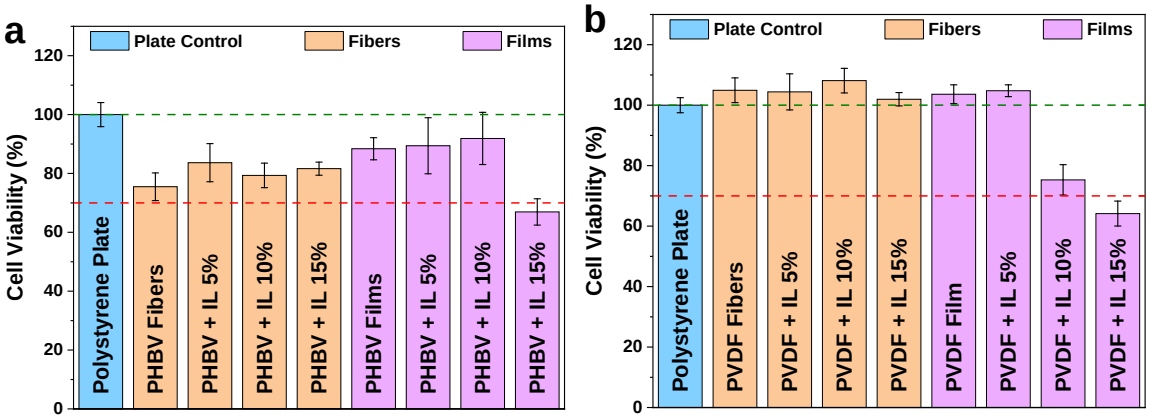

Figure 5.10. Viability assay of C2C12 myoblast cells in contact with extraction media exposed to the different processed samples for 72 h: a) PHBV samples; and b) PVDF samples. (Relative cell activity presented as percentage of the negative control with n = 4 ± Standard Deviation).

According to the ISO standard 10993-5, the samples are considered cytotoxic when cells suffer a viability reduction larger than 30%. Relatively to the PHBV samples, cell viability values higher than 70% are observed for all the samples with the exception of the PHBV+IL 15% films. The same situation has been verified for the PVDF, confirming the cytocompatibility of most prepared samples.

Thus, the introduction of [Chol][Ac] has to be below 15 wt.% in order to use film samples as active scaffolds for tissue engineering applications.

5.4. Conclusions

PVDF and PHBV with different [Chol][Ac] IL contents (0, 5, 10 and 15 wt.%) were processed into electrospun fibers and films, to support advanced muscle tissue repair and regeneration strategies.

The morphology, physico-chemical and thermal properties of the samples were evaluated. It was verified that the IL was homogeneously distributed in all samples. Increasing IL wt.% results in a smaller electrospun PHBV fiber diameter, from 1.73 ± 0.21 μm for neat PHBV to 0.18 ± 0.05 μm for PHBV+IL 10%, while PVDF fiber diameter increases from 0.98 ± 0.19 μm for neat PVDF to 1.31 ± 0.25 μm for PVDF+IL 15%.

Introducing [Chol][Ac] results in porous films with a rougher surface, from 41.63 (neat PHBV) to 85.5 nm (PHBV+IL 15%), and from 87.3 (neat PVDF) to 108.4 nm (PVDF+IL 15%).

The degree of crystallinity of PVDF is slightly affected by the inclusion of the IL and the electroactive β-phase content of the polymer is basically not affected by the inclusion of the IL, being determined by the processing conditions, with the fiber mats showing a β-phase content of ≈80%, and the films ≈65%. Further, the introduction of the IL leads to an overall decrease of the thermal stability of the samples, independently of the polymer and processing conditions.

With respect to the electrical conductivity, σ_i had a value of 1.53×10^{-10} S.cm^{-1} for PVDF+IL 15%, and of 3.46×10^{-8} S.cm^{-1} for PHBV+IL 15%. As for films, σ_i was of 3.27×10^{-10} S.cm^{-1} for PVDF+IL 15%.

Finally, adding the IL resulted in an increase of the wettability of the materials, with the case of the PHBV becoming absorbent.

Both composites in either morphology are compatible with C2C12 myoblasts up to a 10 wt.% [Chol][Ac] concentration, showing their suitability for biomedical applications. These materials show high potential to be used for *in vitro* biomedical applications, with the composite PHBV scaffolds also showing their potential for *in vivo* applications that require biodegradable scaffolds.

5.5. References

1. Greising, S.M., B.T. Corona, C. McGann, J.K. Frankum, and G.L. Warren, *Therapeutic Approaches for Volumetric Muscle Loss Injury: A Systematic Review and Meta-Analysis.* Tissue Eng Part B Rev, 2019. **25**(6): p. 510-525. DOI: 10.1089/ten.TEB.2019.0207

2. Langer, R. and J.P. Vacanti, *Tissue Engineering.* Science, 1993. **260**(5110): p. 920-926. DOI: 10.1126/science.8493529

3. Ribeiro, S., A.C. Gomes, I. Etxebarria, S. Lanceros-Méndez, and C. Ribeiro, *Electroactive biomaterial surface engineering effects on muscle cells differentiation.* Materials Science and Engineering: C, 2018. **92**: p. 868-874. DOI: 10.1016/j.msec.2018.07.044

4. Jana, S., S.K.L. Levengood, and M. Zhang, *Anisotropic Materials for Skeletal-Muscle-Tissue Engineering.* Advanced materials (Deerfield Beach, Fla.), 2016. **28**(48): p. 10588-10612. DOI: 10.1002/adma.201600240

5. Ribeiro, S., T. Ribeiro, C. Ribeiro, D.M. Correia, J.P.S. Farinha, A.C. Gomes, C. Baleizão, and S. Lanceros-Méndez, *Multifunctional Platform Based on Electroactive Polymers and Silica Nanoparticles for Tissue Engineering Applications.* Nanomaterials (Basel, Switzerland), 2018. **8**(11): p. 933. DOI: 10.3390/nano8110933

6. Ribeiro, C., C.M. Costa, D.M. Correia, J. Nunes-Pereira, J. Oliveira, P. Martins, R. Gonçalves, V.F. Cardoso, and S. Lanceros-Méndez, *Electroactive poly(vinylidene fluoride)-based structures for advanced applications.* Nature Protocols, 2018. **13**(4): p. 681-704. DOI: 10.1038/nprot.2017.157

7. Hermenegildo, B., C. Ribeiro, L. Pérez-Álvarez, J.L. Vilas, D.A. Learmonth, R.A. Sousa, P. Martins, and S. Lanceros-Méndez, *Hydrogel-based magnetoelectric microenvironments for tissue stimulation.* Colloids and Surfaces B: Biointerfaces, 2019. **181**: p. 1041-1047. DOI: 10.1016/j.colsurfb.2019.06.023

8. Hitscherich, P., A. Aphale, R. Gordan, R. Whitaker, P. Singh, L.-h. Xie, P. Patra, and E.J. Lee, *Electroactive graphene composite scaffolds for cardiac tissue engineering.* Journal of Biomedical Materials Research Part A, 2018. **106**(11): p. 2923-2933. DOI: 10.1002/jbm.a.36481

9. Ribeiro, S., C. Ribeiro, E.O. Carvalho, C.R. Tubio, N. Castro, N. Pereira, V. Correia, A.C. Gomes, and S. Lanceros-Méndez, *Magnetically Activated Electroactive Microenvironments for Skeletal Muscle Tissue Regeneration.* ACS Applied Bio Materials, 2020. **3**(7): p. 4239-4252. DOI: 10.1021/acsabm.0c00315

10. Ribeiro, S., C. Puckert, C. Ribeiro, A.C. Gomes, M.J. Higgins, and S. Lanceros-Méndez, *Surface Charge-Mediated Cell–Surface Interaction on Piezoelectric Materials.* ACS Applied Materials & Interfaces, 2019. **12**(1): p. 191-199. DOI: 10.1021/acsami.9b17222

11. Meira, R.M., D.M. Correia, S. Ribeiro, P. Costa, A.C. Gomes, F.M. Gama, S. Lanceros-Méndez, and C. Ribeiro, *Ionic-Liquid-Based Electroactive Polymer Composites for Muscle Tissue Engineering.* ACS Applied Polymer Materials, 2019. **1**(10): p. 2649-2658. DOI: 10.1021/acsapm.9b00566

12. Kapat, K., Q.T.H. Shubhra, M. Zhou, and S. Leeuwenburgh, *Piezoelectric Nano-Biomaterials for Biomedicine and Tissue Regeneration.* Advanced Functional Materials, 2020. **30**(44): p. 1909045. DOI: 10.1002/adfm.201909045

13. Amaro, L., D.M. Correia, T. Marques-Almeida, P.M. Martins, L. Pérez, J.L. Vilas, G. Botelho, S. Lanceros-Mendez, and C. Ribeiro, *Tailored Biodegradable and Electroactive Poly(Hydroxybutyrate-Co-Hydroxyvalerate) Based Morphologies for Tissue Engineering Applications.* International journal of molecular sciences, 2018. **19**(8): p. 2149. DOI: 10.3390/ijms19082149

14. Rivera-Briso, A.L. and Á. Serrano-Aroca, *Poly(3-Hydroxybutyrate-co-3-Hydroxyvalerate): Enhancement Strategies for Advanced Applications.* Polymers, 2018. **10**(7): p. 732. DOI: 10.3390/polym10070732

15. Gouvêa, R.F. and C.T. Andrade, *Testing the effect of imidazolium ionic liquid and citrate derivative on the properties of graphene-based PHBV/EVA immiscible blend.* Polymer Testing, 2020. **89**: p. 106615. DOI: 10.1016/j.polymertesting.2020.106615

16. Pramanik, N., S. Bhattacharya, T. Rath, J. De, A. Adhikary, R.K. Basu, and P.P. Kundu, *Polyhydroxybutyrate-co-hydroxyvalerate copolymer modified graphite oxide based 3D scaffold for tissue engineering application.* Materials Science and Engineering: C, 2019. **94**: p. 534-546. DOI: 10.1016/j.msec.2018.10.009

17. Correia, D.M., L.C. Fernandes, M.M. Fernandes, B. Hermenegildo, R.M. Meira, C. Ribeiro, S. Ribeiro, J. Reguera, and S. Lanceros-Méndez, *Ionic Liquid-Based Materials for Biomedical Applications.* Nanomaterials (Basel, Switzerland), 2021. **11**(9): p. 2401. DOI: 10.3390/nano11092401

18. Correia, D.M., L.C. Fernandes, P.M. Martins, C. García-Astrain, C.M. Costa, J. Reguera, and S. Lanceros-Méndez, *Ionic Liquid-Polymer Composites: A New Platform for Multifunctional Applications.* Advanced Functional Materials, 2020: p. 1909736. DOI: 10.1002/adfm.201909736

19. Dias, J.C., D.C. Correia, A.C. Lopes, S. Ribeiro, C. Ribeiro, V. Sencadas, G. Botelho, J.M.S.S. Esperança, J.M. Laza, J.L. Vilas, L.M. León, and S. Lanceros-Méndez, *Development of poly(vinylidene fluoride)/ionic liquid electrospun fibers for tissue engineering applications.* Journal of Materials Science, 2016. **51**(9): p. 4442-4450. DOI: 10.1007/s10853-016-9756-3

20. Kim, M.H., S. An, K. Won, H.J. Kim, and S.H. Lee, *Entrapment of enzymes into cellulose–biopolymer composite hydrogel beads using biocompatible ionic liquid.* Journal of Molecular Catalysis B: Enzymatic, 2012. **75**: p. 68-72. DOI: 10.1016/j.molcatb.2011.11.011

21. Elhi, F., H. Priks, P. Rinne, N. Kaldalu, E. Žusinaite, U. Johanson, A. Aabloo, T. Tamm, and K. Põhako-Esko, *Electromechanically active polymer actuators based on biofriendly choline ionic liquids.* Smart Materials and Structures, 2020. **29**(5): p. 055021. DOI: 10.1088/1361-665x/ab7f24

22. Gomes, J.M., S.S. Silva, and R.L. Reis, *Exploring the Use of Choline Acetate on the Sustainable Development of α-Chitin-Based Sponges.* ACS Sustainable Chemistry & Engineering, 2020. **8**(35): p. 13507-13516. DOI: 10.1021/acssuschemeng.0c05076

23. Sakthivel, M., S.P. Batchu, A.A. Shah, K. Kim, W. Peters, and J.-F. Drillet, *An Electrically Rechargeable Zinc/Air Cell with an Aqueous Choline Acetate Electrolyte.* Materials (Basel, Switzerland), 2020. **13**(13): p. 2975. DOI: 10.3390/ma13132975

24. Maciel, M.M., S. Ribeiro, C. Ribeiro, A. Francesko, A. Maceiras, J.L. Vilas, and S. Lanceros-Méndez, *Relation between fiber orientation and mechanical properties of nano-engineered poly(vinylidene fluoride) electrospun composite fiber mats.* Composites Part B: Engineering, 2018. **139**: p. 146-154. DOI: 10.1016/j.compositesb.2017.11.065

25. Ciuzas, D., E. Krugly, S. Sriubaite, I. Pauliukaityte, O. Baniukaitiene, M. Bulota, and D. Martuzevicius, *Electrospun cellulose fibers from ionic liquid: Practical implications toward robust morphology.* Journal of Applied Polymer Science, 2021. **139**(3): p. 51525. DOI: 10.1002/app.51525

26. Barbosa, J.C., D.M. Correia, R. Gonçalves, V. de Zea Bermudez, M.M. Silva, S. Lanceros-Mendez, and C.M. Costa, *Enhanced ionic conductivity in poly(vinylidene fluoride) electrospun separator membranes blended with different ionic liquids for lithium ion batteries.* Journal of Colloid and Interface Science, 2021. **582**: p. 376-386. DOI: 10.1016/j.jcis.2020.08.046

27. Seo, J.M., G.K. Arumugam, S. Khan, and P.A. Heiden, *Comparison of the Effects of an Ionic Liquid and Triethylbenzylammonium Chloride on the Properties of Electrospun Fibers, 1 - Poly(lactic acid).* Macromolecular Materials and Engineering, 2009. **294**(1): p. 35-44. DOI: 10.1002/mame.200800198

28. Thakur, A., S. Dam, D. Nath, N.V. Chandra Shekar, G. Amarendra, and S. Hussain, *Enhancement of electroactive phases in free-standing, flexible thin films of PVDF with addition of p-block chlorides.* Polymer, 2020. **186**: p. 122074. DOI: 10.1016/j.polymer.2019.122074

29. Fernandes, L.C., D.M. Correia, C. García-Astrain, N. Pereira, M. Tariq, J.M.S.S. Esperança, and S. Lanceros-Méndez, *Ionic-Liquid-Based Printable Materials for Thermochromic and Thermoresistive Applications.* ACS Applied Materials & Interfaces, 2019. **11**(22): p. 20316-20324. DOI: 10.1021/acsami.9b00645

30. de Souza, Í.F.T., V.H. Paschoal, K. Bernardino, T.A. Lima, L.L. Daemen, Y. Z, and M.C.C. Ribeiro, *Vibrational spectroscopy and molecular dynamics simulation of choline oxyanions salts.* Journal of Molecular Liquids, 2021. **340**: p. 117100. DOI: 10.1016/j.molliq.2021.117100

31. Cai, X., T. Lei, D. Sun, and L. Lin, *A critical analysis of the α, β and γ phases in poly(vinylidene fluoride) using FTIR.* RSC Advances, 2017. **7**(25): p. 15382-15389. DOI: 10.1039/c7ra01267e

32. Correia, D.M., C.M. Costa, J.C. Rodríguez-Hernández, I. Tort Ausina, L.T. Biosca, C. Torregrosa Cabanilles, J.M. Meseguer-Dueñas, S. Lanceros-Méndez, and J.L. Gomez Ribelles, *Effect of Ionic Liquid Content on the Crystallization Kinetics and Morphology of Semicrystalline Poly(vinylidene Fluoride)/Ionic Liquid Blends.* Crystal Growth & Design, 2020. **20**(8): p. 4967-4979. DOI: 10.1021/acs.cgd.0c00042

33. Li, W., H. Li, and Y.-M. Zhang, *Preparation and investigation of PVDF/PMMA/TiO2 composite film.* Journal of Materials Science, 2009. **44**(11): p. 2977-2984. DOI: 10.1007/s10853-009-3395-x

34. de Jesus Silva, A.J., M.M. Contreras, C.R. Nascimento, and M.F. da Costa, *Kinetics of thermal degradation and lifetime study of poly(vinylidene fluoride) (PVDF) subjected to bioethanol fuel accelerated aging.* Heliyon, 2020. **6**(7): p. e04573-e04573. DOI: 10.1016/j.heliyon.2020.e04573

35. Antunes, A., A. Popelka, O. Aljarod, M.K. Hassan, P. Kasak, and A.S. Luyt, *Accelerated Weathering Effects on Poly(3-hydroxybutyrate-co-3-hydroxyvalerate) (PHBV) and PHBV/TiO(2) Nanocomposites.* Polymers, 2020. **12**(8): p. 1743. DOI: 10.3390/polym12081743

36. Laschuk, N.O., E.B. Easton, and O.V. Zenkina, *Reducing the resistance for the use of electrochemical impedance spectroscopy analysis in materials chemistry.* RSC Advances, 2021. **11**(45): p. 27925-27936. Available from.

37. Leones, R., C. Costa, A. Machado, J. Esperança, M.M. Silva, and S. Lanceros-Méndez, *Effect of Ionic Liquid Anion Type in the Performance of Solid Polymer Electrolytes Based on Poly (Vinylidene fluoride-trifluoroethylene).* Electroanalysis, 2015. **27**(2): p. 457-464. Available from.

38. Costa, C.M., J. Nunes-Pereira, L.C. Rodrigues, M.M. Silva, J.L.G. Ribelles, and S. Lanceros-Méndez, *Novel poly(vinylidene fluoride-trifluoroethylene)/poly(ethylene oxide) blends for battery separators in lithium-ion applications.* Electrochimica Acta, 2013. **88**: p. 473-476. DOI: 10.1016/j.electacta.2012.10.098

39. Barbosa, J.C., D.M. Correia, A. Fidalgo-Marijuan, R. Gonçalves, M. Fernandes, V. de Zea Bermudez, M.M. Silva, S. Lanceros-Mendez, and C.M. Costa, *Sustainable Lithium-Ion Battery Separators Based on Poly(3-Hydroxybutyrate-Co-Hydroxyvalerate) Pristine and Composite Electrospun Membranes.* Energy Technology, 2021: p. 2100761. DOI: 10.1002/ente.202100761

40. Serra, J.P., R.S. Pinto, J.C. Barbosa, D.M. Correia, R. Gonçalves, M.M. Silva, S. Lanceros-Mendez, and C.M. Costa, *Ionic liquid based Fluoropolymer solid electrolytes for Lithium-ion batteries.* Sustainable Materials and Technologies, 2020. **25**: p. e00176. DOI: 10.1016/j.susmat.2020.e00176

41. Martins, P.M., S. Ribeiro, C. Ribeiro, V. Sencadas, A.C. Gomes, F.M. Gama, and S. Lanceros-Méndez, *Effect of poling state and morphology of piezoelectric poly(vinylidene fluoride) membranes for skeletal muscle tissue engineering.* RSC Advances, 2013. **3**(39): p. 17938-17944. DOI: 10.1039/c3ra43499k

Chapter 6

Advanced biodegradable microenvironments for tissue regeneration applications

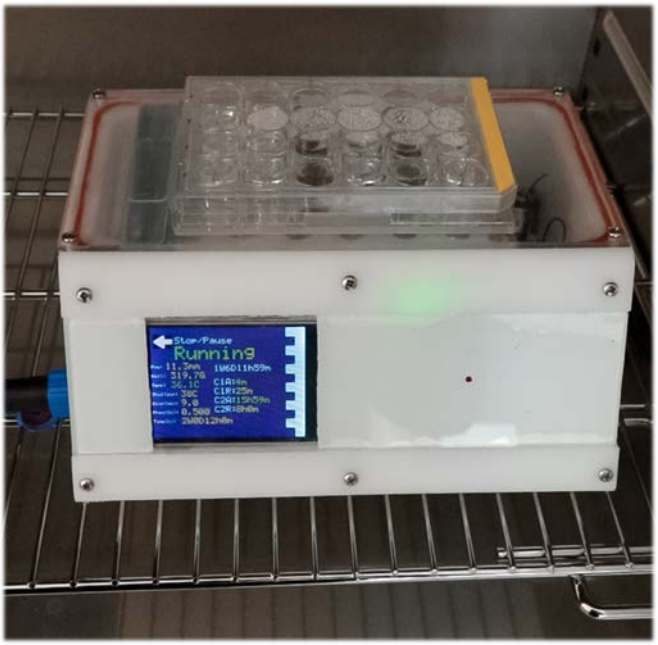

Polymer samples degrading in a bioreactor.

The ultimate goal of tissue engineering is for its materials, techniques and strategies to be applied directly in the body. In order to achieve this, it requires smart materials capable of being used *in vivo* with no ill consequences for the host, and that degrade harmlessly once their purpose is fulfilled. And it requires these materials to have similar capabilities to others currently in use.

This chapter details de development of novel PGLA based electroactive and magnetoactive scaffolds, with a short-term biodegradation, for *in vivo* use in tissue regeneration applications.

6.1. Introduction

Tissue engineering (TE) is a therapeutic approach dealing with tissue damage or degeneration, that aims to grow new tissue from autologous samples, in either *in-vitro* or *in-vivo* conditions, bypassing the need for donors or waiting lists [1]. However, it requires materials with specific tailored properties, in order to achieve a level of biomimetism that allows the development of healthy and functional tissue.

Volumetric muscle loss, due to disease or serious trauma, is a particularly serious case of tissue damage due to the complexity and low regenerability of muscle tissue. Consequently, many therapies result in less-than-desirable results [2]. TE is a potential solution to this problem, but the nature and specific needs of the skeletal muscle fibers result in that no suitable TE solutions have yet been developed. A suitable solution should be able to provide the cells with both passive stimuli, such as mechanotransduction, by means of materials with specific stiffness and/or scaffolds comprised of oriented fibers [3, 4], and active stimuli, such as dynamic electrical and mechanical, mimicking the natural growth conditions of muscle tissue [5]. Additionally, all of the materials involved should be biocompatible and, ideally, biodegradable, allowing the stimuli to be applied in a controllable manner through the regeneration process.

Smart materials, defined as materials that react and change one or more of their physical-chemical properties in response to specific stimuli, such as mechanical, chemical, electrical, or magnetic [6], have the potential to address these challenges. In particular, polymer based smart materials can be processed into different morphologies, including films, fibers, and microspheres [7], and have been studied for TE applications in bone [8], cardiac [9], and skeletal muscle tissues, where it has been verified that active oriented polymer fiber scaffolds promote cell development and tissue regeneration [3, 4]. One particular process, electrospinning, allows a fine control of micro- and nanofiber properties, so that they can be tuned to the specific needs of target tissues and microenvironments, improving cell and tissue regeneration [4].

Some of the most common biodegradable polymers used in TE strategies are poly(α-hydroxy esters), such as poly(lactic acid) (PLA), poly(glycolic acid) (PGA), and the various poly(lactic-co-glycolide) (PLGA) copolymers [10].

Approved for medical use by both the US Food and Drug Administration (FDA) and the European Medicines Agency (EMA) [11], PLGA is often preferred instead of its homopolymers due to superior control of its degradability, allowing for application-specific fine tuning. This polymer is both biocompatible and biodegradable, with its degradation occurring by a hydrolytic bulk degradation process, via random scission mechanism, and its byproducts being lactic acid and glycolic acid, which are removed from living organisms via the renal system [12]. PLGA has been processed in a variety of morphologies, such as micro and nanoparticles (NP), 3D scaffolds and fibers [12], with biomedical applications in drug delivery, diagnostics and TE [13].

In order to tune physical-chemical properties of the polymers or to induce specific responses, such as magnetic or electrical conductivity, polymer composites are being developed for biomedical applications [13-15]. Among the most used fillers are magnetic ones, explored in areas such as hyperthermia, magnetomechanical [16], and magnetoelectric effects [8], among others, and conductive fillers, explored in the area of electroactive stimuli [9].

Regarding magnetic fillers for polymer composites, iron (II, III) oxide (Fe_3O_4) is a biocompatible material that has been studied for a variety of applications, from sensors and actuators to biomedicine and environmental remediation [16, 17]. Fe_3O_4 NPs present superparamagnetic behavior at sizes under 20 nm and is ferrimagnetic between 20 and 300 nm [18], making it interesting for magnetically controlling the application of stimuli in polymer-based scaffolds.

Ionic liquids (IL), defined as salts with a melting temperature below 100 ºC, high electrochemical and thermal stability, and a variety of properties determined by their specific anions and cations, are an interesting class of materials for applications in actuators, biosensors and batteries [19], and the biocompatibility and biodegradability of many IL is a valuable for TE applications [20]. Due to its good ionic conductivity (3.98 $mS.cm^{-1}$), choline bis(trifluoromethylsulfonyl)imide ([Chol][TFSI]) has been studied for electrolyte [21], biocatalysis and microbial fuel cells [22] applications. Its choline cation (Chol) is both biodegradable and biocompatible, as it is a molecule that supports various biological functions [23]. However, [Chol][TFSI] may present some toxicity in large concentrations, due to the effects of the bis(trifluoromethylsulfonyl)imide anion (TFSI) [24].

Although PLGA is a biodegradable and biocompatible material, it is neither conductive nor can it be actuated to provide mechanical stimuli to tissues. By introducing fillers, such as the conductive [Chol][TFSI] IL or Fe_3O_4 NPs, the present work proposes to bridge this gap in the properties of PLGA, improving its suitability for TE applications. The morphology, physico-chemical, thermal and conductive properties of PLGA microfibers and films, and the effect of IL and NP content on those properties is evaluated.

6.2. Experimental

6.2.1. Materials

PLGA 50:50 (reference Resomer 504H), was acquired from Sigma-Aldrich. Fe_3O_4 nanopowder (99%, 30 nm), was purchased from Nanostructured & Amorphous Materials. [Chol][TFSI] (99%) IL was acquired from Iolitec. Chloroform (Chromasolv 99.8%) (CF), was purchased from Honeywell, and N,N-dimethylformamide (DMF, 99.5%) from Merck. Tetrahydrofuran (reference TE02282500) (THF) was purchased from Scharlab.

6.2.2. Sample Processing

6.2.2.1. Pristine and composite films

The films were processed with a method similar to that described by Lu *et al.* [25]. For neat PLGA films, PLGA was dissolved in CF with a concentration of 15 weight percentage (wt.%), and the solution was kept under agitation with a magnetic stirrer for 2 h.

For the PLGA+IL solutions with different IL contents (5, 10 and 15 wt.%), in a first step the IL [Chol][TFSI] was added to CF and mixed under magnetic stirring for 30 min. PLGA (15 wt.%) was then added to the solution under agitation until complete dissolution. For the preparation of films with magnetic NPs, Fe_3O_4 NPs (5, 10 and 15 wt.%) were first dispersed in CF in an ultrasound bath for 4 h to ensure good dispersion and prevent NP agglomeration. PLGA (15 wt.%) was then added to the solution and mechanically stirred until complete dissolution.

After solution preparation, the polymer solutions were poured onto a glass substrate and spread with a film applicator for a 1000 μm thickness, and the solvent allowed to evaporate at room temperature (RT) for 24 h. Afterwards, the films on glass were submerged in distilled water for 2 h, and then carefully lifted from the substrate, before being dried at RT for 48 hours. Samples with an average thickness of ~100 μm were obtained by this procedure.

6.2.2.2. Pristine and composite electrospun fibers

Electrospun PLGA, PLGA+Fe_3O_4 and PLGA+IL fibers were obtained following two distinct procedures. In order to optimize the process, two co-solvent systems were used: a ratio of 60:40 CF/DMF (PLGA1), and 50:50 DMF/THF (PLGA2) for the IL and magnetic composites, respectively. Neat PLGA fibers were produced in both co-solvent systems, with PLGA (30 wt.%) added to each co-solvent system, and the solutions kept under magnetic agitation for 2h.

For the PLGA1+IL solutions (5, 10 and 15 wt.%), [Chol][TFSI] was added to 60:40 CF/DMF and kept under magnetic agitation for 30 minutes. Then, PLGA (30 wt.%) was added to the solution under agitation until complete dissolution of the polymer. For PLGA2+Fe_3O_4 (5, 10 and 15 wt.%), NPs were dispersed in a 50:50 DMF/THF solution in an ultrasound bath for 4 h to ensure good dispersion and prevent NP agglomeration. Then, PLGA (30 wt.%) was slowly added, and the solution was mechanically stirred until complete dissolution of the polymer.

The prepared solutions were placed in 10 mL plastic syringes fitted with a steel needle with 0.41 mm inner diameter. The electrospinning process was conducted by applying high voltage with a Matsusada AU-30P1-L power supply. A syringe pump (Syringepump NE-300) fed a constant flow of polymer solution into the needle tip. The electrospun fibers were collected on a grounded drum with 80 mm diameter and rotating at 1500 rpm. The specific conditions for each polymer solution and concentration are detailed in **Table 6.1**. The temperature was kept between 20-25 ºC, and relative ambient humidity between 40 and 50%. Samples of the fibers were then detached for characterization. Samples with an average thickness of~50 μm were obtained.

Table 6.1. Electrospin conditions for the prepared fibers.

	Flow Rate (mL/h)	Applied voltage (kV)	Collector Distance (cm)
PLGA1	0.5	15.1	8
PLGA1+5% IL	0.3	15.8	8
PLGA1+10% IL	0.3	15.8	8
PLGA1+15% IL	0.3	15.8	8
PLGA2	0.4	10	15
PLGA2+5% Fe_3O_4	0.4	12	15
PLGA2+10% Fe_3O_4	0.3	15	15
PLGA2+15% Fe_3O_4	0.3	16	15

The solutions to be electrospun were initially prepared with the 60:40 mixture of CF and DMF, under the conditions previously detailed. While it was possible to properly electrospin PLGA1+IL fibers with this binary-solvent system, the same did not occur for a PLGA1+Fe_3O_4 solution (**Figure 6.1**).

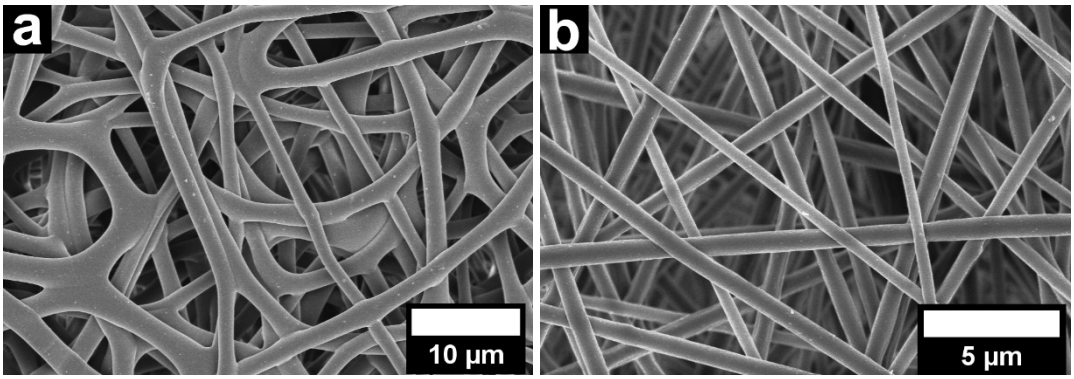

Figure 6.1. Effect of the solvent on the electrospinnability of PLGA. a) PLGA with 5 wt.% Fe_3O_4, in CF-DMF binary-solvent; b) PLGA with 5 wt.% Fe_3O_4, in DMF-THF binary-solvent. Note the scale and the absence of merged fibers in b).

The problems identified during the electrospinning process, including dripping solution from the needle tip, formation of fibers only at short distances and high voltages, allowed to conclude that this binary solvent does not present enough conductivity for a stable process at these conditions, an issue not present when adding a conductive IL. Thus, a different binary solvent, a 50:50 mixture of DMF and THF [26], was used for the PLGA2+Fe_3O_4 solution, given the higher conductivity of THF, while other properties remain similar to CF (**Table 6.2**) [27].

Table 6.2. Properties of the solvents used in this study (η is the viscosity, ε is the dielectric constant, σ the conductivity and δ is the solubility parameter [27]

Solvent	Boiling point (°C)	η (mPa.s)	σ (μS.cm^{-1})	ε	δ (cal$^{1/2}$.cm$^{3/2}$)
DMF	153	0.920	6.0E-2	36.70	12.1
CF	61	0.563	1.0E-4	4.80	9.3
THF	66	0.480	4.5E1	7.60	9.1

6.2.3. Sample characterization

Scanning Electron Microscopy (SEM) was used to assess the morphology of the samples, using a Hitachi S-4800 field emission SEM at an accelerating voltage of 5 kV. The PLGA1+IL fiber mats were coated with a 15 nm thick layer of gold using a Quorum Emitech K550 Sputter Coater with the Film Thickness Monitor option, at 25 mA and a pressure of 0.09 mbar. Regarding the PLGA2+Fe_3O_4 fiber mats, they were left uncoated. For each sample, microfiber diameter and distribution were calculated by measuring 120 fibers, at magnifications of x1.5 kX, 5.0 kX and 20 kX, using the ImageJ software. PLGA films were frozen in liquid nitrogen and cut, so the cross-section of the film could be analyzed.

Detailed surface characterization of the films was performed by a CSI Nano-Observer Atomic Force Microscopy (AFM) microscope, with AppNano ANSCM-PT tips, and MAGT tips for magnetic force microscopy (MFM). Obtained data was then analyzed with the Gwyddion software. Further characterization was performed with a Carl Zeiss EVO-40 Scanning Electron Microscope equipped with an Oxford Instruments X-Max Microanalysis EDS-Detector, at an accelerating voltage of 20 kV and x2.5 kX magnification.

Fourier Transform Infrared Spectroscopy (FTIR) analysis was conducted at RT with a JASCO FT/IR-6100 in ATR mode, using 64 scans between 4000 and 500 cm^{-1} with a resolution of 4 cm^{-1}.

The thermal behavior of the samples was evaluated by Thermogravimetric Analysis (TGA) and by Differential Scanning Calorimetry (DSC). For TGA, a PerkinElmer TGA 4000 was used. The samples were heated from 25 to 800 ºC at a rate of 10 $ºC.min^{-1}$ and under a nitrogen flow rate of 20 $mL.min^{-1}$. The DSC analysis was performed with a Mettler Toledo DSC822e, equipped with a sample robot, at a heating rate of 10 $°C.min^{-1}$ under nitrogen flow of 50 $mL.min^{-1}$. STAR software was used to analyze the data.

The contact angle (CA) of the samples was measured using a Data-Physics Contact Angle System OCA 15EC and the SCA20 software, by separately depositing five 3 µL of ultrapure water drops on the surface of the membranes, and averaging the mean value of the CA on each side of the drop.

The ionic conductivity σ_i of the composite samples with IL was measured at RT using an Autolab PGSTAT-12 (Eco Chemie), at frequencies between 500 mHz and 50 kHz, using a constant volume support equipped with gold blocking electrodes placed within a Buchi TO 50 oven, and it was calculated as previously described in **Equation 3.2** in **Chapter 3**. The electrical DC conductivity of neat PLGA samples was measured by IV curves, using a Keithley 6487 picoammeter/voltage source.

The magnetic properties of the PLGA2+Fe_3O_4 samples were evaluated by measuring the magnetization (M_H) along the field direction of the magnetic field (H), up to 18 kOe, with a Microsense 2.2 Tesla Vibrating Sample Magnetometer (VSM). The Law of Approach to Saturation, as described by **Equations 2.1** and **2.2** (described in **Chapter 2**), was then applied to determine the saturation magnetization (M_S) [28, 29].

Once M_S is known for all the samples, **Equation 3.3** (as described in **Chapter 3**) was used to determine the effective NP content in the composite samples [8].

The tensile characteristics of the samples were evaluated in specimens with approximately 8 mm width. Each specimen had their thickness measured and registered, as well as their exact width. Stress-strain measurements were conducted by a universal testing machine (Shimadzu model AG-IS), with a load cell of 50 N, with a grip separation of about 15 mm, at RT, with a testing speed of 1 $mm.min^{-1}$ for 20 minutes or until rupture of the specimen. Initially, a single specimen per sample was tested, but the nature of the fiber specimens returned irregular results, caused by individual fibers either breaking randomly, so 3 specimens, for each filler wt.%, were tested, with mean results calculated.

The indirect cytotoxicity of the processed samples was evaluated by using the procedure described in **Section 5.2.3.2** (**Chapter 5**).

Finally, for the degradation studies, circular specimens were cut with approximately 1.5 cm^2, and placed in a 24-well culture plate with 1mL of a sterile phosphate-buffered saline solution (PBS, pH 7.4), and placed in an oven at 37 ^oC for 3, 7 and 14 days.

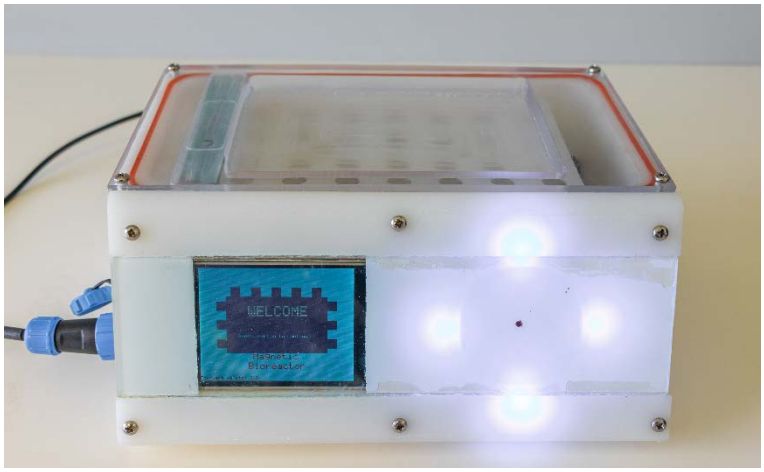

Figure 6.2. Magnetic bioreactor [30, 31] utilized to provide active magnetic stimuli to the processed samples

After each period, the corresponding specimens were removed from the culture plate, placed in previously-weighed aluminium foil, and left to dry at 37 ºC for 24 h, before being weighed again and the mass loss registered. Furthermore, additional specimens with NP (5, 10 and 15 wt.%) were placed in a magnetic bioreactor [30, 31] (**Figure 6.2**), for dynamic magnetic stimuli, where they were subjected to 5 min of magnetic stimulation, at 0.3 Hz for a displacement of 16 mm (Active Cycle 1), followed by 25 min of rest (Rest Cycle 1). These cycles were repeated for 16 h (Active Cycle 2), and then the samples were left resting for 8h (Rest Cycle 2).

6.3. Results and discussion

6.3.1. Morphological features, vibrational spectra and wettability

6.3.1.1. Morphology

The morphology of the electrospun fibers and films with different filler contents was analyzed by SEM. **Figure 6.3 a-f** shows representative SEM images of neat, 5 and 15 filler wt.% fiber mats and films, for both fillers.

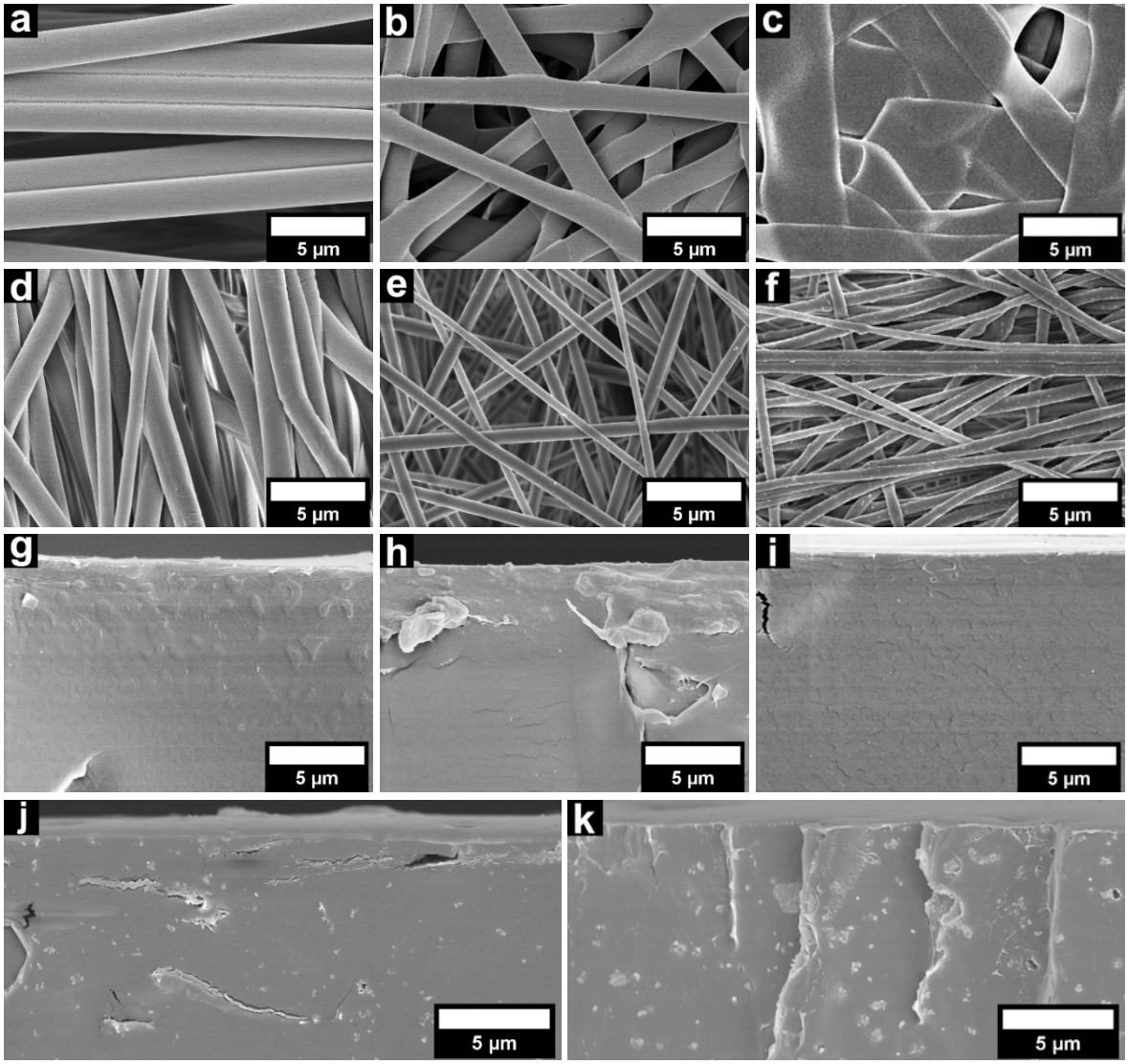

Figure 6.3. Representative SEM images of the samples. Surface of electrospun fiber mats: a) PLGA1; b) PLGA1+IL 5%; c) PLGA1+IL 15%; d) PLGA2; e) PLGA2+Fe_3O_4 5%; f) PLGA2+Fe_3O_4 15%. Cross-section of the films: g) PLGA; h) PLGA+IL 5%; i) PLGA+IL 15%; j) PLGA+Fe_3O_4 5%; k) PLGA+Fe_3O_4 15%.

Independently of the co-solvent system, PLGA oriented electrospun fibers are obtained (**Figure 6.3 a-f**). Upon IL incorporation into the PLGA matrix (**Figure 6.3 b-c**), the 5 wt.% concentration leads to the formation of fibers with a random orientation and the fusion of some small fibers.

With increasing IL content (**Figure 6.3 a-c**), fibers flatten, growing larger and tending to collapse and form flat ribbons, fusing with nearby ones (**Figure 6.3-c**), which made it not

possible to analyze their individual diameters for the fibers with the highest IL wt.%. The inclusion of Fe_3O_4 NPs, on the other hand, resulted in the opposite effect, and thinner fibers were obtained as NPs content increases. It was verified that adding even low quantities of a filler resulted in a noticeable decrease in PLGA fiber orientation (**Figure 6.3 a-f**), for the same processing parameters. The diameter distribution of the fibers is presented as a box plot [32] in **Figure 6.4**.

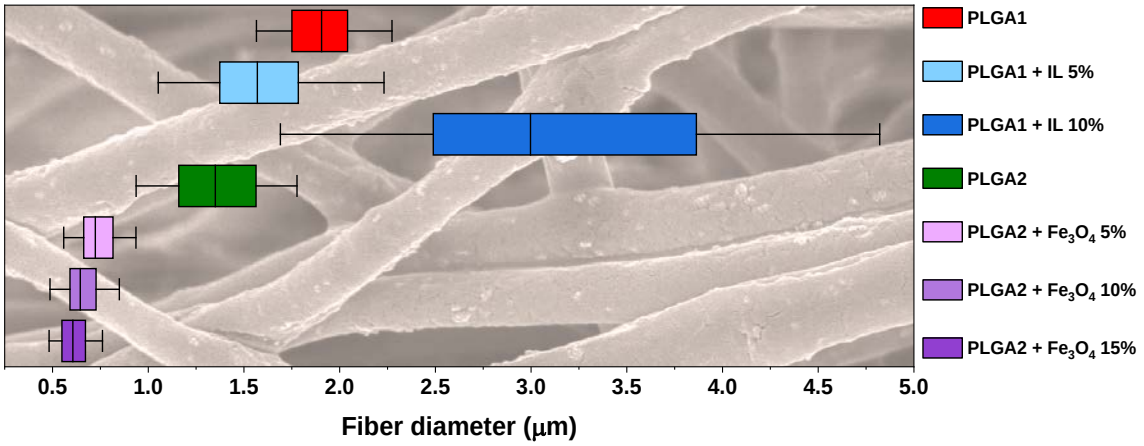

Figure 6.4. Tukey-style box plot with the diameters of the processed fibers (background: PLGA2+Fe_3O_4 15% fibers).

PLGA1 fibers present a mean diameter of 1.92 ± 0.24 µm, which initially decreased with the introduction of the IL to 1.64 ± 0.39 µm for PLGA1+IL 5%, the formation of ribbons and their merging resulting in a strong increase to 3.26 ± 1.04 µm for PLGA1+IL 10%. The initial fiber-thinning effect has been previously reported and is attributed to the ionic charges from the IL leading to a higher jet stretching [20, 33], with the subsequent increase in diameter with increasing IL content a result of the previously mentioned fiber flattening. Regarding the fibers with NPs, neat PLGA2 presents a mean diameter of 1.36 ± 0.28 µm, and the introduction of the NPs results in a reduction of the mean diameters, to 0.75 ± 0.13 µm for PLGA2+Fe_3O_4 5%, 0.67 ± 0.12 µm for PLGA2+Fe_3O_4 10% and 0.62 ± 0.09 µm for PLGA2+Fe_3O_4 15% fibers.

The morphology of the PLGA films and PLGA film composites was also evaluated by SEM. As shown in **Figure 6.3-g**, PLGA films present a non-porous, homogeneous compact surface, and remains so independently of the IL wt.% (**Figure 6.3 g-i**) or NPs wt.% (**Figure 6.3 j-k**), the latter being observed homogeneously distributed all along the PLGA matrix.

In order to determine the distribution of both IL and NPs into the PLGA fibers and films, a surface SEM-EDX analysis was performed, to detect specific elements present in either the IL (sulfur, S) or the NP (iron, Fe) (**Figure 6.5**). The uniform distribution of S element indicates that the IL is homogeneously distributed in the PLGA matrix, regardless of their morphology. Similar homogeneous distribution is observed for Fe in PLGA+Fe_3O_4 composites, although a few NP agglomerates could be identified in the films.

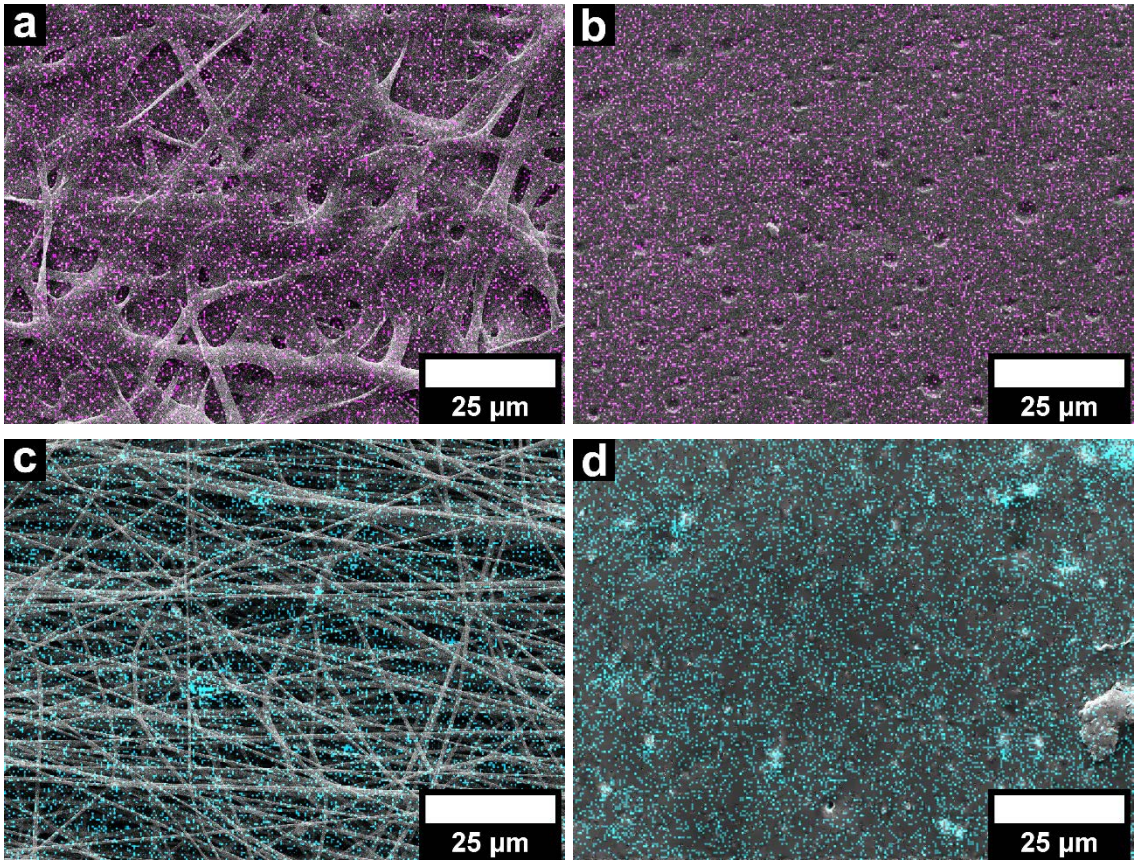

Figure 6.5. Representative EDX distribution maps of the fillers in samples of PLGA1+15% IL a) fibers and b) film; PLGA2+15% Fe_3O_4 c) fibers and d) film.

Further analysis by AFM was performed on representative samples with 0 and 15 wt.% of Fe_3O_4 and IL. The resulting 3D images and accompanying roughness data are presented in **Figure 6.6**.

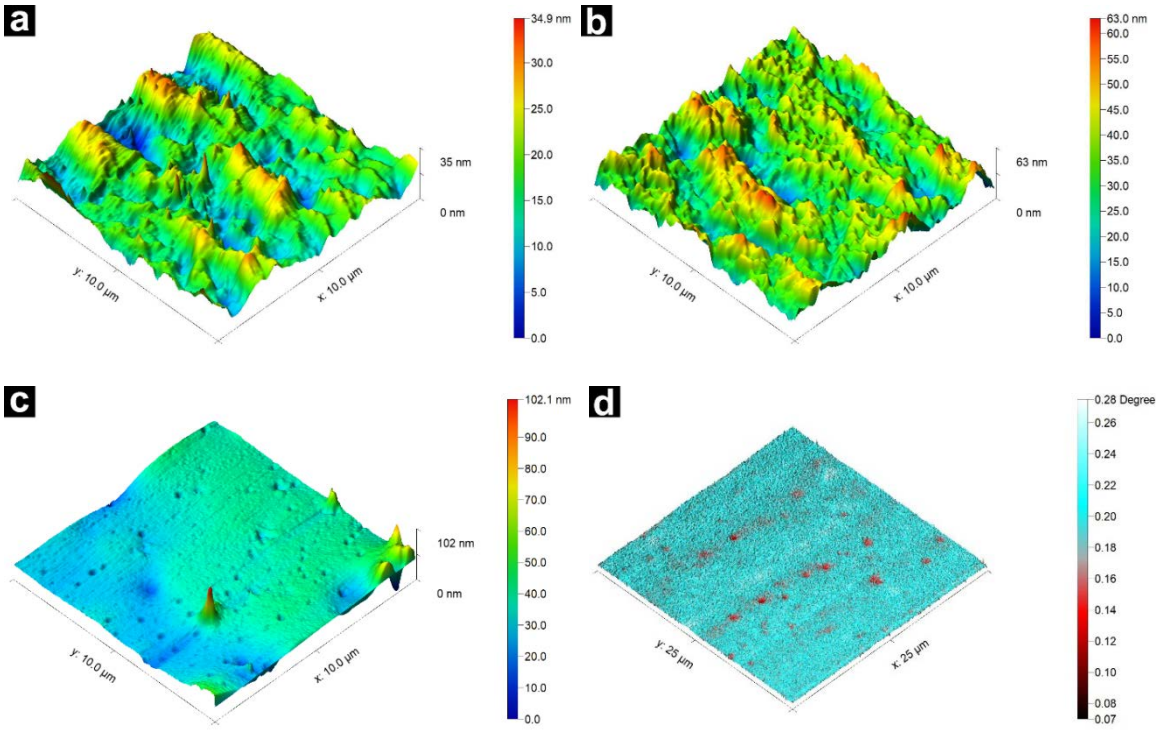

Figure 6.6. 3D AFM topographic images of the surface of the films: a) PLGA; b) PLGA+IL 15%; c) PLGA+Fe_3O_4 15%. d) Phase-lift MFM of the PLGA+Fe_3O_4 15%.

The AFM analysis reveals that the introduction of the IL leads to changes in the surface topography of the materials, with the IL incorporation increasing the mean roughness of the films from 3.84 to 6.58 nm, as observed in **Figure 6.6 a-b**. A similar effect, although with reduced magnitude, was observed for the films with Fe_3O_4 NPs, with the mean roughness increasing to 5.07 nm (**Figure 6.6-c**). These results, and the increase in surface roughness from the introduction of IL, are in line with those observed in the literature and are related to the heterogeneities related to the presence of IL in different parts of the surface of the samples [34]. Phase-lift MFM analysis (**Figure 6.6-d**) of the PLGA+Fe_3O_4 15% film sample confirms both the presence of some agglomerates and the good overall distribution of the NPs, as indicated by SEM and SEM-EDX analysis. These results are summarized in **Table 6.3**.

Table 6.3. Roughness data of the representative samples (Sq is RMS roughness and Sa is Mean roughness)

Sample	PLGA	PLGA+IL 15%	PLGA+Fe_3O_4 15%
Sq (nm)	4.84	8.36	6.46
Sa (nm)	3.84	6.58	5.07

6.3.1.2. Vibrational spectra

FTIR-ATR measurements were performed (**Figure 6.7**) to identify possible chemical changes or interactions as a result of the incorporation of fillers in the polymer matrix

The characteristic bands of PLGA [35], CO bands (1090-1172 cm^{-1}, for C-O-C stretch), and CH_3 (1386-1452 cm^{-1}, for C-H stretching vibration of methyl groups), remain unchanged in the PLGA spectra of the different samples, independently of the presence of filler and sample morphology, thus indicating that the processing conditions have no relevant effect on the vibrational spectra of the PLGA and that there are no strong interactions between fillers and polymer matrix, as no band shifts of new bands are observed (**Figure 6.7**).

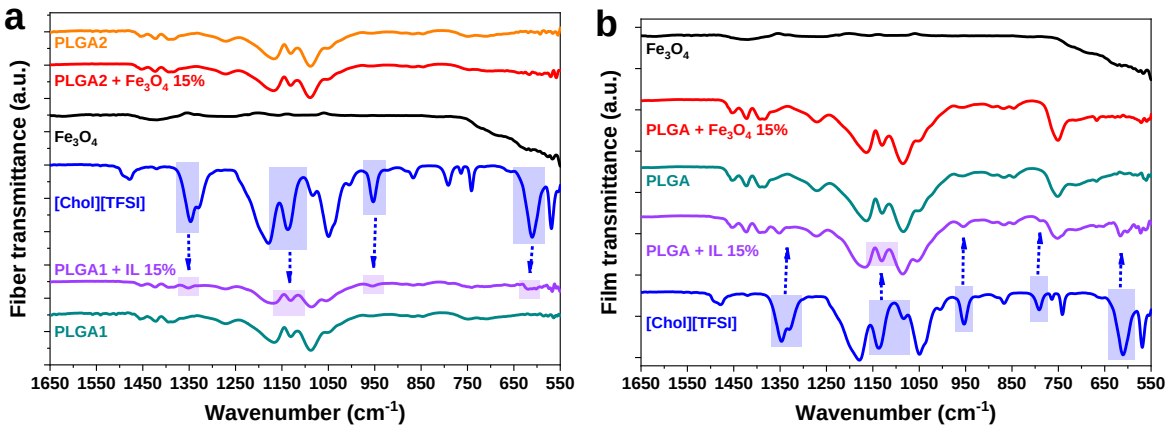

Figure 6.7. Representative FTIR-ATR spectra for PLGA+IL and PLGA+Fe_3O_4: a) electrospun fibers and b) films. [Chol][TFSI] and Fe_3O_4 spectra are provided as well. Arrows indicate areas where the influence of the fillers was detected

The presence of the IL in both PGLA hybrid materials can be identified by the presence of specific characteristic bands of [Chol][TFSI] (**Figure 6.7**). The following bands are observed in both morphologies of the composites with IL: the absorption bands at 1347 cm^{-1}, related to a twisting vibration of the CH_2 molecule in the [Chol] cation; the bands in the region between 1136 cm^{-1} and 1083 cm^{-1}, causing a flattening of the existing peaks in PLGA and are attributed, respectively, to a symmetric stretching vibration of SO_2 molecule in [TFSI] anion and to a stretching vibration of CO molecule in [Chol] cation; the band at 953 cm^{-1} (enhancing an existing peak of PLGA) is attributed to a rocking vibration of CH_3 molecule in [Chol] cation; the band at 791 cm^{-1}, attributed to a stretching vibration of CS molecule in the [TFSI] anion; and the band at 610 cm^{-1}, attributed to an antisymmetric bending of SO_2 molecule in [TFSI] anion. All of these bands are observed independently of the sample morphology [36, 37].

6.3.1.3. Wettability

The effect of both IL and NPs into the surface wettability of the samples was evaluated by CA measurements (**Figure 6.8**).

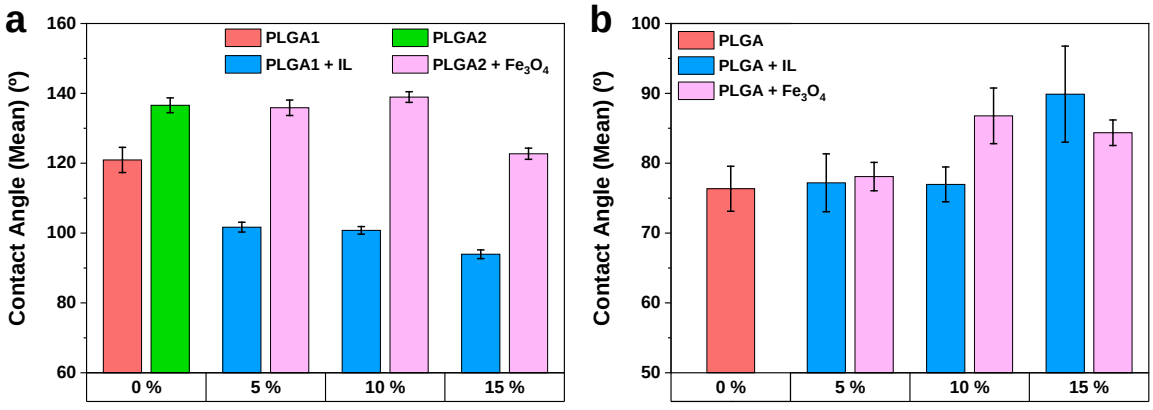

Figure 6.8. CA measurements of neat PLGA (1 and 2), PLGA+IL and PLGA+Fe_3O_4 for a) electrospun fiber mats and b) films.

The incorporation of [Chol][TSFI] into the PLGA matrix of electrospun fibers leads to a decrease of the CA, from ~121º for neat PLGA1 to ~94º for PLGA1+IL 15%, due to the hygroscopic nature of ILs. As for the Fe_3O_4 NPs, their effect on PLGA fibers was observed only for the highest wt.%, decreasing the CA from ~137º for neat PLGA2 to ~123º for PLGA2+Fe_3O_4 15%. The films with NPs behaved similarly to those with IL, and in these composites the increase in rugosity translates in an increase in hydrophobicity.

Thus, although the incorporation of low concentrations of fillers into PLGA films results in no relevant variations of the CA, the higher concentrations (15% wt. IL, 10% wt. Fe_3O_4) lead the composite to become more hydrophilic, which is attributed both to the nature of the fillers and the increase in rugosity, as shown in the AFM analysis.

6.3.2. Thermal and mechanical properties

6.3.2.1. Thermal properties

The influence of both IL and Fe_3O_4 NPs into the thermal properties of PLGA was evaluated by DSC and TGA measurements. **Figure 6.9 a-b** shows the DSC thermograms of electrospun fibers and films, respectively.

Due to the amorphous nature of the selected PLGA formulation, no melting temperature is present in the samples. The glass transition temperature (T_g) of neat PLGA fiber mats is observed between 47 and 52 °C. Independently of the filler type and content, the T_g is be observed in both composite electrospun fibers. (**Figure 6.9-a**). Nevertheless, a small decrease in T_g is observed for the PLGA2 fiber mats, attributed to their smaller diameter and more compact microstructure, as previously shown in the SEM images.

The inclusion of the IL results in a decrease of the T_g, as observed in **Figure 6.9-a**, from 51 ºC (PLGA1 fibers) to 39 ºC (PLGA1+IL 15%), a result of the plasticizing effect of the IL [38]. On the other hand, the inclusion of Fe_3O_4 NP results in a small increase in T_g, from 48 ºC (PLGA2 fibers) to 52 ºC (PLGA2+Fe_3O_4 15%), as the electrostatic interactions of the NPs with the polymer chain decrease polymer chain mobility [39]. In the composite polymer films (**Figure 6.9-b**), the T_g could not be identified.

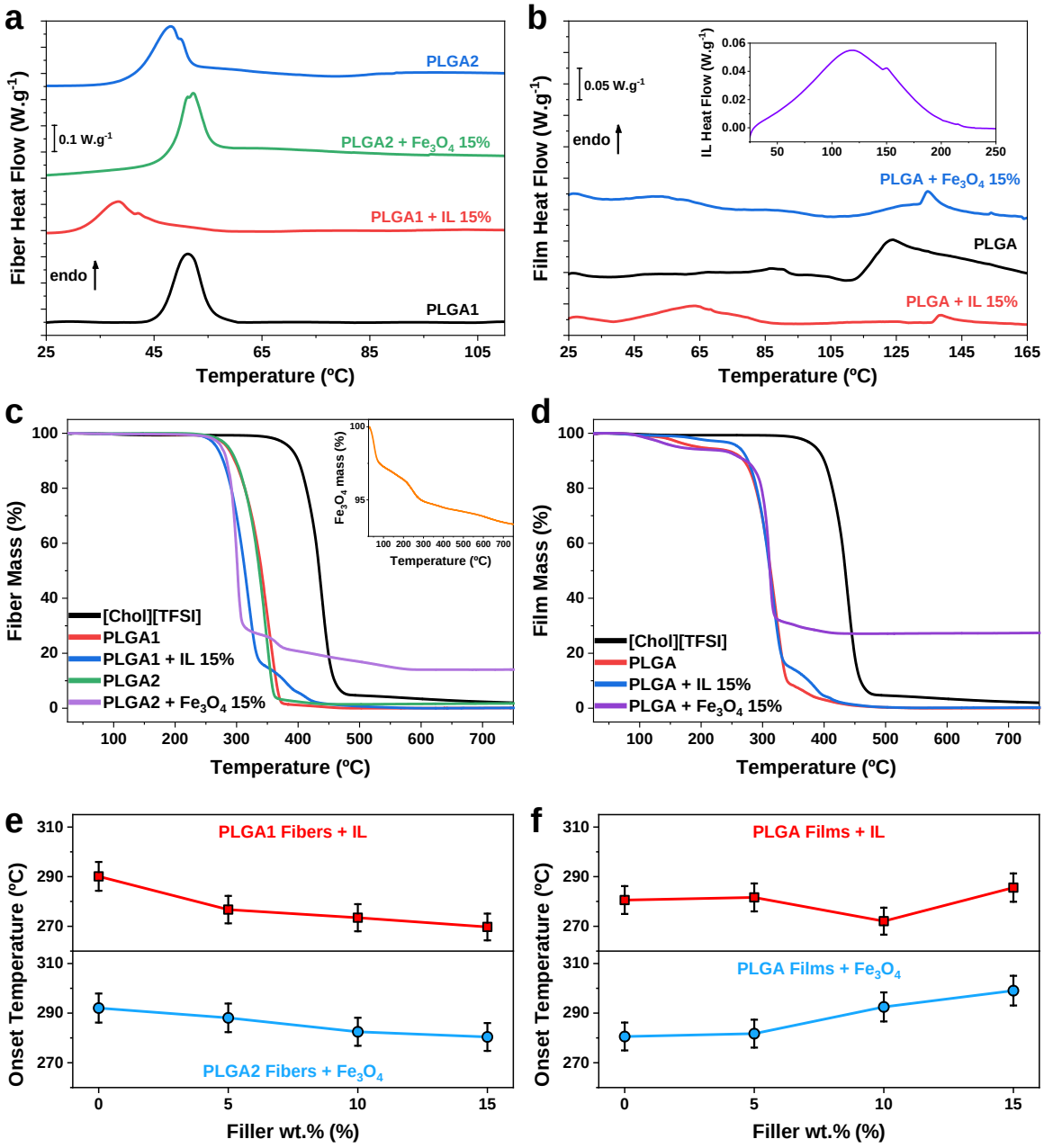

Figure 6.9. Representative DSC thermograms for a) electrospun fiber mats, and b) films (inset, thermogram for [Chol][TFSI]). Representative TGA curves for: c) electrospun fiber mats (inset, for Fe_3O_4 NPs), and d) films. Variation of the onset temperature for polymer degradation as function of filler wt.% for: e) electrospun fiber mats and f) films.

The thermal stability of the samples was assessed by TGA (**Figure 6.9 c-d**). Independently of the processing conditions and sample morphology, PLGA presents a single degradation step at ~290ºC corresponding to random chain scissions of the polymer chains [40] (**Figure 6.9 c-d**).

Upon the inclusion of IL into PLGA fibers, an additional degradation step is observed, between 350-370º, corresponding to the degradation of the IL [41] (for the PLGA1+IL fibers), as well as a reduction of the thermal stability of the polymer fibers (**Figure 6.9-e**). The PLGA2+Fe_3O_4 fibers present a similar behavior, corresponding to the degradation of the polymer in the interface region of the NPs.

For the film samples (**Figure 6.9-d**), two degradation steps are observed for the neat PLGA and the PLGA+Fe_3O_4 films. The first step (~140 ºC for neat PLGA, between 90-125 ºC for the PLGA+Fe_3O_4 film) is attributed to the release of bound water and the degradation of impurities present in the samples, such as residual solvents, and the second (~280 ºC for neat PLGA, and 280-300 ºC for the PLGA+Fe_3O_4 films) corresponds to the polymer degradation. Contrary to the fibers, the inclusion of fillers results in an overall increase of the thermal stability of the polymer films (**Figure 6.9-f**), which is very small for the inclusion of IL and more pronounced for the inclusion of Fe_3O_4 NPs. Furthermore, the inclusion of the IL results in the appearance of a third degradation step for the films, corresponding to the IL degradation. These results are summarized in **Table 6.4**.

Table 6.4. Onset temperatures for the film samples. Associated error of ± 2%

	PLGA+IL			PLGA+Fe_3O_4	
Sample, Filler wt.% (%)	**1st onset (ºC)**	**2nd onset (ºC)**	**3rd onset (ºC)**	**1st onset (ºC)**	**2nd onset (ºC)**
Fiber, 0	290.11	-	-	292.04	-
Fiber, 5	276.73	355.78	-	288.10	372.31
Fiber, 10	273.46	364.04	-	282.48	351.32
Fiber, 15	269.72	367.27	-	280.39	355.92
Film, 0	139.93	280.57	-	139.93	280.57
Film, 5	118.61	281.63	355.37	123.26	281.74
Film, 10	120.68	272.06	373.90	106.48	292.50
Film, 15	163.12	285.59	369.04	93.28	299.05

6.3.2.2. Mechanical Properties

In order to determine the influence of both fillers into the mechanical properties of PLGA fibers and films, stress-strain measurements were performed. Representative stress/strain curves are presented in **Figure 6.10**. The consistency of the PLGA1+IL 15% fibers was not adequate to conducting this test, having a gel-like consistency due to high IL content, so the PLGA1+IL 10% sample is presented for comparison.

The stress/strain curves, for both sample morphologies, display the typical behavior of PLGA [42], with an initial elastic region in the 1.3-2.6% strain region for the fibers, and 0.7-2.5% for films, followed by a clear yielding and a plastic deformation region. PLGA1 fibers presented much less mechanical resistance than PLGA2 fibers, breaking at ~11% strain, while PLGA2 fibers broke at ~55%, with PLGA films not breaking before the end of the test. The IL increased PLGA1 fibers resistance, with breaking occurring at ~110% strain for PLGA1+IL 10%, while the NP reduced the resistance of the fibers to breakage, which occurred at ~70% for PLGA2+Fe_3O_4 15%. None of the composite films reached the rupture strain before the end of the test.

From the stress/strain curves presented in **Figure 6.10 a-b**, the Young modulus and the elongation at yield of the specimens was calculated, and presented in **Figure 6.10 c-f**.

From this data, it can be seen that the IL causes the Young modulus of the PLGA fibers to decrease from about 5336 ± 22 Pa for PLGA1, to 3595 ± 22 Pa for PLGA1+IL 5% and 2615 ± 124 Pa for PLGA1+IL 10%. As for the influence of the Fe_3O_4 NPs, there is an overall decrease of the Young modulus, from 3330 ± 28 Pa for PLGA2 to 2665 ± 24 Pa for PLGA2+Fe_3O_4 5% and 1754 ± 9 Pa for PLGA2+Fe_3O_4 10%, before a marked increase to 2958 ± 13 Pa for the PLGA2+Fe_3O_4 15%. It was also observed that, while the inclusion of Fe_3O_4 NPs does not greatly affect the elongation at yield of the PLGA fibers, the IL does, reducing it to about half at 10 wt.% of IL. These Young moduli values indicate that both fillers act as defects for the composite PLGA fiber mats, which is in agreement with the literature [42].

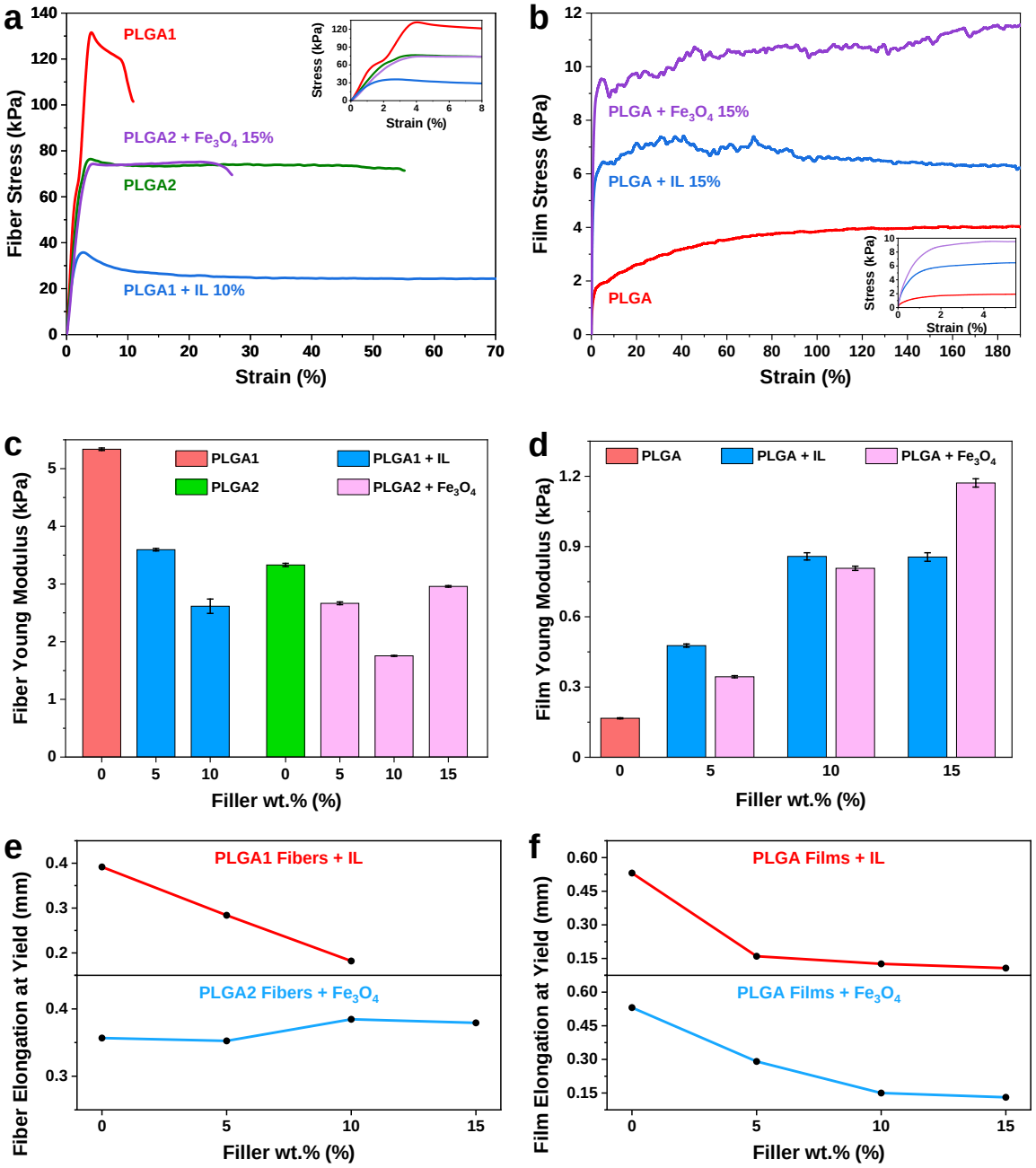

Figure 6.10. Representative stress/strain curves for: a) fibers (inset, detail of curves at low strain), and b) films (detail of curves at low strain). Young Modulus as a function of filler wt.% for: c) fibers and d) films. Elongation at yield as a function of filler wt.% for e) fibers and f) films.

Regarding the composite films, both fillers cause an increase in the Young modulus, from 167 ± 2 Pa for PLGA to 855 ± 18 Pa for PLGA+IL 15%, and to 1171 ± 18 Pa for PLGA+Fe_3O_4 15%, acting therefore as reinforcements for the material [43].

The introduction of the fillers resulted in a decrease of the elongation at yield of the films with increasing filler concentration, very rapidly for the IL composite samples and more gradual for the NP ones.

6.3.3. Functional response

6.3.3.1. Ionic Conductivity

The ionic conductivity as a result of the presence of cations and anions from the IL of both PLGA+IL morphologies with 15 wt.% of IL was evaluated by impedance spectroscopy measurements. **Figure 6.11-a** shows the typical Nyquist profiles obtained at RT and the characteristic semicircle of these measurements that occurs due to the charge transfer processes.

The ionic conductivity of the different PLGA+IL samples was calculated using **Equation 3.2**, the results presented in **Figure 6.11-b**. Both samples present a similar behaviour and it is possible to observe that an increase in temperature results in an increase in the ionic conductivity, attributed to an increase of the segmental motion of the polymer chains [44].

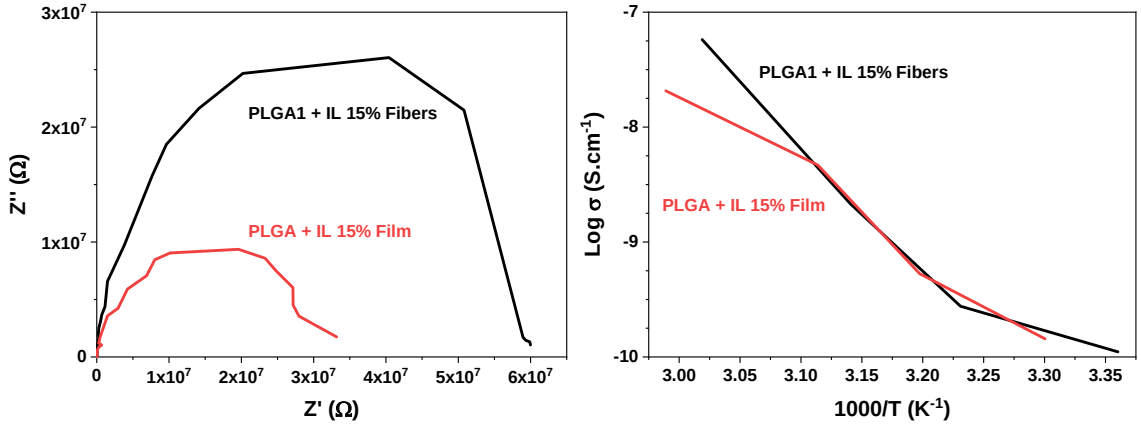

Figure 6.11. a) Nyquist plot at RT and b) Arrhenius plots for the ionic conductivities of PLGA+IL electrospun membranes and films.

PLGA+IL 15% fibers present an ionic conductivity of 1.11 x 10^{-10} S.cm^{-1}, while the ionic conductivity of PLGA+IL 15% films is 1.44 x 10^{-10} S.cm^{-1}, compared to the electrical conductivity of neat PLGA of 1.79 x 10^{-14} S.cm^{-1} for films and of 1.35 x 10^{-14} for fiber mats.

Overall, the presence of the IL allowed to increase the electrical conductivity of the polymer in 4 orders of magnitude, due to the presence of the mobile charged species provided by the incorporation of the IL.

6.3.3.2. Magnetic properties

VSM was used to obtain the hysteresis curves of the samples with magnetic NP content, determine the magnetic characteristics of the composites, and the real NP content within the samples. **Figure 6.12 a-b** shows the expected ferrimagnetic [18] hysteresis curves of the PLGA+Fe_3O_4 samples, at room-temperature.

From the insets present in **Figure 6.12 a-b**, it is observed that Fe_3O_4 NPs present a maximum magnetization of ~68 emu.g^{-1} at ~15 kOe applied magnetic field, and the aforementioned ferrimagnetic behavior (**Figure 6.12 a-b**, left insets). All samples reach M_S at ~15 kOe, and M_S increases with NP content, from 2.35 emu.g^{-1} for PLGA2+Fe_3O_4 5% fiber mats to 7.43 emu.g^{-1} for PLGA2+Fe_3O_4 15% fiber mats, and from 2.47 emu.g^{-1} for PLGA+Fe_3O_4 5% films to 9.21 emu.g^{-1} for PLGA+Fe_3O_4 15% films (**Table 6.5**).

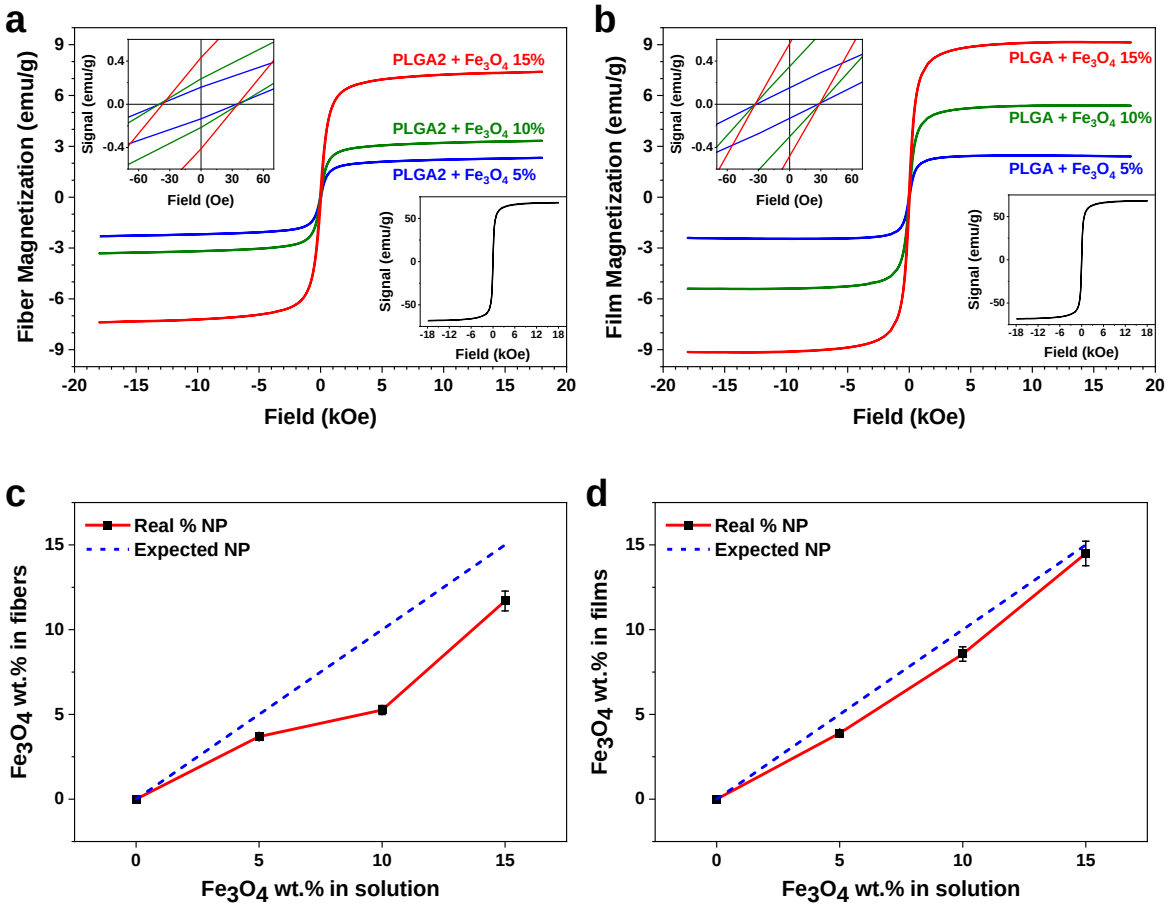

Figure 6.12. RT hysteresis loops for: a) PLGA2+Fe_3O_4 fiber mats, and b) PLGA+Fe_3O_4 films; left inset: Detail of the respective hysteresis loops; right inset: RT hysteresis loop for pure Fe_3O_4 NP. Relation between the wt.% of Fe_3O_4 NP within the solution and those within: c) PLGA2+Fe_3O_4 fibers, and d) PLGA+Fe_3O_4 films. The blue dotted line indicates the linear theoretical behavior.

The wt.% of NPs within the PLGA samples was evaluated using **Equation 3.3**. **Figure 6.12 c-d** and **Table 6.5** show the effective NP content in each sample, its evolution versus the theoretical values, and the resulting yield. The variations in yield between the samples are attributed to particle deposition, particularly during the electrospinning process, that result in some loss.

Table 6.5. NP yields in the PLGA Fe_3O_4 composite fibers.

Sample	M_S (emu/g)	wt.% Fe_3O_4 in sample (%)	Experimental Yield (%)
Fe_3O_4 NPs	68.21	100.00	-
PLGA2+Fe_3O_4 5% Fibers	2.35	3.69	73.81
PLGA2+Fe_3O_4 10% Fibers	3.34	5.26	52.60
PLGA2+Fe_3O_4 15% Fibers	7.43	11.69	77.95
PLGA+Fe_3O_4 5% Film	2.47	3.89	77.83
PLGA+Fe_3O_4 10% Film	5.44	8.56	85.62
PLGA+Fe_3O_4 15% Film	9.21	14.50	96.65

6.3.3.3. Cytotoxicity and degradability assays

Although PLGA is approved for use in medical devices [11], the introduction of fillers in the polymer matrix can lead to cytotoxic effects. In this way, the cytotoxicity of the different PLGA composites with IL and NPs was evaluated. The study of metabolic activity of the C2C12 myoblasts, assessed by MTS assay, was applied to all samples and the results after 72 h are presented in **Figure 6.13**.

According to the ISO standard 10993-5, samples are considered cytotoxic when cells suffer a viability reduction larger than 30%. The measured cell viability values for the PLGA samples with IL revealed that the fibers became cytotoxic, as well as the films with the exception of the PLGA+IL 5% film. Cytotoxicity is neither observed for the PLGA1 nor PLGA2 fibers and for the PLGA films, or as is described in the literature, in situations where the IL is encapsulated in non-degradable fibers, preventing the release of the toxic [TFSI] anion [20]. Thus, the cytotoxicity observed for all of the PLGA+IL samples is attributed to an increase in acidity of the medium, due to the degradation of the polymer and the subsequent presence of its acid byproducts [45], and the release of encapsulated [Chol][TFSI] [24].

In contrast to this, the introduction of the Fe_3O_4 NPs did not cause any cytotoxicity in the samples, regardless of the wt.% of the filler or the morphology of the polymer. Therefore, whereas the processed samples with Fe_3O_4 NPs can be used for biomedical applications independently of the filler content and morphology, the samples with IL can be just be used in the form of films and for filler content up to 5% wt.

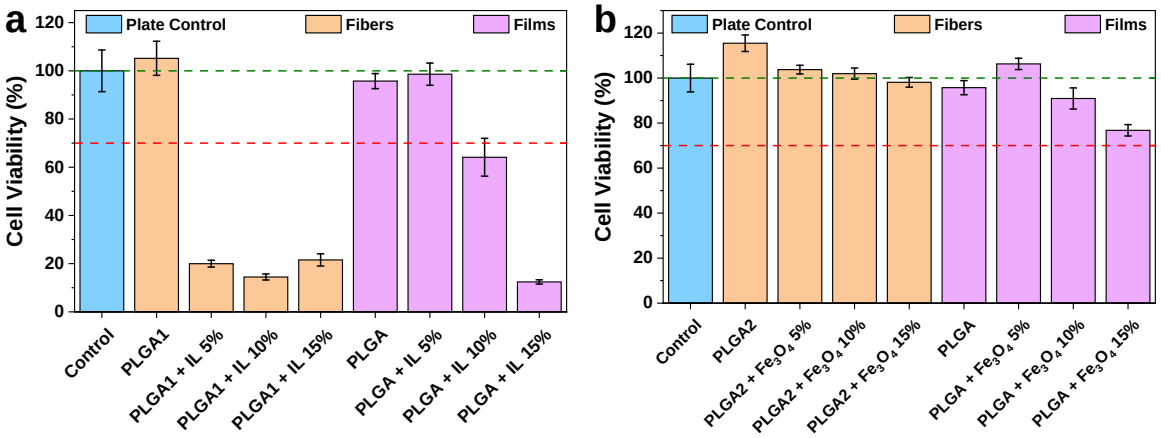

Figure 6.13. Cell viability assay of C2C12 myoblast cells after 72 h for PLGA samples with: a) IL; b) Fe_3O_4 (Relative cell activity presented as percentage of the negative control with n = 4 ± SD).

For biomedical applications in general, and TE specifically, the time-frame of degradable materials is a relevant issue to properly relate to the tissue regeneration time. The degradation times of PLGA, in the 50:50 co-polymer ratio, are usually described as being between 1-2 weeks to 1-2 months [10, 15, 46]. However, no studies have been conducted on the effect of active magnetic stimulation on the degradation rates of this polymer. **Figure 6.14** details the results of both the static and the dynamic degradation assay conducted on the PLGA2 pristine fiber mat samples and the corresponding composites with 15% wt. Fe_3O_4, as well as for the pristine PLGA films and the corresponding magnetic composites with 15% wt. Fe_3O_4. Additionally, and for a complementary qualitative analysis, representative photos from the samples are presented in **Figure 6.15.**

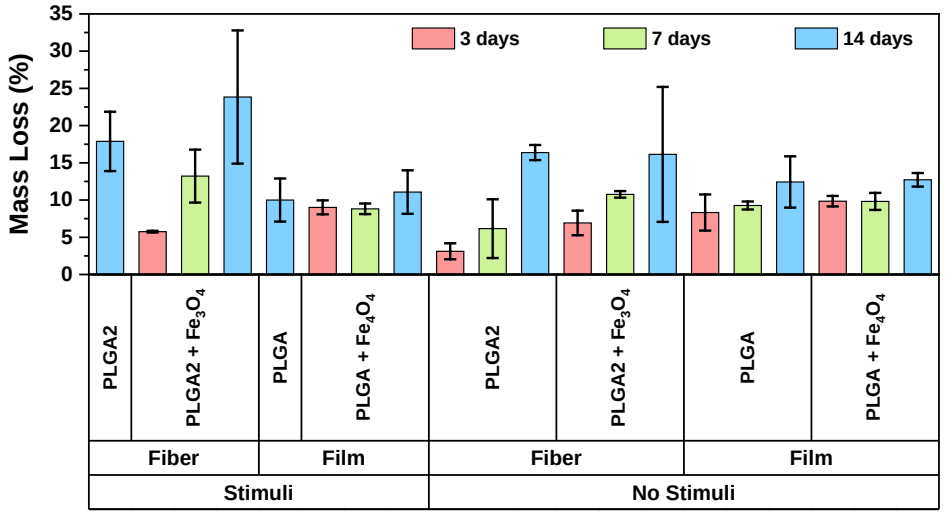

Figure 6.14. Mass loss from active and passive degradability assays for the PLGA samples.

PLGA degrades by a hydrolytic bulk degradation process, via random scission mechanism, with an initial degradation stage where a sharp molecular weight reduction is accompanied by negligible mass loss, followed by a period where the loss of mass increases sharply [47]. The byproducts of PLGA degradation are lactic acid and glycolic acid, which are removed from living organisms via the renal system [12], but *in vitro* conditions may result in an apparent increase of toxicity of the material due to an increase in acidity of the medium.

Figure 6.14 shows that the samples without NPs do not register relevant variations in the degradation pattern with the application of dynamic magnetic stimuli, as corresponding to non-magnetic materials, and it is verified that the fiber mat samples degrade at a faster rate than the film samples. This is attributed to the larger surface to volume ratio of the fibers when compared to the bulk film, which allows a faster water diffusion and increased mass loss rate [48].

The introduction of Fe_3O_4 NPs, however, has a profound effect on the degradation of both composite fibers and films. After 3, 7 and 14 days, the fiber samples under static conditions presented mean mass losses of 7, 11 and 16% (respectively), while those under dynamic conditions presented mean mass losses of 6, 13 and 24%. The film samples under static conditions had, at those same time intervals, mean mass losses of 10, 10 and 13% (respectively), while those under dynamic conditions presented mean mass losses of 9, 9 and 11%.

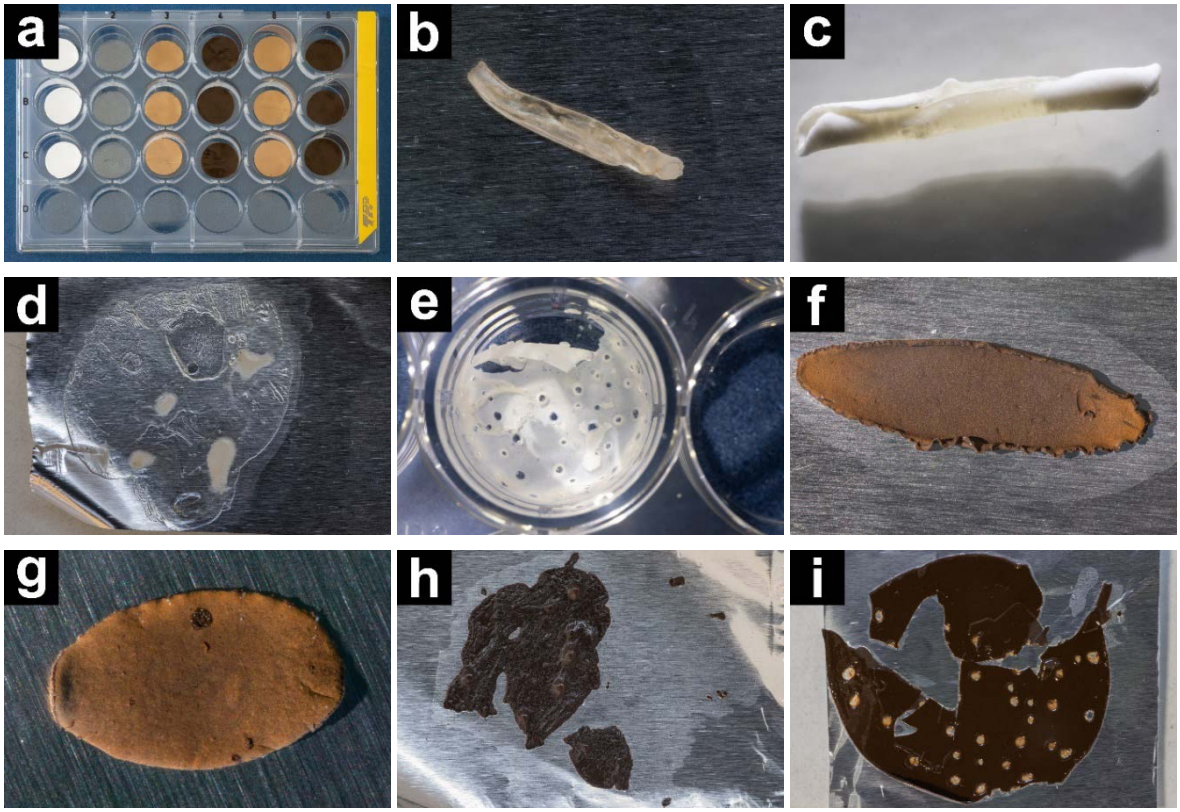

Figure 6.15. a) Samples before the assay. Representative photos, after 14-day degradation assay, of: b) PLGA2 fibers with active stimuli; c) PLGA2 fibers; d) PLGA film with active stimuli; e) PLGA film; f) PLGA2+Fe_3O_4 15% fibers with active stimuli; g) PLGA2+Fe_3O_4 15% fibers; h) PLGA+Fe_3O_4 15% films af with active stimuli; i) PLGA+Fe_3O_4 15% films.

Although the mass loss difference may not be large, by analysing **Figure 6.15**, it is observed that the samples subject to dynamic stimuli present a much larger loss of structural integrity, which indicates that, while the difference in mass of the samples may not be large, those subject to dynamic stimuli no longer have the capacity to be used for their intended purpose. This is particularly noticeable in the case of the composite films (**Figure 6.15**), where those subject to a dynamic stimulus, i.e. samples undergoing a magnetically induced magnetomechanical stimuli around the magnetic NP, lost not only some of their mass, but also their complete structural integrity. This proves that dynamic stimuli accelerates the degradation of a PLGA polymer matrix loaded with magnetic NPs in both of the analysed morphologies.

6.4. Conclusions

Magnetoactive and electroactive biodegradable polymer composites in the form of fibers and films were developed to support novel tissue engineering approaches for muscle tissue repair and regeneration, by embedding magnetic Fe_3O_4 NP and [Chol][TFSI] IL, respectively, in a PLGA matrix, with filler contents up to 15% wt.

Increasing wt.% of IL resulted in collapsed and fused fibers, with a larger diameter when compared to neat polymer, and in increased rugosity of the films. The T_g of the fibers, and the thermal stability in both morphologies, were both reduced by the inclusion of IL, with fiber wettability increasing while that of the films decreased. A decrease in the Young modulus and elongation at yield was verified for fibers, while the films presented an increase in the Young modulus and decreased in elongation. The ionic conductivity increased to 1.11×10^{-10} $S.cm^{-1}$ for the PLGA1+IL 15% fibers, and to 1.44×10^{-10} $S.cm^{-1}$ for PLGA+IL 15% films, a 4-order of magnitude increase when compared to neat PLGA. Only the film samples with 5% wt. of IL proved biocompatible.

Higher wt.% of Fe_3O_4 NP resulted in thinner fibers and increased rugosity of the films. The thermal stability was reduced for both morphologies, although no changes in the T_g were verified. Wettability increased for fibers with 15% wt. of NPs, and decreased for all film samples. The incorporation efficiency of the magnetic NPs was between 52 and 78% for fibers and 77-97% for films. A decrease in the Young modulus and increase in elongation at yield was verified for fibers, while the films presented an inverse behaviour. The degradability of the PLGA+Fe_3O_4 samples was increased with the application of dynamic magnetic stimulation, and all PLGA+Fe_3O_4 samples proved biocompatible. Thus, electro- and magnetoactive biodegradable materials have been developed, suitable for tissue regeneration applications.

6.5. References

1. Langer, R. and J.P. Vacanti, *Tissue Engineering.* Science, 1993. **260**(5110): p. 920-926. DOI: 10.1126/science.8493529

2. Greising, S.M., B.T. Corona, C. McGann, J.K. Frankum, and G.L. Warren, *Therapeutic Approaches for Volumetric Muscle Loss Injury: A Systematic Review and Meta-Analysis.* Tissue Eng Part B Rev, 2019. **25**(6): p. 510-525. DOI: 10.1089/ten.TEB.2019.0207

3. Ribeiro, S., A.C. Gomes, I. Etxebarria, S. Lanceros-Méndez, and C. Ribeiro, *Electroactive biomaterial surface engineering effects on muscle cells differentiation.* Materials Science and Engineering: C, 2018. **92**: p. 868-874. DOI: 10.1016/j.msec.2018.07.044

4. Jana, S., S.K.L. Levengood, and M. Zhang, *Anisotropic Materials for Skeletal-Muscle-Tissue Engineering.* Advanced materials (Deerfield Beach, Fla.), 2016. **28**(48): p. 10588-10612. DOI: 10.1002/adma.201600240

5. Ribeiro, S., T. Ribeiro, C. Ribeiro, D.M. Correia, J.P.S. Farinha, A.C. Gomes, C. Baleizão, and S. Lanceros-Méndez, *Multifunctional Platform Based on Electroactive Polymers and Silica Nanoparticles for Tissue Engineering Applications.* Nanomaterials (Basel, Switzerland), 2018. **8**(11): p. 933. DOI: 10.3390/nano8110933

6. Shehata, N., M.A. Abdelkareem, E.T. Sayed, D.E. Egirani, and A.W. Opukumo, *Smart Materials: The Next Generation*, in *Reference Module in Materials Science and Materials Engineering*. 2021, Elsevier. DOI: 10.1016/b978-0-12-815732-9.00062-0

7. Ribeiro, C., C.M. Costa, D.M. Correia, J. Nunes-Pereira, J. Oliveira, P. Martins, R. Gonçalves, V.F. Cardoso, and S. Lanceros-Méndez, *Electroactive poly(vinylidene fluoride)-based structures for advanced applications.* Nature Protocols, 2018. **13**(4): p. 681-704. DOI: 10.1038/nprot.2017.157

8. Hermenegildo, B., C. Ribeiro, L. Pérez-Álvarez, J.L. Vilas, D.A. Learmonth, R.A. Sousa, P. Martins, and S. Lanceros-Méndez, *Hydrogel-based magnetoelectric microenvironments for tissue stimulation.* Colloids and Surfaces B: Biointerfaces, 2019. **181**: p. 1041-1047. DOI: 10.1016/j.colsurfb.2019.06.023

9. Hitscherich, P., A. Aphale, R. Gordan, R. Whitaker, P. Singh, L.-h. Xie, P. Patra, and E.J. Lee, *Electroactive graphene composite scaffolds for cardiac tissue engineering.* Journal of Biomedical Materials Research Part A, 2018. **106**(11): p. 2923-2933. DOI: 10.1002/jbm.a.36481

10. Gentile, P., V. Chiono, I. Carmagnola, and P.V. Hatton, *An overview of poly(lactic-co-glycolic) acid (PLGA)-based biomaterials for bone tissue engineering.* International journal of molecular sciences, 2014. **15**(3): p. 3640-3659. DOI: 10.3390/ijms15033640

11. Chereddy, K.K., G. Vandermeulen, and V. Préat, *PLGA based drug delivery systems: Promising carriers for wound healing activity.* Wound Repair and Regeneration, 2016. **24**(2): p. 223-236. DOI: 10.1111/wrr.12404

12. Martins, C., F. Sousa, F. Araújo, and B. Sarmento, *Functionalizing PLGA and PLGA Derivatives for Drug Delivery and Tissue Regeneration Applications.* Advanced Healthcare Materials, 2017. **7**(1): p. 1701035. DOI: 10.1002/adhm.201701035

13. Lü, J.-M., X. Wang, C. Marin-Muller, H. Wang, P.H. Lin, Q. Yao, and C. Chen, *Current advances in research and clinical applications of PLGA-based nanotechnology.* Expert review of molecular diagnostics, 2009. **9**(4): p. 325-341. DOI: 10.1586/erm.09.15

14. He, Z., F. Rault, M. Lewandowski, E. Mohsenzadeh, and F. Salaün, *Electrospun PVDF Nanofibers for Piezoelectric Applications: A Review of the Influence of Electrospinning Parameters on the β Phase and Crystallinity Enhancement.* Polymers, 2021. **13**(2): p. 174. DOI: 10.3390/polym13020174

15. Middleton, J.C. and A.J. Tipton, *Synthetic biodegradable polymers as orthopedic devices.* Biomaterials, 2000. **21**(23): p. 2335-2346. DOI: 10.1016/s0142-9612(00)00101-0

16. Wang, Y., Y. Miao, G. Li, M. Su, X. Chen, H. Zhang, Y. Zhang, W. Jiao, Y. He, J. Yi, X. Liu, and H. Fan, *Engineering ferrite nanoparticles with enhanced magnetic response for advanced biomedical applications.* Materials Today Advances, 2020. **8**: p. 100119. DOI: 10.1016/j.mtadv.2020.100119

17. Shen, Y., B. Jiang, and Y. Xing, *Recent advances in the application of magnetic Fe3O4 nanomaterials for the removal of emerging contaminants.* Environmental Science and Pollution Research, 2021. DOI: 10.1007/s11356-020-11877-8

18. Li, Q., C.W. Kartikowati, S. Horie, T. Ogi, T. Iwaki, and K. Okuyama, *Correlation between particle size/domain structure and magnetic properties of highly crystalline Fe(3)O(4) nanoparticles.* Scientific reports, 2017. **7**(1): p. 9894-9894. DOI: 10.1038/s41598-017-09897-5

19. Correia, D.M., L.C. Fernandes, P.M. Martins, C. García-Astrain, C.M. Costa, J. Reguera, and S. Lanceros-Méndez, *Ionic Liquid-Polymer Composites: A New Platform for Multifunctional Applications.* Advanced Functional Materials, 2020: p. 1909736. DOI: 10.1002/adfm.201909736

20. Dias, J.C., D.C. Correia, A.C. Lopes, S. Ribeiro, C. Ribeiro, V. Sencadas, G. Botelho, J.M.S.S. Esperança, J.M. Laza, J.L. Vilas, L.M. León, and S. Lanceros-Méndez, *Development of poly(vinylidene fluoride)/ionic liquid electrospun fibers for tissue engineering applications.* Journal of Materials Science, 2016. **51**(9): p. 4442-4450. DOI: 10.1007/s10853-016-9756-3

21. Suominen, M., S. Lehtimäki, R. Yewale, P. Damlin, S. Tuukkanen, and C. Kvarnström, *Electropolymerized polyazulene as active material in flexible supercapacitors.* Journal of Power Sources, 2017. **356**: p. 181-190. DOI: 10.1016/j.jpowsour.2017.04.082

22. Haj Kacem, S., S. Galai, A. Pérez de los Ríos, F.J. Hernández Fernández, and I. Smaali, *New efficient laccase immobilization strategy using ionic liquids for biocatalysis and microbial fuel cells applications.* Journal of Chemical Technology & Biotechnology, 2017. **93**(1): p. 174-183. DOI: 10.1002/jctb.5337

23. Niesyto, K. and D. Neugebauer, *Synthesis and Characterization of Ionic Graft Copolymers: Introduction and In Vitro Release of Antibacterial Drug by Anion Exchange.* Polymers, 2020. **12**(9): p. 2159. DOI: 10.3390/polym12092159

24. Mena, I.F., E. Diaz, J. Palomar, J.J. Rodriguez, and A.F. Mohedano, *Cation and anion effect on the biodegradability and toxicity of imidazolium– and choline–based ionic liquids.* Chemosphere, 2020. **240**: p. 124947. DOI: 10.1016/j.chemosphere.2019.124947

25. Lu, L., C.A. Garcia, and A.G. Mikos, *In vitro degradation of thin poly(DL-lactic-co-glycolic acid) films.* Journal of Biomedical Materials Research, 1999. **46**(2): p. 236-244. DOI: 10.1002/(sici)1097-4636(199908)46:2<236::aid-jbm13>3.0.co;2-f

26. Liu, X., S.G. Baldursdottir, J. Aho, H. Qu, L.P. Christensen, J. Rantanen, and M. Yang, *Electrospinnability of Poly Lactic-co-glycolic Acid (PLGA): the Role of Solvent Type and Solvent Composition.* Pharmaceutical Research, 2017. **34**(4): p. 738-749. DOI: 10.1007/s11095-017-2100-z

27. Casasola, R., N.L. Thomas, A. Trybala, and S. Georgiadou, *Electrospun poly lactic acid (PLA) fibres: Effect of different solvent systems on fibre morphology and diameter.* Polymer, 2014. **55**(18): p. 4728-4737. DOI: 10.1016/j.polymer.2014.06.032

28. Morrish, A.H., *The Analysis of the Magnetization Curves of Bulk Material*, in *The Physical Principles of Magnetism*, R.J. Herrick, Editor. 2001, IEEE Press: USA. p. 382.403. DOI: 10.1109/9780470546581

29. Grössinger, R., *A critical examination of the law of approach to saturation. I. Fit procedure.* Physica Status Solidi (a), 1981. **66**(2): p. 665-674. DOI: 10.1002/pssa.2210660231

30. Castro, N., *Design, Construction and Validation of a New Generation of Bioreactors for Tissue Engineering Applications.*, in *Department of Graphic Design and Engineering Projects*. 2020, University of the Basque Country: Basque Country, Spain. Available from: http://hdl.handle.net/10810/50412.

31. Castro, N., M.M. Fernandes, C. Ribeiro, V. Correia, R. Minguez, and S. Lanceros-Méndez, *Magnetic Bioreactor for Magneto-, Mechano- and Electroactive Tissue Engineering Strategies.* Sensors, 2020. **20**(12): p. 3340. DOI: 10.3390/s20123340

32. Krzywinski, M. and N. Altman, *Visualizing samples with box plots.* Nature Methods, 2014. **11**(2): p. 119-120. DOI: 10.1038/nmeth.2813

33. Barbosa, J.C., D.M. Correia, R. Gonçalves, V. de Zea Bermudez, M.M. Silva, S. Lanceros-Mendez, and C.M. Costa, *Enhanced ionic conductivity in poly(vinylidene fluoride) electrospun separator membranes blended with different ionic liquids for lithium ion batteries.* Journal of Colloid and Interface Science, 2021. **582**: p. 376-386. DOI: 10.1016/j.jcis.2020.08.046

34. Mendes, J.P., J.M.S.S. Esperança, M.J. Medeiros, A. Pawlicka, and M.M. Silva, *Structural, morphological, ionic conductivity, and thermal properties of pectin-based polymer electrolytes.* Molecular Crystals and Liquid Crystals, 2017. **643**(1): p. 266-273. DOI: 10.1080/15421406.2016.1263111

35. Dixon, D., B.J. Meenan, and J. Manson, *PEG Functionalized Gold Nanoparticle Loaded PLGA Films for Drug Delivery.* Journal of Nano Research, 2014. **27**: p. 83-94. DOI: 10.4028/www.scientific.net/jnanor.27.83

36. Rey, I., P. Johansson, J. Lindgren, J.C. Lassègues, J. Grondin, and L. Servant, *Spectroscopic and Theoretical Study of (CF3SO2)2N- (TFSI-) and (CF3SO2)2NH (HTFSI).* The Journal of Physical Chemistry A, 1998. **102**(19): p. 3249-3258. DOI: 10.1021/jp980375v

37. de Souza, Í.F.T., V.H. Paschoal, K. Bernardino, T.A. Lima, L.L. Daemen, Y. Z, and M.C.C. Ribeiro, *Vibrational spectroscopy and molecular dynamics simulation of choline oxyanions salts.* Journal of Molecular Liquids, 2021. **340**: p. 117100. DOI: 10.1016/j.molliq.2021.117100

38. Scott, M.P., C.S. Brazel, M.G. Benton, J.W. Mays, J.D. Holbrey, and R.D. Rogers, *Application of ionic liquids as plasticizers for poly(methyl methacrylate).* Chemical Communications, 2002(13): p. 1370-1371. DOI: 10.1039/b204316p

39. Palacios, J., C. Albano, G. González, R.V. Castillo, A. Karam, and M. Covis, *Characterization and thermal degradation of poly(d ,l -lactide-co -glycolide) composites with nanofillers.* Polymer Engineering & Science, 2012. **53**(7): p. 1414-1429. DOI: 10.1002/pen.23396

40. Silva, M.F., A.A.W. Hechenleitner, J.M. Irache, A.J.A.d. Oliveira, and E.A.G. Pineda, *Study of Thermal Degradation of PLGA, PLGA Nanospheres and PLGA/Maghemite Superparamagnetic Nanospheres.* Materials Research, 2015. **18**(6): p. 1400-1406. DOI: 10.1590/1516-1439.045415

41. Hermenegildo, B., D.M. Correia, C. Ribeiro, J.P. Serra, L. Pérez, J.L. Vilas-Vilela, and S. Lanceros-Méndez, *Tuning magnetic response and ionic conductivity of electrospun hybrid membranes for tissue regeneration strategies.* Polymers for Advanced Technologies, 2022. DOI: 10.1002/pat.5596

42. Yu, Y., L. Kong, L. Li, N. Li, and P. Yan, *Antitumor Activity of Doxorubicin-Loaded Carbon Nanotubes Incorporated Poly(Lactic-Co-Glycolic Acid) Electrospun Composite Nanofibers.* Nanoscale research letters, 2015. **10**(1): p. 1044-1044. DOI: 10.1186/s11671-015-1044-7

43. Costa, P., J.R. Dios, J. Cardoso, J.J. Campo, C.R. Tubio, B.F. Gonçalves, N. Castro, and S. Lanceros-Méndez, *Polycarbonate based multifunctional self-sensing 2D and 3D printed structures for aeronautic applications.* Smart Materials and Structures, 2021. **30**(8): p. 085032. DOI: 10.1088/1361-665x/ac0cbe

44. Leones, R., C. Costa, A. Machado, J. Esperança, M.M. Silva, and S. Lanceros-Méndez, *Effect of Ionic Liquid Anion Type in the Performance of Solid Polymer Electrolytes Based on Poly (Vinylidene fluoride-trifluoroethylene).* Electroanalysis, 2015. **27**(2): p. 457-464. Available from.

45. Keles, H., A. Naylor, F. Clegg, and C. Sammon, *Investigation of factors influencing the hydrolytic degradation of single PLGA microparticles.* Polymer Degradation and Stability, 2015. **119**: p. 228-241. DOI: 10.1016/j.polymdegradstab.2015.04.025

46. Miller, R.A., J.M. Brady, and D.E. Cutright, *Degradation rates of oral resorbable implants (polylactates and polyglycolates): Rate modification with changes in PLA/PGA copolymer ratios.* Journal of Biomedical Materials Research, 1977. **11**(5): p. 711-719. DOI: 10.1002/jbm.820110507

47. Machatschek, R. and A. Lendlein, *Fundamental insights in PLGA degradation from thin film studies.* Journal of Controlled Release, 2020. **319**: p. 276-284. DOI: 10.1016/j.jconrel.2019.12.044

48. Uhrich, K.E., S.M. Cannizzaro, R.S. Langer, and K.M. Shakesheff, *Polymeric Systems for Controlled Drug Release.* Chemical Reviews, 1999. **99**(11): p. 3181-3198. DOI: 10.1021/cr940351u

Chapter 7

Conclusions and Future Work

Outline of main achievements and next steps.

This work aimed to address some of the current challenges that tissue engineering strategies face, regarding the development of materials that can mimic the microenvironments of organisms, so as to achieve proper tissue repair, particularly in the case of skeletal muscle tissue regeneration. To do so, it focused on the development and characterization of smart, polymer-based, microfibers and films, suitable for either *in vitro* or *in vivo* applications.

This chapter contains the final remarks, general conclusions of this thesis, and considerations for future work.

7.1. Conclusions

The number of individuals with tissue-related illnesses or injuries is on the rise, partly due to the aging of the population in industrialized countries. The resulting pressure on the lives of the patients, due to the increase in disability-adjusted life years, and, on healthcare systems, makes the development of strategies that do not rely on classic therapies or organ transplants a pressing necessity. Tissue engineering (TE) is currently the main approach to solve this problem, but it still requires the development of new materials capable of mimicking the natural microenvironments of tissues, in terms of their structure, biochemistry, and provided stimuli.

In this context, this thesis has been focused on the development of new smart materials, capable of delivering piezoelectric, electric and mechanical stimuli, tuned and targeted for both *in vitro* and *in vivo* tissue regeneration therapies. This main goal has been achieved, with several non-degradable and biodegradable composite materials that have been developed and characterized, aimed at regeneration strategies for specific tissues.

Different materials have been developed and characterized: a hybrid of a biodegradable hydrogel and composite microspheres of piezoelectric poly(vinylidene fluoride) (PVDF) and magnetic cobalt ferrite ($CoFe_2O_4$) nanoparticles (NP), in order to create a biocompatible magnetoelectric material for tissue regeneration; oriented and non-oriented piezoelectric PVDF microfibers were combined with the ionic liquid (IL) choline bis(trifluoromethylsulfonyl)imide ([Chol][TFSI]) and with magnetite (Fe_3O_4) NPs, resulting in materials with improved conductivity and magnetic properties; PVDF microfibers were also coated with polyaniline (PANI) or polypyrrole (PPy) conductive polymers, creating biocompatible materials with both piezoelectric and conductive properties without metallic elements or cytotoxicity from materials such as graphene; fibers and films of poly(hydroxybutyrate-co-hydroxyvalerate) (PHBV) and PVDF were blended with the IL choline acetate ([Chol][Ac]), creating biocompatible, and in the case of PHBV, biodegradable materials for *in vitro* and *in vivo* TE applications that require conductive materials; and finally, poly(lactide-co-glycolide) (PLGA), with NP loads of Fe_3O_4 and IL loads of [Chol][TFSI] was processed into fibers and films that possess conductive and magnetic properties.

Of these novel materials, most of them were completely biocompatible, and some presented a restricted biocompatible profile, dependent on filler concentration and morphology. Therefore, it was shown that the methods chosen are suitable for processing these materials for biomedical applications.

The fillers influence was verified in more than in the biocompatibility of the materials. Regarding the morphology of materials processed by electrohydrodynamic techniques, the chosen metal oxide NPs have a profound effect, and it was observed that a small weight percentage (wt.%) greatly reduces the diameter of spheres or the thickness of fibers, while these values increase slightly with the increase of NP content, due to attractive effects between the NPs causing their agglomeration. The behavior of ILs as fillers is not as consistent, with the outcome of their influence depending largely on IL-polymer interactions, and on the conductivity of the IL itself. On films, fillers also have a marked influence, and their introduction results in the appearance of pores, and in an increase of the surface rugosity in the order of 50-100%.

Regarding the influence of the fillers on the physico-chemical nature of the materials, although their presence could be detected by Fourier-Transform Infrared Spectroscopy (FTIR), by the appearance of new vibration bands, their impact varied from very limited to null, with no changes to the typical vibration bands of the polymers, and with the electroactive β-phase of PVDF either remaining stable or increasing by a very small amount.

As for the influence of the fillers on the crystallinity degree of PVDF, a low wt.% of [Chol][TFSI] encourages the crystallization of PVDF fibers, but, at higher concentrations, the IL inhibits crystallite formation; it was also shown that any concentration of [Chol][Ac] has a detrimental effect on the crystallinity degree of PVDF fibers, while a 5 wt.% of this IL promotes crystallization in PVDF films, with higher wt.% acting as an inhibitory agents as well. The crystallinity degree of PHBV fibers is similarly affected, and it was observed that IL concentrations higher than 5 wt.% hinder the crystallization in fibers. PHBV films, on the other hand, showed to changes in their crystallization degree with the incorporation of [Chol][Ac].

Regarding the ionic conductivity (σ_i) of the composite polymers, the inclusion of either IL, at a concentration of 15 wt.%, increased the σ_i of their polymer matrix between 3 and 4 orders of magnitude, while the electric conductivity (σ) of the coated PVDF fibers coated with PPy was of 1.19 $S.m^{-1}$, and that of those coated with PANI was of 3.84×10^{-3} $S.m^{-1}$,

The wettability of PVDF and PHBV fibers and films increased upon the introduction of [Chol][Ac], drastically so in the case of PHBV materials, which became absorbent. PVDF fibers coated with PANI or PPy also became absorbent. As for of PLGA fibers and films, the wettability of the fibers increased upon introduction of the IL, an effect only verified for the highest wt.% of Fe_3O_4 NPs. As for the films, both fillers cause an increase in the hydrophobicity.

Fe_3O_4 NPs and the [Chol][TFSI] IL caused a decrease in the Young modulus of PLGA fibers, with the IL also reducing the elongation at yield of the fibers, while the inclusion of Fe_3O_4 had the opposite effect. For PLGA films, both fillers augmented the Young modulus of the composites and reduced their elongation at yield. The active stimulation assay, allowed by the inclusion of the Fe_3O_4 NPs, greatly increased the degradation of the composite PLGA materials. Finally, although PLGA fibers and films with Fe_3O_4 demonstrated to be bio compatible, the same was not verified for all the samples with the [Chol][TFSI] IL, with only the PLGA+IL 5% film sample presenting a suitable compatibility profile.

7.2. Future work

In this thesis, new composite materials for TE applications have been developed. Nevertheless, the work presented here should not be seen as finalized, or as the final word on these materials. Science is a continuously evolving body of knowledge, and, taking inspiration from that most famous 1969 quote, this work is a small step for a man, on a long road for Mankind.

For example, and taking the specific case of electrospun fibers, their morphology can be further studied, by optimizing both the preparation conditions, such as filler wt.%, as well as the processing parameters. Their diameter can be tuned both for smaller or larger diameters, as can the diameter distribution maps, in order to further perfect the microenvironment for specific types of cells and tissues.

Similarly, the new properties of the materials, granted by the inclusion of the chosen fillers can also be tuned. For instance, the NP loads can be tuned in order to obtain more or less sensitivity to external magnetic fields, as well as the resulting effect. Similarly, and as demonstrated, changes in the filler load can influence a number of other properties of the materials, such as their wettability or surface roughness. These two parameters would be influenced by any change in the filler wt.%, and therefore a study could be conducted in order to determine the ideal load of each of the studied fillers, in their respective polymers and morphologies, so as to obtain the most adequate physico-chemical effects and properties for specific cells and tissues.

One other such parameter that depends on the load of the fillers, specifically ILs, is conductivity. Similar to what was described before, studies to determine the ideal ratio between IL wt.% and the resulting conductivity of the composite polymer scaffolds could be performed in the future.

Any of these studies and future works would also need to tackle concerns with biocompatibility and, in some cases, biodegradability. As shown in **Chapter 5**, differences in the concentration of a filler, such as an IL in that specific chapter, can result in different toxicological profiles of a material and mark it as unsuitable for biomedical applications. Therefore, any and all future studies intent on optimizing these materials would also need to take in account the relation between concentration and toxicity, so that composite materials currently identified as adequate for biomedical use do not become unsuitable for such.

Still on the matter of biocompatibility, the assessment of it is often conducted with indirect measurement of the cytotoxicity of a material to very specific cellular lines, often derived from animals. Further work can be performed on this, by expanding the *in vitro* tests to include the human cells and tissues intended to be regenerated; by conducting cytotoxicity tests of the cells and tissues in direct contact with the materials, in order to evaluate effects of the surface morphology of the materials in their suitability for biomedical applications; and in conducting in vivo trials as well, for the materials intended for such application, in order to understand if the behavior of the material suffers any changes when implanted in a living host and surrounded by all the mechanisms, organs and systems that are present in a living animal and not in a laboratory model.

Finally, different approaches may be taken for the concepts discussed in this thesis. Different ILs may be introduced in these polymeric matrixes, with the intent of improving their biocompatibility or their conductivity. Different NPs and polymers, with different biocompatible and biodegradable profiles, may be used to process microspheres to be introduced in a hydrogel intent for *in vivo* TE.

Therefore, and notwithstanding the interesting results obtained and presented in this work, the possible research paths and possibilities are numerous, interesting and challenging.

Curriculum Vitae & Contributions

Bruno Filipe da Costa Hermenegildo

BCMaterials – Basque Center for Materials, Applications and Nanostructures

Edificio Martina Casiano, Planta 3

Parque Científico UPV/EHU

Barrio Sarriena, s/n, 48940 Leioa, Bizkaia

email: bruno.hermenegildo@bcmaterials.net

ORCID: https://orcid.org/0000-0003-4854-8596

PERSONAL INFORMATION

Gender: Male

Date of Birth: November 26th, 1984

Language skills: Portuguese, English, Spanish

RESEARCH TOPICS

Polymers, composite materials, biophysics, smart materials, tissue engineering.

Polymer processing, electrospinning, DSC, TGA, FTIR, magnetic properties, mechanical tests, degradation tests.

EDUCATION

PhD:	University of the Basque Country – UPV/EHU (2018-Present)
Thesis Title:	Electro and magnetically active polymer-based hybrid microenvironments for muscle tissue engineering
Advisors:	Prof. Senentxu Lanceros-Méndez (BCMaterials) Prof. Leyre Pérez-Álvarez (UPV/EHU)

MSc Biophysics: University of Minho – Braga, Portugal (2018)

BSc Physics: University of Minho – Braga, Portugal (2016)

RESEARCH GRANTS

Research Grantee, February 2017 – September 2017

"Functional and smart materials and surfaces for advanced applications – microfluidic devices for ecotoxicological studies"

Advisor: Senentxu Lanceros-Méndez

Scientific Initiation Grantee, May 2015 – July 2015

"Electrobio – preparation and characterization of polymer microspheres integrated in hydrogels"

Advisor: Senentxu Lanceros-Méndez

Scientific Initiation Grantee, November 2012 – February 2013

"Photophysical study of new fluorescent hydrogels"

Advisor: Elisabete Maria dos Santos Castanheira Coutinho

Scientific Initiation Grantee, February 2011 – May 2011

"Study of the interaction of fluorescent molecules with lipid membranes, with and without cholesterol, using UV-Vis molecular spectroscopy techniques"

Advisor: Elisabete Maria dos Santos Castanheira Coutinho

Research Initiation Grantee, October 2009 – September 2010

"Study of the interaction of fluorescent molecules with lipid membranes, with and without cholesterol, using UV-Vis spectroscopy techniques"

Advisor: Elisabete Maria dos Santos Castanheira Coutinho

RESEARCH STAYS ABROAD

MSc, ERASMUS+:

Basque Center for Materials, Applications and Structures, Derio, Spain (4 months; September-December 2017)

Advisor: Dr. Senentxu Lanceros-Méndez

PhD:

Universidade do Minho, Braga, Portugal (3 months; December-February 2019)

Advisor: Dr. Clarisse Marta de Oliveira Ribeiro

Universidade do Minho, Braga, Portugal (2 months; March-April 2021)

Advisor: Dr. Clarisse Marta de Oliveira Ribeiro

SCIENTIFIC PUBLICATIONS

Part of the thesis:

1. B. Hermenegildo, R. M. Meira, D. M. Correia, A.G. Díez, S. Ribeiro, J.P. Serra, C. Ribeiro, L. Pérez-Álvarez, José L. Vilas-Vilela, S. Lanceros-Méndez, *Biodegradable ionic and magnetically active microenvironments for tissue regeneration applications*. Submitted

2. B. Hermenegildo, R. M. Meira, A.G. Díez, D. M. Correia, S. Ribeiro, J.P. Serra, C. Ribeiro, L. Pérez-Álvarez, José L. Vilas-Vilela, S. Lanceros-Méndez, *Ionic liquid modified electroactive polymer-based microenvironments for tissue engineering*. Submitted

3. B. Hermenegildo, D. M. Correia, C. Ribeiro, J.P. Serra, L. Pérez-Álvarez, José L. Vilas-Vilela, S. Lanceros-Méndez, *Tuning magnetic response and ionic conductivity of electrospun hybrid membranes for tissue regeneration strategies*. Polymers for Advanced Technologies, 2022. DOI: 10.1002/pat.5596

4. Hermenegildo, B., C. Ribeiro, N. Peřinka, P. Martins, M. Trchová, M. Hajná, J. Stejskal, and S. Lanceros-Méndez, *Electroactive poly(vinylidene fluoride) electrospun fiber mats coated with polyaniline and polypyrrole for tissue regeneration applications.* Reactive and Functional Polymers, 2022. **170**: p. 105118. DOI: 10.1016/j.reactfunctpolym.2021.105118

5. Hermenegildo, B., C. Ribeiro, L. Pérez-Álvarez, J.L. Vilas, D.A. Learmonth, R.A. Sousa, P. Martins, and S. Lanceros-Méndez, *Hydrogel-based magnetoelectric microenvironments for tissue stimulation*. Colloids and Surfaces B: Biointerfaces, 2019. **181**: p. 1041-1047. DOI: 10.1016/j.colsurfb.2019.06.023

Other articles:

1. S. Ribeiro, M. Soares, B. Hermenegildo, V. Correia, A. García Díez, S. Lanceros-Méndez, C. Ribeiro, *Advanced electroactive microenvironments from bioactive polymers: a new conceptual weapon to address cancer*. Submitted

2. Correia, D.M., L.C. Fernandes, M.M. Fernandes, B. Hermenegildo, R.M. Meira, C. Ribeiro, S. Ribeiro, J. Reguera, and S. Lanceros-Méndez, *Ionic Liquid-Based Materials for Biomedical Applications.* Nanomaterials (Basel, Switzerland), 2021. **11**(9): p. 2401. DOI: 10.3390/nano11092401

3. Abreu, A.S., B.F.C. Hermenegildo, P.M.T. Ferreira, M.J.R.P. Queiroz, and E.M.S. Castanheira, *Interaction of fluorescent quinolin-2-one and coumarin derivatives including dipeptides with lipid bilayers.* RSC Advances, 2016. **6**(76): p. 72141-72148. DOI: 10.1039/c6ra14376h

4. Vilaça, H., G. Pereira, T.G. Castro, B.F. Hermenegildo, J. Shi, T.Q. Faria, N. Micaêlo, R.M.M. Brito, B. Xu, E.M.S. Castanheira, J.A. Martins, and P.M.T. Ferreira, *New self-assembled supramolecular hydrogels based on dehydropeptides.* Journal of Materials Chemistry B, 2015. **3**(30): p. 6355-6367. DOI: 10.1039/c5tb00501a

5. Hermenegildo, B.F., G. Pereira, A.S. Abreu, E.M.S. Castanheira, P.M.T. Ferreira, and M.-J.R.P. Queiroz, *Phenanthrenyl-indole as a fluorescent probe for peptides and lipid membranes.* Journal of Photochemistry and Photobiology A: Chemistry, 2011. **221**(1): p. 47-57. DOI: 10.1016/j.jphotochem.2011.04.022

CONTRIBUTIONS TO MEETINGS

1. **B. Hermenegildo**, R.M. Meira, D. Correia, L. Pérez-Álvarez, José L. Vilas-Vilela, S. Lanceros-Méndez. *Hybrid fibrous materials for advanced tissue engineering*. "NanoPT International Online Conference", University of Minho, Braga, Portugal, 23-24 September 2020. Available at http://confstreaming.archivephantomsnet.net/nanoPT2020/nanoPT2020_online_AbstractsBook.pdf. Oral contribution

2. **B. Hermenegildo**, D. Correia, L. Pérez-Álvarez, José L. Vilas-Vilela, S. Lanceros-Méndez. *Hybrid fibrous microenvironments for muscle tissue engineering*. "NanoBio&Med2019 International Conference", Barcelona, Spain, November 19-21, 2019. Available at http://nanobiomedconf.archivephantomsnet.net/FILES/nanoBioMed2019_Abstracts_Book.pdf. Poster contribution

3. **B. Hermenegildo**, C. Ribeiro, L. Pérez-Álvarez, José L. Vilas-Vilela, David A. Learmonth, Rui A. Sousa, P. Martins, S. Lanceros-Méndez. *Magnetically active hydrogel microenvironments for tissue stimulation.* "TNT2019 International Conference", San Sebastian/Donosti, Spain, September 30 - October 04 2019. Available at http://tntconf.archivephantomsnet.net/2019/TNT2019_abstractsbook.pdf. Oral contribution

4. **B. Hermenegildo**, A. R. Guimarães, C. Ribeiro, D.M.Correia, S. Lanceros-Méndez. *Hydrogels loaded with electroactive spheres for tissue engineering applications.* "XX Conferência Nacional de Física", University of Minho, Braga, Portugal, 8-10 September 2016. Available at https://eventos.spf.pt/ficheiros/files/Fisica2016_Resumos_VF.pdf. Oral contribution

5. **Ana C. L. Hortelão**, Helena Vilaça, Bruno F. C. Hermenegildo, Goreti Pereira, Bing Xu, Maria-João R. P. Queiroz, José A. Martins, Paula M. T. Ferreira, Elisabete M. S. Castanheira. *New biocompatible peptide-based hydrogels as drug nanocarriers*. "RICI6 - 6th Iberian Meeting on Colloids and Interfaces", Guimarães/Braga, Portugal, 8-10 July 2015. Available at http://hdl.handle.net/1822/37836. Poster contribution

6. **Ana Hortelão**, Bruno F. C. Hermenegildo, Helena Vilaça, Goreti Pereira, Bing Xu, Maria-João R. P. Queiroz, José A. Martins, Paula M. T. Ferreira, Elisabete M. S. Castanheira. *Biocompatible peptide-based hydrogels as nanocarriers for a new antitumoral drug*. "TNT2014 International Conference", Barcelona, Spain, 27-31 October 2014. Available at http://hdl.handle.net/1822/30743. Poster contribution

7. **A. S. Abreu**, E. M. S. Castanheira, B. F. Hermenegildo, M.-J.R.P. Queiroz, P.M.T. Ferreira. *Fluorescence studies of 3-amino-4-phenylquinolin-2-one in solution and in lipid membranes*. "XXII Encontro Nacional da Sociedade Portuguesa de Química", Braga, Portugal, 3-6 July 2011. Available at http://hdl.handle.net/1822/13600. Poster contribution

8. **Ana S. Abreu**, Elisabete M. S. Castanheira, B. F. Hermenegildo, Maria-João R.P. Queiroz and Paula M.T. Ferreira. *Interaction of new fluorescent 2-quinolinone and coumarin derivatives with phospholipid monolayers and lipid vesicles*. "RICI4 - 4th Iberian Meeting on Colloids and Interfaces", Porto, Portugal, 13-15 July 2011. Available at http://hdl.handle.net/1822/13598. Poster contribution

9. **Ana S. Abreu**, Bruno F. Hermenegildo, Goreti Pereira, Elisabete M.S. Castanheira, Paula M.T. Ferreira, Maria-João R.P. Queiroz. *Phenanthrenyl-indole as a fluorescent probe for peptides and lipid membranes*. "X Encontro Nacional de Fotoquímica", Porto, Portugal, 9-10 December 2010, Available at http://hdl.handle.net/1822/13803. Poster contribution

Copyright and Licencing information

Book cover

Composite cover from the following:

Anatomy figure:

Composite image adapted from the following licensed works by high_resolution – stock.adobe.com: #211792477; #211792601, #211792478; #212080083; #212079640.

Muscle fiber:

Image adapted from #305669795, by crevis – stock.adobe.com.

Nanoparticle rain:

Image adapted from #197080463, by vrx123 – stock.adobe.com.

Microfiber floor:

SEM image of PVDF fibers, colorized, by author.

Chapter 1. Introduction

Cover image:

Arrowhead adapted from "Pointe de flèche à pédoncule et épaulements en chaille", by Didier Descouens, and licensed under CC BY-SA 4.0. Original work available in https://commons.wikimedia.org/wiki/File:Fleche_Cartailhac_MHNT_PRE_2009.0.232.2_simple.jpg.

Agamemnon Mask adapted from "Agamemnon Mask", by Jebulon, and licensed under CC0 1.0. Original work available in https://commons.wikimedia.org/wiki/File:Agamemnon_mask_NAMA_Athens_Greece.jpg.

Screw adapted from "An old and rusted screw", by Subhrajyoti07, and licensed under CC BY-SA 4.0. Original work available in https://commons.wikimedia.org/wiki/File:An_old_and_rusted_screw.jpg.

Green bottle photograph, photo by the author.

Medical equipment adapted from photo in album "Medicines", by Bicanski, and licensed under CC0. Original work available in https://pixnio.com/media/medicine-medical-healthcare-health-equipment.

Figure 1.2

Silk adapted from "Silkworm cocoons (conforming to line) used to Yūki-tsumugi. In Oyama city, Japan", by タバコはマーダー, and licensed under CC BY-SA 4.0. Original work available in https://commons.wikimedia.org/wiki/File:Silkworm_cocoons_in_Japan_for_Yuki_tsumugi.jpg.

Nylon stockings adapted from "A girl wearing white shoes and skirt", by Beryl_snw, and licensed under CC0 1.0. Original work available in https://commons.wikimedia.org/wiki/File:A_girl_wearing_white_shoes_and_skirt;_April_2016_(04).jpg.

Rubber duck, photo by the author.

Figure 1.3

Copper statue of pharaoh Pepi I adapted from "By_ovedc_-_Egyptian_Museum_(Cairo)_-_085", by Ovedc, and licensed under CC BY-SA 4.0. Original work available in https://commons.wikimedia.org/wiki/File:By_ovedc_-_Egyptian_Museum_(Cairo)_-_085.jpg.

Painting of the Colossus of Rhodes adapted from "The Colossus of Rhodes" engraving, by Marten van Heemskerck, a Public Domain work of art.

Indonesian smiths adapted from "Hand-made Kris", by Sandhi Irawan, and licensed under CC BY-SA 4.0. Original work available in https://commons.wikimedia.org/wiki/File:Hand-made_Kris.jpg.

Figure 1.7

Composite of own work and the "Human skeletal and muscular system on female model" image, by Ryan Hoyme (massagenerds), licensed under CC0 1.0. Ryan Hoyme's original work is available in https://commons.wikimedia.org/wiki/File:Skeleton_and_muscles.png.

Chapter 7. Conclusions and Future Work

Cover image:

Remix from the following Public Domain works, licensed under CC0 1.0: "Microbiologist", https://openclipart.org/detail/253489/microbiologist, and "Nuclear Scientist", https://openclipart.org/detail/279068/nuclear-scientist-researcher, by Juhele.